Varga-Vass, Anna (2015) *Large-scale dynamic hydrofracturing, healing and fracture network characterization.* PhD thesis.

Large-scale dynamic hydrofracturing, healing and fracture network characterization

Anna Varga-Vass

BSc, MSc

Submitted in the fulfillment of the requirements for the degree of Doctor of Philosophy

School of Geographical and Earth Sciences
College of Science and Engineering
University of Glasgow

November 2015

Abstract

Permeability of a rock is a dynamic property that varies spatially and temporally. Fractures provide the most efficient channels for fluid flow and thus directly contribute to the permeability of the system. Fractures usually form as a result of a combination of tectonic stresses, gravity (i.e. lithostatic pressure) and fluid pressures. High pressure gradients alone can cause fracturing, the process which is termed as hydrofracturing that can determine caprock (seal) stability or reservoir integrity. Fluids also transport mass and heat, and are responsible for the formation of veins by precipitating minerals within open fractures. Veining (healing) thus directly influences the rock's permeability. Upon deformation these closed factures (veins) can refracture and the cycle starts again. This fracturing-healing-refacturing cycle is a fundamental part in studying the deformation dynamics and permeability evolution of rock systems. This is generally accompanied by fracture network characterization focusing on network topology that determines network connectivity. Fracture characterization allows to acquire quantitative and qualitative data on fractures and forms an important part of reservoir modeling.

This thesis highlights the importance of fracture-healing and veins' mechanical properties on the deformation dynamics. It shows that permeability varies spatially and temporally, and that healed systems (veined rocks) should not be treated as fractured systems (rocks without veins). Field observations also demonstrate the influence of contrasting mechanical properties, in addition to the complexities of vein microstructures that can form in low-porosity and permeability layered sequences. The thesis also presents graph theory as a characterization method to obtain statistical measures on evolving network connectivity. It also proposes what measures a good reservoir should have to exhibit potentially large permeability and robustness against healing.

The results presented in the thesis can have applications for hydrocarbon and geothermal reservoir exploration, mining industry, underground waste disposal, CO_2 injection or groundwater modeling.

Table of contents

List of tables

List of figures

Acknowledgements

This thesis is a result of a long journey; not just a physical one with moving –yet again- to a new country but also a personal journey. This PhD opened my mind to the great academic world, a world that I had no idea what it contained. It enlightened me, made me stronger and taught me to fight. It changed me emotionally and mentally. Certainly, as every PhD student I too thought I could not do it but it looks like I was wrong and I have many people to thank for it.

First and foremost, I would like to express my sincere gratitude to my supervisor, Dr. Daniel Koehn. His continuous academic and personal support throughout these three years was invaluable. The support I have received from him made this PhD possible. I hugely appreciate all the time he spent on me, his patience and his continuous attempt to reassure me when I lost confidence. I feel extremely honored that I had the opportunity to work with him. He certainly became one of my role models.

I would also like to thank the staff at the department. John Gilleece for preparing my thin sections and helping me with my fluid inclusion wafers. Peter Chung for all the technical support at the scanning electron microscope. Dawn Stewart Bradshaw and Namrata Lal for all the finance, whereas Jacqueline McKie and Margaret Jackson for the all the administrative support.

I am also very grateful to Enrique Gomez-Rivas from the University of Aberdeen for helping me with the fluid inclusion measurements and for the many insightful scientific discussions. Furthermore, I am thankful to Giancarlo Molli from the University of Pisa, who guided and accompanied us during the field work in Italy and shared us his extremely deep geological knowledge of the area. I thank Steven Roper from the School of Mathematics and Statistics, University of Glasgow, who I had extremely valuable discussions which eventually led me to the application of graph theory on geological networks. I would also like to thank Daniel Keszthelyi from the University of Oslo for providing me their flour experiment data. My former supervisor, Steffi Burchardt from the University of Uppsala also needs to be mentioned and thanked as she called my attention to this project.

I would like to gratefully acknowledge the funding source that allowed me to carry out research, attend conferences and thus travel to places I would have never gone. The project was carried out within the framework of the German Society for Petroleum and Coal Science and Technology (DGMK) and was funded by the companies ExxonMobil Production Deutschland GmbH, GDF SUEZ E&P Deutschland GmbH, RWE Dea AG and Wintershall Holding GmbH. I would like to thank the companies for their financial support and for their permission to publish the outcomes of this research.

I would also like to thank my internal examiner, Professor Roderick Brown, and my external examiner, Dr David Healy from the University of Aberdeen, for their reviews and suggestions that improved the thesis to its current form.

Special mention goes to Gary, Wendy, Uli and Nicolas who I have had the privilege to meet and to call them as my friends. Gary, who was initially just the grumpy IT guy but became very important to me. He always knew I would make it. Wendy, who not only put tons of energy in organizing workshops and travels for us but also brought the sunshine into my life. Her genuine caring and concern towards me gave me energy to push through hard times. Wendy, you are a gem! Uli and Nicolas, your friendship meant a lot. It is as simple as that.

I owe my deepest gratitude to my family. I cannot thank my parents enough for my upbringing, for their love and support. I would like to dedicate this thesis to them. They always believed in me and did not hide their proud towards me. The best and the highest education has always been a priority for them and they have pushed us kids all the way to accomplish this providing a solid ground for our futures. This is an invaluable gift, so thank you Mum and Dad.

Last but not least, I could have not accomplished this research without the love, support and patience of my husband, Miki. Even though there were times when the research seemed never ending, I was overwhelmed, depressed and felt like everything was so confusing and disordered, he was my rock and the one who I found comfort in. He has seen the worst version of Anna and yet he stood by me. I am extremely lucky to have a husband like him.

Author's declaration

I hereby declare and confirm that this thesis is my own work and materials from other sources have been properly and fully acknowledged. The thesis represents my interpretation of results and my own views. I also confirm that the presented material has not been submitted to any other degrees at the University of Glasgow or other institutions.

The thesis incorporates large amount of text and figures from *Vass, A., Koehn, D., Toussaint, R., Ghani, I., Piazolo, S., 2014: The importance of fracture-healing on the deformation of fluid-filled layered systems. Journal of Structural Geology, 67, 94-106*. The thesis author was the principal researcher who carried out all the experiments, interpreted the results, created the figures and wrote the entire paper. The text that is included from the paper appeared in the first draft of manuscript that none of the co-authors have seen or commented upon, therefore reflects the thesis author's own work and views.

Anna Varga-Vass

November 2015, Glasgow

1 Introduction

This chapter introduces and highlights all the basic terms andprocesses that are necessary to interpret the results and understand the conclusions of this thesis. The chapter starts with the examination of rock deformation, stress and strain, and then focuses on brittle deformation. The influence of fluid pressures in the deformation (e.g. hydrofracturing) will be then outlined. The fluid-rock interaction that could directly follow deformation is presented in the next subchapter, with an emphasis on transport modes and veins. The dynamic permeability subchapter then deals with the alternating cycles of deformation and fluid-rock interaction. Afterwards, the research motivation and questions, as well as the overall thesis structure are presented.

1.1 Rock deformation

Rocks are constantly subjected to external forces that could lead to deformation. This deformation might trigger significant changes in the rocks' behavior and therefore it is important to understand the mechanics behind the process.

Deformation is a collective term that refers to the transformation of a rock body. It is achieved by the combination of the four deformation elements: distortion (strain), translation, rotation and volume change (Fossen, 2010; van der Pluijm and Marshak, 2004). The result is a deformed rock due to an applied force to the body or its surface. Force triggers stress on a surface and at any given point in a body. Stress (σ) by definition is the force exerted on a unit area and therefore has the unit of N/m^2 or Pa. It is a tensor quantity and has a normal component acting perpendicular (σ_n) and a shear component acting parallel to a surface (σ_s). The stress state at a point can be expressed by a stress ellipsoid where the axes represent the principal stresses σ_1, σ_2, σ_3, where $\sigma_1 > \sigma_2 > \sigma_3$.

If the media has no or very low shear resistance, like fluids, the force acting on a unit surface area is called pressure (P). Pressure by definition has the same unit as the stress but is a scalar quantity, which means the magnitude is the same regardless of the direction. An example of this is the hydrostatic pressure which is the pressure exerted by a fluid column (fluid in rest) on a unit surface area. Hydrostatic pressure is therefore a function of the fluid density, gravitational acceleration and the height of the fluid column on a unit surface area. Not only fluids, but rocks can also experience pressures if we consider that they do not have shear resistance. The stress acting on it becomes independent of the direction leading to an isotropic stress state ($\sigma_1 = \sigma_2 = \sigma_3$). The pressure then is only controlled by the depth at which this rock sits, the rock density and the gravitational acceleration. This stress is called lithostatic pressure.

Deformation can be triggered by a variety of mechanisms and processes such as gravity-induced compaction, different tectonic forces (e.g. extension, compression), fluid pressures, thermal expansion, chemical reactions or induced stresses (e.g. drilling). The degree of deformation is not only affected by the stress and pressure, but also the temperature, rock fabric and grain size, fluid content, as well as the strain rate. An increase in temperature will weaken the rock which leads to fracturing at lower differential stresses. Pre-existing fabric in the rock, such as foliation, will influence the deformation characteristic depending on the orientation of the applied forces. The fabric gives the rock mechanical anisotropy, therefore might act as a preferred orientation for deformation. Increasing grain size in the brittle regime lowers the rock strength by providing larger planes of weakness (i.e. grain-grain contacts) where fracture propagation might take place (Eberhardt et al., 1999). Strain rate describes the rate at which a certain amount of distortion (strain) accumulates. It is defined by the elongation (length change divided by the initial length) per unit time. This means that for the same time if the strain rate is high, the rock undergoes larger deformation (i.e. it elongates more). Small strain rate will allow the rock to accommodate more plastic strain, whereas at increasing strain rate the rock might not be able to accommodate that much plastic strain and will fracture earlier. However, if the temperature is high even larger strain rates could cause a rock to deform without fracturing. It is quite clear that the different types of rocks behave differently in response to the same amount of strain and that the same amount of elongation is achieved by different magnitudes of stress.

The parameter that relates the stress to the strain (elongation) is called the Young’s modulus (E) (or stiffness). The Young’s modulus is a parameter that characterizes the elasticity of the material. It represents the resistance of a material to elastic deformation. An elastic material recovers to its original shape (original elongation) after the stress is removed. The Young's modulus is proportional to the applied stress and is inversely proportional to the elongation. This relationship is called the Hooke's Law and describes the linear elastic behavior of materials. Rocks can only deform elastically until they reach their elastic limit (yield stress). After this point the rock will deform where the strain is permanent and the material does not fracture. Fluids behave in a viscous manner where strain is non-recoverable. In this case the parameter viscosity (μ) provides the relationship between the stress and the strain rate. However, most of the materials behave in a complex manner in response to stress, therefore combinations of elasticity, plasticity and viscosity are needed to characterize the different rheologies of the systems.

If strain is distributed and the rock has not fractured, ductile deformation is taking place. However, after a rock has undergone some elastic and/or plastic deformation and the strain becomes localized, a rock can deform in a brittle manner. Ductile structures include folds, shear zones, whereas fractures and faults belong to the brittle structures. In the upper 10 km of the crust rocks mainly deform in a brittle manner, whereas below 10 km ductile deformation is becomes progressively more common (Fossen, 2010). As the research concerns mainly brittle structures and upper crustal rocks, I will focus on those here and will describe their formation.

1.1.1 Brittle failure and fractured rock systems

A solid material undergoes brittle deformation if it experiences fracturing and/or sliding. Brittle deformation does not necessarily involve failure; poorly consolidated sediments might undergo grain rotation or frictional sliding along grain contacts. Lithified sediments, on the other hand, can fail in a brittle manner which involves fracturing. Fractures are discontinuities in the rock where there is a reduction or loss of cohesion, and observable displacement. They form due to external and/or internal forces, when the tensile or shear strength of the rock is overcome. Fracture propagation takes places until (1) the strength cannot be overcome anymore, (2) the amount of fluid is not enough to maintain the high fluid pressures and/or (3) the crack initiation releases the driving effective stress (Oliver and Bons, 2001). Fractures can be of a variety of scales (micron to kilometer), and they are usually classified based on the displacement relative to their planes (Pollard and Segall, 1987). Mode I fractures show displacement perpendicular to the fracture plane and can be termed as extensional or tensile fractures (Fig. 1.1d). When the displacement is parallel to the fracture and propagation plane, failure is achieved by Mode II fractures (sliding or in-plane shear). Mode III fractures (tearing or out-of-plane shearing) represent the third category where the displacement is also parallel to the fracture plane but perpendicular to the propagation plane. As the same fracture exhibit both Mode II and III along its edges, one can collectively term these as shear fractures (Fig. 1.1f). Field evidence, lab and modeling experiments also show that there is a transition between the extensional and shear fractures (Engelder, 1999; Hancock, 1985; Koehn et al., 2005; Ramsey and Chester, 2004). These have been termed as hybrid fractures and show mixed-mode fracturing, i.e. both an extensional and shear component can be observed (Fig. 1.1e).

Since the stresses on a surface (plane) depend on the plane’s orientation, it is useful to analyze how the stress varies on different planes. A widely used 2D graphical representation of rock failure is the Mohr circle that, in combination with the Mohr-Coulomb-Griffith failure criterion, provides a key tool for describing all the possible stress states on planes and the occurring failure modes (Fig. 1.1). Plotting the σ_1 and σ_3 on the horizontal axis (σ_n) and finding the center by $(\sigma_1 + \sigma_3)/2$, one can construct the Mohr-circle. The diameter of the circle is the differential stress ($\Delta\sigma$) and each point on this circle represents a differently oriented plane. The α represents the angle between the σ_1 and the normal to the plane, which is the same as the angle between σ_3 and the plane (Fig. 1.1b). Stress states on a plane can be obtained by plotting double α from the center of the circle counterclockwise. By projecting this point onto the horizontal and vertical axis, the σ_n and σ_s can be found. Certainly, each plane has its conjugate pair which falls on the lower half of the circle. The stresses are the same magnitude but the shear stress differs in sign.

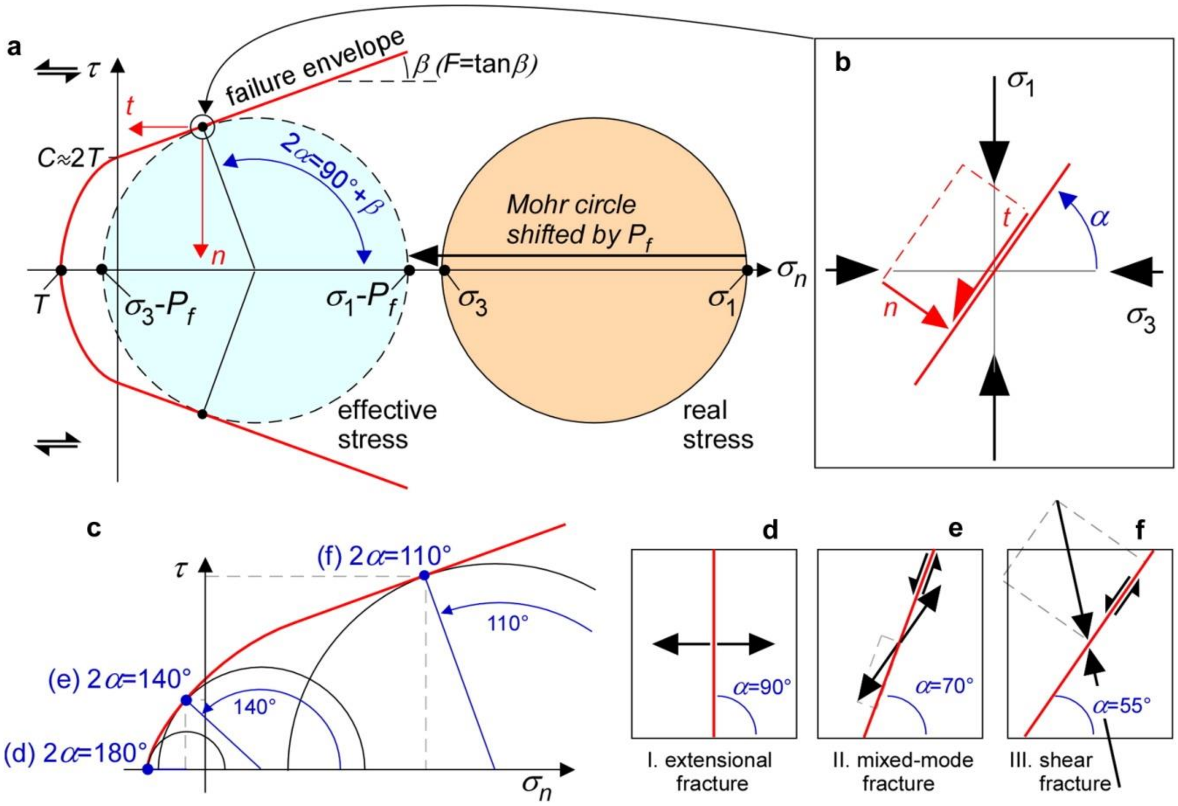

Fig. 1.1 Mohr diagram showing brittle failure of planes with various orientations relative to the principal stresses.
Image from Bons et al. (2012). (a) Mohr-diagram including the Mohr-Griffith-Coulomb failure envelope with a slope of the internal angle of friction (β). The horizontal axis represents the normal stress component (σ_n), whereas the vertical one the shear stress (σ_s). Maximum (σ_1) and minimum (σ_3) principal stresses are plotted on the σ_n axis. T is the tensile strength, C is the cohesion of the rock. Influence of fluid pressure (P_f) is also shown. (b) Failure plane exhibiting an angle of α to the σ_3. Normal (n) and shear (t) stress components are indicated. (c) Planes with various orientations to the principal stresses and their failure in different senses; (d) mode I extensional, (e) mode II mixed shear and (f) mode III pure shear fractures.

Fracturing is highly dependent on the rock properties, such as pre-existing anisotropies in the rock and mechanical parameters. Weakness planes (fractures, cleavage, bedding contacts) might cause fracturing at lower stresses if they are preferably oriented relative to the principal stresses (see Fig. 1.1c). Other pre-existing features, such as filled fractures (veins) could behave as sites of lower cohesion relative to the host rock. Opening of these veins could therefore predate any new crack formation. Mechanical parameters, such as breaking strength or Young's modulus also influence the fracture initiation and propagation. Breaking strength of a brittle material (rock) represents the maximum stress that the rock can withstand without failing. A rock with lower breaking strength will therefore fail earlier. A difference in Young's modulus for different layers causes the layers to develop different magnitude of differential stresses. A competent layer (high Young's modulus) develops larger differential stress compared to an incompetent one, and therefore will fracture earlier. In a layered sequence this can result in a highly heterogeneous fracture pattern where some layers are extremely fractured, while others lack fractures. Fracture heights in these systems are generally confined by the horizontal layers, whereas spacing is proportional to the layer thickness (Narr and Suppe, 1991). Consequently, the development of fractures in layered sequences has been examined by their dependence on layer thickness, lithology and mechanical properties. Experimental studies initially argued that spacing decreases with increasing strain (Narr and Suppe, 1991; Wu and Pollard, 1995). It has been shown, however, that fracture spacing decreases with increasing strain only until a critical threshold (spacing to layer thickness ratio), after which the fracture-normal stress changes from tensile to compressive inhibiting any further fracture infilling (that is fracture formation between existing ones). Additional strain therefore is accommodated by the opening of, or slip, along existing fractures. This process has been termed as fracture saturation (Bai et al., 2000; Bai and Pollard, 2000b; Becker and Gross, 1996; Wu and Pollard, 1995). Schöpfer et al. (2011) also added that at saturation the fracture spacing is dependent on the layer's tensile to interface shear strength ratio. Moreover, through-going fractures in these layered sequences have been considered as the onset of sequence-scaled saturation instead of layer-scaled (Becker and Gross, 1996; Gross and Eyal, 2007). In addition to spacing, fracture heights in layered sequences have also provoked many studies, where the fracture propagation has been attributed to factors such as mechanical stratigraphy (Young's modulus, breaking strength, rigidity, and the contrast of these between the layers), layer thickness, interface strength, in situ stress contrast and fracture aperture (Arslan et al., 2012; Gu and Siebrits, 2008; McDermott et al., 2013; Narr and Suppe, 1991; Rijken and Cooke, 2001; Smith et al., 2001).

1.1.2 Role of fluids in deformation, hydrofracturing

Fluids are constantly present in the Earth's crust due to a variety of processes. During underwater sedimentation fluids can be trapped in the pore spaces. The more porous the material, the more fluids it can contain. Sand lenses and sandstones generally have higher porosities and therefore the potential to contain large amount of fluids. Sedimentation of smaller grains, such as mud, can also trap significant amount of fluids as muds appear in suspension states. The amount of fluid trapped in the layers is strongly dependent on the sedimentation rate. At slow sedimentation the fluids have more time to escape from the pores, whereas at high rates they can instantly become trapped. During lithification, where sediments get compacted under pressure, these fluids are expelled, which makes sedimentation a major fluid source. Fluids can also be of meteoric origin (i.e. surface water circulating downward) or be expelled from the magma in thermal regimes. Geochemical evidence also suggests that in many cases fluids from the mantle can migrate upward and contribute to crustal processes (Bea et al., 2001; Bradshaw, 1989; Burnard and Polya, 2004; Mao et al., 2008; Navon et al., 1988). Fluids can also be generated through maturation of organic matter that produces hydrocarbons, or through dehydration reactions (McCulloch and Gamble, 1991; Schmidt and Poli, 1998). Dehydration reactions are those that release the embedded water from the crystal structure of hydrous minerals, such as chlorite or clay minerals.

Fluid pressures, just like the other stresses in the crust, are highly heterogeneous and dynamic. If the pores in the rock are interconnected with each other and with the surface, the fluid pressure at any point is hydrostatic. This, however, is rarely the case, which causes the fluid pressure to rise above hydrostatic, occasionally approaching the lithostatic pressure (Bredehoeft and Hanshaw, 1968; Cobbold et al., 2001; Wangen, 1992). There are certain processes in the crust that directly increase fluid pressures. Osborne and Swarbrick (1997) classified the triggering processes into three main categories: (1) increasing compressive stress, (2) change in the rock porosity or in the fluid volume, and (3) fluid movement. Fluid pressures increase with depth and therefore diverge from the hydrostatic pressure. Pressure profiles, however, can be disturbed in heterogeneous systems containing fractures, faults or seals. A low permeability layer embedded in a higher permeability sequence can act as dynamic seal which allows fluid pressure build-up in the area below. In this case the seal’s pressure profile shows extremely high (reaching lithostatic) fluid pressures at the lower boundary of the seal and gradual decrease towards the upper boundary (Cobbold and Rodrigues, 2007). Change in the pore or fluid volume in the rock influence the pore pressure relative to the principal stresses. Fluid overpressures can thus be induced by a variety of processes including rock deformation (fracturing, compression, folding, sliding), secondary cementation, dewatering mechanisms (subduction, thermal expansion of fluid, liquefaction, mineral transformation, hydrocarbon generation) or change in fluid density (Bethke, 1985; Cox, 2005; Fyfe et al., 1978; Oliver, 1986; Oliver, 1996; Swarbrick et al., 2002). For the fluid pressure to increase in these cases, however, the drainage rate (fluid flow) in the rock should be significantly lower than the rate of the triggering process. The relationship between the fluid-filled pores and the stresses applied to the rock is the key element in studying the fluid pressure evolution.

The importance of fluid pressures in tectonic processes were first highlighted by the groundbreaking study of Hubbert and Rubey (1959). They demonstrated that high fluid pressures developed in low permeability rock formations, such as shales, are responsible for their lubricating effect, which made it possible for the large thrust sheets to be pushed over these nearly horizontal surfaces. The involvement of fluids in other faulting processes is also widely known. Fluids can control the strength of the fault zones, influence fault-stability, rupture propagation and arrest, and they also might be responsible for fault creep and fault reactivation (Blanpied et al., 1998; Evans and Chester, 1995; Faulkner et al., 2010; Healy, 2008; Hickman et al., 1995; Renard et al., 2000; Sibson, 1996; Sibson et al., 1975). The effects of fluid pressures can also be seen in fault zones in the form of hydrothermal veins, which I will describe later in detail.

The process when the rock suite fails due to locally elevated fluid pressure is called hydrofracturing. Hydrofracturing can be of induced or natural origin. Induced hydrofracturing has been used as a well-stimulation technique to enhance the well productivity by injecting high-pressured fluids and thus fracturing the surrounding rock to induce flow towards the well (Calò et al., 2014; Hubbert and Willis, 1957; Shalev et al., 2013; Shapiro and Dinske, 2009; Valkó and Economides, 1995). Induced hydrofracturing has also been used to measure in situ stress orientations and magnitudes (Bredehoeft et al., 1976; Haimson, 1978; Hickman and Zoback, 1983). Natural hydrofracturing is based on similar principals and occurs when the natural system has a local overpressure. The process is recognized as an important fracturing mechanism in rocks (Engelder and Lacazette, 1990; Hunt, 1990; Nermoen et al., 2010; Rodrigues et al., 2009).

A porous rock with fluids represents a two-fold stress system, where the rock and the fluid have different stress magnitudes but are directly affected by each other. The fluid pressure counteracts the stress applied to the rock (stress normal to the grains), which results in a decreased stress state called the effective stress (Biot, 1941; Terzaghi, 1923). Implementing this in the Mohr-diagram results in the shift of the Mohr-circle by the amount of the fluid pressure (Fig. 1.1a). Fluid pressure acts against the principal stresses and this competition determines both the failure and fracture propagation. If the fluid pressure (P_f) overcomes the minimum principal stress plus the tensile strength of the rock (T), the mean stress decreases (differential stress remains the same) and the circle gets closer to the failure envelope, resulting in tensile (mode I) failure (Fig. 1.1a). Upon failure, the P_f drops due to the stress release since the fluid has more space because of the fracture opening that dissipated the energy. This itself can lead to the closure of the hydrofracture if the P_f drops below the lithostatic stress (P_{lith}). However, fractures can propagate as P_f builds up in response to further deformation or fluid supply (see later). Fluid pressures therefore weaken the rock by lowering their yield strengths.

This classical view of effective stress assumes that the total stress in the fluid-filled system is constant. Experimental and analytical studies, as well as borehole pressure data have shown this is not always a valid assumption (Altmann et al., 2014; Cobbold and Rodrigues, 2007; Hillis, 2003; Mourgues and Cobbold, 2003; Rice and Cleary, 1976; Rozhko, 2010; Rozhko et al., 2007). It has been demonstrated that fluids exert (seeping) forces, termed as seepage forces, on all the elements in the solid framework. This frictional drag force induced by pressure gradients has two major consequences: (1) it lowers the total stress and (2) re-orientates the stress tensors. In a horizontal sedimentary sequence both the total vertical stress and the fluid pressure gradients are vertical. Any change in the fluid pressure, however, will cause both the effective vertical and horizontal stresses to change. The total vertical stress is unaffected by fluid pressure variations, whereas the minimum horizontal stress is coupled to it. Increasing pore pressure results in increasing minimum horizontal stress, where the former rises steeper than the latter. These lead to a change in the total stress (differential stress), which alters the classical Mohr-circle shift since the circle will not only offset along the horizontal axis, but shrink in size (Hillis, 2003; Mourgues and Cobbold, 2003).

In addition to these, re-orientation of the principal stresses were demonstrated and accounted for the formation of horizontal factures/veins under lithostatic conditions (Cobbold and Rodrigues, 2007; Mourgues and Cobbold, 2003; Mourgues et al., 2011). As pointed out by Mourgues et al. (2011), these poroelastic effects (pore pressure/stress coupling) are also highly dependent on the size of the overpressured zones. For basin-scale overpressures the coupling is two times larger than for localized zones.

Fluid pressures can therefore locally modify the principal stresses, especially in combination with anisotropies of the mechanical properties and heterogeneities in a rock (Cornet and Valette, 1984; Healy, 2008; Hu and Angelier, 2004).

Fluid pressure gradients involvement in deformation processes directly make them applicable to (1) reservoir (hydrocarbon/geothermal) modeling, (2) ore and (3) water exploration, (4) the prediction and modeling underground pollutant transport, (5) CO_2 injection, (6) natural gas storage and (7) underground (nuclear) waste management. Both the importance of hydrofracturing and the lack of detection of the process in nature have provoked a great amount of numerical models (Dahm, 2000; Flekkøy et al., 2002; Ghani et al., 2013; Goren et al., 2010; Goren et al., 2011; Johnsen et al., 2006; McNamara et al., 2000; Olson et al., 2009; Tzschichholz et al., 1994; Wangen, 2011). Description of the different coupled models that are most relevant to the research will be described in the literature review chapter.

1.2 Fluid-rock interaction

Fractures provide open space within rocks. Whether these fractures stay open or closed will depend on (1) the orientation of the fractures relative to the stresses acting on the fracture walls, (2) the fluid pressure, (3) the wallrock permeability and (4) any existing material within the fracture that might keep it propped open (Oliver and Bons, 2001). If the factures remain open, they provide pathways for fluid, mass and heat transport. The extent to which the fluids interact with the host rock depends on the type of transport, the chemistry (e.g.

pH conditions and reduction potential) and mineralogy of the host rock, as well as the pressure-temperature conditions between the fluids and the host rock. The latter two can cause disequilibrium between the fluid and rock, which needs to exist long enough for any interaction (alteration/precipitation/dissolution) to take place (Oliver and Bons, 2001). The time scale over which the interaction occurs therefore not only depends on the disequilibrium magnitude, but also on how long the disequilibrium and its driving forces are sustained.

In the following I will briefly outline the different transport modes within the crust that play major roles in the occurring fluid-rock interactions. As interaction can cause mineral precipitation within fractures forming veins, I will describe these and their microstructures, as well as the analyses that could be carried out on them. The fracturing-healing cycle generally results in dynamic (spatial and temporal) permeability, which I will discuss at the end.

1.2.1 Transport modes

Two main modes of transport can be distinguished based on the mechanics: fluid and diffusional flow (Fig. 1.2). Fluid flow is one of the most effective transportation modes in the crust as it occurs fast and can carry solutions over long (up to kilometre scale) distances (Jamtveit and Yardley, 1997). We can distinguish between a flow that is occurring via channels in the rock (advective flow) and a flow where the fluids travel with the fractures. The latter is termed as ‘mobile hydrofractures’ (Bons, 2001b) and will not be discussed further as it is irrelevant to this research. Pervasive fluid flow refers to a flow through the matrix of the host rock. In this case the porosity provides the channel and thus implies that in intact rocks this type of flow will be limited but the fluid interaction with the host rock is expected to be greater since (1) the fluid filtrates through larger rock masses and (2) the flow is slower due to the limited space. Flow through fractures or faults, on the other hand, is characterized as a faster event but there is less impact on the host rock. The common feature in all these different flows is that they are driven by gradients triggered by hydraulic head. This process is governed by Darcy’s law. Darcy’s law defines fluid flow in porous media as

$$q = -K\frac{dh}{dl} \tag{1.1}$$

where the flow rate (*q*) is a function of the hydraulic conductivity (*K*), hydraulic head (*h*) and the distance (*l*). Considering hydraulic potential instead of hydraulic head, and the conductivity as a function of permeability, fluid viscosity and density, this equation can be rewritten as

$$q = -\frac{k}{\mu}\frac{d\Phi}{dL} \tag{1.2}$$

where *k* is the rock's permeability, *μ* is the fluid viscosity and *Φ* is the hydraulic potential. Equation 1.2 therefore shows that fluid flow will be driven by a gradient in the hydraulic potential, which can be triggered by fluid overpressure, topographic relief, fluid density change or deformation (Chi and Xue, 2011).

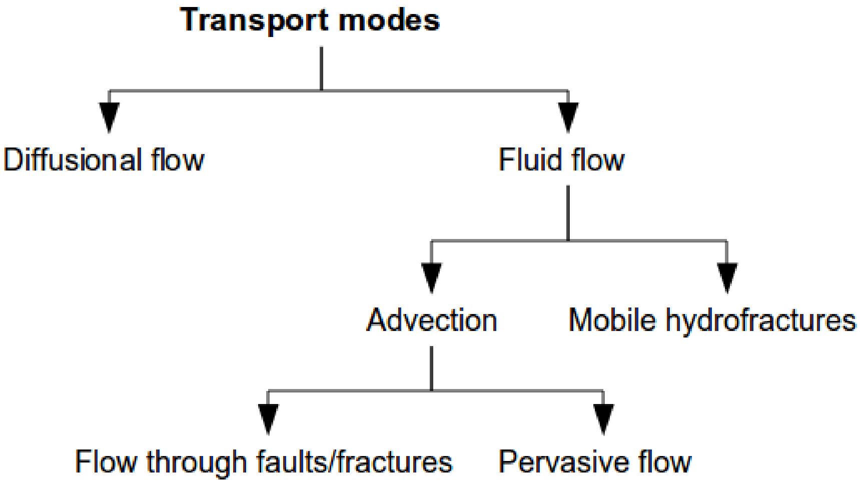

Fig. 1.2 Main types of fluid and mass transport modes occurring within the crust.

Diffusional flow represents a separate group as the driving agents here are temperature, pressure or chemical gradients. These gradients can arise for a variety of reasons such as mechanical heterogeneities, solubility of minerals, crystal growth or precipitation sites. Disequilibrium can be generated when the fluid pressure in a fluid-filled fracture approaches the fracture normal stress, whereas the rock around it experiences higher stresses (Bons et al., 2012; Fisher and Brantley, 1992). This results in a stress heterogeneity and will cause diffusion from the host rock to the fluid-filled fracture. Veins formed via diffusion are often accompanied by dissolution surfaces, stylolites, through which soluble material is transported and precipitated in veins. Diffusion is considered as a slower process which is relevant mainly at smaller scales, millimeter-centimeter scale but can go up to a meter (Oliver and Bons, 2001). In spite of this, diffusion has been recognized as an important healing mechanism which contributes to the episodic fluid flow in fault systems (Evans and Chester, 1995; Renard et al., 2000; Sibson et al., 1975), as well as to the formation of pressure fringes (Koehn et al., 2000). Detailed description of the different transport modes in the Earth's crust can be found in Oliver and Bons (2001), Cox (2005) and Chi and Xue (2011).

Irrespective of how the fracture was formed (due to tectonic forces, high fluid pressures or both) and what type of material transport occurred thereafter, the fractures can be subjected to closure and mineral precipitation that will result in vein formation.

1.2.2 Veins, their microstructures and analyses

Veins are mineral assemblages that precipitated from fluids along open spaces or fluid-filled cracks in the rocks. They occur on a variety of scales (few microns to meters), crustal depths, shapes, textures and consist of a variety of minerals. Veins provide key information on paleo fluid flow, mass transport and fluid-rock interaction in the rock suite. Since they form after the host rock, they also reflect the different deformation events that occurred after veining. Veins have been thus a subject of extensive studies for several decades. These studies are underlain by the pioneer works of (Durney and Ramsay, 1973; Passchier and Trouw, 2005; Ramsay and Huber, 1983).

Veins can be classified into three major categories depending on the growth direction which determines the crystal morphology as well. These categories are the antitaxial, syntaxial and stretching veins (Fig. 1.3). Antitaxial veins represent crystal growth from the vein center towards the host rock walls usually without any growth competition, which is probably due to no or just narrow aperture (Bons and Jessell, 1997; Fisher and Brantley, 1992; Koehn et al., 2000). The vein center is often marked by small equidimensional crystals or wall rock fragments forming the median line or zone that represents the nucleation site for crystal growth. Crystal morphology in these veins is usually fibrous, where the fibers are characterized by a relatively constant, high (> 10) length to width ratio (Oliver and Bons, 2001). According to Oliver and Bons (2001), truly fibrous veins only occur in low-grade (low P/T) metamorphic rocks because the diffusion and the recrystallization under these conditions are slower than in higher temperatures.

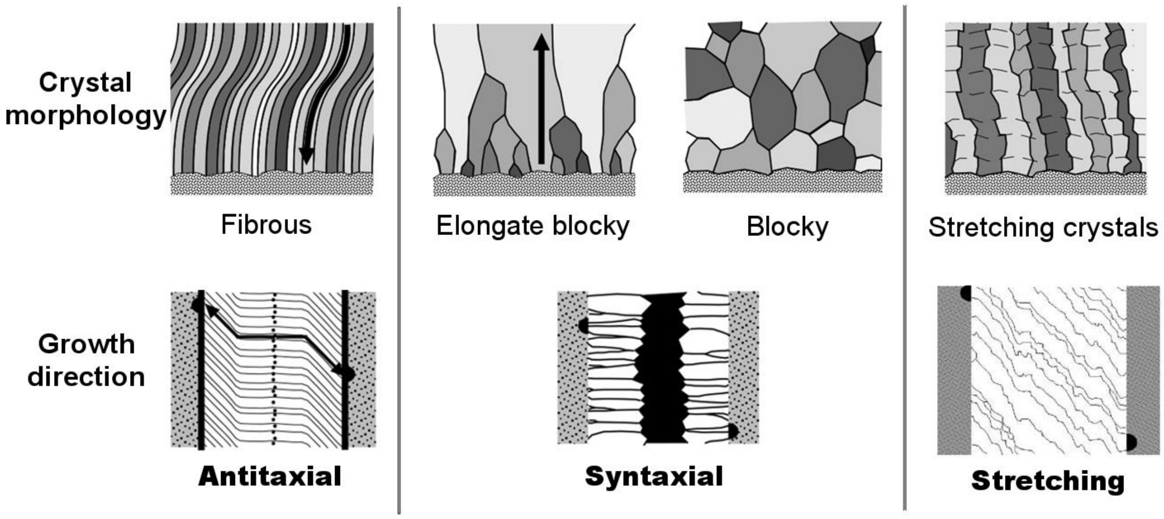

Fig. 1.3 Different basic vein microstructures and inferred growth directions. Figure modified after Bons and Montenari (2005) and Bons et al. (2012).

Syntaxial veins form as a result of crystal growth outwards from the wall rock. Crystals grow either from both sides of the host rock (bitaxial growth, Hilgers et al. (2001)), or from only one side (unitaxial growth, Hilgers et al. (2001)) (Fisher et al., 1995). As opposed to the antitaxial veins, crystals in the syntaxial veins are strongly controlled by growth competition, where the some crystal seeds overgrow their neighbors and new crystal formation is inhibited because it is energetically more favorable for the existing crystals to extend than for new ones to nucleate (Bons, 2001a; Hilgers and Urai, 2002a). This results in elongate blocky textures with a mixture of narrowing and widening crystals towards the growth direction (i.e. vein center) (Bons et al., 2012). Crystal growth along the vein is heterogeneous in the sense that the fracture could heal entirely at one location, whereas further away it is still just partly healed. If the fluid pressures are high enough, the healed vein can fracture allowing fluid flow within. This mechanism is called crack-sealing (or crack-healing) that creates inclusion bands (parallel to the vein-wall rock) or trails (perpendicular to the wall, parallel to the growth direction indicating the opening trajectory) (Ramsay, 1980). These bands and trails represent one crack-seal cycle, and can be made up of host rock fragments, new minerals or fluid inclusions. The crystal morphology of these veins led researchers to believe that crystal growth took place in fluid-filled (i.e. open) cracks (Fisher and Brantley, 1992; Koehn et al., 2000; Urai et al., 1991). In case the fluid is supersaturated, the crystal nucleation can impede crystal growth, which allows the development of equidimensional, blocky grains. These blocky veins could be related to fault zones, but also to dynamic recrystallization or repeated fracturing during vein formation (Oliver and Bons, 2001).

Stretching veins comprise crystals that span from one wall to the other and form due to repeated crack-seal cycles. These veins are also termed as ataxial (Passchier and Trouw, 2005). The difference between the syntaxial and stretching veins is that the latter does not show growth competition and the crack plane is not constant.

Once the vein microstructure has been examined, different geochemical analyses could be carried out. One of the most common analyses is to compare the chemistry of the host rock close and further away from the vein in order to determine possible depletion of elements that would indicate diffusion in a closed system. Isotopic signatures (e.g. oxygen and carbon) could also be examined to establish the fluid source, whereas minor (e.g. Ti, Al, Mg, Mn, Fe) and trace element (e.g. Y, Nd, Sr, Pb, U) analyses could lead to information on the fluid composition (Bons et al., 2012). Moreover, fluid inclusion microthermometry could give pressure/temperature conditions that formed the veins.

Even though microstructures of the veins preserve the deformation history of the rock, there are still a lot of uncertainties regarding the relationship between the microstructures and (1) geological conditions, (2) transport mechanisms or (3) the extent of fluid-rock interaction. In addition to this, the distinction between hydrofractures from dilatational fractures based on the vein microstructures is also unknown. Fault-related veins clearly indicate tectonic formation, whereas veins with regular patterns are assumed to be formed due to tectonic forces. On the other hand, formation of crack-seal textures and wide (tens of centimeters) veins would indicate fluid involvement, whereas multidirectional veins are inferred to be hydrofractures (Chi and Xue, 2011). These are only suggestions as a clear relation has not yet been determined. Field work and investigating vein microstructures, in addition to micro – and macroscale modeling of fracturing, vein growth and propagation would highly contribute to our understanding of the processes and would thus help to determine the possible relationships.

1.2.3 Dynamic permeability

Although it has been mentioned earlier that the permeability is a dynamic measure, due to its importance it will be discussed further in this section.

Permeability is an intrinsic rock property. It can be related both to the primary porosity that formed with the rock and the secondary porosity that formed later due to different processes. It is apparent that permeability has spatial and temporal variations. Spatial variability can be attributed to the distribution of pores within the rock. A connected pore network can provide a framework for fluid percolation. Porous rocks, however, do not necessarily have large permeabilities as the pores can be isolated and their distribution can be extremely heterogeneous. Cracks and fractures triggered by deformation, or dissolution due to chemical reactions are secondary processes that could not only connect isolated pores but also create new open space within a rock suite allowing faster fluid flow. Similarly to the pores, the dissolution areas and fractures can also be heterogeneous with regard to size, spatial distribution or aperture giving rise to variable permeability in layered sequences.

Tectonic settings also influence the permeability as the deformation structures vary widely due to the existing and dominant stress orientations (Faulkner and Armitage, 2013). A decrease in permeability can be related to mechanical (e.g. compaction or formation of collapse structures) and chemical processes (e.g. healing of fractures via mineral precipitation). While these processes show spatial variability, it is apparent that they also directly cause temporal variations in the permeability values. Evolution of rock systems usually consists of alternating or coeval cycles of permeability increasing and decreasing processes. One of the best examples of these are the fault systems that play a major role in fluid circulation. In active fault zones the increasing stress in the fault core can be released by local fracturing forming different fault rocks (breccias, gouges or cataclasites) in the core and extensional fractures in the core and damage zones.

These open spaces or voids can then attract fluids from the surroundings. In case where the fluids are supersaturated with different elements, precipitation can heal the fractures. The textures of these veins have shed light on the episodic fracturing and crack-sealing that occur in fault zones (Sibson et al., 1975). It has been argued that healing of the fractures and faults has two significant and competing effects on the system (Tenthorey et al., 2003). First of all, it can strengthen the rock aggregate by increasing cementation and cohesion, which directly causes permeability decrease. Second of all, it simultaneously weakens the system as the low permeability can result in elevated fluid pressure that in turn can cause further failure. This feedback between the pressure of the fluid and the surrounding rock leads to permeability being an extremely dynamic property.

1.3 Research motivations and questions

The research has been carried out within the framework of the DGMK (German Society for Petroleum and Coal Science and Technology) basic research project 718 “Mineral Vein Dynamics Modeling”, also called FRACS. The first phase of this project started in 2009 and included seven universities (University of Glasgow, Johannes Gutenberg University of Mainz, Karlsruhe Institute of Technology, RWTH Aachen University, Eberhard Karls University of Tübingen, University of Bayreuth and ETH Zürich). The second phase which started in 2012, however, only incorporated the first five listed universities. The project aimed to study the dynamics of vein systems throughout several subprojects relating to mechanics, transport and reaction processes. The main topic therefore set the tone for my project as well.

The core of my project was natural hydrofracturing and dynamic, large-scale permeability evolution of fluid-filled systems. As mentioned earlier, various numerical models have been developed to simulate hydrofracturing. However, most of these models lacked the intimate coupling between the fluid diffusion and deformation, as well as real (scaled) values. Their spatial and temporal resolutions were limited, they mostly dealt with granular media and they did not consider healing of fractures. These limitations provided motivation for further work in terms of numerical modeling.

In order to understand, compare and possibly validate the model results, field work was carried out. A few veins were presumed mineral-filled hydrofractures, therefore were of interest with regard to their microstructures and origin. The host rocks in the field area also fit in the projects framework, as it comprised low-permeability shales.

Dynamic permeability is directly related to the fracture-healing-refracturing cycle that creates fracture and vein networks. Characterizing and comparing these could reveal major permeability differences between the networks. Previous studies have only dealt with characterizing networks in their current form/stage and have not looked at dynamic properties that would be essential to understand the network and thus permeability evolution. In addition to this, the multidisciplinary approach using graph theory from mathematics has not yet been applied to geological fracture networks[1].

My research therefore was inspired by the importance of and the knowledge gap understanding the dynamic nature of permeability, and thus addressed many questions:

- What are the dynamics of fracturing in a multilayered reservoir rock over time?
- How does the healing affect the rock behavior?
- How do the different healing properties affect the healing and the refracturing process?
- What is the stress evolution during fracturing, healing and refracturing?
- Can we assign characteristic fracture patterns to certain conditions?

---

[1] Recent discovery has revealed that Andresen et al. (2013) applied graph theory to compare outcrop fracture patterns with its Discrete Fracture Network model equivalent.

- What influences fracture/vein spacing in the rock?
- How does the permeability evolve over time?
- What does the model tell us about natural systems?
- Can we reproduce fracture/veining patterns found in nature using numerical modeling?
- What are the fluid flow characteristics in natural hydrofractures in the Internal Ligurian Unit, Italy?
- Can graph theory be applied to geological networks?
- Can we quantify and compare the connectivity of different networks?
- How can we quantify a good reservoir?
- Do the connectivity and other topological information relate to mechanical properties of the rocks?

These questions have been approached using various methods to seek answers that would advance our understanding of dynamic permeability and natural hydrofracturing.

1.4 Thesis structure

The thesis is based on three main topics: (1) deformation and veining in the Internal Ligurian Unit, Italy; (2) importance of fracture-healing on the deformation of fluid-filled systems and (3) characterizing fracture networks using the graph theory. The thesis structure follows this order, as first field work needs to take place to observe and examine natural veins. The different patterns and the characteristics of fractures, veins and other deformation structures seen in the field can then be reproduced and/or provide at least valuable information to interpret the numerical model results. Using the same model, various fracture networks can be generated and then characterized in a quantitative and qualitative manner to describe the differences between them. These are the reasons for presenting the chapters in such order.

First, I present the literature review chapter where I outline the most important literature for each topic. This is followed by a methods chapter including the description of all the methods that I used to gather data. The thesis then moves on to the core chapters, the results. Each topic will be presented in a separate chapter, which will include the results and the discussion of these, and will end with a conclusion of that topic. The thesis ends with a short summary including final remarks on the research.

2 Literature review

2.1 Geological setting and structural evolution of the Internal Ligurian Unit in the Northern Apennines (Italy)

2.1.1 The Northern Apennines

The Northern Apennines forms the backbone of the Apennine peninsula (Fig. 2.1). Tectonically it is bordered by the Sestri-Voltaggio Line in the northwest that separates it from the Western Alps. On the south it shares a boundary with the Central Apennines along the Ancona-Anzio Line and with the Southern Apennines along the Ortona-Roccamorfina Line (Molli, 2008; Patacca and Scandone, 1989) (Fig. 2.1).

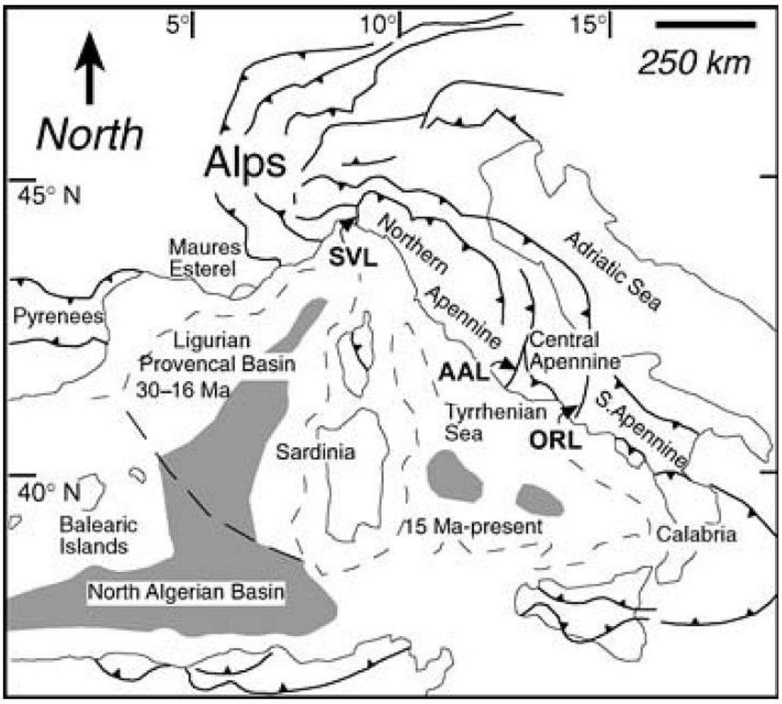

Fig. 2.1 Tectonic map of the Central-Western Mediterannean showing the Northern Apennines. SVL = Sestri-Voltaggio Line, AAL = Ancona-Anzio Line, ORL = Ortona-Roccamorfina Line. Figure from Molli (2008).

In order to understand the evolution of the Northern Apennines, it is useful to outline briefly the Mesozoic-Cenozoic paleogeography and geodynamic evolution of the Central-Western Mediterranean region. Two major oceanic basins dominated the Mediterranean from the end of the Paleozoic. The East Mediterranean domain opened in the Late Permian as a westward extension of the Neotethys, and the Alpine Tethys of Jurassic age that was an eastern extension of the Central Atlantic Ocean (Stampfli, 2000). The Alpine Tethys included several smaller oceanic basins (e.g. Ligurian-Piemonte Basin, other known as Ligurian Provencal Basin) that separated many microplates, such as the Baleric Islands, Corsica, Sardinia, AlKaPeCa microcontinents, Adria and Apulia (Stampfli, 2000; Stampfli, 2005; Stampfli and Hochard, 2009). While some authors argue that Adria was a single continental plate, others consider it as a collage of more continental plates, like the Campano-Lucana or Apulia (Carminati et al., 2012). These different opinions, however, do not affect the Mesozoic and Cenozoic geodynamic reconstructions as it is very likely that the present-day configuration of Italy (from now on referred to as the Adriatic plate) was already established by the Middle Triassic (Stampfli, 2005).

The evolution of the Central Western Mediterranean was mainly controlled by the movements of the three major plates (Europe, Adria and Africa) and the existing microplates within the area. The convergence of Africa towards Europe resulted in a continuous E-SE-dipping subduction zone between Europe, Corsica-Sardinia and Adria in the Early-Late Cretaceous (Bracciali et al., 2007; Carminati et al., 2012; Molli, 2008) (Fig. 2.2a). This led to a W-vergent accretionary prism which formed the Western Alps and the Alpine belt of Corsica. In the Early-Middle Eocene, however, the subduction halted due to the arrival of the Corsican distal continental margin, which caused an orogenic collapse, slab break-off and rapid exhumation of Corsica, where the induced erosion supplied debris for turbidite sequences (Argnani, 2009; Molli, 2008; Molli and Malavieille, 2011). This polarity flip led to the initiation of a W-NW Apenninic subduction from the Late Eocene – Middle Oligocene (Fig. 2.2b). The change in subduction is widely recognized in early W-vergent deformation structures that are overprinted by E-vergent deformation (Argnani, 2012). The Apennine accretion over the Adriatic margin took place during the Late Oligocene due to the counterclockwise rotation of Corsica-Sardinia (Advokaat et al., 2014) and the N-S Adria movement. The Apennine-related back-arc rifting and the rollback of the subduction hinge formed the present-day Ligurian Sea (Late Oligocene – Early Miocene) (Fig. 2.2c), whereas further south it caused the opening of the Tyrrhenian Sea in the Late Miocene (Molli, 2008; Rosenbaum et al., 2002) (Fig. 2.2d). The identified late orogenic structures (faults and folds) indicate orogen-parallel, i.e. NW-SE, compression during the last ~8 million years (Carosi et al., 2002; Carosi et al., 2004).

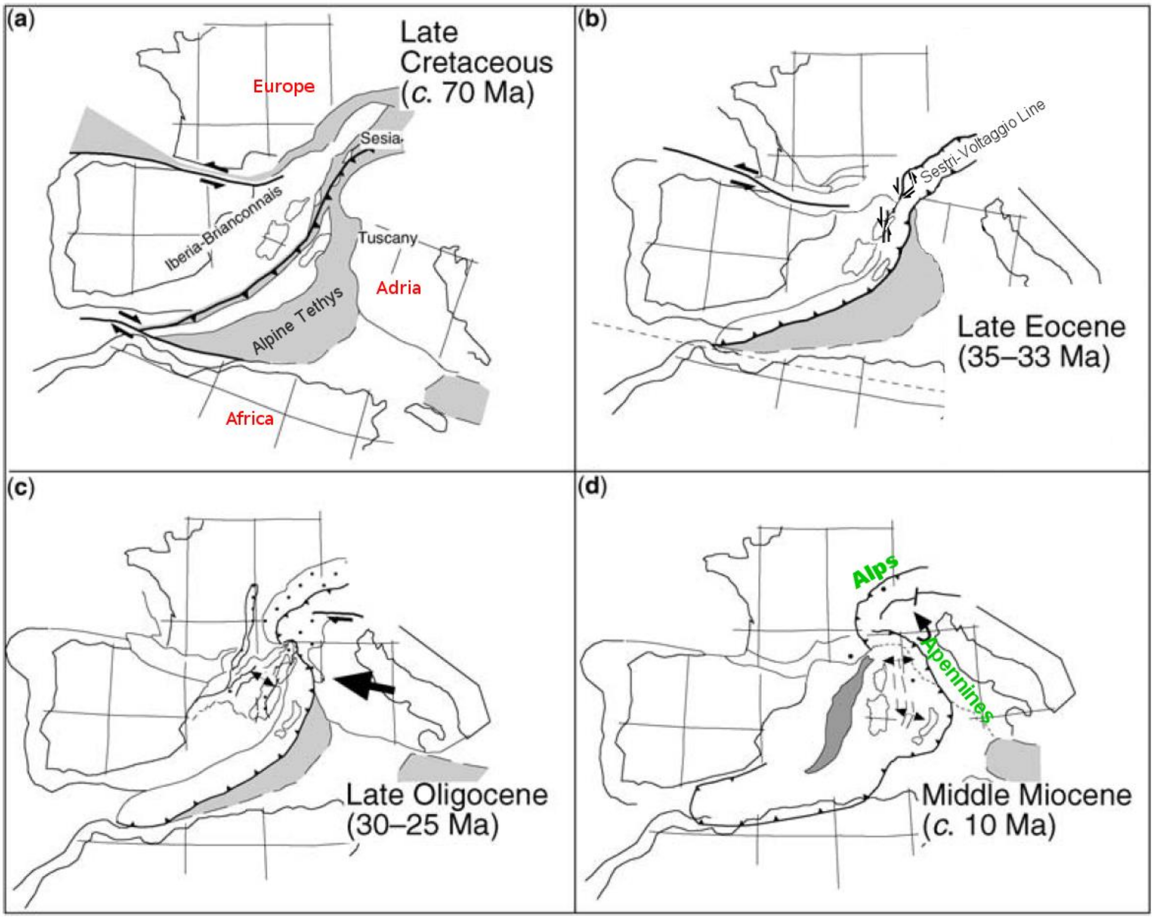

Fig. 2.2 Paleotectonics of the Central-Western Mediterranean from the Late Cretaceous showing the formation of Alps and Apennines.
Figure modified after Molli (2008).

The Paleogene geodynamics of the Central-Western Mediterranean therefore can be characterized by a dynamic subduction zone between Europe/Corsica and Adria that (1) changed polarity from E to W and (2) migrated from a NE-SW to a NNW-SSE orientation. This subduction and accretion formed the Northern Apennines.

The Northern Apennines is usually grouped into five major units based on their tectonic and stratigraphic variations (Molli, 2008; van Wamel et al., 1985):

- Late, post-orogenic continental to shallow marine sediments (Late Eocene to Pliocene) lying uncomfortably on the Ligurian Units;

- Umbria-Romagna-Marche Units (Jurassic to Pleistocene) comprising carbonates and shallow-marine continental sediments;

- Tuscan Units (Late Carboniferous to Early Miocene) that includes carbonates, shales and siliciclastic turbidites;

- Sub-Ligurian Units (Cretaceous to Miocene) with sandstones, siliciclastics and marls;

- Ligurian Units (Late Jurassic to Miocene) comprising ophiolites and a wide range of sedimentary deposits.

The Umbria-Romagna-Marche Units together with the Tuscan Units form the lower nappes of the Apenninnic wedge and have an Adriatic plate origin, whereas the upper nappe (Ligurian Units) originated from the Alpine Tethys (Perrone et al., 2014). The Ligurian Unit can be further divided into two groups: the Internal Ligurian Unit and the External Ligurian Unit. In the following, I will outline the stratigraphy of the Internal Ligurian Unit and place it in a tectonic framework.

2.1.2 The Internal Ligurian Unit

The Internal Ligurian Unit (ILU) is considered to be one of the best preserved and most complete examples of oceanic lithosphere of the Alpine Tethys (Marroni, 1994). The lowermost part of this unit is the ophiolite sequence that represents the oceanic basement of the Liguria-Piemonte basin and therefore has a Jurassic age. The ophiolite is overlain by hemipelagic and pelagic sediments: radiolarian cherts, Calpionella Limestone (Early Cretaceous) and Palombini Shales (Early-Late Cretaceous) (Marroni, 1994; Marroni and Pandolfi, 2007; van Wamel et al., 1985). The Palombini Shale grades into the overlying Val Lavagna Shale Unit. Three subunits have been identified within the Val Lavagna: the Manganiferous Shale, Verzi Marls and the Zoned Shales (Marroni, 1991; van Wamel et al., 1985; van Zutphen et al., 1985). The Val Lavagna, together with overlying Gottero Sandstone, are considered to be distal and proximal turbidite sequences (Marroni, 1991; Nilsen and Abbate, 1984). The upper boundary of the Gottero marks an unconformity with the overlying sequence, the Bocco Shale, which represents debris flow and slide deposition (Bracciali et al., 2007).

Deposits within the ILU were confirmed to have Corsica plate origin (Bracciali et al., 2007; Nilsen and Abbate, 1984), which fits the geodynamic evolution of the area described earlier. The complete ILU sequence in general reflects nicely the evolution of the advancing accretionary wedge which was thrust over the Tuscan and Umbria-Romagna-Marche Units during the Late Oligocene – Middle Miocene (Argnani, 2009; Codegone et al., 2012).

The deformation history of the ILU is quite complex, it involved the entire sequence, and only a few studies in the late ‘80s and early ‘90s attempted to define and characterize deformation events (Table 1).

	D1	**D2**	**D3**	**D4**	**D5**
[1], [2], [3]	Tight, isoclinal, SW facing folds with NW-plunging axes. Axial planar foliation.	Open folds with vertical axes and NW strike. No foliation.	Tight to open, asymmetrical folds with NE vergence. Flat-lying crenulation cleavage.	Open folds with steep axial plane. No foliation.	Gentle folds
[4], [5], [6], [7]	Non-cylindrical, isoclinals folds facing NW/SE to NE/SW and have axes orientation of NE/SE, plunging NE to NW. Axial planar foliation.	Assymetrical folds with NE vergence and axes orientation of SE to S, and N/NW plunge. Axial planar foliation.	Open folds with subvertical axial planes and axes oriented SE to S. Fracture cleavage.	[4] Open folds with subvertical axial planes	

Table 1 Deformation events and their characteristics according to different researchers. [1] van Zutphen et al. (1985), [2] van Wamel et al. (1985), [3] van Wamel (1987), [4] Marroni (1991), [5] Marroni (1994), [6] Leoni et al. (1996), [7] Marroni and Pandolfi (1996).

The researchers agree that the first deformation phase corresponds to the east-dipping subduction zone and the underplating of the oceanic lithosphere (Leoni et al., 1996; Marroni, 1991; Marroni, 1994; Meneghini et al., 2007; van Wamel et al., 1985). Its timing is therefore probably latest Early Paleocene (Hoogerduijn Strating, 1994; van Wamel, 1987). D2 has been associated with extension

(Hoogerduijn Strating, 1994), exhumation (Marroni, 1991) and thrusting (Marroni, 1994). The subsequent deformation events are even more debatable but it is a currently accepted view that all the deformation took place before the thrusting (i.e. stacking of nappes on the Adria continental margin), and therefore was completed by the Early Oligocene (van Wamel, 1987).

Constructing the pressure-temperature path (P-T) for the ILU is also problematic. Currently only one study exists that investigated crystallinity, polytypism and b_0 of illite in the Palombini Shales to construct the P-T conditions of metamorphism (Leoni et al., 1996). Other lithologies (ranging from the Calpionella Limestone to the Bocco Shales) were not sampled, therefore the presented P-T data were purely inferred from the Palombini Shales. Their results show/suggest that the Calpionella Limestone and the Palombini shale metamorphosed under 2-3 kbar and 160-210°C; the Val Lavagna Shale and Gottero Sandstone under ~4 kbars and 235-285°C; whereas the Bocco Shale under 2-3 kbars and 200-250°C. It is, however, generally agreed upon that the ILU had undergone polyphase metamorphism under sub-greenschist facies conditions (Molli, 2008).

These metamorphic conditions, along with the geodynamic evolution of the ILU made it possible to compare the formation with two other accretionary wedges, the Franciscan Complex of California and the Kodiak Complex of Alaska (Meneghini et al., 2009). Stratigraphy of these complexes is comparable with the ILU and show complete oceanic lithosphere with ophiolites at the bottom and trench deposits on the top. Structural styles are also similar representing polyphase deformation under low metamorphic conditions.

The deformation within the ILU mobilized fluids which precipitated minerals in fractures creating veins. In the following, the identified veins within the ILU will be outlined.

2.1.3 Veins in the Internal Ligurian Unit

Veins in the ILU have only been studied by the one group of researchers, which essentially means that three published papers outlining the veins are quite similar in content and share the same views (Marroni, 1991; Marroni, 1994; Meneghini et al., 2007). They distinguished six different veins sets:

A. early, bedding-parallel veins (pre-D1 phase),

B. veins filling boudin necks (D1 phase),

C. bedding-perpendicular fibrous veins (D1 phase),

D. shear veins of bedding surfaces (D2 phase),

E. bed-perpendicular and parallel tension gashes (D2 phase),

F. fibrous veins perpendicular to the foliation (D2 phase).

The oldest veins (Group A) were identified as pre-tectonic (pre-D1), bedding-parallel quartz and calcite veins with mosaic (blocky) structures. The type calcite twinning within the veins suggested Meneghini et al. (2007) that calcite crystallization might have occurred between temperatures 150°C and 300°C. These veins occur in shaly matrix (Val Lavagna and Palombini) and have large lateral (several meters) continuity along the bed and cleavage interfaces. The veins have a dirty appearance due to the large amount of host rock inclusions, opaque seams and vein-parallel pressure solution surfaces (stylolites), and thus have been termed as “dirty veins” in the literature. They have been interpreted as hydrofractures formed in poorly lithified sediments during tectonic burial. The alternating inclusion and crystallization bands, as well as the cleavage (vein) parallel stylolites led the researchers to believe that during the formation of these veins multiple opening and mineralization phases occurred due to the fluid pressure fluctuations that caused dilatation and collapse of fracture walls (Meneghini et al., 2007). Dirty veins have also been found within the Kodiak Formation in Alaska and have been again attributed to the precipitation within cyclic dilatant then collapsed fractures (Meneghini et al., 2009).

The more competent (silty and sandy layers) frequently showed boudinage structures. Between the boudins, blocky calcite veins were identified (Group B). These veins were either bedding-perpendicular or showed high angles to the bedding, in which case they appeared in conjugate sets. Within the competent layers the researchers distinguished another bedding-perpendicular, calcite vein set (Group C). These, locally conjugate, veins showed fibrous textures (antitaxial growth). At the vein-wallrock boundary, however, syntaxial quartz growth was also found. Both vein sets (Group B and C) were folded by the D1 and D2 events. According to Meneghini et al. (2007) the Group B veins formed due to build-up of fluid pressures below lithified, more competent layers which caused a local switch from the predominant horizontal compression (generated by the accretion) to layer-perpendicular failure. Veins in the Group C then formed during folding and layer-parallel extension.

Veins that presumably formed during the second phase of deformation, were only studied by Marroni (1991; 1994) but extremely briefly. He described shear veins (Group D) along bedding surfaces, subvertical and subhorizontal tension gashes filled with fibrous and calcite minerals in competent layers (Group E), and syntectonic, foliation-perpendicular antitaxial calcite veins (Group F). According to Marroni, all the D2 deformation structures, including the veins, show post-accretion flexural slip.

More studies on veins have been carried out in the Tuscan Units (Mazzarini et al., 2010; Montomoli, 2002). Even though the identified veins there are similar to those described by Marroni, and Meneghini et al. in the ILU, caution must be taken to relate the veining stages due to the different tectonic evolution of the nappes.

2.2 Numerical and coupled models for rock deformation and hydrofractures

Studying rock deformation is crucial to understand the evolution of different structures found in nature (e.g. fold and thrust belts, faults, fractures). As these features cover large time and spatial scales, and in nature only the end result (e.g. already evolved folds or faults) can be observed, researchers needed to develop tools to (1) study the boundary conditions (pressure, temperature, strain) that lead to the onset of deformation and (2) to examine the temporal - spatial evolution of deformation structures. One of these tools was the numerical models (methods). Numerical models made it possible to create a wide range of experiments, scenarios that can neither be reproduced during laboratory experiments nor be observed simultaneous to the process. Results from the different models have led to enhancements in analyses of structures and deformation dynamics.

A wide range of numerical methods have been developed (Bons et al., 2008; Peiró and Sherwin, 2005) including:

- models with different lattice data structures (e.g. Lattice-Boltzmann Method for experiments on fluid dynamics);
- boundary models (e.g. for simulating grain growth);
- Finite Difference Method (FDM), which is ideal to simulate constant geometries (i.e. a rock system which does not deform) where only different properties (e.g. temperature) vary in time and space;
- Finite Volume Method (FVM), typically used for simulating fluid dynamics;
- Finite Element Method (FEM) for simulating linear and nonlinear material mechanics (e.g. deforming rocks);
- Discrete Element Method (DEM), where the particles (i.e. discrete elements) in the lattice are connected to each other either by the particle boundaries or by rheological elements (e.g. springs).

The choice of method for the simulations depends on the scientific problem one wants to solve. Since each method has its limitations it is common to use coupled models like FEM-DEM or DEM-FVM (Catalano et al., 2014; Eberhardt et al., 2004; Munjiza et al., 1995). In general, the Discrete Element Method is probably the most commonly used to simulate brittle fracturing. In the following I will therefore first describe the DEM in more detail, and then I outline the different coupled models that have been used to simulate deforming saturated porous media.

2.2.1 The Discrete Element Method

The Discrete Element Method (DEM) provides a framework where the mechanical interaction between the particles depends explicitly on the increment in the experiment (e.g. time step) or the rate of deformation. The particles are treated as independent entities, rigid bodies that can undergo both rotation and translation giving rise to local kinematic and static variables.

Particles are usually chosen to be spheres (or cylinders in 2D) (Cundall and Strack, 1979). Spheres represent a simple geometry and thus make calculations much easier. The interaction between particles can be defined several ways: the particles are connected if they are (1) directly in contact with one another (Wang and Mora, 2008), (2) not directly in contact but are in the neighboring zone (Scholtés and Donzé, 2013), (3) connected to each other by springs; or (4) their centers are closer to each other than their total radii (Catalano, 2012). These contact zones and the previously mentioned local kinematic and static variables determine how the entire material behaves (deforms).

The classical DEM computational cycle involves two basic algorithms. Firstly, the interaction forces (normal, tangential and contact forces) between the particles are being calculated based on constitutive laws. Secondly, as the deformation takes places and the particles move, the model needs to find the new positions of each particle. In order to do so, Newton’s Second Law of Motion is being applied to obtain the translational and rotational accelerations of particles. By time integrating these values the model finds the new positions after each time step. This also updates the interactions and interaction forces between particles.

The DEM model (similarly to other models) also includes boundary walls (basically rows of particles) through which the boundary conditions can be applied. The boundary particles, as opposed to the non-boundary ones, are not affected by the updated interaction forces. The user specifies the boundary conditions in terms of stress and/or strain which ultimately defines the position of the walls throughout the entire simulation.

The simplicity, efficiency and flexibility of the DEM contribute to its success and wide range of uses. The small number of input parameters and the ability to measure small-scale mechanical properties also make it an attractive method to use. Due to DEM’s discontinuous characteristics, it also provides a powerful tool to simulate a deforming solid phase (rock) (Cook and Jensen, 2002). Considering, however, that every rock has a pore system which can be occupied by fluids (either pore fluids or external fluid flows), there has been a great need to create coupled models that include both the solid and fluid phases. These models are usually termed as coupled hydro-mechanical models and are often used to simulate hydrofracturing.

2.2.2 Coupled hydro-mechanical models

Modeling deforming saturated porous media has long been of great interest due to its applicability to geotechnical (e.g. rock and soil stability) and geological (e.g. hydrofracturing, liquefaction) problems. Coupled models face the same complexity due to the involvement of (1) elastic deformation of the matrix triggered by fluid pressure, (2) fluid flow inside the fracture and (3) fracture propagation (Adachi et al., 2007). A variety of numerical models have been developed which implement the solid-fluid coupling, i.e. the poromechanical effects (poroelasticity), in a different way. Two major approaches exist: continuum-based and microscale models (Catalano et al., 2014). Continuum-based models (e.g. DEM, FVM) use a separate grid that is usually larger than the solid framework to solve the fluid problem. The porosity and the velocity of the fluid are averaged over this mesh, and these values provide the input variables to the continuum formulations. The advantage of these models is the low computational cost but they cannot examine accurately the fluid effects at the particle scale due to the larger fluid mesh and the averaged variables (Catalano et al., 2014). The microscale models (e.g. FEM, Lattice-Boltzmann Method) overcome this issue by introducing smaller fluid mesh (Wangen, 2011) but this simultaneously increases the computational costs.

A popular approach is therefore to implement the fluid phase in models based on the DEM (Flekkøy et al., 2002; Ghani et al., 2013; Johnsen et al., 2006). While the solid framework is described in a discrete manner, the fluid usually follows the continuum description[2]. The rigid, incompressible particles collectively represent the porous media which deforms due to the forces generated by the fluid pressure gradients. The deformation, which changes the permeability, directly affects the fluid pressure evolution and this is the crucial solid-fluid coupling that many models lack. The first study that incorporated this coupling was carried out by Flekkøy et al. (2002). They used a triangular lattice for the solid framework where linear elastic springs connected the particles. The triangular lattice was chosen as it exhibits isotropic elastic behavior. Fracturing was defined by removing the elastic springs that overcome a predefined breaking strength threshold. Only mode I failure was considered.

The basic algorithm for the fluid pressure evolution and its coupling to the solid framework was implemented from the influential work of McNamara et al. (2000). The pressure evolution was calculated based on the fluid mass and the solid mass conservation, along with the local Darcy flow. The pressure derivate was obtained as the difference between the diffusion of the fluid pressure relative to the solid particles (i.e. Darcy flow) and the advection (i.e. pressure change due to solid faction density change) (Ghani et al., 2013; McNamara et al., 2000). The basic assumptions in the Flekkøy et al.' model (2002) included (1) the negligence of the expansion/compression of the solid on the fluid pressure, (2) negligence of the rapid porosity variations and (3) viscous fluid flow where the flow velocities within the fractures and the pressure gradients show a linear relationship. The model was given an initial background permeability that was changing due to fracturing (i.e. solid fraction density change). They utilized the smoothing function described by McNamara et al. (2000) to calculate the solid fraction density and its change on the pressure lattice sites. The function translates the mass (discrete positions) and velocity of each solid particle into continuous solid fraction and velocity field (Vinningland et al., 2007a). This is achieved by locating the four nearest fluid grid nodes for each solid particle. The solid deformation is calculated based on the forces exerted on the elastic springs both by the particles and by the fluid. The latter is the pressure force that is distributed over the neighboring particles using the smoothing function.

---

[2] The continuum description essentially means that the occupying space in entirely filled by material. In this specific case the fluid fills the space between the solid particles (i.e. fills the pore network).

The smoothing function provides the basis for the two-way solid-fluid coupling in the models.

Coupling between the solid-fluid can also be approached by investigating a solid-gas system. One of the most commonly used experimental setup for such system is the Hele-Shaw cell (Johnsen et al., 2006; Johnsen et al., 2008; Vinningland et al., 2007a; Vinningland et al., 2007c). The Hele-Shaw cell consists of two glass plates that are separated from each other by a 1 mm thick silicon frame. The confined space in between the glass plates is filled with air having atmospheric pressure and beads (grains) with a certain composition (usually glass). The Hele-Shaw cell is a well-established tool for simulating aerofractures (fracturing due to air injection) (Niebling et al., 2012) and the Rayleigh-Taylor instability (Vinningland et al., 2007c). The Rayleigh-Taylor instability is a known phenomenon from hydrodynamics, where a dense Newtonian fluid[3] is positioned on top of a less dense fluid. If the dense fluid is replaced by granular material (e.g. glass beads), this setup can represent geological phenomena such as underwater sedimentation, fluidized beds, turbidite deposition or liquefaction (Johnsen et al., 2006; Niebling et al., 2010; Vinningland et al., 2007a; Vinningland et al., 2007c). Experiments in a Hele-Shaw cell are usually carried out along with numerical simulations. The numerical models share similar basic assumptions, such as neglecting the gas/fluid inertia, the interparticle friction and the particle rotation. While all the models are based on the same algorithms introduced by McNamara et al. (2000), some consider the fluid compressible (McNamara et al., 2000; Vinningland et al., 2007a; Vinningland et al., 2007c; Vinningland et al., 2010), whereas others consider it incompressible (Niebling et al., 2010; Niebling et al., 2012). Niebling et al. (2010), however, proved that the fluid compressibility only played a small effect on the dynamics and structures of the Rayleigh-Taylor instability. They showed that the fluid viscosity, on the other hand, had a major influence on the instability with regard to the mixing behavior of particles: low fluid viscosities showed ballistic mixing with the solid particles, whereas high viscosity fluids mixed with the solid particles in a turbulent-dispersive manner.

---

[3] A Newtonian fluid exhibits a linear relationship between the local viscous stresses arising from the flow and the local strain rate.

The importance of poroelasticity was revealed by many porosity-controlled models (Flekkøy et al., 2002; Ghani et al., 2013; Goren et al., 2010; Johnsen et al., 2006; Mourgues and Cobbold, 2003; Olson et al., 2009; Shalev et al., 2013; Wangen, 2002). These proved that the driving stress for hydrofracturing is highly dependent on the fluid pressure feedback on the porous medium. Even though this fact is being shown more and more through analytical and numerical models, it is a still widely neglected factor in different simulations. This is partly because the widespread and existing classical view of the effective stress and the Mohr-circle shifting towards the failure envelope without any change of the differential stress. The poroelasticity might also be ignored due to its complex characteristics and difficulty to implement in models. The increasing computer powers, the evolving numerical models and the deepening knowledge on the subject, however, are leading to no excuses not to consider the intimate solid-fluid coupling in analytical and numerical simulations. The numerical and other coupled computer models gave insight into a crucial phenomenon which is also directly applicable to the hydrofracturing of porous media.

2.3 Graph theory and complex networks

Graph theory is the study of graphs which can be traced back to the famous mathematician, Leonhard Euler, and his famous Seven Bridges of Königsberg paper published in 1736 (Norman et al., 1986). Euler attempted to solve the problem to find a walk in the city of Königsberg which traversed all the seven bridges but only once. The separated landmasses represented the main points which were connected to each other by bridges (lines). This problem and its representation provided the foundation for the graph theory.

Graphs are mathematical structures that consist of vertices (or nodes) that are connected to each other by lines (edges) (Fig. 2.3).

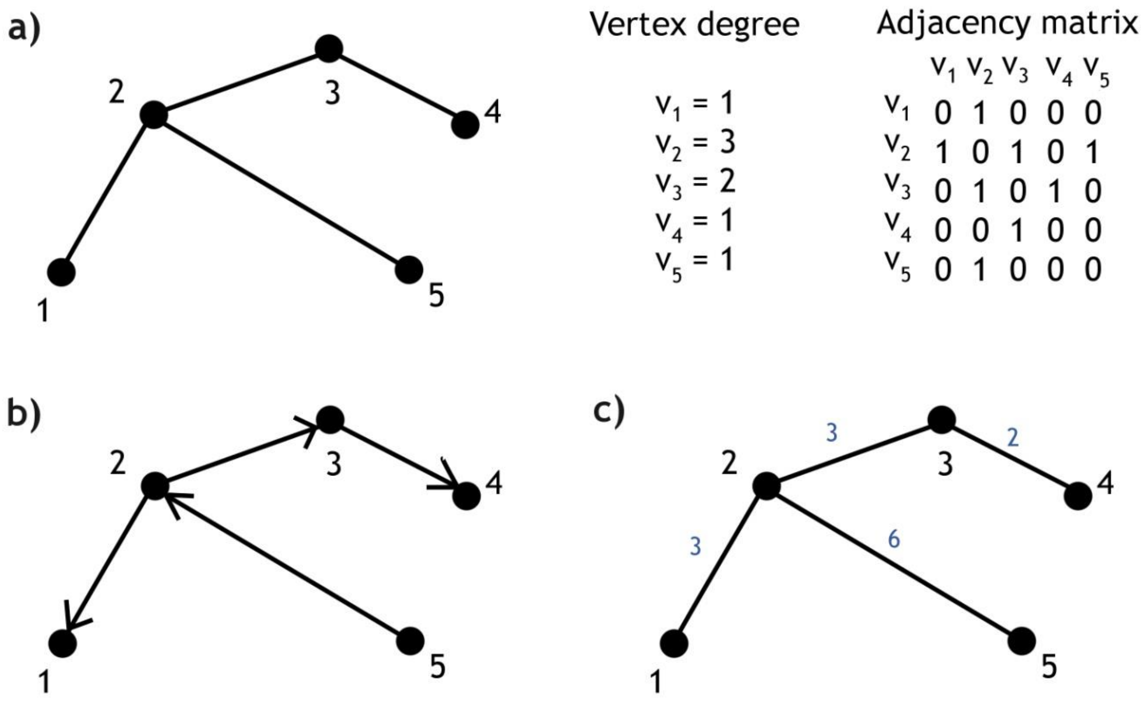

Fig. 2.3 Basic examples of graphs.
a) Undirected, unweighted graph with numbered vertices (dots) which are connected by edges.The degree of vertices (number of neighbors) and the graphs' adjacency matrix is also shown. b) Directed, unweighted graph where the connection only exists in the arrows' directions. c) Undirected, weighted graph where the edges are assigned numerical values. Edges with larger values will be of larger weight during any calculation.

The simplest graph is an undirected graph where the edges are lines that connect the vertices in both directions. Directed graphs, on the other hand, are made up of arrows indicating the direction of the edges, which means that the vertices are only connected in one direction. An example of this could be fluid flow, where the fluid flows from A to B but not the other way around. A graph can also be weighted by applying numerical values to either its vertices, edges or both. These numerical values can be based on characteristics such as edge length or number of vertex neighbors. Labeling the graph this way allows identifying elements of the graph that contribute more to the structure and therefore are more important.

Vertices *i* and *j* are connected or adjacent if an edge exists between them. It is common to represent the connectivity of a graph by its adjacency matrix. The adjacency matrix is a square matrix where the entries show if there is an edge between the vertices (1 – there is an edge between vertices *i* and *j*, 0 – there is no edge between vertices *i* and *j*). For a graph with no loops this will give 0 to the diagonal elements. Undirected graphs have a symmetric adjacency matrix since $a_{ij}=a_{ji}$. The adjacency matrix of a directed graph will also include the direction of edges; if the edge points from vertex *i* to vertex *j* then a_{ij}=0 but a_{ji}=1.

Two vertices that are not directly connected to each other (i.e. are not neighbors) might be still reachable from one to the other. The sequence of edges that lead from vertex *i* to *j* is called a path and the number of edges it contains is the path length. Certainly, several paths can exist between two vertices. In this case, one might be interested in the shortest path which means the minimum number of edges traversed to get from vertex *i* to *j* (Fig. 2.4) In general, a graph is said to be connected if a path exists between every pair of vertices.

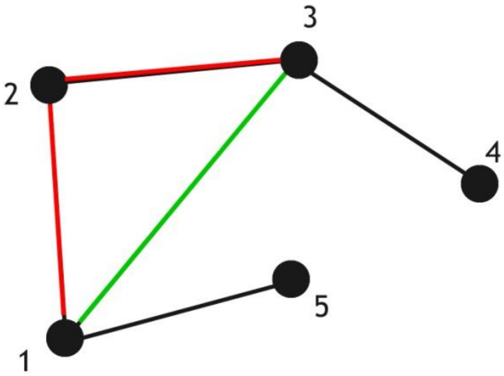

Fig. 2.4 A simple, undirected graph explaining the definition of paths.
Connection between vertex 1 and 3 exist through two different paths: red indicates a path with a length of two, whereas green shows a path with a length of one. This is the shortest path between them.

The total number of vertices (N) defines the order of the graph, whereas the total number of edges represents the size of the network in graph theory. It is, however, a common practice to use N as the size of the network, and in this work I will also do so unless otherwise specified. A graph is called a complete graph if all possible pairs of vertices are connected and the graph exhibits its maximum edge number, $\frac{N(N-1)}{2}$. Trees represent one class of the undirected graphs, where each edge has exactly one parent vertex which results in N-1 edges. Trees therefore have a typical hierarchical structure providing a graph where deletion of any edge disconnects the tree.

Graphs are characterized by a wide range of measures. The number of edges that each vertex has gives the vertex degree. The vertex degree is three when the vertex is a triple junction as it has three edges towards its neighbors. A vertex has zero degree if it does not have any edges and therefore is disconnected from the graph. Vertices in directed graphs have both in-degrees (the number of edges terminating at the vertex) and out-degrees (the number of edges starting at the vertex). Each vertex will therefore have a total vertex degree that is the sum of the in- and out-degree. The probability that a randomly chosen vertex has degree k defines the degree distribution $P(k)$.In case of directed graphs two distributions, $P(k^{in})$ and $P(k^{out})$, need to be considered. The degree distribution provides the most basic measure of the graph's topology.

Internal structures of the graphs can be well described by distance measurements. The most efficient transfer between any pairs of vertices is the shortest path between them. For this reason, the average shortest path length (L) gives a good indication of the graph structure and is defined by

$$L = \frac{1}{N(N-1)} \sum_{i \neq j} d_{ij} , \tag{2.1}$$

where N is the number of vertices and d_{ij} is the length of the shortest path between vertex i and j (Watts and Strogatz, 1998). While this definition provides a good measure for connected graph, it diverges for disconnected ones since if vertex i and j is not connected, $d_{ij}=\infty$. One way to eliminate this problem is to only calculate with vertices that belong to the largest connected component. However, if there are many unconnected vertices then L will diverge even more and would not be representative of the entire graph. For unconnected graphs a new measure, the so-called global efficiency (E), was introduced (Latora and Marchiori, 2001; Marchiori and Latora, 2000) which calculates with the harmonic mean of the shortest path length and is defined by

$$E = \frac{1}{N(N-1)} \sum_{i \neq j} \frac{1}{d_{ij}} . \tag{2.2}$$

This formula avoids the divergence of Equation 1.2 since $1/\infty = 0$ and therefore is more suitable for calculations on disconnected graphs.

Graphs can also be evaluated using the clustering concept. Clustering refers to the tendency of forming cliques near any vertex and is measured by the clustering coefficient. Two main clustering coefficients exist, global and local. The global clustering coefficient, also known as transitivity (*T*), is calculated as

$$T = \frac{3 * number\ of\ triangles}{number\ of\ connected\ triplets\ of\ vertices}, \tag{2.3}$$

where the triplets are three vertices that are connected by two or three edges (Newman, 2003; Newman et al., 2001). In the latter case, the triplet is closed and called a triangle. The local clustering coefficient (c_i) introduced by Watts and Strogatz (1998) shows how close a given *i* vertex's neighbors are of being a complete graph, therefore is calculated as

$$c_i = \frac{2e_i}{k_i(k_i - 1)}, \tag{2.4}$$

where the e_i is the number of edges between the *i* vertex's neighbors and the k_i is the degree of vertex *i* (Fig. 2.5). It is worth noting that Equation 2.4 is identical to the graph density measure. The difference is that the graph density takes into account the total number of edges and vertices (N), therefore gives an overall measurement, which provides information on how complete the entire network is. The local clustering coefficient, on the other hand, looks at subgraphs, little clusters of vertices within the graph and calculates the same measure locally. Averaging the local clustering coefficients of each vertex gives the (mean) clustering coefficient of the entire graph by

$$C = \frac{1}{N} \sum_i c_i \, . \tag{2.5}$$

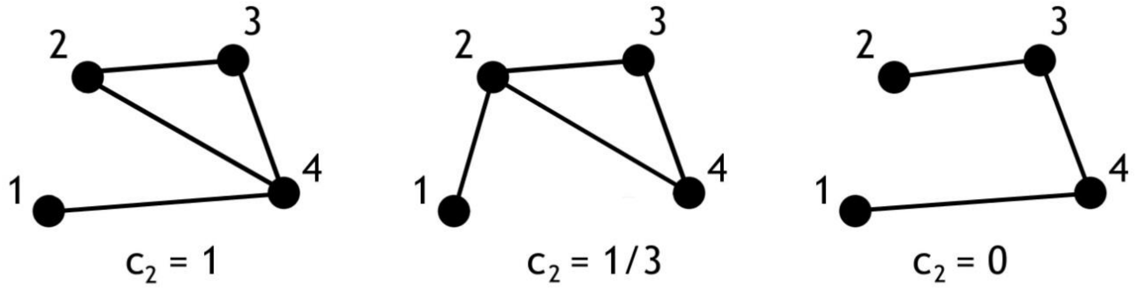

Fig. 2.5 Simple sketches explaining the local clustering coefficient.
A vertex has a local clustering coefficient of 1 if all the possible connections are present between its neighbors; and 0 if its neighbors are not connected at all or it only has one neighbor.

Quantifying graph heterogeneity is another important measurement that has long interested researchers. On way to characterize graph heterogeneity is by analyzing the vertex degree variance (Snijders, 1981). While this gives valuable heterogeneity information for large graphs with a wide spread of vertex degrees, graphs with a small range of vertex degrees would not stand out. In this case it might be more effective to look at the entropy of vertex degree distribution. Entropy generally refers to the lack of predictability and provides information about the amount of randomness in the analyzable data. In graph theory one can calculate the entropy of any list of data, such as the shortest paths between any pairs of vertices or local clustering coefficients. Yet, the entropy of vertex degree distribution provides the classic measure of a graph's heterogeneity (Costa et al., 2007; Wang et al., 2006). The entropy (*H*) is calculated as

$$H = -\sum_{k} P(k) \log P(k), \tag{2.6}$$

where $P(k)$ is the probability that the vertex has a degree of k (Costa et al., 2007).

Another network characteristic is to examine whether there is a preferential attachment of the vertices with regard to their degrees, i.e. do vertices with similar degrees tend to cluster together or low-degree vertices rather connect to high-degree ones? This degree-correlation is referred to as graph assortativity or assortative mixing, and is generally defined by the assortative coefficient (Pearson correlation coefficient) as

$$r = \frac{M^{-1}\sum_i j_i k_i - \left[M^{-1}\sum_i \frac{1}{2}\left(j_i + k_i\right)\right]^2}{M^{-1}\sum_i \frac{1}{2}\left(j_i^2 + k_i^2\right) - \left[M^{-1}\sum_i \frac{1}{2}\left(j_i + k_i\right)\right]^2} \tag{2.7}$$

where j_i and k_i are the vertex degrees at the end of the *i*th edge in a graph with i=1,… M (M being the number of edges in the graph) (Newman, 2002). The coefficient lies between $-1 \le r \le 1$, where -1 marks a disassortative and 1 an assortative network. Disassortative mixing refers to the preferential attachments of nodes with different degrees, whereas an assortative mixing represents a network with similar-degree connectivity.

There is a wide variety of further measurements that can characterize graphs, such as the graph diameter (largest value of d_{ij}), betweenness centrality (measuring the importance of a single vertex in a network) or distribution of sizes of clusters. Deciding what measurement one should apply during analysis depends on their type of network and their scope.

Graph theory and the study of complex networks are intimately coupled. A complex network is defined as a network with complex, irregular structure that is dynamic, i.e. the network and its characteristic features evolves in time (Boccaletti et al., 2006). Complex networks surround us and they appear in a variety of forms. The Internet, World Wide Web (WWW), road networks, transportation routes, power grids, epidemics or social networks (Facebook) are typical examples of large-scale networks. Complex networks also exist in the human body; the protein-protein interaction, the brain which builds up by interconnected neurons or the gene structure where a defect in the network can cause serious illness. Due to the networks extensive appearance and importance, understanding their characteristics soon became crucial. The pioneer work of Erdős and Rényi (1959; 1960) provided the foundation for network analysis. In their study they implemented the graph theory from mathematics and treated networks as graphs. This enabled a uniform approach to study different kind of networks. They introduced the random network model (Erdős-Rényi model) where creating connections (edges) between the vertices was based on a probability function. The result was a random graph (Erdős-Rényi graph) which evolved to a network at a threshold probability. The vertex degrees of this graph followed a Poisson (normal) distribution, which means that the majority of vertices have the same amount of neighbors (edges), whereas very small number of vertices have less or more connections than the average (Bollobás, 1998). This model, however, did not consider the possibility that the number of vertices may increase, i.e. the network may grow. The model did not assume either that there might be some kind of natural selection process, principle, in creating connections between vertices. The Erdős-Rényi model was a significant contribution to network studies and influenced researchers for decades.

Technological improvements in computer sciences (e.g. increasing computer powers) and the spreading of internet during the late 20th century made it possible to collect and analyze large datasets from real networks, such as WWW documents. The study of these networks showed that the Erdős-Rényi random model did not represent the real networks due to its assumptions. The pioneer work of Barabási and Albert (1999) revealed two crucial characteristics of real networks that are found to be identical irrespective of the nature of networks. First of all, they showed that real networks, contrary to the Erdős-Rényi random model, increase in vertex number, i.e. they grow in time. This feature produces a dynamically evolving network where each measure is time-dependent. Second of all, while the Erdős-Rényi model assumed that the connections between vertices are random, Barabási and Albert showed that there is an organizing principle, which they called preferential attachment. Preferential attachment suggests that the connections between vertices are actually based on the vertex degrees. New connections, edges, are more likely to develop at vertices with high degrees. In a social network example this means that a person is more likely to know someone who has many friends. These two characteristics, the network growth and the preferential attachment, led Barabási and Albert (1999) to develop a model representing the real networks. This model produced networks where the vertex degrees, contrary to the Erdős-Rényi model, followed a power-law distribution. Since power-laws have the same functional form at all scales, these networks were termed as scale-free networks (Albert and Barabási, 2002; Barabási, 2009; Barabási and Albert, 1999; Barabási and Bonabeau, 2003). Their power-law vertex degree distribution essentially means that there is a large number of vertices having just a few neighbors (connections), and there is not many vertices that have a lot of neighbors. These few vertices with a large amount of connections are usually called hubs. The inhomogeneous structure of these networks results in two crucial characteristics affecting the network vulnerability (Albert et al., 2000; Barabási, 2009; Barabási and Bonabeau, 2003; Callaway et al., 2000). The network will be robust against random, accidental failures (vertex removals), since the probability to remove a vertex with a small degree is higher than to remove the hubs. This is due to the fact that there are significantly more vertices with few connections and choosing these for removal is therefore higher. The network, in this case, will shrink but will remain intact. Albert et al. (2000) found that removing as much as 5% of the vertices will not affect the communication between the remaining 95%. However, a directed attack on the network, hubs, will destroy the structure. Describing and understanding these two features have direct and crucial application on networks such as the Internet (e.g. router failure) or power grids (failure of a transmission line).

Real networks have another important characteristic, and that is to create shortcuts between vertices. This bridging allows a more efficient communication in the network by decreasing the shortest path lengths between vertices. Many networks have found to exhibit small average shortest path length in spite of their large sizes. This characteristic is termed as small-world property and was first investigated in social studies (Milgram, 1967). Analyzing networks in terms of shortest path lengths revealed that both real and random networks (graphs) are associated with this property (Boccaletti et al., 2006). In order to distinguish between real and random networks, Watts and Strogatz (1998) proposed the definition small-world on networks that have both small average shortest path lengths and high clustering coefficients. This definition therefore only applies to real networks, as those typically exhibit high clustering.

The importance and implication of different networks have provoked extensive amount of research. Review articles (Albert and Barabási, 2002; Boccaletti et al., 2006; Costa et al., 2007; Newman, 2003) and books (Barrat et al., 2008; Dorogovtsev and Mendes, 2002; Watts, 1999) in the subject can provide further information and reference on complex networks.

2.4 Fracture network characterization in geology

Characterizing geological fracture networks is of great importance in exploration. It is used to understand reservoir characteristics and incorporate these in reservoir modeling to increase production and to decrease exploration risks. In long-term nuclear waste storage, on the other hand, fractures networks should be avoided. Fracture network characterization usually involves acquisition of fracture data and subsequent analysis to obtain statistical distributions that are unique for various networks. Data acquisition is usually carried out on outcrops that are subsurface analogues, well cores or images presenting fractures at various scales (wellbore images, thin sections, outcrop surfaces, numerical or experimental model images). Data acquisition on outcrops and well cores require sampling methods, such as linear scanline, circular scanline, window and aerial sampling, and a recently proposed augmented circular scanline method (Mauldon et al., 2001; Pahl, 1981; Priest and Hudson, 1981; Rohrbaugh et al., 2002; Watkins et al., 2015; Wu and Pollard, 1995; Zeeb et al., 2013).

Fractures can be characterized based on their geometries. These include length, aperture, orientation, frequency, angle between fractures and the statistical distribution of these (Adler and Thovert, 1999). The relationship between the fractures, i.e. topology, can capture crucial properties, such as connectivity. This has initiated many studies that attempted to obtain topological information on various networks (Hafver et al., 2014; Kobchenko et al., 2013; Sanderson and Nixon, 2015). Topology is usually approached via identifying fracture junctions and dead ends, which is essentially assigning vertices and edges. While some studies used graph theory to characterize fracture networks (Andresen et al., 2013; Santiago et al., 2014), they (1) lacked identifying dynamic measures that show how single fractures evolve to larger networks increasing connectivity, (2) did not relate topological measures to the mechanical properties of the systems and (3) did not highlight measures necessary for a good reservoir with high permeability and robustness against healing. The aim, therefore, was to fill this gap by quantifying fracture network evolution within various systems of different mechanical parameters.

3 Methods

3.1 Field work

Field mapping was carried out during two weeks in September 2013 and 2014. The studied area was stretching between Riva Trigoso and Framura, Italy, along the coast of the Ligurian Sea (Fig. 3.1a). This location was chosen due to the following reasons:

- thick shale sequences can be found here, which lithology is in the focus of the FRACS project;
- the shale has a high density of veins, which makes it possible to study a variety of vein types with regard to their formation;
- high fluid pressures were presumed to play an important role in the vein formation, i.e. the veins are believed to be of hydrofracture origin (see Chapter 2.1.3);
- the complexity of veining encouraged our scientific curiosity;
- the literature on the structures and veins in the area is limited, relatively old and only reflects the views of the same group of researchers.

The outcrops in the studied area are one of the best representations of the entire ILU sequence (Fig. 3.1). The bottom of the sequence (the ophiolite) is juxtaposed to the Palombini Shale at Framura.Moving northwest, this first grades into the Val Lavagna, then the thick Gottero Sandstone unit, which dominates the area around Deiva Marina. Moneglia shows an alternating Palombini and Val Lavagna sequence, which is then followed by the Gottero stretching up until Riva. In Riva the Bocco Shale representing the top of the ILU also outcrops in a thin zone. The Val Lavagna then comes back and characterizes the northwestern part of the studied area. The coastline is clearly shaped by the geology. Since shale is weaker than the sandstone, areas where the Val Lavagna and Palombini crop out were favored by erosion processes, creating bays where the towns (Riva

Trigoso, Moneglia and Framura) are located. Hard sandstones resisting the erosion separate the bays.

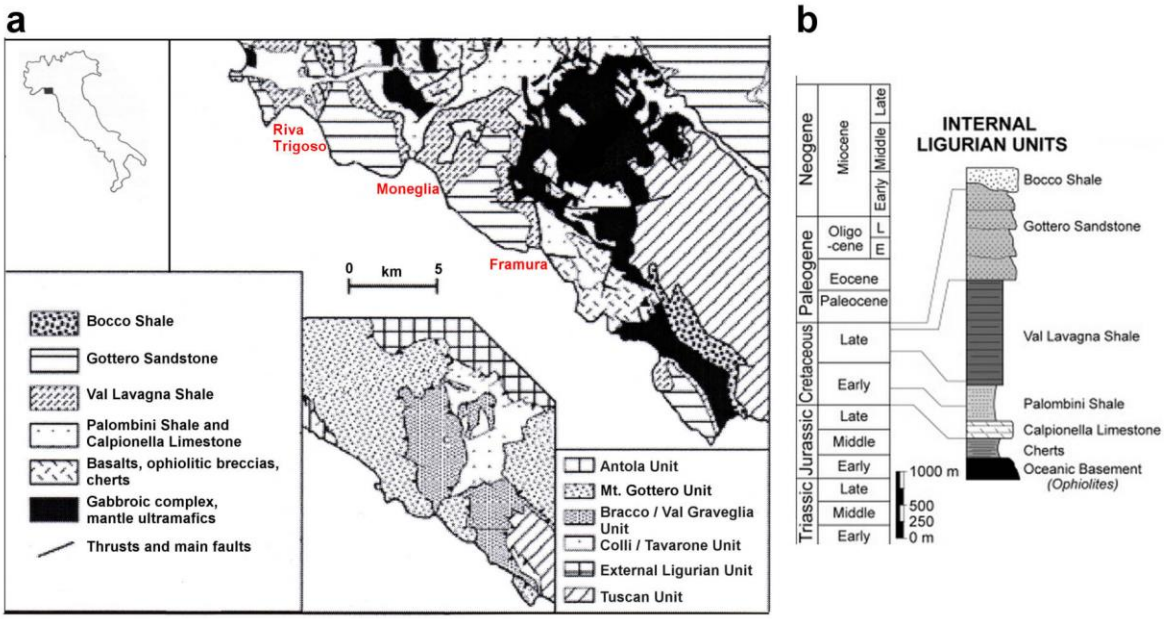

Fig. 3.1 Location and geological map of the studied area (a), along with the stratigraphic column of the Internal Ligurian Unit (b).
Map after Marroni (1996), stratigraphic column after Codegone et al. (2012).

While the focus was on the outcrops directly along the coast (purely because of their easy accessibility and good exposure quality), outcrops further up in the hills along different hiking trails were also examined. As the goal was to examine the veining and place it in the deformation framework of the ILU, both mapping of the structures (e.g. observing bedding-cleavage relationships, measuring orientations) and sampling were necessary. The available geological map and cross-sections, along with the literature were only considered as guidelines. Although the stratigraphical description of the ILU had helped to identify the different rock units on the field, the observed structures were not influenced by the literature.

3.1.1 Rotating and unfolding vein orientations on stereonet

Rotation and unfolding of planar and linear structures measured in the field are common methods to obtain the orientation of the structures before the folding events took place. The pre-folding orientations can give indications of the previous stress field that might have been responsible for their formations. The common way to obtain this information is to use the stereographic projection. The stereographic projection makes it possible to represent three-dimensional structures in a two-dimensional diagram called stereonet. Structural geologists usually use the Schmidt net (also called equal-area net) which preserves the area of the structures. Planes (e.g. beddings, veins) are represented as lines, whereas lines (e.g. fold axes, striations) appear as points on the stereonet. It is sometimes better to use the poles to the planes (i.e. the line perpendicular to the plane) instead of the great circles representing the planes. The rotation and unfolding of structures also requires poles rather than planes.

During the field work in Italy, a large number of veins were observed in folded layers where it was possible to measure (1) the bedding which included the veins, (2) the current vein orientations in the bed and (3) the fold axis that represented the rotation axis of the folding resulting in the current bed orientation. The veins, regularly found in conjugate sets, were confined to the bed and it was clear that they were folded along with the layer by the same fold axis (i.e. folding event). This gave the opportunity to obtain the vein orientations before the folding took place. Since fold axes were in all cases inclined obtaining the pre-folding vein orientations could be achieved by first rotating the fold axis to horizontal and rotating all the data with the same amount, then unfolding the bed including the veins. In the following I will outline the steps that lead to the rotated and unfolded vein orientations. This operation can be done both manually and using computer plotting programs. In order to obtain correct results using plotting programs, it is necessary to understand the underlying principles. It is also worth to check if the results that the program produces are in fact correct, i.e. they represent the true pre-folding orientations. For these reasons first I will outline the operation steps necessary for manual use, and then for using computer plotting programs.

For the manual method, one needs a stereonet (Schmidt net) and a tracing paper on which the required measurements (in our case bedding, veins and fold axis) should be plotted. Both the bedding and the veins need to be represented by their poles. For plotting the poles to these planes one needs to first mark off the strike direction on the primitive circle, rotate the tracing paper so that this strike overlays the north of the stereonet and count the dip from the stereonet center. For the line measurements, the trend needs to be marked off on the primitive circle and rotated to either of the stereonet's north, south, east or west. Counting the plunge value starting from the primitive circle along the straight line inwards will give the line orientation.

Once all the required measurements are plotted (Fig. 3.2a), the fold axis needs to be rotated to horizontal (i.e. so that it would have a plunge of zero) (Fig. 3.2b). In order to do this the fold axis has to lie on the E-W small circle, and by counting back its plunge (this will be the rotation magnitude) it is being moved onto the primitive circle. All the other data, i.e. the bedding and veins, need to be rotated with the same amount along the small circles. As we are rotating these along the same axis as the fold, the tracing paper should not be moved at this point. This means that the further away are the data from the E-W small circle the less effect will the rotation have on their orientations. When all the data is rotated the focus shifts to unfold the bedding and the veins[4] that it comprises.

An unfolded bed means a horizontal bed of which the pole is vertical (i.e. it lies in the center of the stereonet). First, the rotated pole to the bedding (RPB) needs to lie on the E-W small circle. At this point it is necessary to know if the bedding is normal or overturned. For a normal bed the pole should be moved to the stereonet center by its dip value. This essentially means that the shorter route to the center should be considered. However, if the bed is overturned the rotation magnitude will be the longer route, which is the difference of 180° and the dip value. This is because the overturned bed first needs to be rotated to the vertical (the pole lies on the primitive circle) and then to the horizontal (Fig. 3.2c). Either way, the rotation magnitude is obtained. Similar to the previous case, the stereonet should stay in the same position and all the rotated poles to the veins (RPV) need to be moved along the small circles counting in the same direction as moving the RPV. The unfolded and rotated poles to veins (URPV) are obtained, which then can be plotted as planes (Fig. 3.2d). Representing the veins as planes on the stereonet at this point is worthwhile in order to imply the stresses that might have formed the veins.

---

[4] Even though unfolding the veins is essentially rotation of the data, I will still use the term unfolding so that there is a clear distinction between the two steps: the rotation of the fold axis to the horizontal and unfolding the rotated bedding.

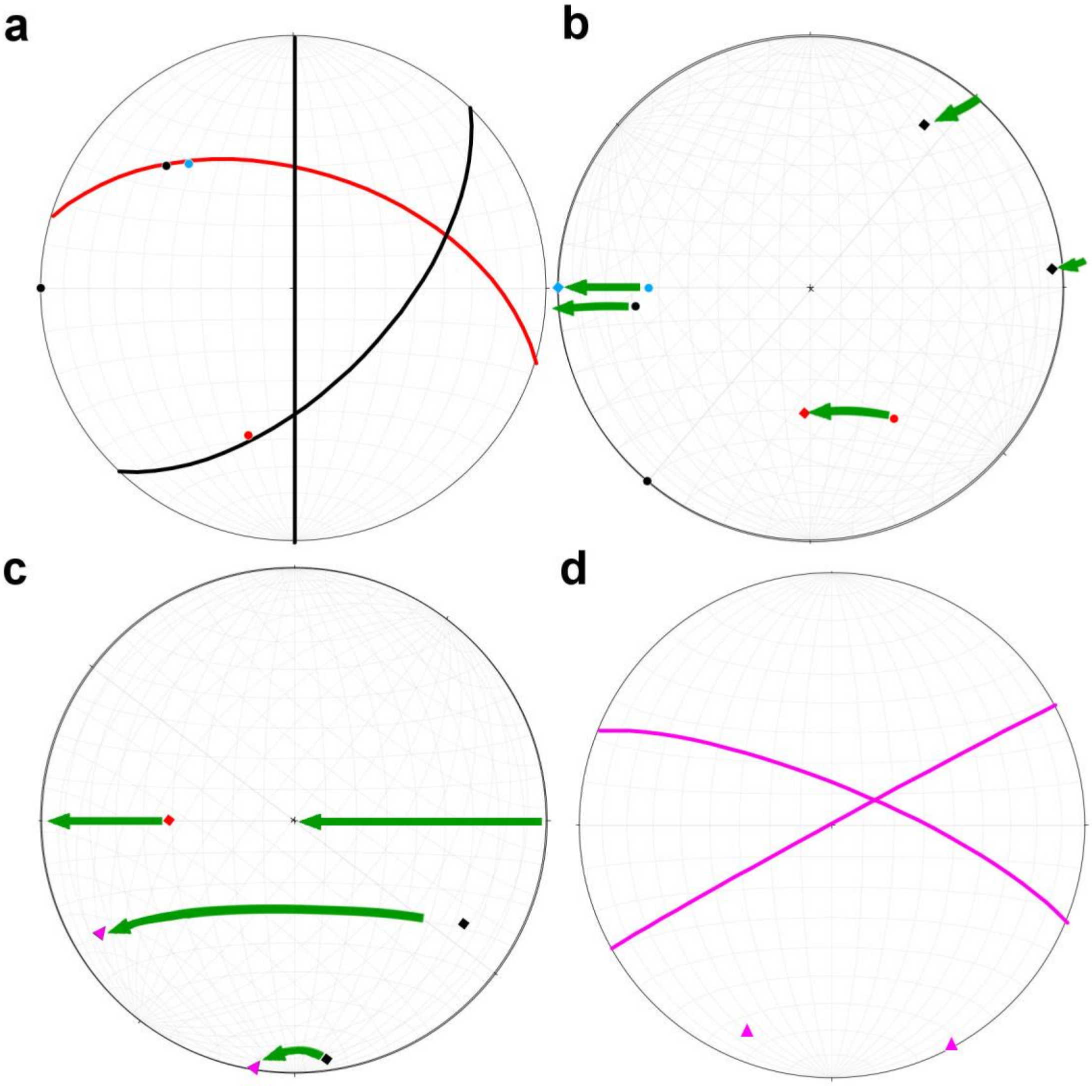

Fig. 3.2 Stereonets showing the steps required for rotation and unfolding data.
(a) Field measurements plotted on the stereonet. Planes also plotted as poles (black – conjugate vein, red – bedding, blue – fold axis). Bedding is overturned. (b) First, fold axis is rotated to horizontal. All the poles need to be rotated with the same magnitude along the small circles. (c) Unfolding of the overturned bed. Bed rotated first to vertical, then to horizontal. Poles again are rotated with the same magnitude along the small circles. (d) Rotated and unfolded conjugate veins (poles and planes).

Using a plotting program will make the rotation and unfolding much faster, simpler and more accurate. I used the Stereonet (version 9.2.0) (Allmendinger et al., 2013; Cardozo and Allmendinger, 2013), which is an open source software that can be used either online or downloaded and installed on all the major operating systems (Microsoft Windows, Mac OS or Linux-based OS, such as Ubuntu). Inputting the data can either be through importing measurements from a text file or by manually entering it. As I was interested in studying the pre-folding vein orientations in each individual location (with different bedding and fold axis) to get a more accurate representation, I entered the data for each location manually. I input the plane data as strike and dip (according to the right-hand rule), the lines as trend and plunge; the same format I measured them on the field. The planes again were plotted as poles. First the fold axis needs to be rotated to horizontal. Calculating and plotting this are not necessary, as only the rotation axis should be known for rotating the veins. Under the menu option “Calculations” we find the “Rotate data”. Here the azimuth and plunge of the rotation axis, along with the magnitude of rotation can be defined. The rotation azimuth will be the sum of the fold axis trend and 90°. The rotation axis will plunge zero, and the rotation magnitude will be the plunge of the fold axis. By selecting the required dataset to be rotated (pole to the bedding and poles to the veins), the program calculates and plots the RPB and RPV. In case a negative plunge appears, the data has to be converted to the lower hemisphere to obtain the correct value.

For the second step, that is unfolding the rotated data, two options exist. In case the bedding is normal, one could use the “Unfold bedding” under the “Calculations” menu option. By selecting the dataset (e.g. RPV) and the bedding itself, the program unfolds data (resulting in the URPV) and plots them on the stereonet. As it is not possible to specify the type of bedding (normal or overturned) under this menu option, a different approach needs to be applied for unfolding overturned beds. Similarly to the first step, the “Rotate data” menu option will be used. In order to get the azimuth of the rotation axis and the magnitude of rotation, it is necessary to calculate the plane from the RPB (pRPB). The rotation azimuth equals the strike of that plane, whereas the rotation magnitude can be calculated as the difference between 180° and the dip of the pRPB. The latter gives the same result as the sum of the RPB plunge and 90°. This method also works for normal bedding. In case of a normal bed, however, the rotation azimuth will be the strike of the pRPB plus 180°, whereas the dip of the pRPB equals the rotation magnitude. Regardless of the calculation method, the URPV are obtained and again if either of the data has a negative plunge, it has to be converted to the lower hemisphere. Finally, the URPV should be plotted as planes to correlate the vein orientations to stress directions.

3.1.2 Microstructural analysis

Polished thin sections of the characteristic vein types identified in the field were obtained for microstructural analysis. First, all the thin sections were examined under optical microscope to gather information on the mineralogy and texture of the veins. Focus was on the veins and vein-wall rock interface, whereas the host was not examined as it was irrelevant for the scope for the project. Those vein samples that were assumed to be mineral-filled hydrofractures (i.e. dirty veins and the bed-parallel and perpendicular set) were then investigated under scanning electron microscope (SEM) (ISAAC Instruments FEI Quanta 200F Environmental SEM) at the University of Glasgow. Prior to the analysis carbon coating was necessary to improve image resolution. Analysis included obtaining secondary and backscattered images, chemical analysis of crystals and different zones (e.g. through the vein) using EDAX microanalysis software. In addition to these, electron backscatter diffraction (EBSD) was also carried out to obtain crystal orientation maps. During EBSD analysis the sample needs to be tilted approximately 70° to the electron beam to optimize contrast. Once removing the background intensity and adjusting the resolution, measurements were set up with one micron step size. The electron beam then scanned over a hexagonal grid of points and for each point the crystal orientation was measured. Crystal orientations were assigned colors using a preset color key. These samples were also analyzed using cathodoluminescence (CL) detector attached to the SEM. CL was used mainly to examine crystal growth within the veins that could be related to processes such as growth from different fluid chemistry or change in precipitation conditions (e.g. pressure, temperature, oxidation).

3.1.3 Fluid inclusion microthermometry

Fluid inclusions are micron-scale volumes of fluids that entrapped in the crystals during mineral precipitation. They can be of primary or secondary origin, and contain various phases within (solid, fluid, gas). Fluid inclusion microthermometry is a powerful tool to obtain information on the ambient environment during mineral precipitation. The method is based on three assumptions: (1) the inclusions were trapped from a homogeneous (single phase) fluid, (2) the inclusion volume remains constant and (3) the inclusions represent a closed system, i.e. nothing was added or removed from the inclusion after trapping. The assumptions are not valid for leaked inclusions. Leakage of the inclusions is very likely to happen if (1) the inclusion-host mineral has good cleavage, (2) the inclusions are close to or are along grain boundaries and/or (3) the host experienced deformation or higher temperatures than the formation.

Analysis cannot be carried out if the inclusions lack of phases (known as metastability) or if the trapping itself was heterogeneous. All these can impede the measurements and/or lower the accuracy of the results. Therefore it is crucial to perceive the likelihood of these processes and judge whether it is possible to carry out measurements and do these measurements reflect correct results. In addition to this, one must know what they are about to measure, which fluid phase do the inclusions represent and what will the temperatures correspond to. It is thus important to define the present phases, as well as the types of inclusions (primary, secondary or pseudosecondary) prior to measurements (Fig. 3.3). Primary inclusions are those trapped during the primary growth of a mineral. They are usually aligned parallel to growth zones, crystal faces, or appear in three-dimensional random distribution. Secondary inclusions usually occur as planar groups that terminate at crystal boundaries cutting through growth zones. They usually outline healed fractures. Pseudosecondary inclusions are similar to the secondary ones except they terminate at growth zones. Although these criteria should be sufficient to recognize the inclusions' origin, frequently it is not possible. In samples where the crystals are lacking of well-developed shapes (e.g. they are subhedral or euhedral) or growth zones it is not possible to determine the origins of inclusions (Shepherd et al., 1985).

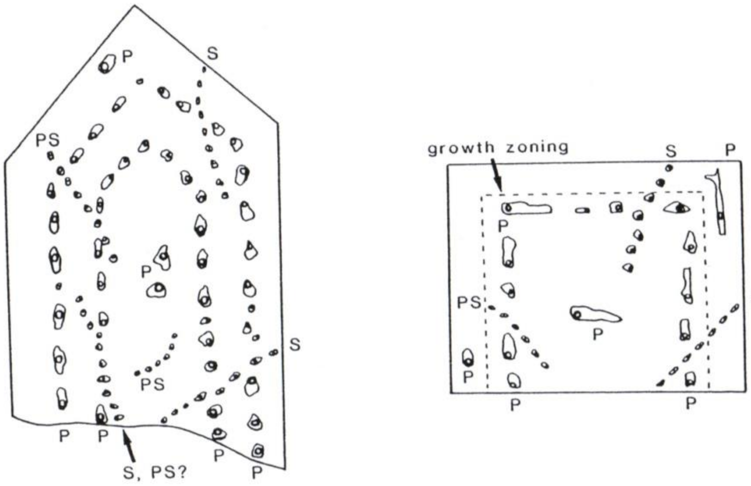

Fig. 3.3 Ideal occurence of primary (P), pseudosecondary (PS) and secondary (S) inclusions within crystals (Shepherd et al., 1985).

Accurate fluid inclusion measurements will give information about the pressure-temperature conditions during veining, the vein-forming fluid chemistry and possible migration pathways (Shepherd et al., 1985). In order to achieve accurate results, choosing the right sample during field work is essential. It is therefore important to think ahead and specifically look for certain types of samples. When it comes to veins it is best to have a vein with large (i.e. visible), well-developed and most importantly, clear crystals. Milky crystals or those that incorporate dark host rock segments worsen the visibility of the fluid inclusions. It is also worth noting that the distribution of inclusions and their characteristics can be extremely heterogeneous along the vein plane. This can refer to features such as the amount of inclusions, their sizes or their visibility. While some samples could lack (good) inclusions, others might have many. Due to this heterogeneous characteristic it is usually worth to sample the veins both along their strikes and dip directions several times.

Four types of veins in the Val Lavagna Shale were sampled in the field: a bed-parallel calcite, a non-dirty bed-parallel quartz vein, blobs of mineralization (also bed-parallel) and a bed-perpendicular vein crosscutting this one. While many other vein types were also observed (see Chapter 4.2), these ones could not be related structurally to the others. In addition to this, blobs and the non-dirty veins were the only ones that showed large, relatively clear quartz crystals in the hand specimens. The other veins were not only very thin, but they also mainly included deformed calcites that were milky. Once samples were collected double polished wafers of approximately 130 μm thickness were made.

The analysis was carried out at the University of Aberdeen using a Linkam PR600 temperature controller and a Linkam CS196 cooling system connected to a THMSG600 thermometric stage. The analysis of the samples consisted of a cooling and a heating cycle. The cooling cycle would have provided salinity values of the trapped fluids. First, the stage was heated up to 102°C to vaporize the moisture within the chamber. Cooling this down to -10°C while opening the valves and allowing liquid nitrogen to flow through the chamber allowed the complete dehumidification of the chamber. Once closing the valves and cooling the stage down to -150-180°C, various temperature ramps could be set up depending on the type of inclusion. For a brine liquid and a vapor the temperature could go up by 20°C/minute to around -40°C, where the rate needs to be decreased (3-5°C/minute) to observe the first and last ice melting temperatures. This stage could also be set up as two separate ramps.

Minimum homogenization temperatures of the trapped fluids were obtained through the heating cycle. Rate for heating was generally 20°C/minute until the vapor bubble started moving very fast when it was reduced to 5-10°C/minute. When the bubble appeared to be homogenized with the liquid, the temperature was hold constant for several minutes. This allowed time to focus through the inclusion to see if the bubble moved away to another corner, and to examine whether the vapor indeed disappeared. It is quite common that the bubble disappears but reappears as the temperature is kept at that level. In case the vapor reappeared, the heating rate was set to 1°C/minute to get an accurate temperature. The vapor disappearance marks the minimum temperature at which the fluid was trapped and the crystal formed. The homogenization temperature (T_H) therefore does not correspond to the trapping temperature (T_T), which is usually higher. The T_H and T_T lie on a constant density line, an isochore, the slope of which is a function of bulk density (degree of fill). Degree of fill can be calculated as V_L/V_L+V_V, where V_L is the liquid and V_V is the vapor degree.

The slope of the isochore, dP/dT (bar/°C), of a known system can be calculated. For a two-phase H_2O-NaCl system the slope of the isochore is obtained through the T_H and the salinity-dependent fitting parameters (a_s, b_s, c_s) (salinity – S), as

$$\frac{dP}{dT} = a_s + b_s * T_H + c_s * T_H^2 \ , \tag{3.1}$$

where

$$a_s = 18.28 + 1.4413 * S + 0.0047241 * S^2 - 0.0024213 * S^3 + 0.000038064 * S^4 \tag{3.2}$$

$$\begin{aligned} b_s = {} & 0.019041 - 1.5268 \times 10^{-2} * S + 5.66012 \times 10^{-4} * S^2 \\ & - 4.2329 \times 10^{-6} * S^3 - 3.0354 \times 10^{-8} * S^4 \end{aligned} \tag{3.3}$$

$$c_s = -1.5988 \times 10^{-4} + 3.6892 \times 10^{-6} * S^2 + 4.1674 \times 10^{-8} * S^3 - 3.3008 \times 10^{-10} * S^4 \tag{3.4}$$

(Bodnar and Vityk, 1994).

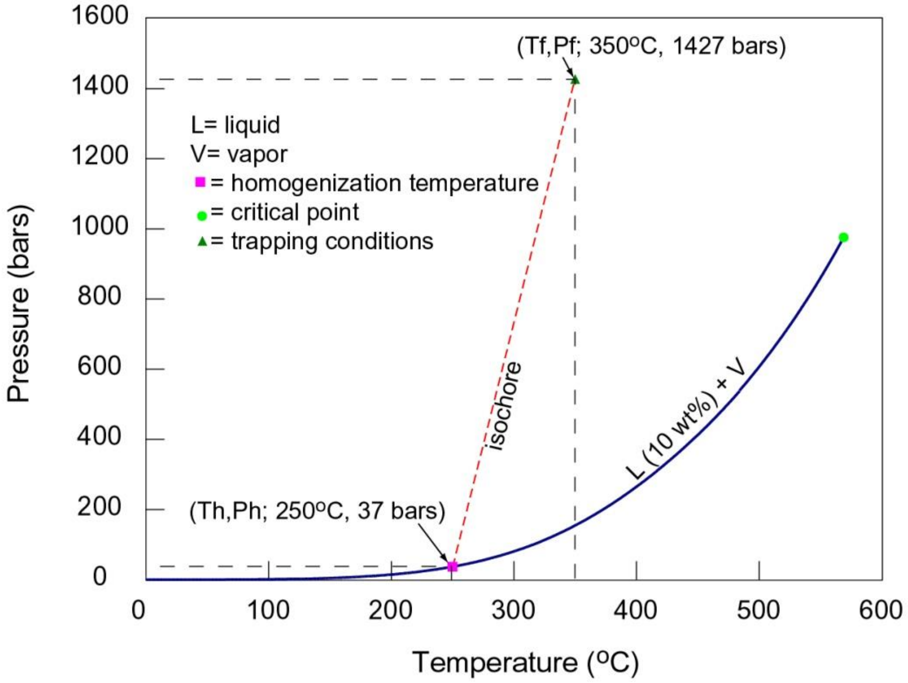

Fig. 3.4 Pressure-temperature curve for a H_2O-NaCl inclusion with 10 (wt)% NaCl.
An inclusion homogenizing at 250°C (T_H) corresponds to a vapor pressure of 37 bars. The isochore of this system can be calculated. If there is no independent geothermometer and the inclusion did not trap from a boiling fluid, the trapping pressure (corresponding to the fluid pressure, P_f) will lie on any points along the isochore. With a known trapping temperature (fluid temperature, T_f) the intersection represents the P_f. Figure from Atkinson (2002).

Calculating fluid pressures from inclusion data using T_H requires approximation and therefore should be treated accordingly. A system with known composition is characterized by a pressure-temperature stability curve. In a two-phase (liquid-vapor) system the vapor pressure can be read off as the equivalent of the homogenization temperature trajectory on the liquid-vapor curve (Fig. 3.4). This vapor pressure corresponds to the absolute pressure minimum at which the inclusion trapped (P_{Tmin}). The T_T and the trapping pressure P_T, however, will lie at any point on the isochore (unless the inclusions is from a boiling fluid), and thus without further data they cannot be obtained. In order to get the trapping pressure an independent geothermometer is required. These can refer to distribution of elements within crystals or isotope fractionations that are temperature-dependent. These measurements also generate uncertainties with regards to accuracy and thus decrease the overall accuracy of the pressure determinations. It is therefore important to have a geothermometer as precise and accurate as possible to limit the uncertainties. An independent geothermometer marks the T_T, which by intersecting the isochore gives the P_T. P_T of inclusions with two immiscible fluids or daughter minerals could be obtained using different methods but as these are not relevant to the inclusions in this thesis, I will not outline them.

3.2 Elle

Ghani et al. (2013) proposed a numerical scheme (DEM, continuum-model) which was built on the work of McNamara et al. (2000), Flekkøy et al. (2002), Koehn et al. (2005), Vinningland et al. (2007c), Niebling et al. (2010) and Goren et al. (2010; 2011). I outline the extended model of Koehn et al. (2005) and Ghani et al. (2013) to study the interplay between gravitational, tectonic and fluid forces as well as fracture healing.

The Latte extension of the Elle modeling environment is being used to simulate the dynamic fracturing and healing of a pressurized sedimentary sequence (Bons et al., 2008; Koehn et al., 2005). The basic framework for the simulations is a 2D hybrid triangular lattice data structure where equal sized, disk-shaped particles (nodes) are connected to their neighbors via linear elastic springs representing the discrete elastic solid (Fig. 3.5b). This lattice is superimposed over a stationary square grid through which the continuum diffusion of fluid pressure takes place. The model therefore is underlain by two main computations. One deals with the linear elastic behavior of the system, whereas the other solves the porosity-dependent fluid pressure diffusion.

Deformation of the elastic media is triggered by the net force acting on a solid particle (node). The net force is calculated as the sum of the interaction forces between the neighboring particles (interparticle force), the fluid and the gravitational force on the particles. The deformation is thus governed by the time-dependent force-balance equation

$$m_s\left(1+\frac{\rho_f\phi}{\rho_s(1-\phi)}\right)\frac{du_s}{dt}=F_i-\nabla P\frac{V_s}{1-\phi}+\varphi_{eff}V_s g\ , \tag{3.5}$$

with m_s being the mass of the solid, ρ_f and ρ_s the fluid and solid densities, u_s the velocity of the solid, F_i the interparticle force which keeps the particles from overlapping each other, ∇P the fluid pressure gradient, V_s the volume of the solid, Φ the porosity, $\rho_{eff} = \rho_s - \rho_f$ the effective density of the solid and g the gravitational acceleration (Ghani et al., 2013). The equation is solved by using a standard over-relaxation algorithm. The solution for the equations results in a heterogeneous force network where the load is transmitted through the solid particles (Vinningland et al., 2007b). Fluid pressure evolution in the system is represented via the local fluid pressure changes on each node, and is calculated as

$$\phi\beta\left(\partial_t P + u_s \nabla P\right) + \nabla u_s \left(1+\beta P\right) = \nabla\left[\left(1+\beta P\right)\frac{\kappa}{\mu}\nabla P\right], \tag{3.6}$$

where ß is the fluid compressibility, κ is the permeability of the solid and μ is the fluid viscosity. The first term on the left hand side of equation 3.6 is the Lagrangian derivate of the pore fluid pressure, which calculates the rate of fluid pressure change as a function of solid particle acceleration. The second term is the so-called source term that facilitates this fluid pressure change if the solid particles move in the reference frame. The right hand side of equation 3.2 is the Darcy diffusion of fluid pressure. The pressure diffusion in this continuum grid is calculated using the Pressure Alternating Direction Implicit algorithm (Press et al., 1992). A detailed derivation of the underlying computations can be found in the paper of Ghani et al. (2013) and references therein.

The two lattices are overlapping each other, where the fluid lattice is twice the size of the solid one. Coupling between the two lattices is based on a process where the values in either are passed onto the other lattice. This is achieved by a linear smoothing function, which translates the mass and velocity of individual particles into a continuum solid fraction and velocity field (Vinningland et al., 2007b). The grid nodes obtain fractions of a particle’s mass and velocity based on the particle’s distance to the nodes. This creates a weight map seen on Fig. 3.5c, where the node closest to the particle will have the highest fraction, whereas the node furthest away gets the smallest fraction of the particle’s parameters. The smoothing function also makes it possible to transfer fluid pressure forces of the grids onto the solid particles based on the same weighted principle. Once the fluid pressures are calculated for a given time step, the pressures are passed onto the solid framework and converted to forces that act on each individual particle. These forces exert elastic deformation on the solid framework and may also cause fracturing if the forces exceed the predefined breaking threshold of single bonds. Breaking threshold of a single spring is defined as the maximum stress the spring can sustain without breaking. The distribution of breaking strength plays a major role in the deformation; it determines the overall breaking strength of the system, along with the mode of fracturing that occurs on larger scale (Koehn et al., 2005). Breaking strengths in the system are set to have a normal distribution. In general, however, the overall strength of the system is larger than the individual spring strengths.

Once a fracture (array of broken bonds) is created, it has the ability to heal (close) according the implemented healing function. Healing in the model is defined by four parameters: the healing distance, healing probability, and the elastic and tensile properties of the new springs. The healing distance represents the distance between the broken particle walls and therefore can be regarded as the width of the crack. The healing probability is calculated using Monte-Carlo approach

$$P_{heal} = \begin{cases} 0, & \dfrac{l_{i,j}}{l_{heal}} < d_i \\ P_0 \dfrac{d_i}{l_{i,j}}, & \dfrac{l_{i,j}}{l_{heal}} \geq d_i \end{cases}, \tag{3.7}$$

where $l_{i,j}$ is the distance between particle i and j, d_i is the diameter of particle i and P_0 is the basic healing probability (Vass et al., 2014). Healing is achieved by reconnecting broken particles with an equilibrium length (i.e. unstressed) new spring. These new springs are then attributed with elastic moduli and breaking strengths that can be of different values than the unbroken bonds in the matrix. Both parameters are defined as the average values of the unbroken bonds multiplied by a predefined change in threshold. The breaking strength, similarly to the initial unbroken matrix, has a normal distribution. As the new springs essentially add mass to the system causing local porosity change, veins can be defined as the new springs and a proportion of the connected particles. Veins have two direct affects on the strength of the system. On the particle scale the strength of the vein-host rock connection lies between the strength of the new springs and matrix. This can allow fracturing either in the veins or in the host rock next to the veins. On larger scale, however, the overall strength of the veins is defined by the amount of healed connections. It is apparent that a partly open and a completely healed vein will have different strengths due to the amount of new springs involved.

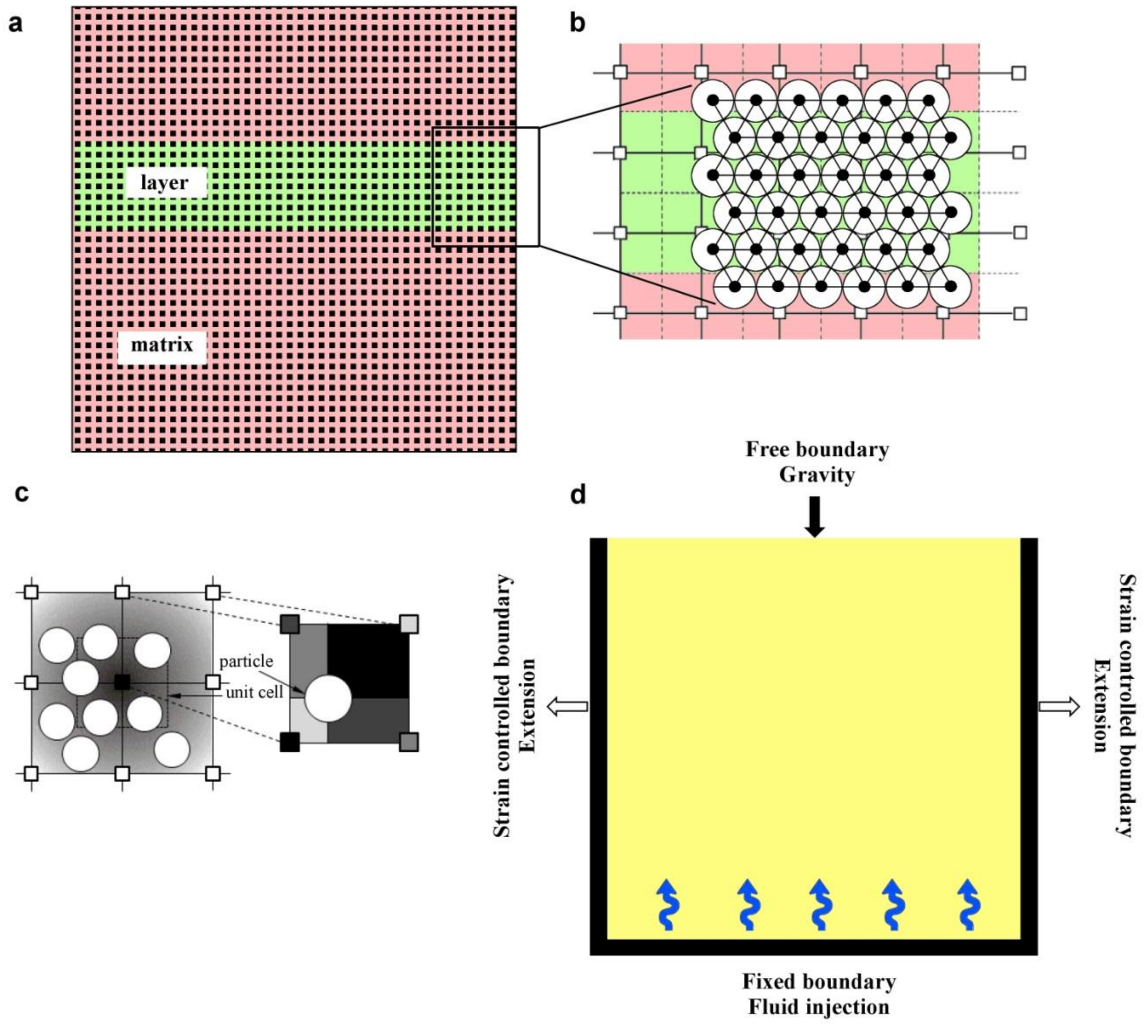

Fig. 3.5 Model configuration and the coupled fluid-solid framework.
(a) Model geometry with an embedded horizontal layer. (b) The DEM solid lattice is represented by a triangular elastic network, which overlays a square grid lattice representing the fluid framework. (c) The implemented smoothing function, which creates a continuum field based by weighting individual particles based on their distances to the grid. (d) Boundary conditions for the model. Figure modified after Vass et al. (2014).

Both the solid and the fluid lattice are confined by boundary conditions (Fig. 3.5d). The solid lattice is constrained by walls on the sides and the bottom of the model that cannot break and are considered as free-slip boundaries (i.e. zero tangential velocity gradients) with repulsive characteristics. The upper boundary is a free boundary where the overlying sediments exert vertical (gravitational) forces on the particles. Particles therefore settle due to their weights and this produces the gravity gradient within the box. Upon deformation the wall on the right hand side is moving outwards assuming a homogeneous deformation in the model prior to the relaxation. This mimics extensional movement in a homogeneous manner. The fluid lattice is confined by periodic boundaries on the sides where no fluid can escape. The upper and the lower boundaries initially have fixed pressure values creating a homogeneous hydrostatic fluid pressure gradient within the model. At any point, therefore, the fluid pressure is a function of the height of the box (i.e. depth) and the overlying sediment. Fluid is then injected along the lower boundary of the model by increasing fluid pressures in the nodes. This will increase the initially hydrostatic pressures, which in turn will cause gradient variations.

All simulations start from a completely relaxed state, where the particles settle according to the gravitational and fluid sources. The onset of simulation first facilitates the fluid injection, then the extension. The injection causes fluid pressure increase, which is calculated for each node and each time step. As the new pressure gradients are obtained the lattice relaxes and the particles start to move according to the new forces acting on them in order to reach the new equilibrium state. The system then checks the spring's breaking strengths. Fracturing (i.e. breaking the springs) not only depends on the bond strength but on the probability as well. A bond will break if its breaking threshold is exceeded more than the other springs'. Once it is removed from the lattice, the model relaxes again, and may continue to break until all the springs' strengths are below the threshold. This fluid step is then followed by the extensional deformation step, where the wall on the right hand side moves outwards. Particles again are moved until they attain their equilibrium position (i.e. model relaxes), and the springs are again checked which can result in a second fracturing event. The simulation then facilitates the healing function, where any broken particles can be reconnected. This terminates one simulation step and the model then loops onto the next one. The particles in the system will remember how many crack-seal cycles did they undergo, and when was the last time they healed and fractured.

The mass balance within the model is different during the fracturing and the healing process. As fracturing takes place and a spring is removed from the solid lattice there is no mass change. However, during the healing cycle a relaxed, non-stressed bond is being reintroduced to the lattice. This new bond is generally longer than the other, unbroken bonds since the deformation causes the particles to move and therefore they might be further away from each other than the unbroken particles (i.e. the particle distance at a fracture is usually larger than the particle distance between unfractured lattice sites). The model at this point calculates how much (additional) mass is needed to achieve equilibrium between the new spring and the lattice. This means that mass is added during healing by increasing the solid fraction within the model. The healed bonds due to their different lengths will therefore create local anisotropy within the model. Progressive deformation and increasing healing thus makes the model more and more anisotropic.

The simulated area, which represents a cross section through the crust, is 200 m high and wide, and is considered to be located at 3000 m depth (making the total depth of 3200 m). The solid has a density of 2700 kg/m^3, whereas the water's is 1000 kg/m^3. Water compressibility is taken to be 4.5×10^{-10} Pa^{-1} and its viscosity 10^{-3} Pas. The Poisson ratio of the model is 0.33 due to the lattice geometry giving rise to isotropic deformation. This value was derived from the continuum form of the stress tensor on an arbitrary lattice site and the standard two-dimensional continuum expression (Flekkøy et al., 2002). One time step in the simulation corresponds to 1000 days. As all the simulations run for 20000 time steps, they represent roughly 54.8 ka. The extensional strain rate is set to 10^{-14} s^{-1}. Elastic and tensile constants in the model are based on a non-dimensional coordinate system where the default values are set to 1.0 (equals 10 GPa) and 0.0017 (equals 17 MPa), respectively. The breaking strength is characterized by a normal distribution between 15 MPa and 300 MPa, which leads to an overall breaking strength of the matrix of 20MPa. The healing probability is set to 0.009 which means that a crack is likely to close within 90 time steps (~247 years). The tensile and elastic properties of the new springs may be different to those of the unbroken bonds. This allows simulating strong/weak and stiff/soft veins embedded in the matrix. A strong/weak vein has new bonds with higher/lower breaking strength, and a stiff/soft vein has higher/lower elastic modulus in comparison with the unbroken bonds. The simulations usually contain a horizontal layer with different properties than the matrix (Fig. 3.5a). The parameters that characterize the matrix, layer and the veins are outlined in the relevant (sub)chapters.

3.3 Mathematica

The research idea to characterize fracture networks as graphs required a software that can carry out both image analysis on unsegmented images and calculations on graphs. Even though Matlab is suitable for both, the segmented image that comes out of the image analysis process cannot be converted to graph – at least there is no such built-in function to do that. Certainly, one could write a function that would make the conversion possible but after further research it appeared that the software Mathematica has a built-in function, therefore this was used for the fracture network characterization.

Mathematica is a computational software program developed and distributed by Wolfram Research. It has long been a powerful tool in scientific, engineering, mathematical or other computational problems. Mathematica has a wide range of functions that work in an integrated platform with large algorithm power. It provided a great system where both the image and the graph (network) analysis could be carried out.

I will first outline the descriptions of the analyzed networks as well as their experimental setups. I then move on to the image pre-processing, which was necessary for the graph conversion. Computations on graphs close the chapter, where I present the measures for network analysis.

3.3.1 Experimental descriptions of the analyzed networks

Two main types of networks provide the base for calculations: mudcracks and hydrobreccia. All the presented networks but one are numerical experiment results obtained through the Elle modeling environment (see Chapter 3.2). The one exception includes flour experiments carried out at the University of Oslo (therefore I refer to them as Oslo flour experiments). Both the numerical and laboratory experimental setups will be outlined separately in the followings.

Mudcracks form as a result of the shrinkage of a muddy layer due to the loss of water. The dried-out layer develops this typical, polygonal crack pattern, which is also similar to those formed during basalt cooling creating hexagonal columns. Mudcrack patterns were produced using the Elle software described in Chapter

3.2. The deformation box in this case represented the top surface of the layer which was shrinking to produce the mudcrack patterns. The layer’s mechanical properties (breaking strength and Young’s modulus) were varied to examine the pattern change. Values are listed in Chapter 6.1.1.

Hydrobreccias form along fault zones as a result of extremely high fluid pressures that break the rock creating breccia, which are usually mineralized. Hydrobreccia can also be modeled as building up fluid pressures under a seal and examining the fracture network evolution. This is how the hydrobreccia pattern was created using the Elle software. The deformation box represented again a vertical section of the crust, with a size of 1000 m and 3000 m of overlying sediment (Fig. 3.6). The box was confined on the sides and at the bottom, while the upper boundary, along which the gravity was applied, was open. A soft seal with a mean Young’s modulus of 5 GPa, breaking strength of 45 MPa and a mean porosity of 6% was embedded in the lower part of the deformation box. The matrix itself had a mean elastic modulus of 5 GPa, breaking strength of 15 MPa and porosity of 20%. Fluid was injected at random locations in each time step below the seal. This therefore allowed the initially hydrostatic fluid pressure to increase under the seal. In this experiment, while gravity was applied on top, the fluid provided the major stress on the system and therefore was the driving force for deformation.

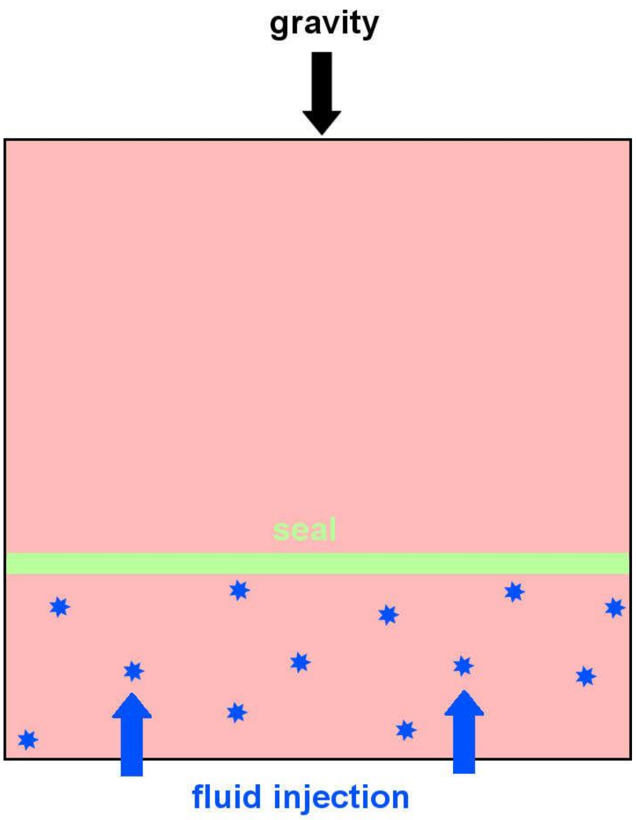

Fig. 3.6 Model configuration for the hydrobreccia experiment.
A strong seal is embedded in a soft and weak matrix. Gravity is applied on top, whereas fluid is injected at random locations under the seal.

The flour experiments were carried out at the University of Oslo as part of a group work during a Master course. The experiments aimed to analyze fracture patterns developed during different strains. The basis of the experiment is stretching a circular rubber sheet (diameter of 70 cm) overlain by a flour layer with various thicknesses. The stretching itself takes place via springs attached to 16 holes placed at equal distances around the rubber sheet. These springs stretch the sheet in a homogeneous manner. A camera mounted over the table captured the fracture evolution, which then provided the basis for analysis.

The reason for choosing these types of fractures (i.e. mudcracks, hydrobreccia and flour experiments) was twofold: (1) their final patterns represented well-connected networks and (2) it was possible to examine the pattern evolution over time.

3.3.2 Image pre-processing

Prior to network analysis, image pre-processing was necessary. In case of the Elle simulation images this was simple. The images were imported into Mathematica (version 10.0.1.0), where they were binarized, color converted, thinned and then converted into graphs. The graph conversion only works on binarized and thinned images. The function itself is based on finding the junctions and end-points of the skeleton (vertices) and creating links between connected ones (edges). This eliminates the shape and the angle of the initial line (in this case fracture), and only concerns about the relationship between the vertices.

In case of the flour experiments, pre-processing was more time-consuming. First, the contrast and sharpness were enhanced to extreme levels so that the software could clearly distinguish the fractures from the background. Binarizing and thinning this image resulted in a skeleton. That skeleton, however, did not represent the true fracture pattern as it can be seen on Fig. 3.7. The two main issues were that some connected fractures were not joined and at several places non-essential pixels were created. The former could be eliminated by applying dilation function that enlarges the skeleton by a defined value. The problem with that was that truly disconnected elements also got joined. I therefore imported the skeleton into Gimp (image manipulation program), where I went through the entire network and joined the necessary segments together. In the meantime the nonessential pixels were also removed. While this was extremely time-consuming, it was the only way to obtain real graph equivalents with no extra vertices or disconnected segments. The finished image was then converted to graph using the MorphologicalGraph[image] function. This, unless the user specifies it otherwise, automatically weights the edges based on their lengths (number of pixels)[5]. Once the graph is created, it can be used for various calculations.

---

[5] Weighted edges only affect the global efficiency values as those are based on the distances between vertices.

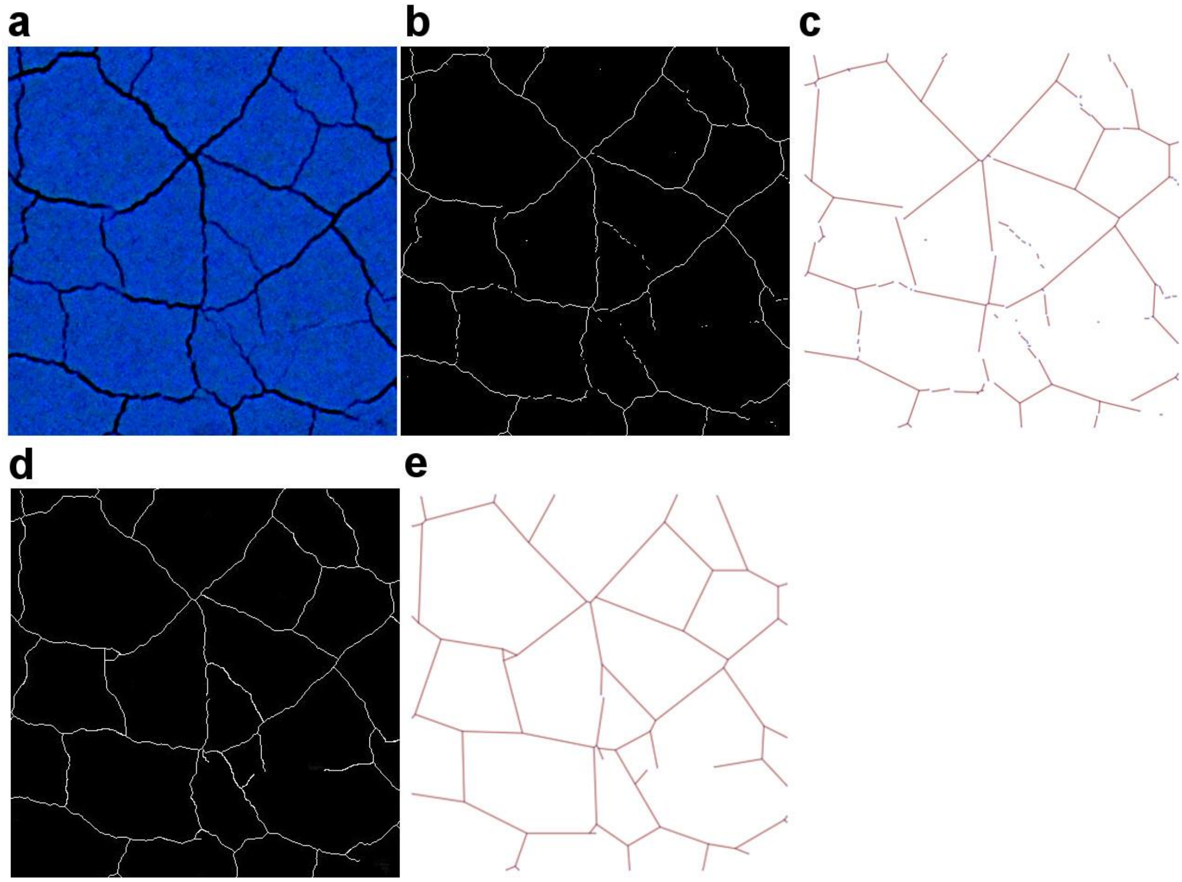

Fig. 3.7 Conversion of an image to graph and the occurring issues.
(a) Pattern cut out from a flour experiment. Contrast was enhanced so that fractures would stand out more. (b) Thinned and graph (c) equivalents of image (a). Not all fracture segments were picked up by the thinning process causing single fractures breaking up into several smaller segments. By manipulating the image, segments are reconnected according to their true connections (d), which results in a graph (e) with true representation of the image (a).

3.3.3 Calculations on graphs

A wide range of measures can characterize graphs. This thesis, however, limited the measures to those that provide essential measures for network connectivity and topology. For a graph g the VertexCount[g] and EdgeCount[g] function gives the number of vertices and edges that make up the graph, whereas GraphDensity[g] shows how far the graph is from being complete (that is all pairs of vertices are connected). Once these basic measures were obtained, VertexDegree[g] function was applied to list the degrees of all vertices. The entropy of the degree distribution was then calculated using Entropy[VertexDegree[g]] to characterize the homogeneity of the degrees in the network. In addition to this, the probability that a randomly chosen vertex has a degree *k* was calculated and illustrated using the probability density function as DiscretePlot[PDF[Di, x], (x, 1, 5)], where Di =

EmpiricalDistribution[VertexDegree[g]] and x corresponds to the degrees between one and five. To characterize the clustering in the network, MeanClusteringCoefficient[g] and GlobalClusteringCoefficient[g] functions were applied, whereas the assortativity was obtained through GraphAssortativity[g] to illustrate the tendency of similar-degree vertex connectivity. For disconnected graphs calculating the global efficiency involved several steps. First, the dist = GraphDistanceMatrix[g] listed the shortest distances between all pairs of vertices in matrix form. As the edges of the graph were weighted automatically based on their lengths, the distances were also weighted. This essentially resulted in real relative distances between vertex pairs. As a vertex has zero distance to itself, the diagonal elements of the distance matrix are zero. These needed to be eliminated as the next step was to get the reciprocal distance, and the reciprocal of zero is undefined. Due to this, the positive distances were picked out using pos = Pick[[dist], Positive[dist]], and then the reciprocal of these were taken by div = 1/[pos]. By adding the values together Total[Total[div]] and multiplying this by 1/N(N-1), where N = VertexCount[g], the global efficiency is obtained.

4 Deformation history of the Internal Ligurian Unit

The purpose of this chapter is to understand, compare and possibly validate the numerical results of chapter 5. In addition, the aim was to observe whether small-scale structures (e.g. veins) reflect larger, kilometer-scale tectonic history. This chapter therefore presents and discusses the findings emerged from the field work in Italy. First, the field observations and measurements of structural features are outlined. I then move on to the description of veins and the pre-folding vein orientations. I end the chapter with presenting the results of the fluid inclusion measurements.

4.1 Field observations and measurements

Overall the bedding in the field area displays a wide range of orientations (Fig. 4.1, Fig. 4.2, Fig. 4.3a-d). In Riva Trigoso while the dip of the beds varies from shallow to steep, their dip direction is relatively constant; it is characterized by two distinct orientations: a few dipping towards the ESE-SE, whereas the majority dips in westerly directions (NW-W-SW) (Fig. 4.3a). Bedding data from Framura fall under the same westerly distribution. In Moneglia, however, bedding measurements are even more dispersing than elsewhere. Here the poles to the bedding occupy three quarters of the stereonet, which indicates that another dip direction, N and NE also appears (Fig. 4.3b). Many layers dip towards the westerly directions similarly to Riva and Framura, but the additional inclinations towards the N and NE result in complex structures in the field (Fig. 4.2).

Cleavages were often difficult to distinguish from the bedding due to the low angles between them. The shallow to steep cleavages were generally dipping towards westerly directions (NW-W-SW), similarly to the bedding (Fig. 4.3h). Observing the bedding-cleavage relationship, where it was possible, helped to identify whether the sequence was normal or overturned. The area was generally characterized by tight, alternating normal and overturned sequences (Fig. 4.2).

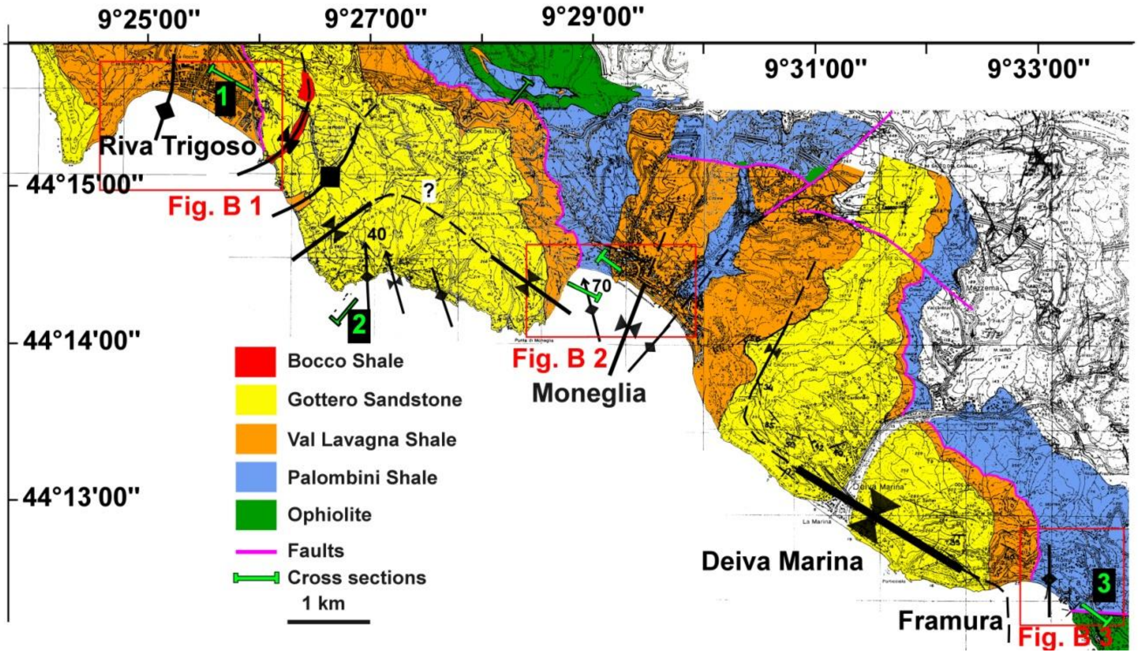

Fig. 4.1 Geological map and the main structures of the studied area.
Map also indicates the location of three cross sections, along with the areas of detailed maps (red rectangles) that can be found in the Appendices (Appendix B). Map compiled based on Anna Varga-Vass, Daniel Koehn and Giancarlo Molli's field work in 2013 and 2014. Non-published map.

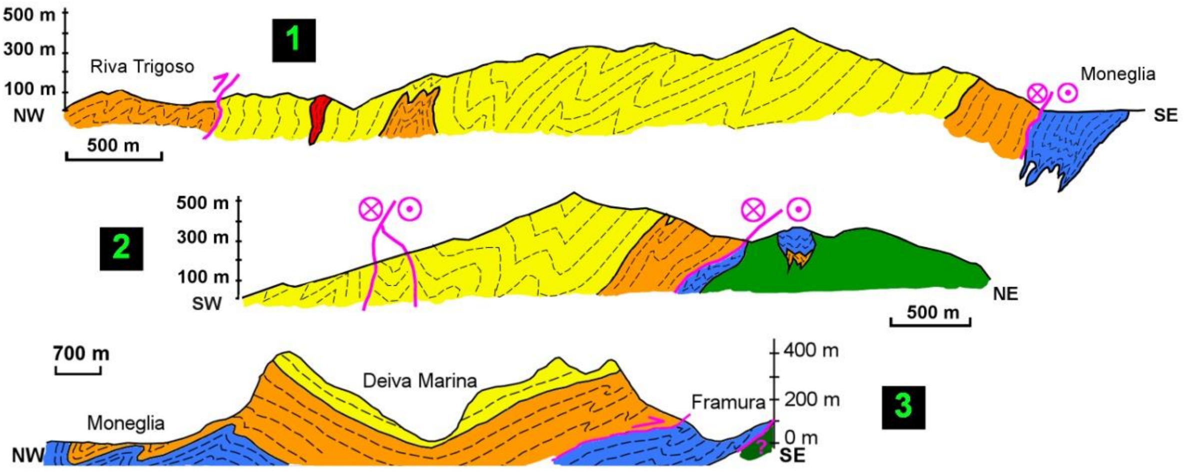

Fig. 4.2 Provisional cross sections of the Internal Ligurian Units in the studied area.
Sections 1 and 2 based on Giancarlo Molli's, whereas Section 3 is based on Daniel Koehn's sketches (non-published sections).

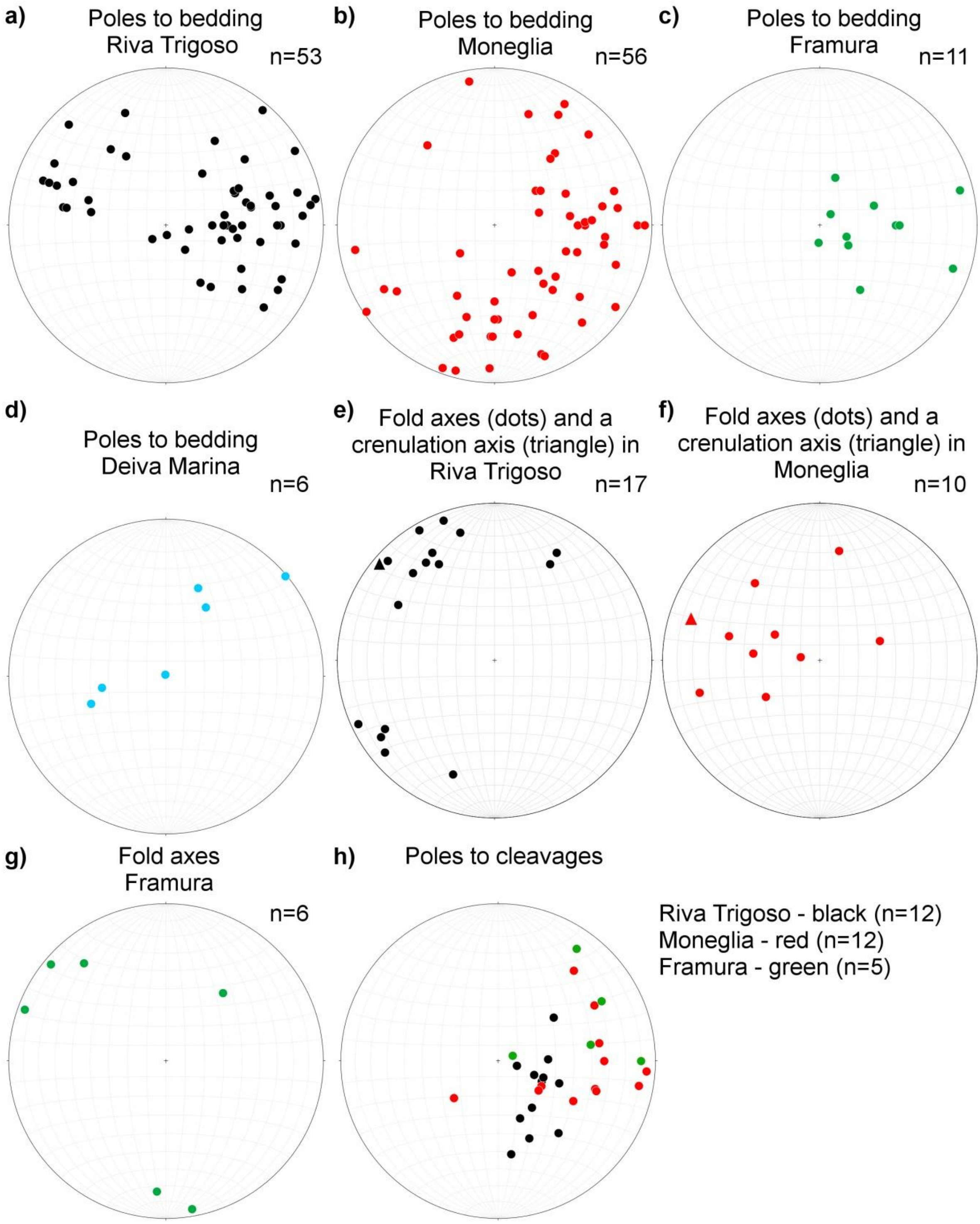

Fig. 4.3 The poles to beddings, fold axes and cleavage planes are presented for each part of the field area.
Two axes of the second crenulation cleavage are also shown on (e) and (f) (labeled as triangles).

Folds were more visible when the sequence included stiffer (e.g. more sandy) layers. The shales instead of folding often seemed to accommodate the deformation by filling the space in between the limbs of the folded stiffer layers. In addition to this, shales further away from the stiffer layers showed either very gentle folds or barely any. This is in accordance with the expectations for folding a multilayered system with different competencies (van der Pluijm and Marshak, 2004). The most commonly observed folds were isoclinal folds that had relatively shallow axial planes (Fig. 4.4a). In addition to this, assymetrical folds with highly non-cylindrical nature (Fig. 4.4b), and locally open folds (especially in Framura) with sub-vertical axial planes were also found.

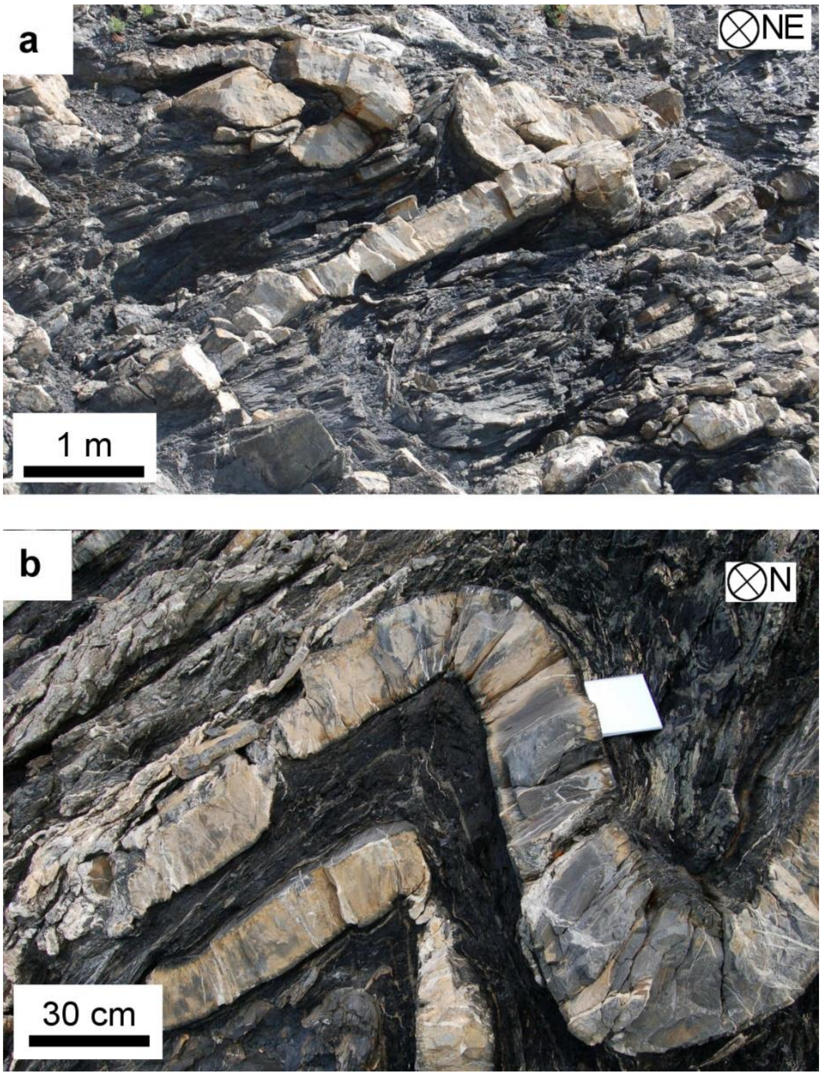

Fig. 4.4 Isoclinal (a) and asymmetrical (b) folds with shallow plunging fold axes in Framura. Locations can be found on Fig. B 3 in Appendix B : (a) at Fr2, (b) at Fr3.

Magnificent 3D folded structures of massive sandstone layers were observed along the coast in the northwestern part of the area, stretching between Riva Trigoso and Moneglia (Fig. 4.5). As these were only accessible by boat close examination was not possible, but the outcrops still gave an insight into the large-scale deformation structures. These outcrops were not representatives of fold superposition, rather a change in strike directions of the main structures (Fig. 4.5a). As seen on Fig. 4.1, the main structures exhibit highly non-cylindrical nature (i.e. orientation change) with frequent alternations of synclines-anticlines.

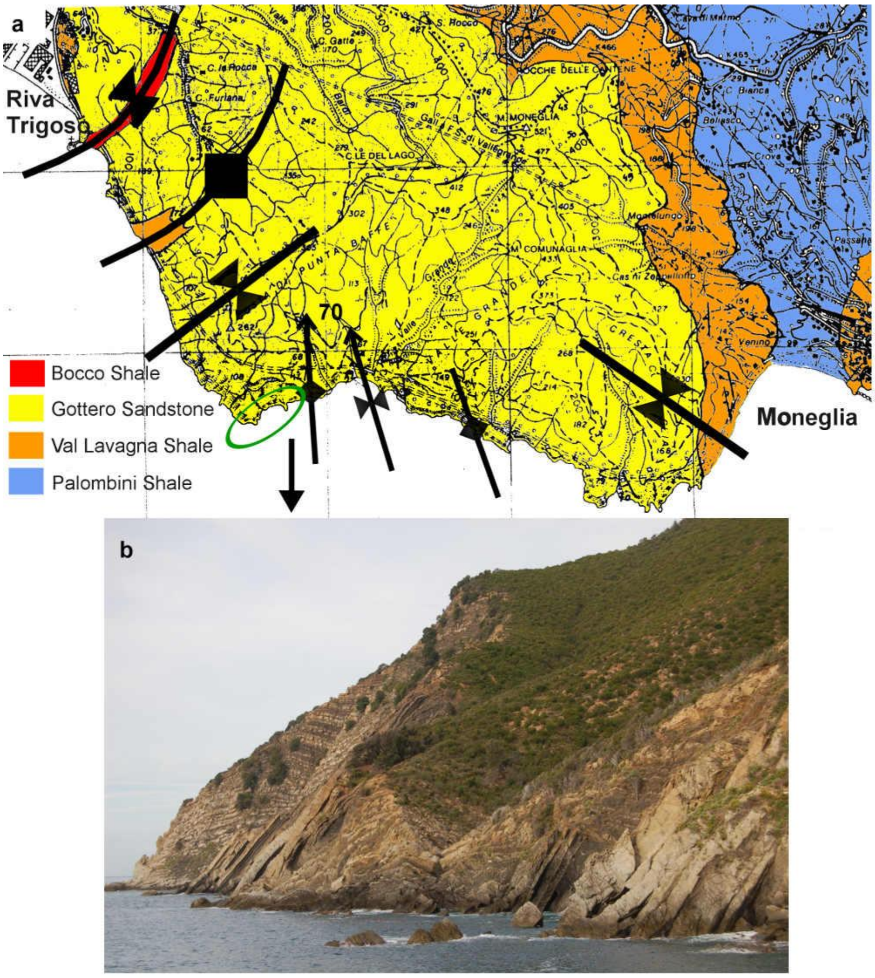

Fig. 4.5. Geological map between Riva Trigoso and Moneglia showing the change in strike of the main structural features (a), and the outcrop equivalent (b) (location indicated above by the green ellipse).

Fold axes were not easy to find or measure on the field. This was due to the highly cleaved shales, thick sandstone layers or just simply the orientation of the outcrops. The measured fold axes in Riva Trigoso and Framura again display similarities. Two general fold axes directions were identified: one plunging shallow towards the NW, whereas the other is perpendicular to this direction, plunging shallow towards the SW (and a couple towards the NE) (Fig. 4.3e and g). Fold axes in Moneglia are not only steeper than measured elsewhere, but also plunge more towards the W (Fig. 4.3f). Although it was rarely possible to establish an age relationship between the two folding directions, a few outcrops showed that the NE-SW-plunging fold axes were folded by the NW-plunging ones.

Even though clearly more than one folding event took place during the structural evolution of the area, crenulation cleavage was difficult to find. In Riva only one was measured where the crenulation axis was plunging shallow towards NW, whereas in Moneglia it was plunging towards the WNW (Fig. 4.3e and g). A few more (five) sets of crenulation were observed in Moneglia (Fig. 4.6). The first cleavage (S1) was striking NE-ENE – SW-WSW with mainly medium dips. The second cleavage (S2) was generally steep and had an orientation of N-NNW – S-SSE. Only one S2 had similar orientation and dip to the S1.

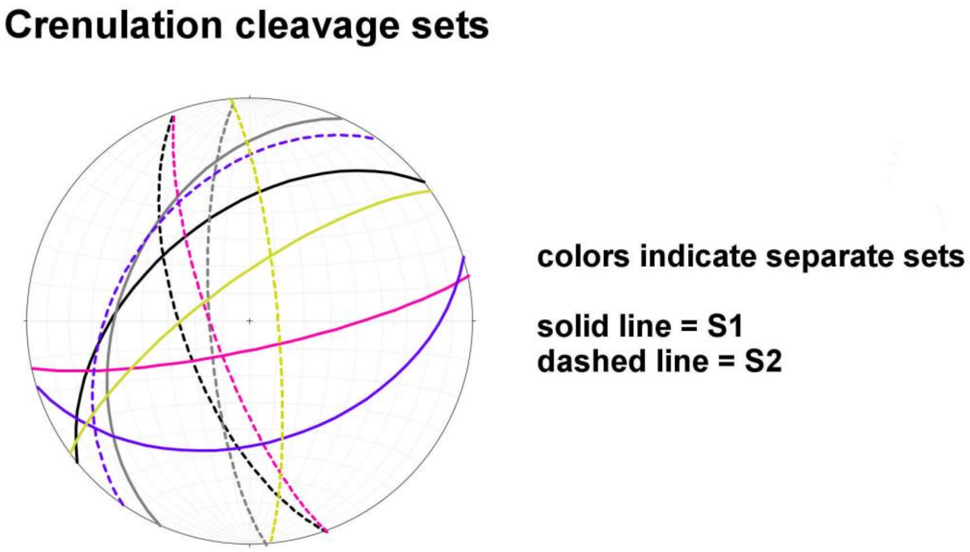

Fig. 4.6 Crenulation cleavage sets measured in Moneglia.
Measurement locations can be found in Appendix B on Fig. B 2 and in Table B 2.

Several faults, mainly in Riva Trigoso, were found both within the shale sequences and in the sandstone (Fig. 4.7). The striations on two steep faults, striking SE and W, showed almost pure sinistral (left-lateral) movements (Fig. 4.7a and b). The SE-striking fault also showed oblique-slip (Fig. 4.7a). Two faults were exhibiting pure dip-slip striations, along with other striations indicating dextral (right-lateral) and oblique strike-slip movements (Fig. 4.7d and e). A young normal fault was also found which did not exhibit any strike-slip movements (Fig. 4.7c). Many faults within the sandstone and between the sandstone and shale were observed (Fig. 4.7f). While it was possible to identify an oblique dextral strike-slip movement on one of them (the NE-striking one), the others were too chaotic for any measurements. The steep fault planes were likely strike-slip, whereas the medium-dipping ones normal faults striking SW and WSW.

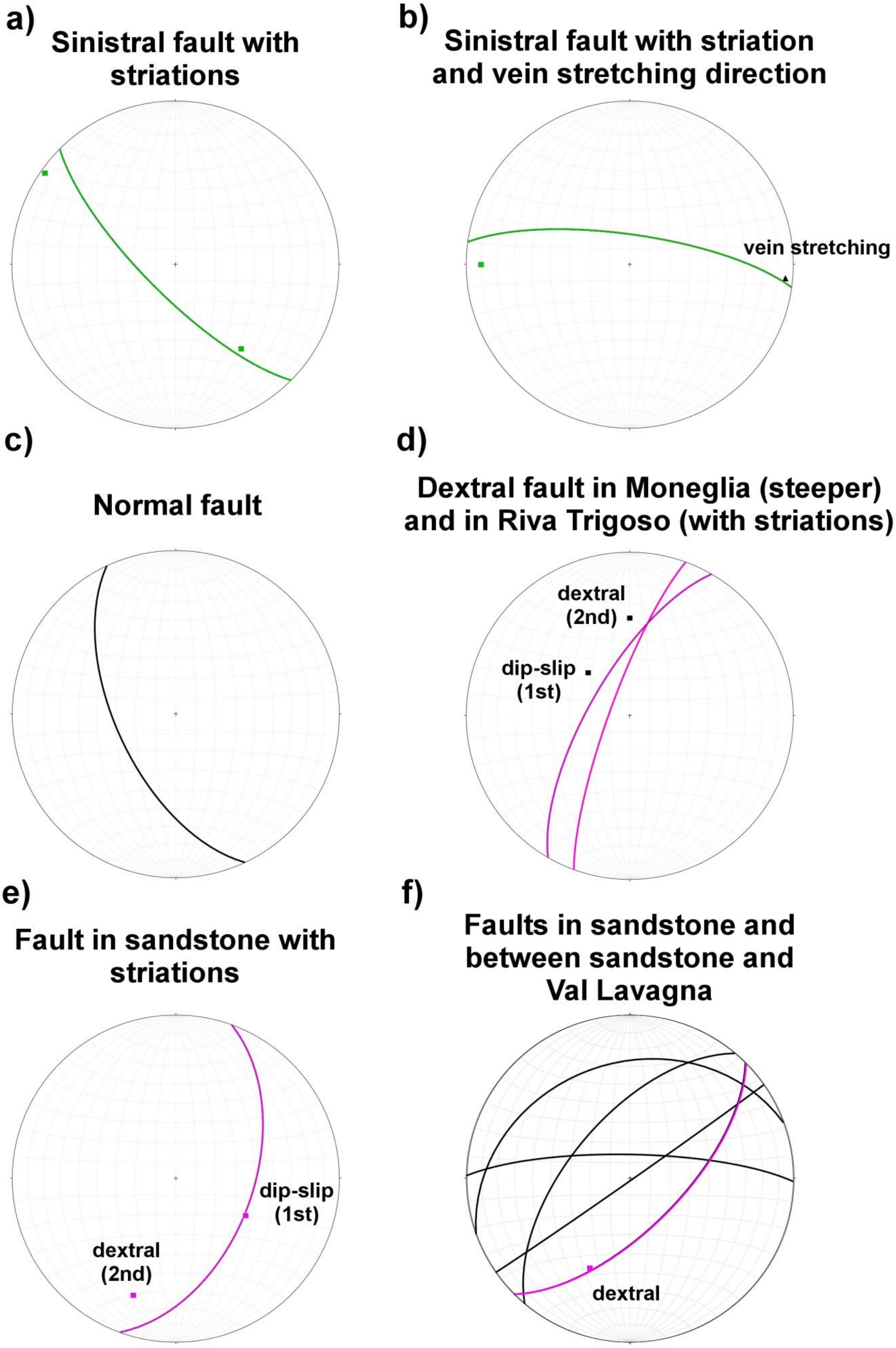

a) Sinistral fault with striations

b) Sinistral fault with striation and vein stretching direction

c) Normal fault

d) Dextral fault in Moneglia (steeper) and in Riva Trigoso (with striations)

e) Fault in sandstone with striations

f) Faults in sandstone and between sandstone and Val Lavagna

Fig. 4.7 Orientations of faults and striations measured in the field area. Measurement locations can be found in Appendix B in Table B 1 to Table B 3.

The orientation of the strike-slip faults, the striations, along with the sense of movements observed in the field make it possible to infer stress directions that might have been responsible for their formations. The strike-slip fault plane generally develops 45° to the maximum horizontal stress direction (σ_1). Examining the fault orientations reveals that all of the faults indicate NE-SW to E-W σ_1 and thus imply horizontal compression in this direction.

Stylolites are also great indications of tectonic stresses (Park and Schot, 1968). They develop as a result of compressive stresses forming a dissolution surface along which insoluble materials accumulate. Their planes are perpendicular, whereas their teeth are parallel to the largest compressive stress. A stylolite forming at high angles to the bedding is termed tectonic stylolite. In Framura within the Palombini Shale eight tectonic stylolites were identified. Two main sets, perpendicular to each other, showed a N-NNE, whereas the other an ENE compression direction (Fig. 4.8).

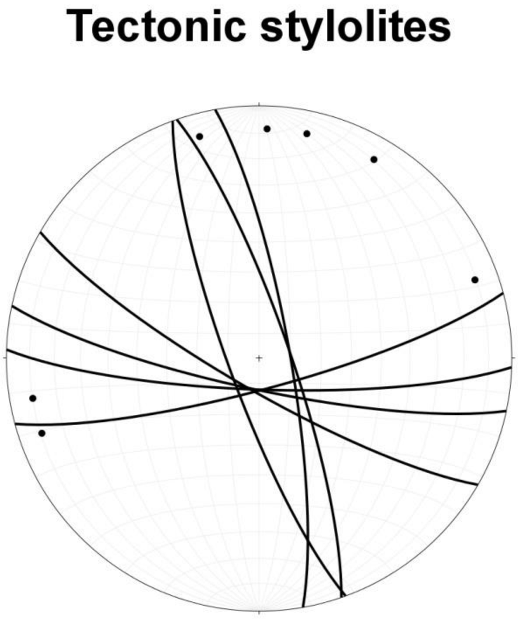

Fig. 4.8 Stereonet illustrating the orientations (planes and poles) of tectonic stylolites found in Framura.
Measurement location can be found in Table B3 in Appendix B.

In many locations the shales hosted sedimentary stylolites that form during sedimentation parallel to the bedding due to the increasing lithostatic stress. In addition to this, vein-parallel stylolites (or dissolution seams) within the veins were also quite common.

4.2 Veins in the field and their microstructures

Veining showed major spatial variations throughout the area. Framura was generally vein-rich. The Palombini outcrops on the beach displayed intense veining. Outcrops in Deiva Marina lacked of veins. Moneglia, however, exhibited intense and complex veining both in the Val Lavagna and the Palombini Shale. In the southeastern part of the Riva Trigoso bay, where the Gottero Sandstone and the Bocco Shale cropped out, veins were extremely rare. Veins re-appeared in the northwestern part of the bay in the Val Lavagna sequence. The general observations were that (1) the beach outcrops were vein-rich; (2) veining was increasingly less abundant at the outcrops on higher topologies; (3) the Gottero Sandstone lacked entirely of veins, even on the beach; and (4) the most intense veining was observed around the Val Lavagna-Palombini boundaries.

The area was characterized by a variety of veins which can be grouped into seven categories:

A. bedding-parallel “dirty” veins,

B. bedding-parallel non-dirty veins,

C. blobs of mineralization,

D. bedding-parallel and perpendicular set,

E. conjugates in the layers,

F. folding-related veins,

G. young crosscutting and fault veins.

4.2.1 Dirty veins

Group A consisted of bedding-parallel veins with widths ranging from 2 to 10 cm (Fig. 4.9). They typically had a long lateral continuity along the bedding interfaces. Within the veins, parallel to the vein-wallrock boundaries, dark and undulating seams of host rock inclusions and/or stylolites were present. These gave the veins a dirty appearance. Group A therefore correspond to the “dirty veins” described previously in the literature (see Chapter 2.1.3).

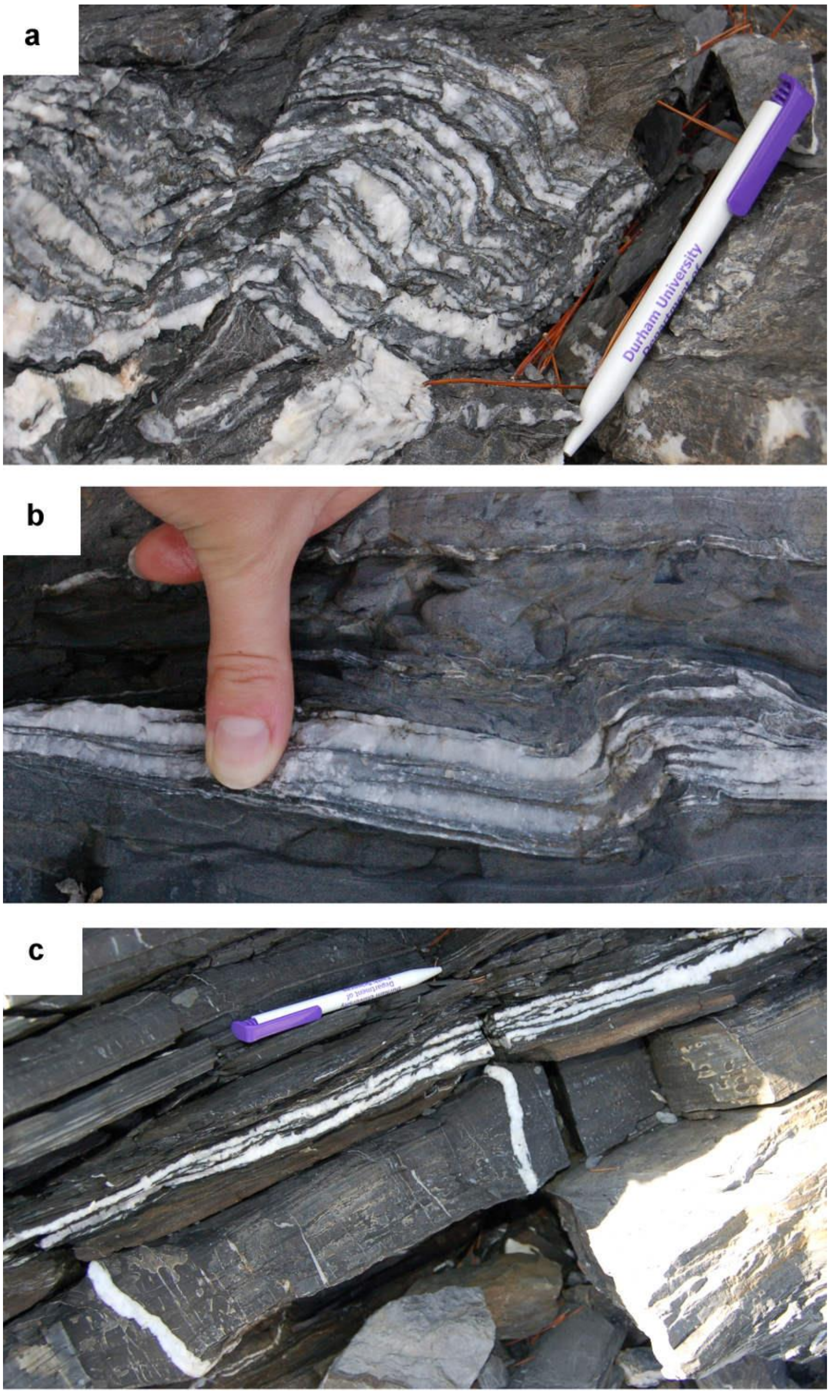

Fig. 4.9 Field pictures illustrating the bedding-parallel "dirty veins" in the Val Lavagna Shale. Image locations can be found in Appendix B in Tables B 1 and B 2.

Examination of the veins under microscope revealed that both calcite and quartz are present as vein-filling minerals (Fig. 4.10). The size of the calcite crystals in the veins varies between a few hundred microns to a few millimeters. They generally have anhedral crystal shapes with a few subhedral grains too. The crystals are heavily twinned and the three cleavage directions are usually very distinct (Fig. 4.10). These, along with the apparent impurities, often make the crystals cloudy. The calcites host a great amount of fluid inclusions (and trails) which are frequently not very clear due to the heavily deformed and cloudy crystal characteristics.

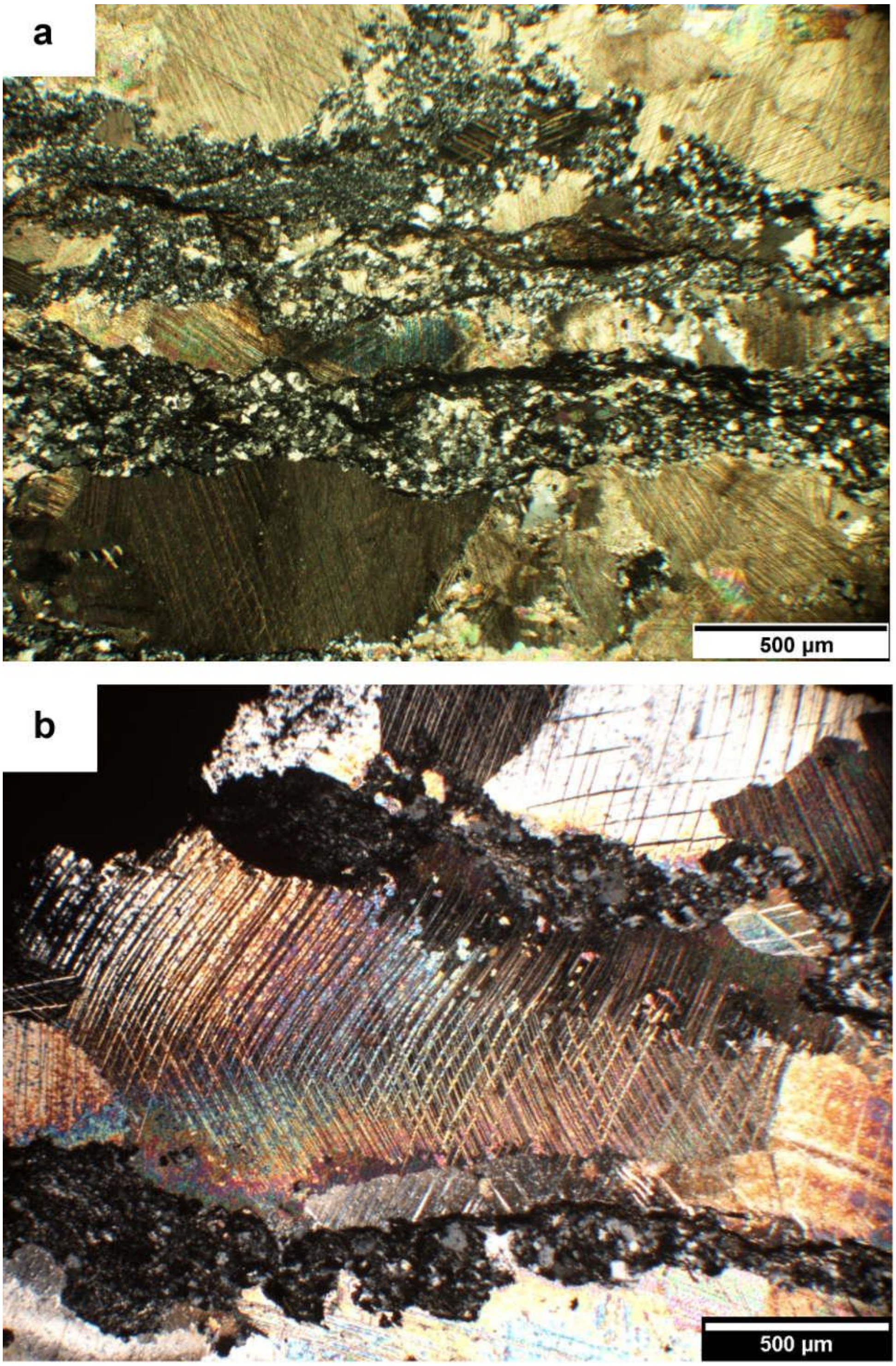

Fig. 4.10 Thin sections under cross polarized light showing the typical microstructure of the dirty veins (a) and the heavily deformed calcite crystals (b).

Occasionally, cracks within and/or in between the larger twinned calcite crystals are filled with non-twinned calcites showing stretching textures (Fig. 4.11a). These late non-twinned crystals contained subgrains. It is also quite common to see less deformed calcite crystals (i.e. less impurities, not well developed twins) adjacent to heavily deformed ones (Fig. 4.11b). The less deformed crystals are usually oriented so that their twin planes are sub-parallel to those in the heavily deformed calcites.

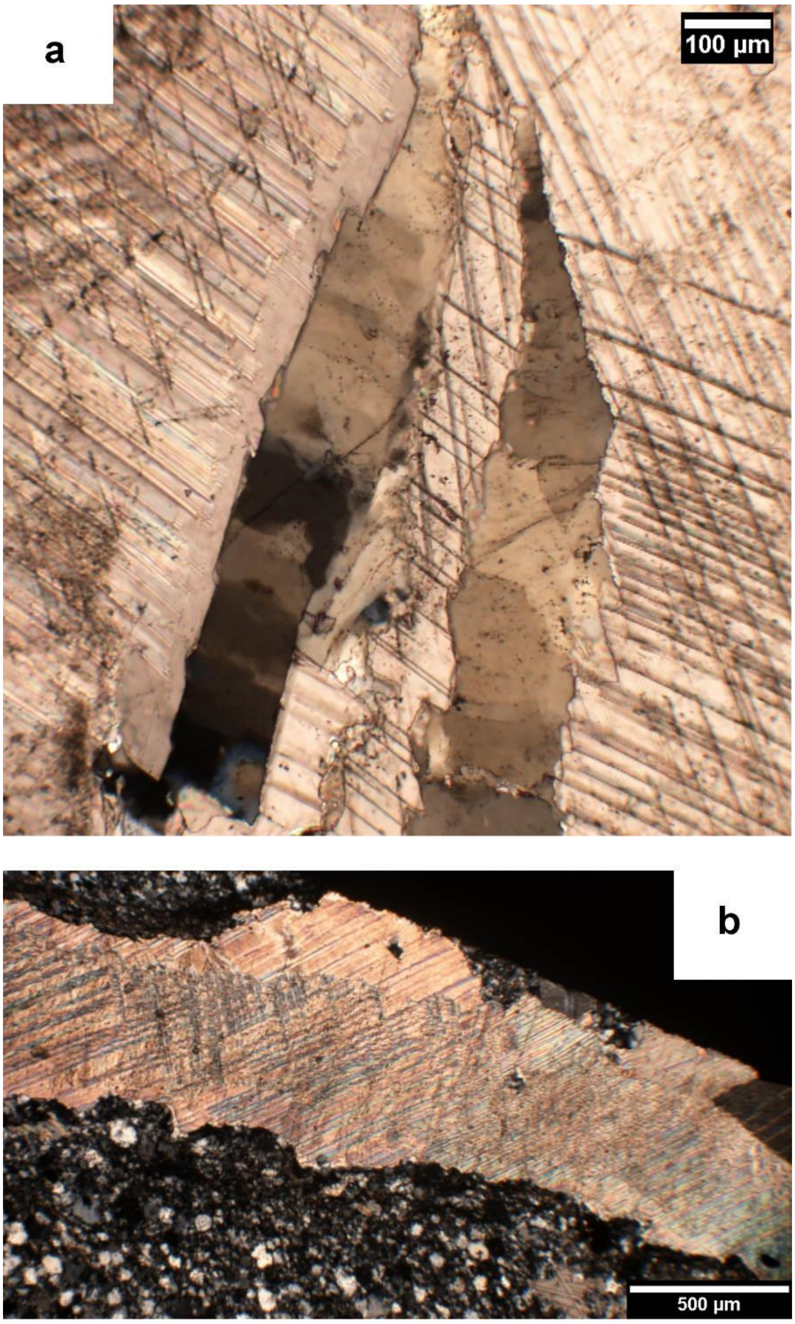

Fig. 4.11 Thin sections of the dirty veins under cross polarized light showing crack-filling, non-twinned calcite with subgrains (a) and juxtaposition of a heavily deformed and a less deformed calcite crystal (b).

Quartz, as the other vein-filling mineral, is subordinate relative to the calcite. Less quartz is present and its grain size is also much smaller (only up to a hundred microns). The quartz crystals have anhedral shapes and occur in between the calcite crystals (Fig. 4.12a). Occasionally small quartz grains surround calcite grains forming selvage (Fig. 4.12b). In these cases, the grains exhibit elongate shapes that are perpendicular to the calcite boundary, showing growth competition in a syntaxial manner. The veins are hosted in a siliciclastic matrix with quartz grains up to a hundred microns (Fig. 4.11b). Frequently, due to the structure of the veins, it is unclear whether the quartz crystals that are filling the calcite veins are matrix inclusions or in fact separate crystals growing in a fracture (vein).

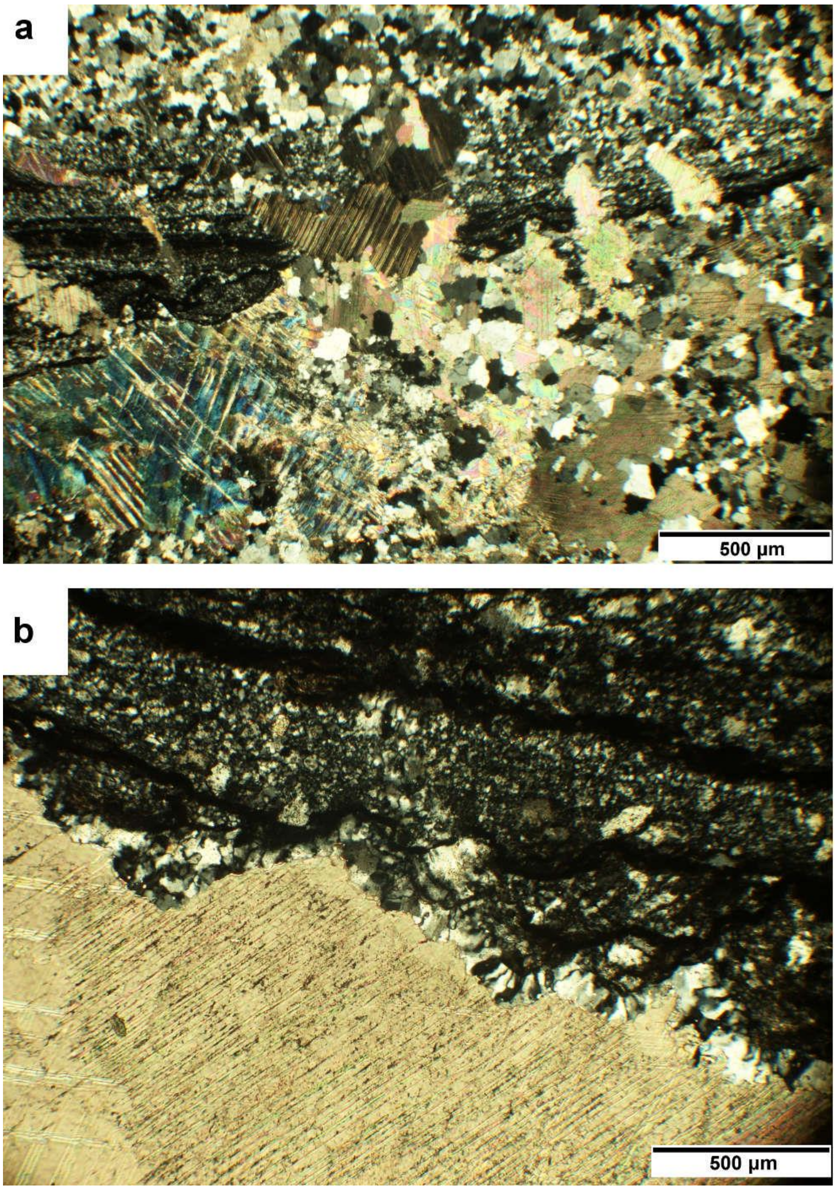

Fig. 4.12 Thin sections of the dirty veins under cross polarized light showing bed-perpendicular veins crossing the dissolution seam (a) and quartz selvage surrounding a calcite crystal (b).

Dissolution seams appear parallel to the veins, and can have widths of up to 400 microns (with a few seams reaching four millimeters). They often surround the vein crystals and dissolve them, which sometimes is the reason for the observed anhedral crystal shapes (Fig. 4.13). The majority of the dissolutions must have formed after the veining as the seams crosscut and dissolve the bedding-parallel veins. However, a few bedding-perpendicular veins can also be observed, and these crosscut the bed-parallel dissolution seams (Fig. 4.12a). The bed-perpendicular veins are bridging over the seams and their crystals are clearly associated with the parallel veins.

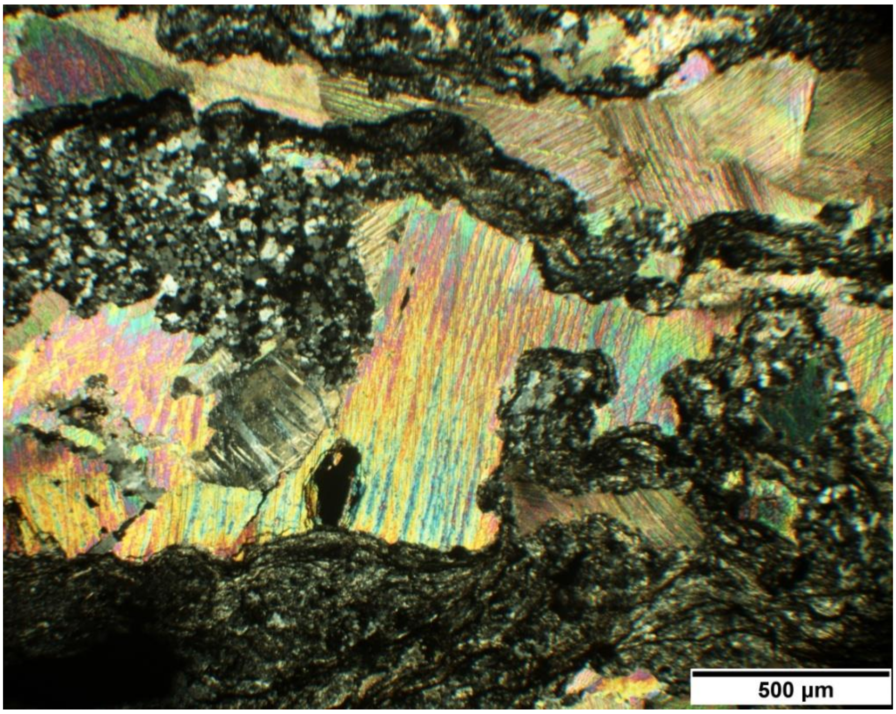

Fig. 4.13 Thin section of the dirty vein under cross polarized light showing calcite dissolution.

CL imaging of the samples was performed on both bedding-parallel and perpendicular veins. In both cases the calcites had bright luminescence with no zonation whatsoever (Fig. 4.14). The bed-perpendicular calcite vein, however, was clearly crosscutting (i.e. was younger than) the bed-parallel vein. The images showed that only the grains in the matrix were ranging from non-luminescence to bright.

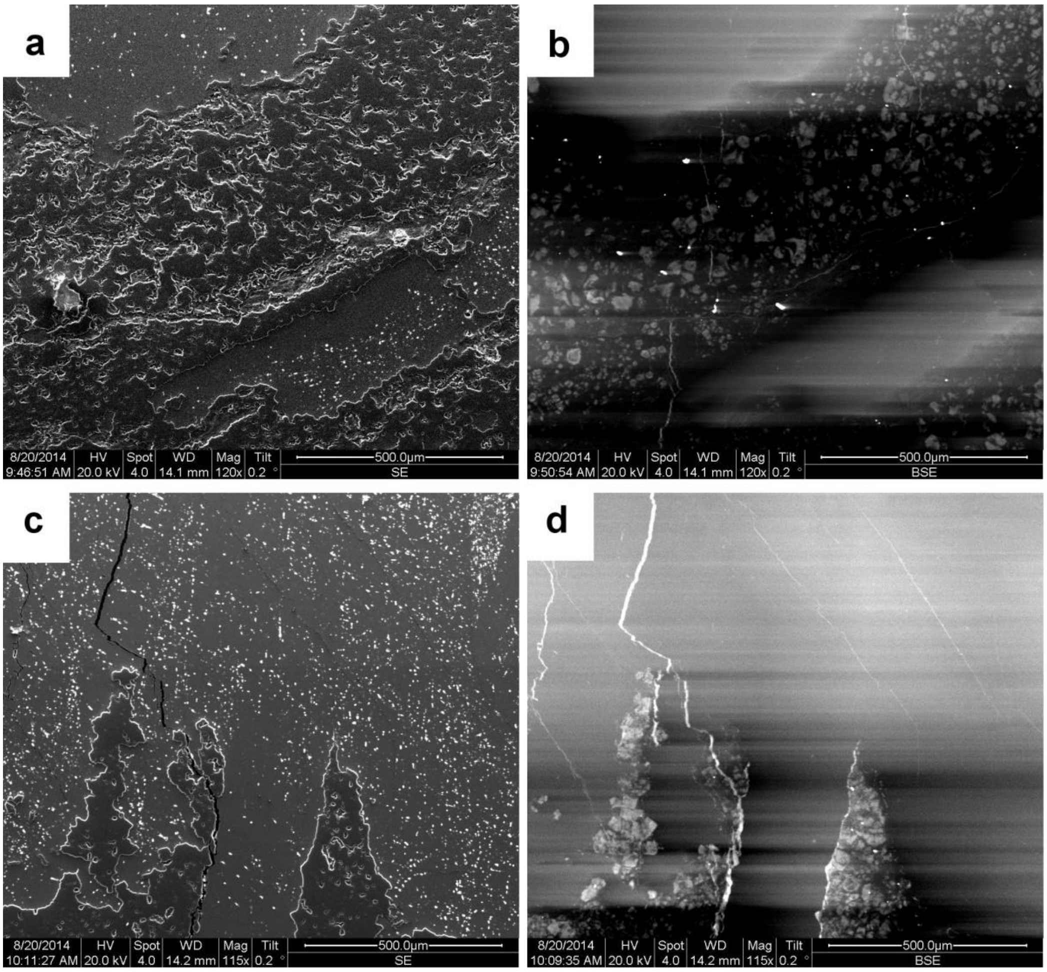

Fig. 4.14 SEM-CL images of the dirty veins.
The bedding-parallel (a and b) and bed-parallel vein crosscut by a perpendicular calcite vein in the center (c and d) do not show any zonation, just homogeneous bright luminescence.

4.2.2 Bed-parallel, non-dirty veins

Many bedding-parallel veins did not have a dirty appearance, i.e. they lacked vein-parallel host rock inclusions and stylolites (Group B) (Fig. 4.15). These also had long lateral continuities and widths of up to 3 cm.

Fig. 4.15 Field image of a bed-parallel, non dirty vein in a fold hinge in the Val Lavagna Shale. Image location can be found in Appendix B in Table B 2.

Their microstructures show completely different characteristics compared to the dirty veins, since (1) no dissolution seams are present, (2) the majority of crystals are blocky or elongated, (3) the crystals touch each other and (4) the calcite is subordinate to the quartz. The quartz grains can reach three millimeters in length and their longer boundaries are parallel to the veins (and thus bedding). Subgrains as well as recrystallized smaller quartz grains are frequent between the larger quartz crystals (Fig. 4.16a).

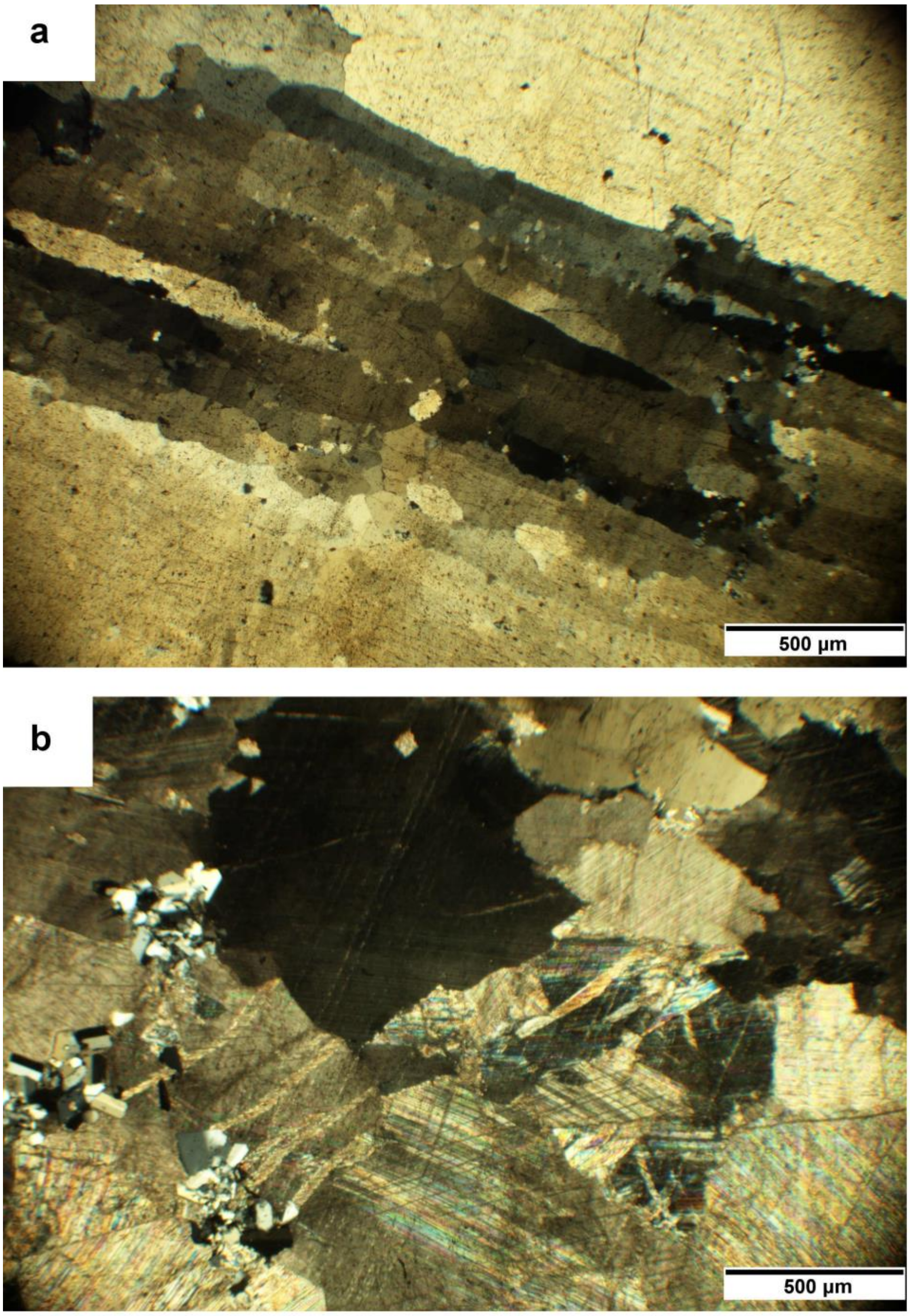

Fig. 4.16 Thin sections under cross polarized light showing the bed-parallel, non-dirty veins. (a) Long quartz grains with recrystallized quartz. The light band perpendicular to the grain boundaries indicates a younger crosscutting vein. (b) Deformed calcites and groups of twinned plagioclase (left of the image).

The calcites within these veins mainly have anhedral shapes (rarely subhedral) (Fig. 4.16b). The crystals are commonly deformed by twinning. There is no distinct boundary between the calcite and quartz grains, i.e. the calcite appear randomly in the vein. A few areas in the thin section, however, revealed a close relationship between the two. As seen on Fig. 4.17, the twinned calcite is consumed by the long quartz grain. The boundaries between the two crystals indicate bulging-type recrystallization, where the crystal with higher dislocation density (in this case the calcite) is consumed by the crystal with smaller dislocation density (quartz) (Passchier and Trouw, 2005). Bulging typically develops under low temperature deformation.

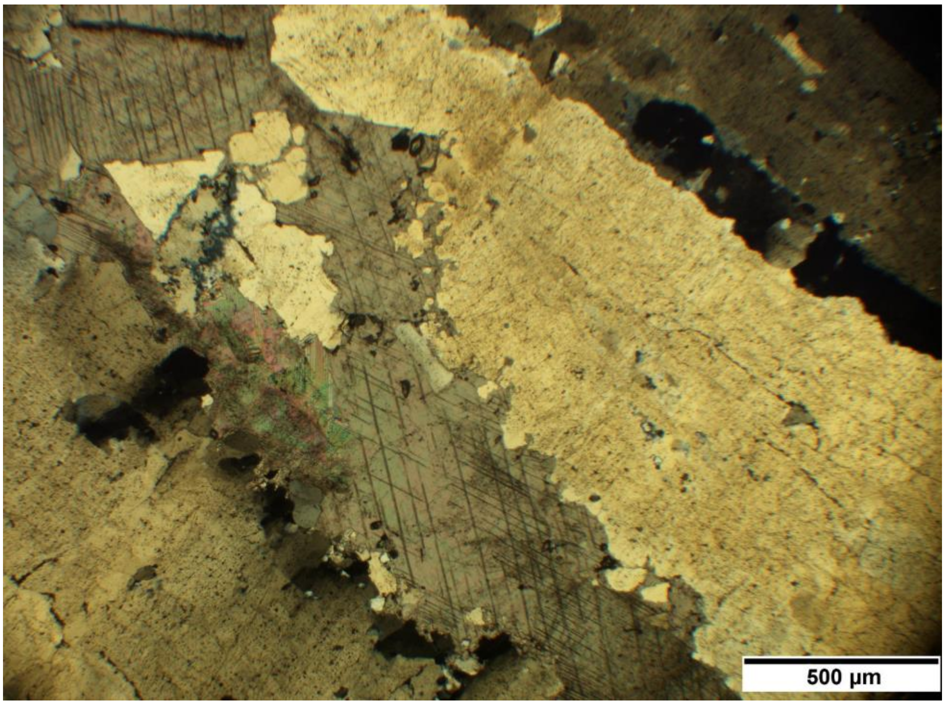

Fig. 4.17 Quartz bulging into the twinned calcite in the non-dirty vein (thin section under cross polarized light).

In addition to the quartz and calcite, other colorless minerals, such as plagioclase and micas, also appear between the grains occasionally (Fig. 4.16b). Perpendicular to the vein (and thus bedding), “ghosts” of younger crosscutting quartz veins (i.e. clear bands of different extinctions) were also observed (Fig. 4.16a).

4.2.3 Blobs of mineralization

Outcrop walls showing bedding-perpendicular section of layers often displayed heavy mineralization on certain layer surfaces (i.e. on the surface perpendicular to the bed) (Fig. 4.18). These blobs of mineralization (Group C) had irregular appearances and surfaces, and were not continuous along the layers. As a result they did not appear as classical veins with well-defined boundaries but rather as separate mineralized bodies that were only confined by the layers. Their short lateral continuity in the field and their nature did not make it possible to relate them to veins observed elsewhere.

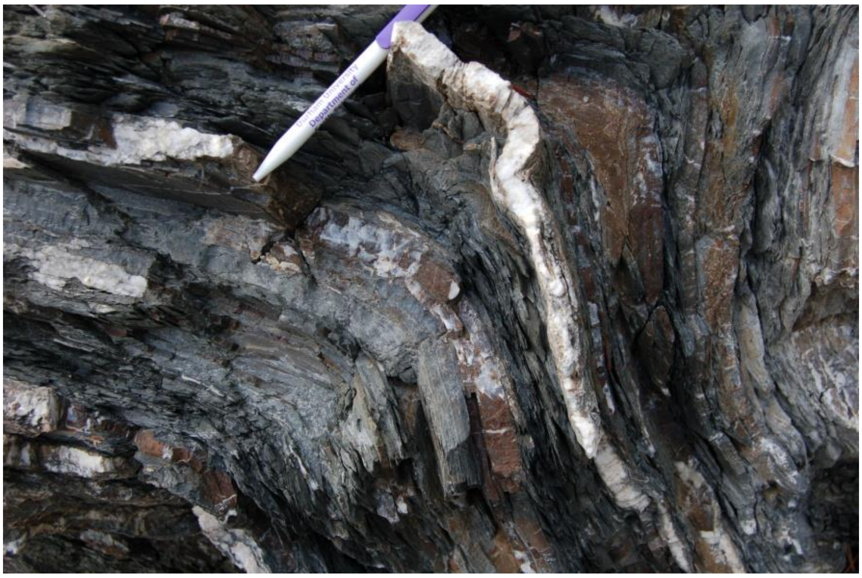

Fig. 4.18 Field example of the blob of mineralization.
Image location can be found in Appendix B in Table B 1.

Examination of these blobs under the microscope revealed a co-existence of quartz and twinned calcites. Dissolution seams were present but did not dominate the samples. The vein-forming crystals, the matrix and the appearing structures within the samples resembled those that were observed in the dirty and non-dirty veins (Fig. 4.19).

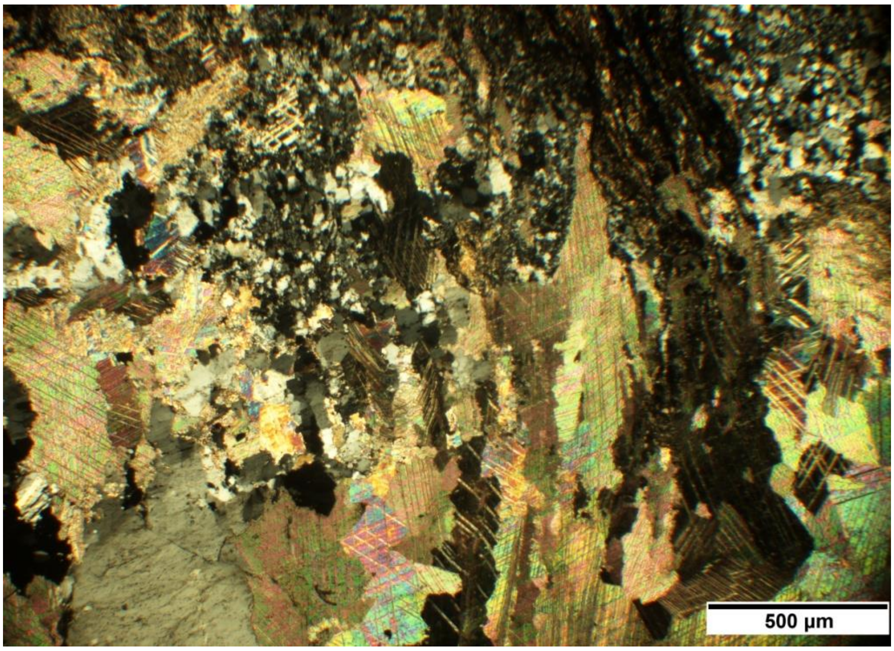

Fig. 4.19 Typical microstructures of the blobs of mineralization.

4.2.4 Bedding-parallel and perpendicular vein set

Certain shale layers were bounded on both sides by bedding-parallel veins which were connected by perpendicular sets of veins (Group D) (Fig. 4.20, Fig. 4.21). This type of veining could be best observed in Moneglia in the Val Lavagna Shale. Both the parallel and the perpendicular veins had maximum widths of up to a few millimeters. The spacing between the parallel veins varied between a few hundred microns and few millimeters. The thickness of the layers containing these sets of veins had an effect on the spacing variations. Thinner layers contained more closely spaced veins than the thicker ones (Fig. 4.20b). This relationship between the layer thickness and the spacing, however, did not seem to be linear as opposed to what has been reported in the literature (see Chapter 1.1.1).

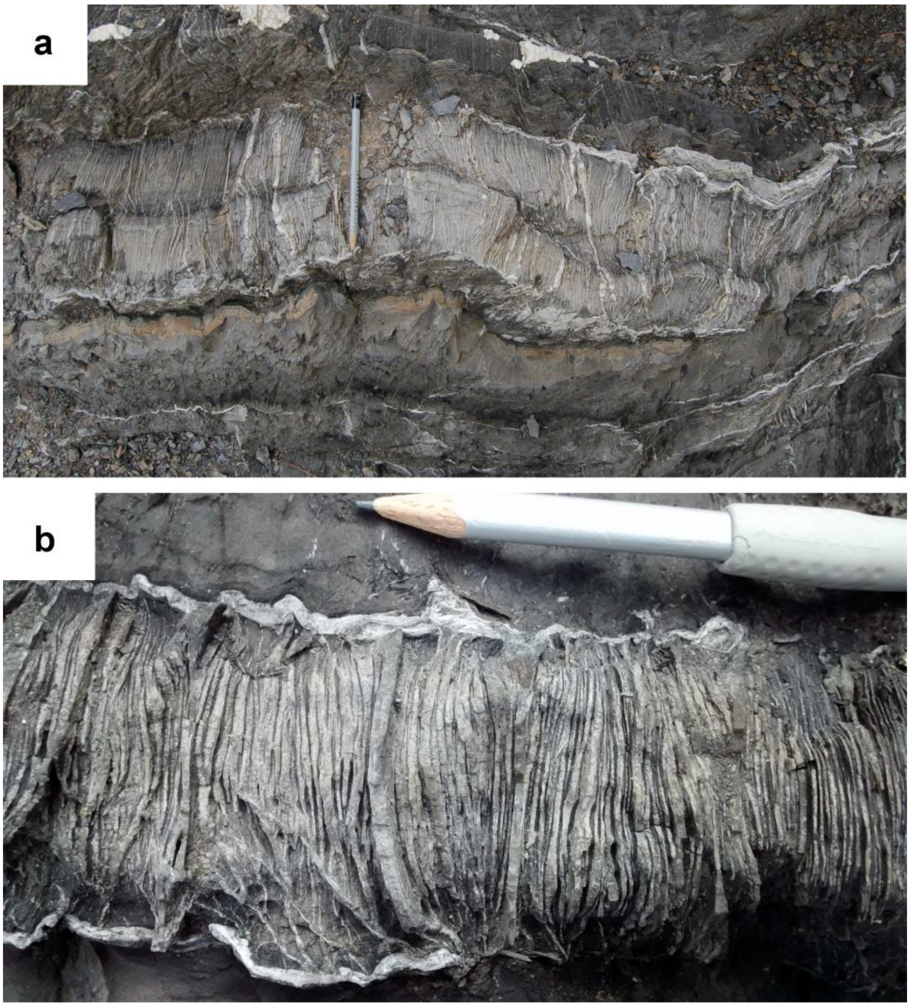

Fig. 4.20 Field examples of the bedding-parallel and perpendicular vein set in the Val Lavagna Shale, Moneglia.
Image locations can be found in Appendix B in Table B 2.

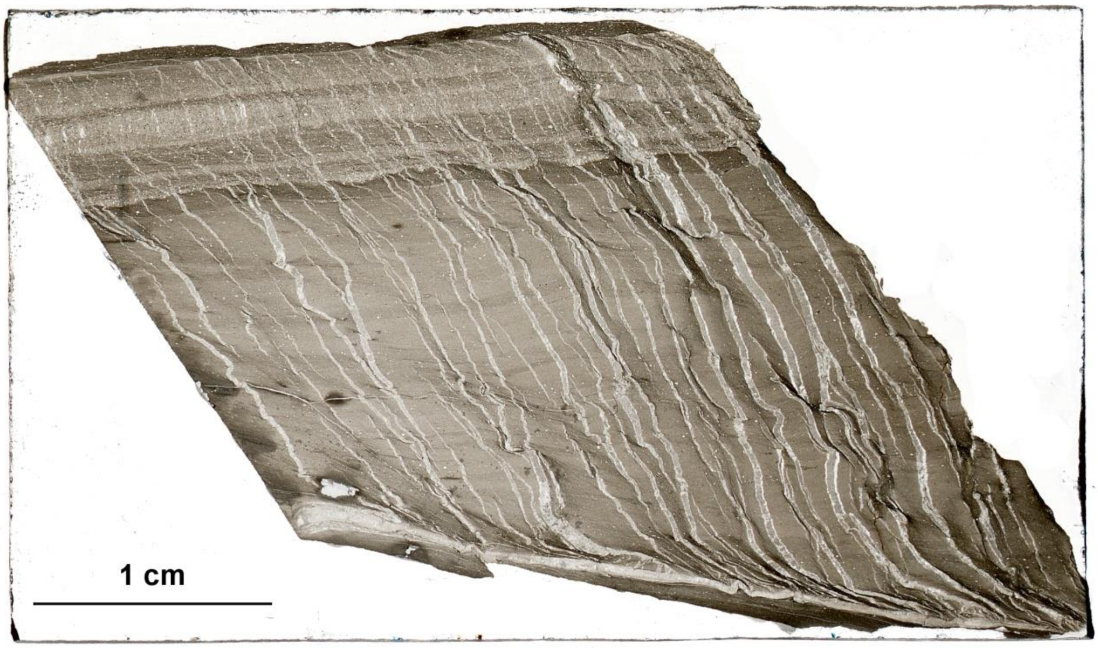

Fig. 4.21 Scanned image of a thin section illustrating the bedding-parallel and perpendicular vein set.

Examining these veins under microscope and SEM revealed that the veins consist of predominantly calcite with occasional quartz grains. The veins have elongated blocky microstructures with some calcite grains stretching from wall to wall. The bed-perpendicular veins clearly originate from the parallel set as there is no distinct boundary between the two and no crosscutting is present. Bed-parallel shearing locally affects the parallel vein sets resulting in small stepping of veins. Layering presented on Fig. 4.21 corresponds to grain size differences of the matrix. These, however, do not seem to control either the widths of the veins or the vein microstructures.

EBSD images of the bedding-parallel veins gave an insight into the crystallographic orientation of the vein-filling minerals. Large calcite crystals that are stretching from wall to wall show well-developed twinning (Fig. 4.22a). These larger grains are generally separated by groups of smaller calcite crystals that are not twinned (or the twinning is barely developed) (Fig. 4.22a and d). Crystal orientations of these two areas are generally similar with the crystals' longest axis (c-axis) forming high angles to the thin section plane (purple color on Fig. 4.22a and d). Small grain sizes and barely developed twinning characterize the vein on Fig. 4.22e. While orientation of the longest axis in this vein is mainly perpendicular to the thin section plane (red color), a few crystals show a slight tilt (lighter colors).

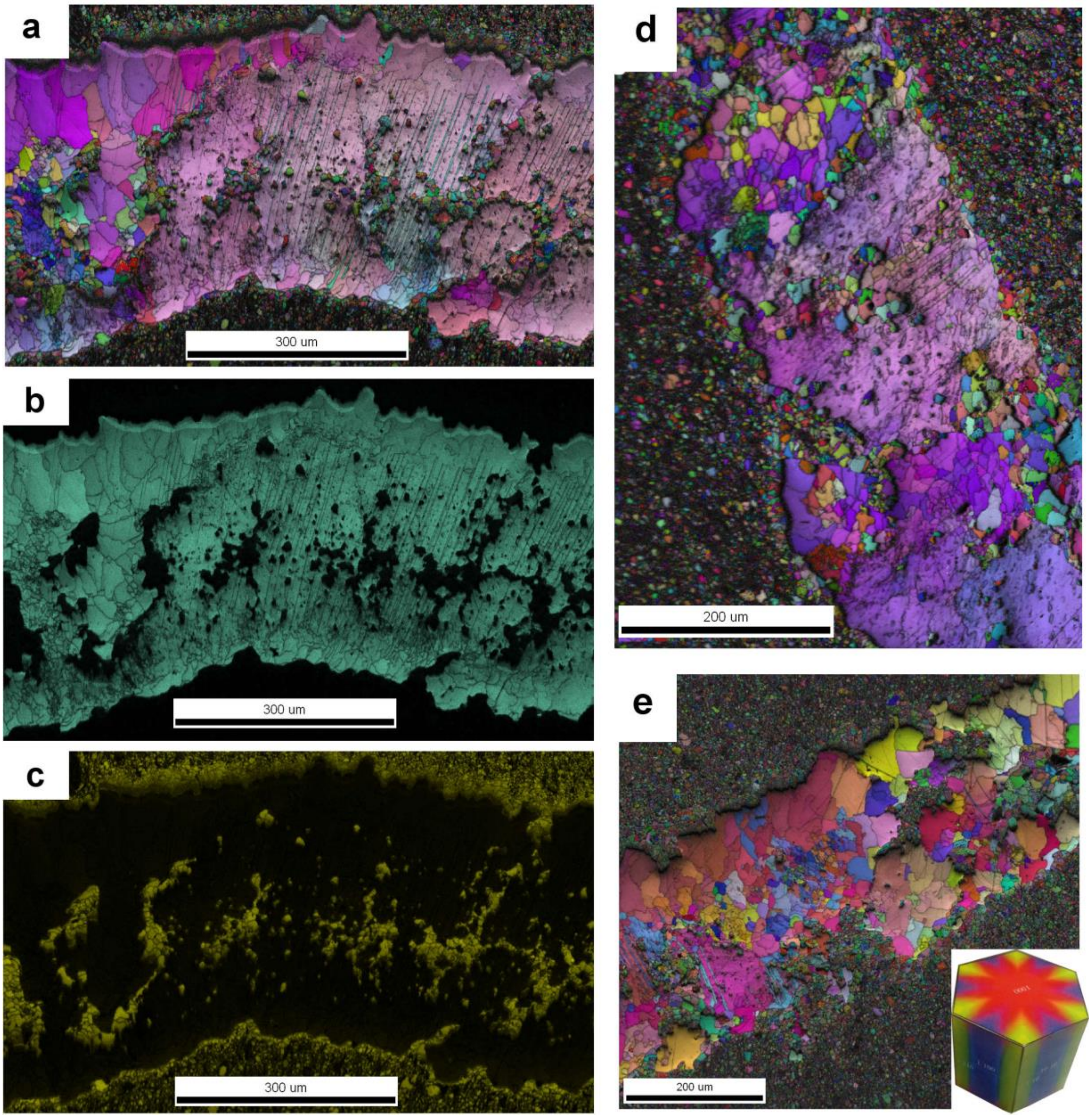

Fig. 4.22 EBSD images representing bed-perpendicular veins of the bed-parallel and perpendicular vein set.
Calcium (b) and silica (c) content of one vein (a) are also shown. Colors on a, b, d and e represent the crystals' c-axis orientations relative to the thin section plane (red = c-axis perpendicular to the plane, blue = c-axis parallel to the plane) as seen on the inset of image (e).

The calcium (Fig. 4.22b) and silica (Fig. 4.22c) contents of the vein on Fig. 4.22a indicate that the smaller, non-twinned crystals are also calcites, whereas the siliciclastic matrix frequently intrude the veins along grain boundaries. These intrusions are not only pure host rock fragments, but occasionally are pure quartz grains exhibiting larger sizes than those in the host rock.

CL-imaging of these samples revealed that while the veins did not show luminescence (neither the calcite, nor the quartz grains), the vein-wall rock interface did (Fig. 4.23). These zones under optical microscope and SEM appeared as host rock interfaces with no change in grain size or other features. Widths of the zones vary on both sides of the veins (as seen on Fig. 4.24), where one side it is usually wider than on the other. The zones are either in direct contact with the calcite grains (Fig. 4.23a) or with quartz grains that occasionally border the calcites (Fig. 4.23b). Quartz grains in these cases do not show luminescence. In order to examine the reason for the luminescence, element maps have been produced. Five major elements were found in the mapped area: Si, Ca, Al, Fe and Mg. Ca showed the most homogenous distribution as it was confined to the vein, and the host rock was completely lacking of it (Fig. 4.24b). While Al, Fe and Mg, exist in the host rock in a homogeneous manner, they are concentrated and absent at the same time in certain areas. There is an apparent concentration of these elements along one side of the vein (Fig. 4.24c, d, e). This coincides with the luminescent zone. There is also a much narrower but still clear concentration line that runs on the other side of the vein (not through the calcite but the quartz area). The depletion of these elements is also apparent on both sides of the vein in approximately 50 nm wide zones. The Si content simultaneously is increased in these depleted Al, Fe and Mg zones (Fig. 4.24a). Overlaying the discussed maps also nicely illustrates that there is a heterogeneous distribution of these five elements that around the vein (Fig. 4.24f).

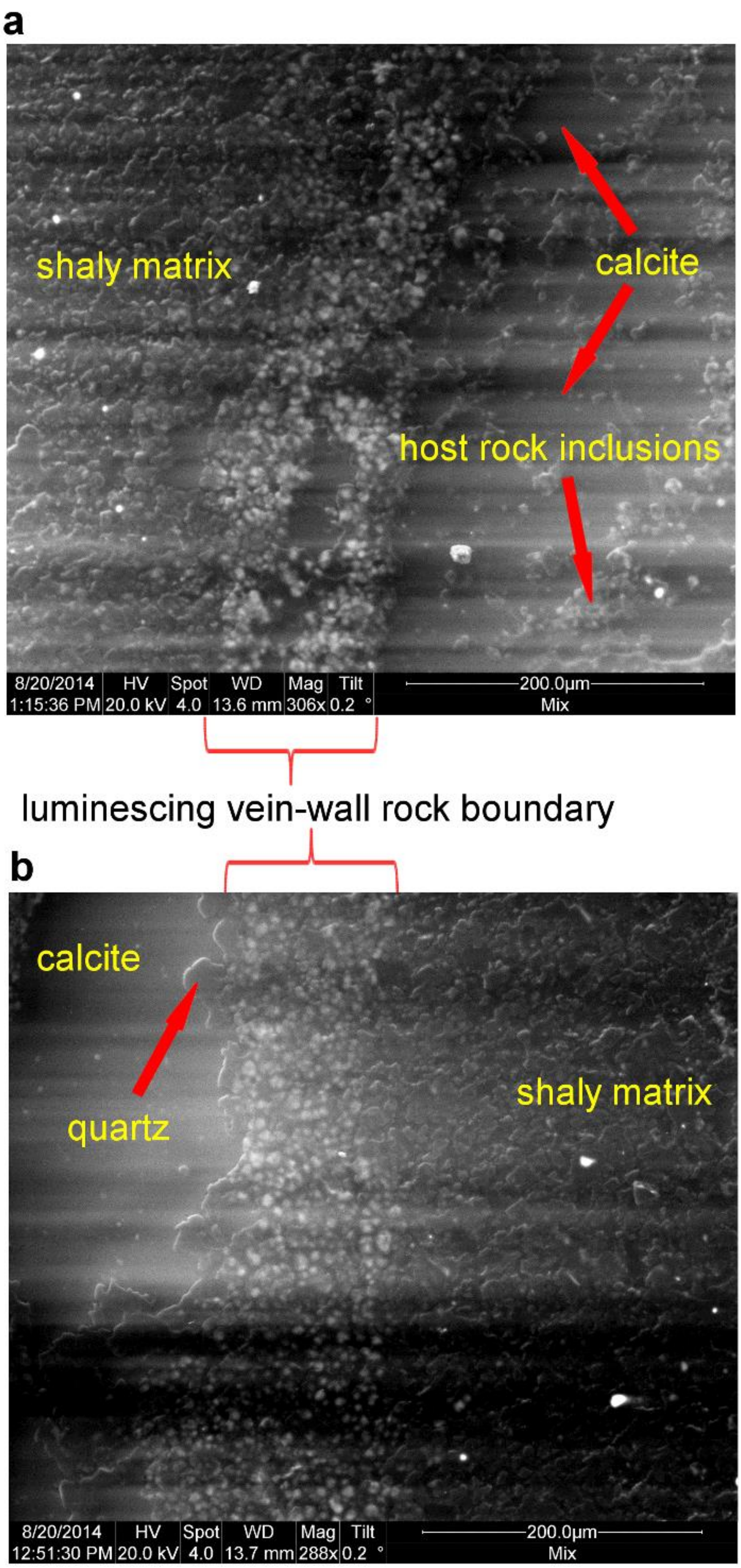

Fig. 4.23 Bed-perpendicular vein showing luminescing zone along the vein-wall rock interface. The calcite vein is either directly in contact with this zone (a) or with quartz grains occurring between the vein and luminescing zone (b).

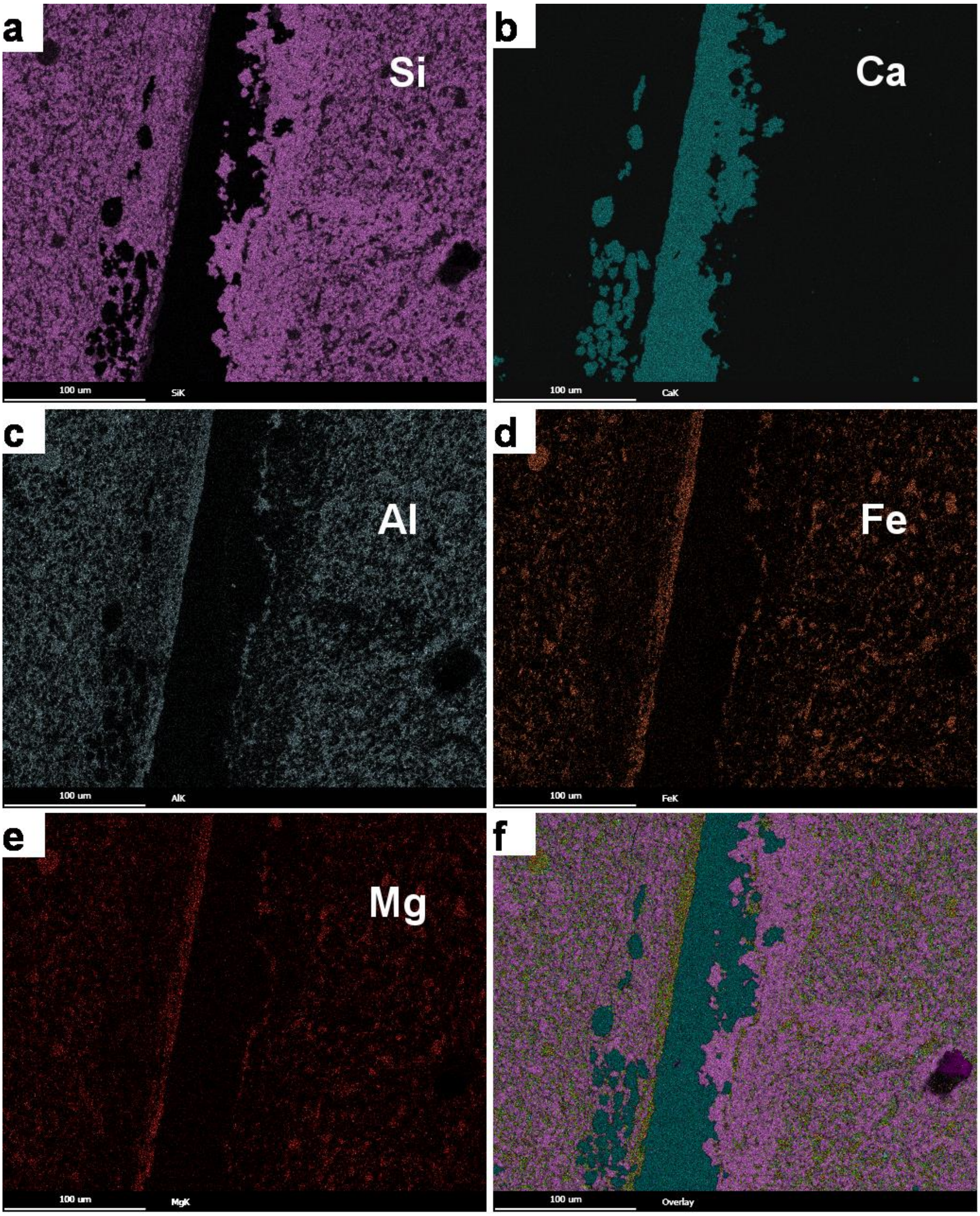

Fig. 4.24 Main element distributions in the bed-perpendicular vein on Fig. 4.23a. Image also shows the overlay of the element maps (f).

4.2.5 Conjugate veins

Conjugate sets of veins (Group E) generally developed normal or at high angles to the bedding (Fig. 4.25). Several crosscutting relationships made it possible to observe relative age of veining. These veins were used to obtain pre-folding vein orientations which I will outline in the next chapter.

Fig. 4.25 Conjugate vein sets in the Val Lavagna Shale, Moneglia.
Image shows bed surface. Location can be found in Appendix B in Table B 2.

The conjugate veins consist of predominantly twinned calcite with subordinate quartz, which mainly occurs along the vein-wallrock boundary. Pure quartz veins seldomly appear. Crystal morphology of the veins can be characterized as both fibrous (Fig. 4.26a) and elongate blocky/blocky (Fig. 4.26b, c and d). However, field and microstructural evidence indicate that the fibrous or blocky nature of veins do not correspond to specific age, veining events or vein directions.

Fibers are heavily deformed, have curved grain boundaries and are occasionally bordered by quartz salvage. There are no signs of growth competition. The median zone is represented by smaller crystal fragments that are either calcite or wall rock. These veins therefore show antitaxial growth in the bed-parallel direction.

Relationship between the calcite and quartz in the veins can be nicely examined on one of the thin section (Fig. 4.26c and d). This section shows that as the vein is getting narrower, less calcite is present and at some point the vein becomes purely quartz-filled. Quartz shows elongate blocky shapes and signs of growth competition indicating syntaxial growth. The crystals also have well-developed facets that are directly in contact with the calcites. Quartz crystals sometimes also appear within the vein, between calcite grains.

Occasional dissolutions parallel to the veins' strike directions are present (Fig. 4.26b). In addition to this, bed-parallel dissolutions (stylolites) frequently cut and dissolve the conjugates (Fig. 4.26d). These dissolutions are quite closely spaced; in one thin section up to seven can appear. While they dissolve most of the veins, some younger veins cut through the seams. The younger veins, however, in turn will be dissolved by a seam elsewhere.

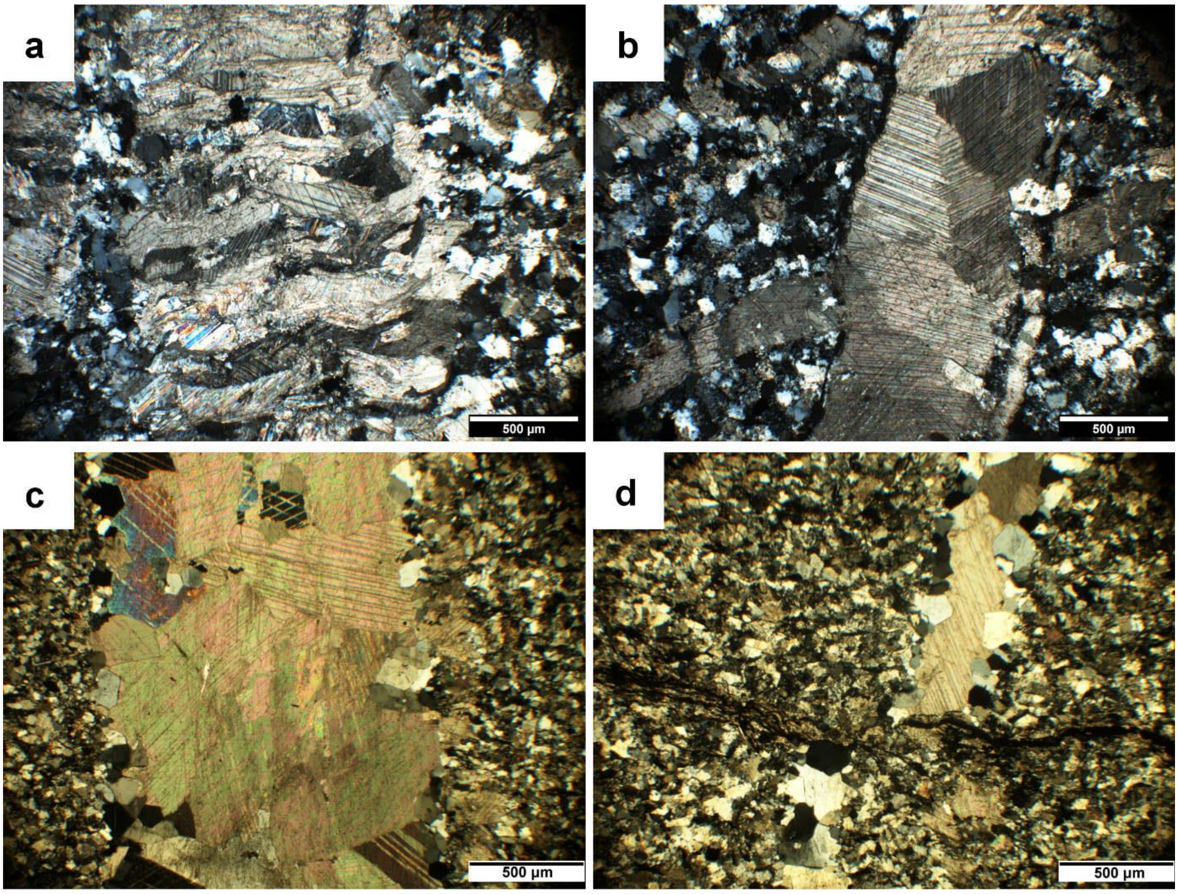

Fig. 4.26 Thin sections illustrating conjugate veins in the Val Lavagna Shale, Riva Trigoso. (a) Bed-parallel section with fibrous, twinned calcite vein. (b) Bed-parallel section with blocky calcite vein exhibiting vein-parallel dissolution. (c) Bed-perpendicular section with blocky calcite vein and elongate blocky quartz along its walls. (d) The same vein as in (d) showing a reduction in width resulting in the disappearance of calcite and the vein becomes purely quartz below the dissolution.

4.2.6 Folding-related veins

Two types of folding-related veins (Group F) were found: veins filling boudin necks and stretching outer arc veins. Layer-parallel extension of a competent layer can cause boudin structures, where the boudins are separated by layer-perpendicular extensional fractures, often called boudin necks (Fossen, 2010). Several veins filling these boudin necks were observed in the field (Fig. 4.27a). These developed in stiff layers bounded by less competent and highly cleaved layers. Stiffer layers that were folded also often showed veins in their outer arcs (Fig. 4.27b). The outer arc of the folded layer undergoes stretching that creates extensional fractures. These fractures were observed in the field as veins.

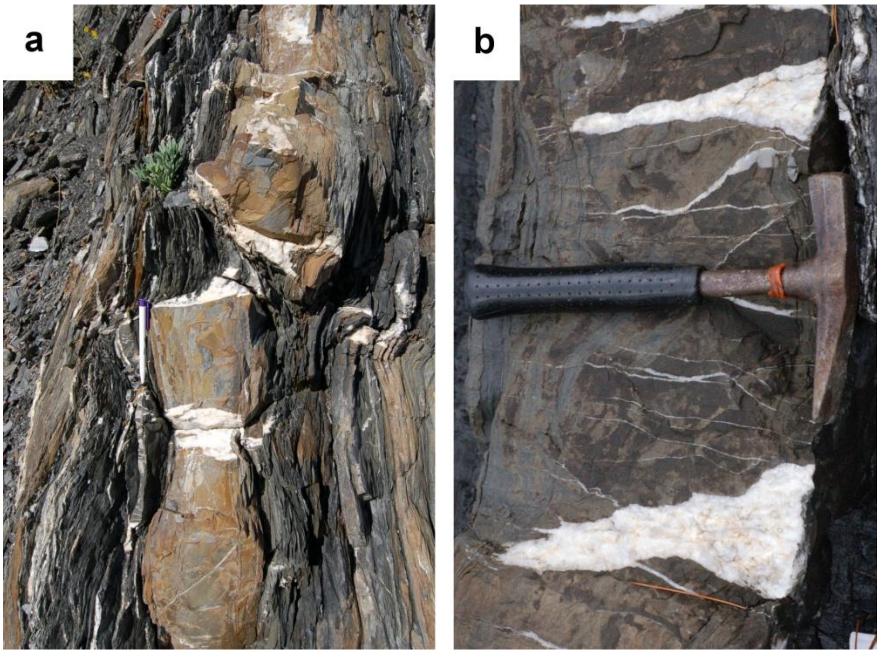

Fig. 4.27 Veins formed in boudin necks (a) and in tensional fractures on the outer arc of the folded layer (b).
Image locations can be found in Appendix B in Table B 1 and Table B 2.

Textures of the folding-related veins were generally identified as blocky in the field. No thin sections have been made for microstructural analysis.

4.2.7 Young crosscutting and fault veins

Veins that crosscut several layers were quite abundant (Group G) (Fig. 4.28a). They had long lateral (up to 10 m) and vertical (few meters) continuity, and were not affected by folding. Their orientation was consistent over the field area dipping towards the W-NW. In addition to this, the identified faults cutting through the sequences occasionally hosted veins too (Fig. 4.28b).

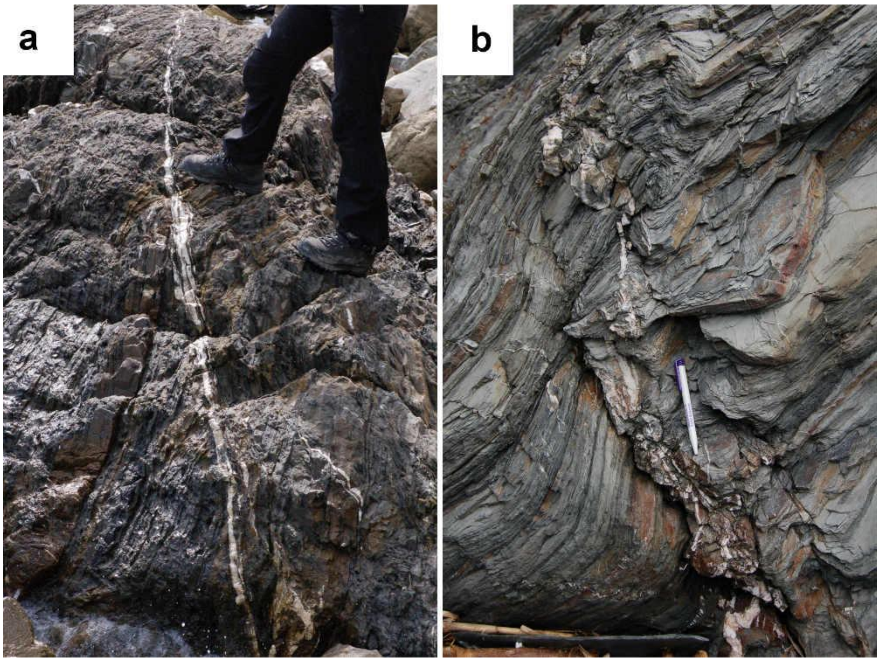

Fig. 4.28 Young crosscutting vein (a) and fault vein (b) in the field.
Image locations can be found in Appendix B in Table B 1 and Table B 2.

4.3 Pre-folding vein orientations

In order to obtain the pre-folding vein orientations, two main types of veins were used: (1) conjugate sets (Group E) and (2) veins that did not form conjugates but were clearly folded by the same folding event. These vein orientations were rotated and unfolded along the fold axes and the bedding measurements. As the veins in all cases pre-dated the NW-plunging folding event (or at least were simultaneous with it), this folding direction was used to rotate and unfold the veins. The exact fold axis orientation that was used in the calculations was either directly measured on the bed that contained the veins or was a general orientation measured in the vicinity of the outcrop. In the following I present the pre-folding vein orientations for each location, Riva Trigoso, Moneglia and Framura.

4.3.1 Riva Trigoso

In Riva Trigoso 33 vein orientations, measured in both normal and overturned layers, were rotated and unfolded on the stereonet. Generally, the complicated cross-cutting relationship prevented to establish age relationships between the veins. Most of the veins became steeper after the rotation and unfolding. Table 2 lists the input data for the calculations, as well as the pre-folding vein orientations. These orientations are plotted on separate stereonets shown on Fig. 4.29.

Stereonet	Bedding	Bedding type	Fold axis	Measured vein	Rotated and unfolded vein
Fig. 4.29a	155/40	Overturned	20-310	244/59	346.7/66.1
				347/52	087.7/88.7
				235/50	344.7/54.7
				252/50	334.6/64.4
				210/50	000.2/39.2
Fig. 4.29b	183/35	Normal	19-317	106/70	095.6/66.3
				013/62	195.9/83.4
				020/55	020.9/88.9
Fig. 4.29c	195/30	Normal	23-325	140/85	137.8/68.8
				026/65	208.8/85.5
Fig. 4.29d	234/40	Overturned	30-300	030/75	344/68.3
				064/80	307.7/60.6
				015/60	352/87.2
				273/40	213.7/24.7
Fig. 4.29e	315/10	Normal	03-326	290/80	288.6/71
				280/86	278.9/77.8
				020/85	020.9/80.8
				002/80	003.5/73.3
Fig. 4.29f	170/31	Overturned	25-317	026/89	030.4/66.3
				248/55	329.7/54.6
				055/78	007.8/88

Stereonet	Bedding	Bedding type	Fold axis	Measured vein	Rotated and unfolded vein
				002/64	059.5/85.6
				304/62	289.9/85
				027/78	033.1/77
				306/60	287.5/83.8
Fig. 4.29g	153/40	Overturned	25-317	356/58	063.3/84.4
				020/55	225.8/85.5
				058/65	193/74.1
				073/89	165.7/82.6
Fig. 4.29h	164/44	Overturned	25-317	045/50	234.6/78.2
				020/56	068.6/86.3
				278/54	326.7/78.8
				305/55	128.9/88.3

Table 2 Input measurements and the pre-folding vein orientations in Riva Trigoso illustrated on Fig. 4.29.
Plane measurements (bedding, vein orientations) are in the forms of strike/dip (according to the right-hand rule), whereas fold axes are in the forms of plunge-trend. Measurement locations of each set can be found in Appendix B in Table B 1.

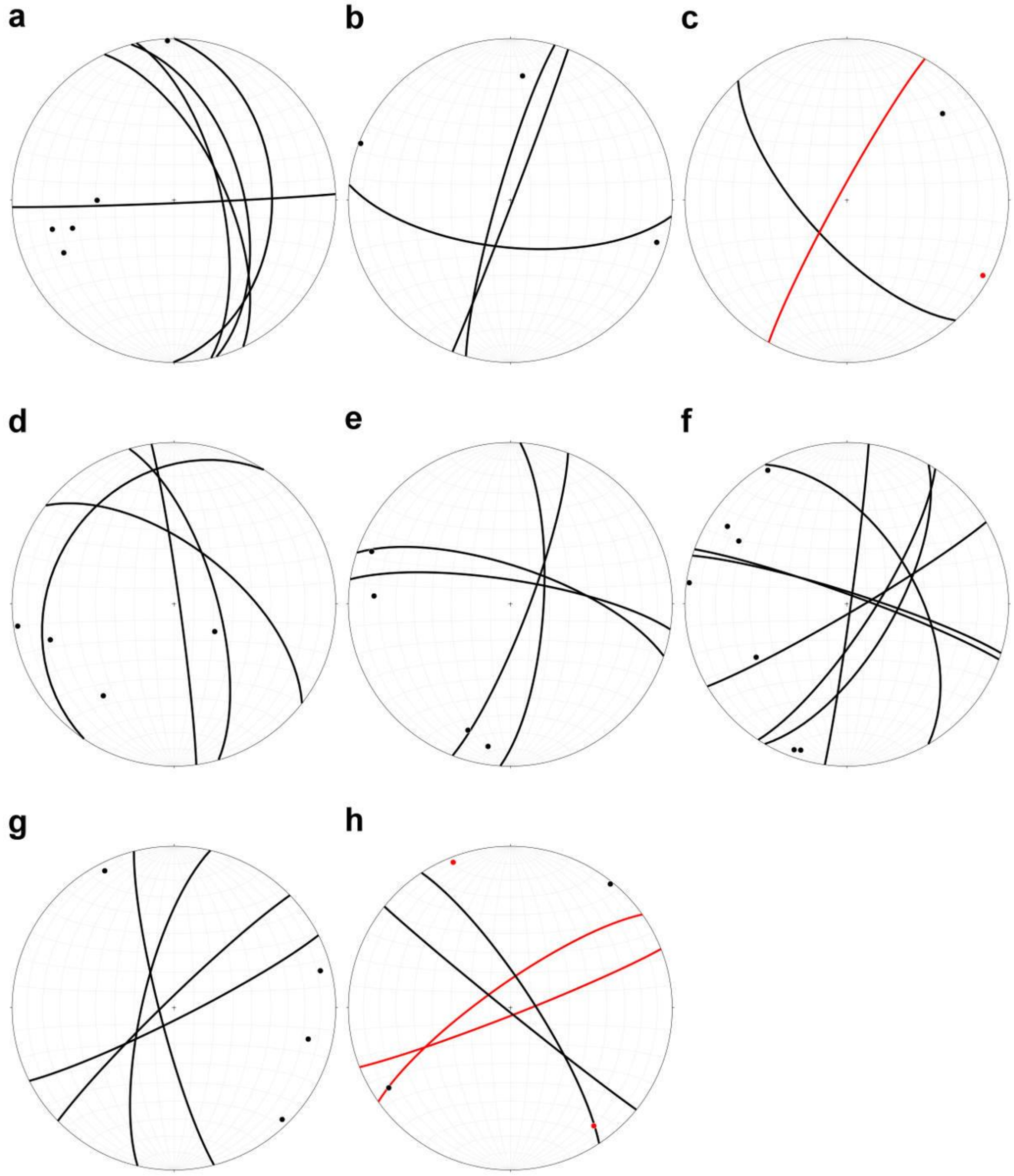

Fig. 4.29 Stereonets presenting pre-folding vein orientations (planes and poles) obtained in Riva Trigoso.
Each stereonet corresponds to different outcrops in the area. Red indicates a younger vein relative to the other vein (or veins) measured on the same outcrop. The older vein on (c) (solid black line) is also accompanied by a vein-parallel stylolite.

Fig. 4.29a: Four medium-dipping veins striking SW-WSW and one striking N were measured in an overturned bed. Crosscutting relationship unfortunately was not possible to recognize. By rotating the veins we obtain a general strike direction from NNW to N and E-W, respectively.

Fig. 4.29b: Rotation and unfolding two veins striking NNE and another striking E yielded similar strike directions but a change in dip magnitudes. While the NNE-striking set became much steeper, almost sub-vertical, the ESE became slightly shallower.

Fig. 4.29c: Two veins perpendicular to each other were measured in a normal bed. The older vein, striking SW, contained a vein-parallel stylolite, whereas the younger vein with NE strike was folded. The pre-folding orientations reveal similar strike directions but a dip change; the old vein became shallower, while the young folded one steeper.

Fig. 4.29d: Four veins oriented between NNE and E in an overturned layer displayed unknown age relationship. The rotation yielded new orientations between NW and NE.

Fig. 4.29e: Two sets of conjugate veins in a normal layer showed N-NNE and W-WNW strike directions. Age relationship between the two sets is unknown. The rotation conserved the strike directions and just slightly changed the dips magnitudes.

Fig. 4.29f: Veins with a variety of strike directions in an overturned bed exhibited a complex crosscutting relationship. The rotated veins can be characterized by NE, N, NW and WNW strike directions.

Fig. 4.29g: Four veins with strike directions ranging from N to ENE displayed complicated crosscutting relationship. The rotation resulted in steeper veins and orientations between NNW and NE.

Fig. 4.29h: Two conjugate vein sets perpendicular to each other showed clear crosscutting relationship. The older set was striking W-NW, whereas the younger NNE-NE. The rotation steepened the veins and shifted the strikes slightly so that the older set became NW and the younger set became NE-oriented.

Integrating the pre-folding vein orientations on one stereonet thus reveals two general vein directions: a NNE-NE and a NW trend (Fig. 4.30).

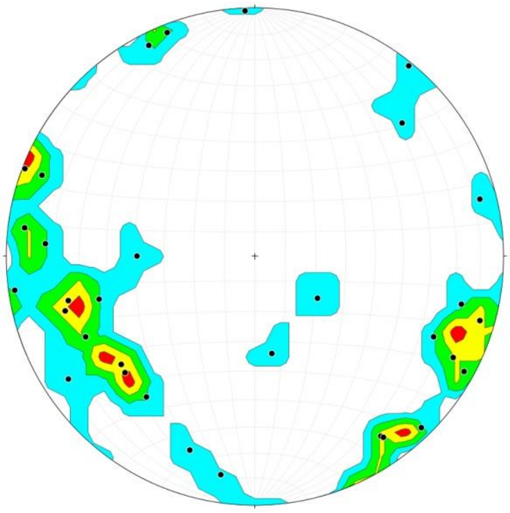

Fig. 4.30 Summary stereonet including the poles to the pre-folding vein orientations in Riva Trigoso.

4.3.2 Moneglia

In Moneglia 37 veins were measured mainly in overturned beds. Input data for the rotations are listed in Table 3, whereas the pre-folding vein orientations are plotted on separate stereonets illustrated on Fig. 4.31.

Stereonet	Bedding	Bedding type	Fold axis	Measured vein	Rotated and unfolded vein
Fig. 4.31a	290/65	Overturned	36-310	180/48	125.8/87
				048/79	057.2/70.3
				042/60	043.9/85.2
				035/25	195.4/73.5
				022/70	241.2/83.4
Fig. 4.31b	290/81	Overturned	63-300	198/21	166.6/82.4
				180/38	332.3/85.1
Fig. 4.31c	287/51	Overturned	36-320	000/90	292.4/76.9
				044/59	241.3/88.8
Fig. 4.31d	200/40	Overturned	34-255	037/50	121.2/88.7
				050/60	288.3/84.3
				335/74	358.3/76.9
Fig. 4.31e	180/44	Normal	33-320	024/29	021.7/71.2
				064/45	051.4/72.9

Stereonet	Bedding	Bedding type	Fold axis	Measured vein	Rotated and unfolded vein
Fig. 4.31f	290/86	Overturned	63-300	048/75	073.5/64.2
				010/40	222.2/80.5
				210/55	127.1/79.5
				198/54	128.3/89.3
				200/58	124.2/87.9
Fig. 4.31g	285/85	Overturned	63-300	010/75	256.5/83.8
				020/44	224.8/89.8
				015/25	206.1/85.4
				180/76	286.7/76.7
				180/20	341.8/89.7
Fig. 4.31h	272/80	Overturned	63-300	180/60	118/86.8
				002/89	087/89.4
Fig. 4.31i	226/33	Overturned	30-300	336/84	060.6/84.4
				034/60	001.1/87.6
				030/70	006.1/78.2
				050/67	347/80
				335/65	231.6/78.8
				326/72	242.6/80.2
				340/76	053.2/89.3
				045/50	171.5/83

Table 3 Input measurements and the pre-folding vein orientations in Moneglia illustrated on Fig. 4.31.
Plane measurements (bedding, vein orientations) are in the forms of strike/dip (according to the right-hand rule), whereas fold axes are in the forms of plunge-trend. Measurement locations of each set can be found in Appendix B in Table B 2.

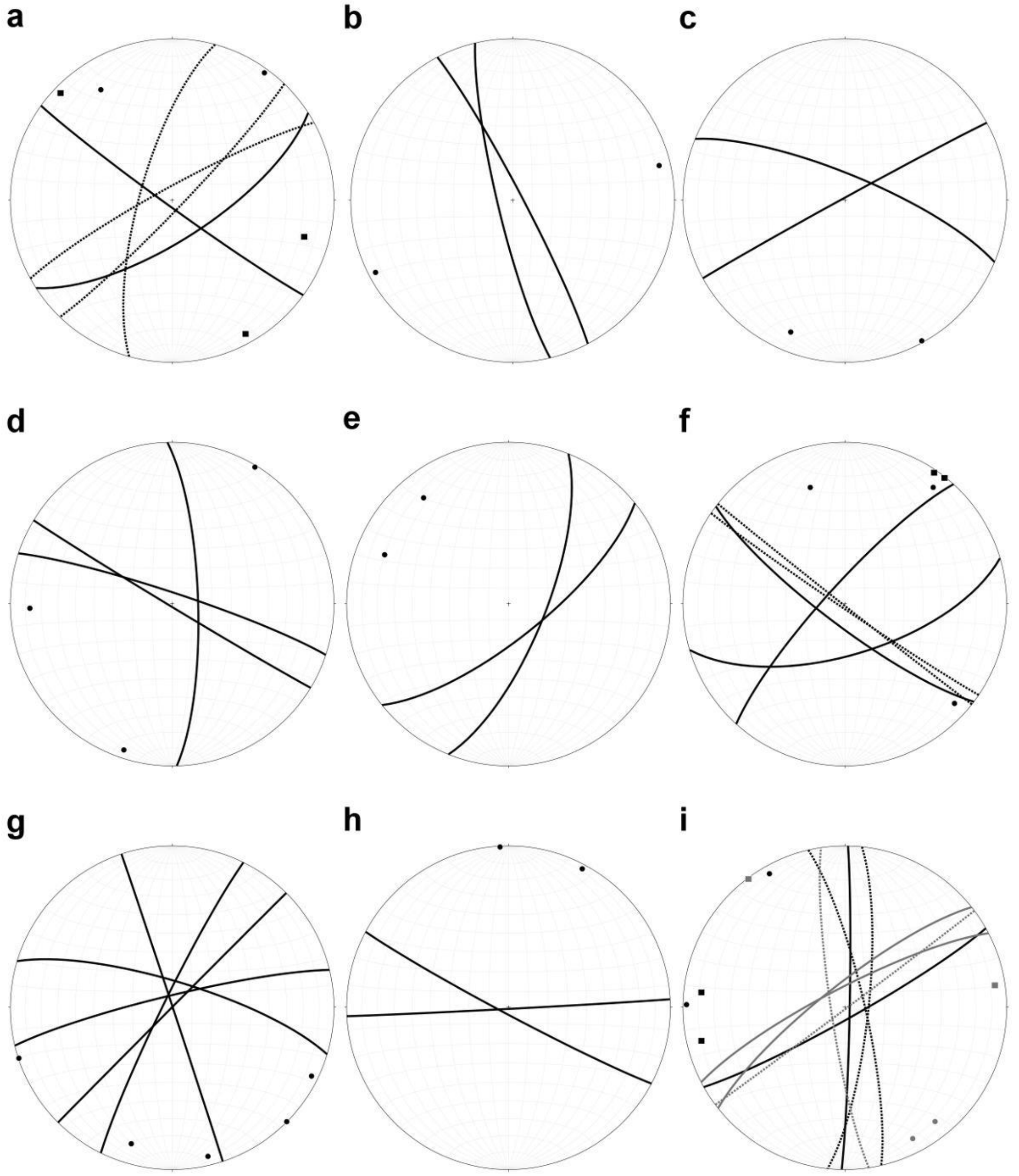

*Fig. 4.31 Stereonets presenting the pre-folding vein orientations in Moneglia.
Each stereonet corresponds to different outcrops in the area. Gray colors and dashed planes correspond to separate conjugate sets.*

Fig. 4.31a: Two conjugate vein sets with unknown age relationship were measured. One set showed an initial N-NNE orientation, whereas the other set consisting of three veins were striking NE. The rotation of the data resulted in the former set to strike NE and SW, and the latter set to be oriented between NNE and NE.

Fig. 4.31b: Rotation of a conjugate set striking S and SSW yielded opposite-dipping steep veins striking SSE and NNW.

Fig. 4.31c: The rotation of a conjugate set with one vein initially striking N-S and another NE resulted in a NW and SW-striking vein, respectively.

Fig. 4.31d: Three veins that formed a conjugate set were striking NNW and NE. The rotation caused the former to be oriented N-S and the latter to be NW.

Fig. 4.31e: Vein orientations in the only normal bed where conjugates were measured displayed NNE and ENE strikes. The rotation did not change the former’s orientation, whereas the latter shifted slightly to the NE. The veins became significantly steeper.

Fig. 4.31f: Rotation of a conjugate set striking SSW resulted in a steep, NW-striking vein set. Another conjugate including three veins striking NE, NNE and SSW yielded new orientations of ENE, SW and SE, respectively.

Fig. 4.31g: While the measured veins were consistent in orientations (N-NNE), the rotation caused them to span out more. The veins became steep striking NE, NNW, WSW and WNW.

Fig. 4.31h: The strike of the conjugate veins changed from N-S to E and SE.

Fig. 4.31i: Four conjugate vein sets with strike directions NW-NNW and NE became much steeper due to the rotation. The vein orientations changed only slightly to N-S, whereas the NE strike remained.

On an overturned bed two veins and a stylolite were found, where one of the veins were dissolved by the stylolite itself. By rotating the orientation of these structures, the veins obtained a NE-ENE, whereas the stylolite a SE orientation (Fig. 4.32).

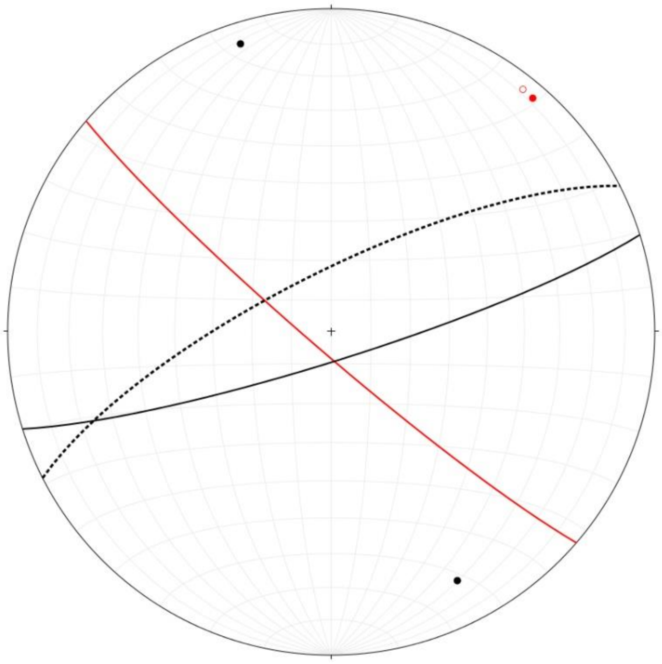

Fig. 4.32 Pre-folding orientations (planes and poles) of a vein (black solid line), a dissolved vein (black dashed line), a stylolite (red) and its teeth (hollow red circle).
Measurement location can be found in Appendix B in Table B 2.

The pre-folding vein orientations in Moneglia are thus characterized by steep to sub-vertical veins with the majority striking around NW-SE and NE-SW (Fig. 4.33).

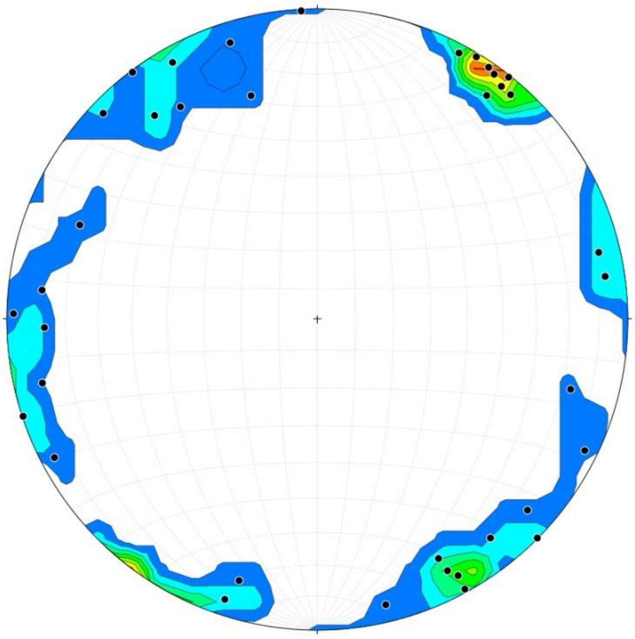

Fig. 4.33 Summary stereonet including the pre-folding vein orientations (poles) in Moneglia.

4.3.3 Framura

In Framura, 30 veins were measured mostly in normal sequences in the Palombini Shale, and then rotated and unfolded on the stereonet. Table 4 lists all the measurements that provided the input data for the calculations, as well as the pre-folding vein orientations that are also plotted on separate stereonets (Fig. 4.34).

Stereonet	Bedding	Bedding type	Fold axis	Measured vein	Rotated and unfolded vein
Fig. 4.34a	180/40	Normal	20-320	208/62	239.9/30.6
				090/64	078/70.4
Fig. 4.34b	134/08	Normal	05-310	150/70	151.4/62.3
				240/54	245.6/56.6
				286/63	287.9/70.1
Fig. 4.34c	274/09	Normal	005-310	120/54	117.3/62.2
				032/71	034.1/75.4
				180/83	178.6/83.7
				080/79	079.9/87.7
				070/70	070.7/78.3
Fig. 4.34d	238/40	Normal	20-320	336/38	010.2/56.8
				290/79	303.3/57.7
				010/43	025.3/74.6
Fig. 4.34e	203/15	Normal	05-310	134/58	124.4/53.8
				160/55	150.8/44.8
Fig. 4.34f	166/81	Overturned	20-320	230/35	356.7/67.8
				263/50	012.4/89.5
Fig. 4.34g	186/25	Normal	05-310	020/13	011.7/37.7
				060/40	044.6/57.7
				258/75	266.7/68.9
				080/80	078/87.6
				044/86	226.2/74.4
				288/83	290.4/88.7
				346/85	165.6/71.6
				025/44	020.7/68

Stereonet	Bedding	Bedding type	Fold axis	Measured vein	Rotated and unfolded vein
Fig. 4.34h	108/26	Normal	05-290	125/85	128.8/60.3
				020/70	011.8/71.2
				087/70	081.4/46.2
				130/65	139.9/41.6
				350/64	343.4/77.9

Table 4 Input measurements and the pre-folding vein orientations in Framura illustrated on Fig. 4.34.
Plane measurements (bedding, vein orientations) are in the forms of strike/dip (according to the right-hand rule), whereas fold axes are in the forms of plunge-trend. Measurement locations of each set can be found in Appendix B in Table B 3.

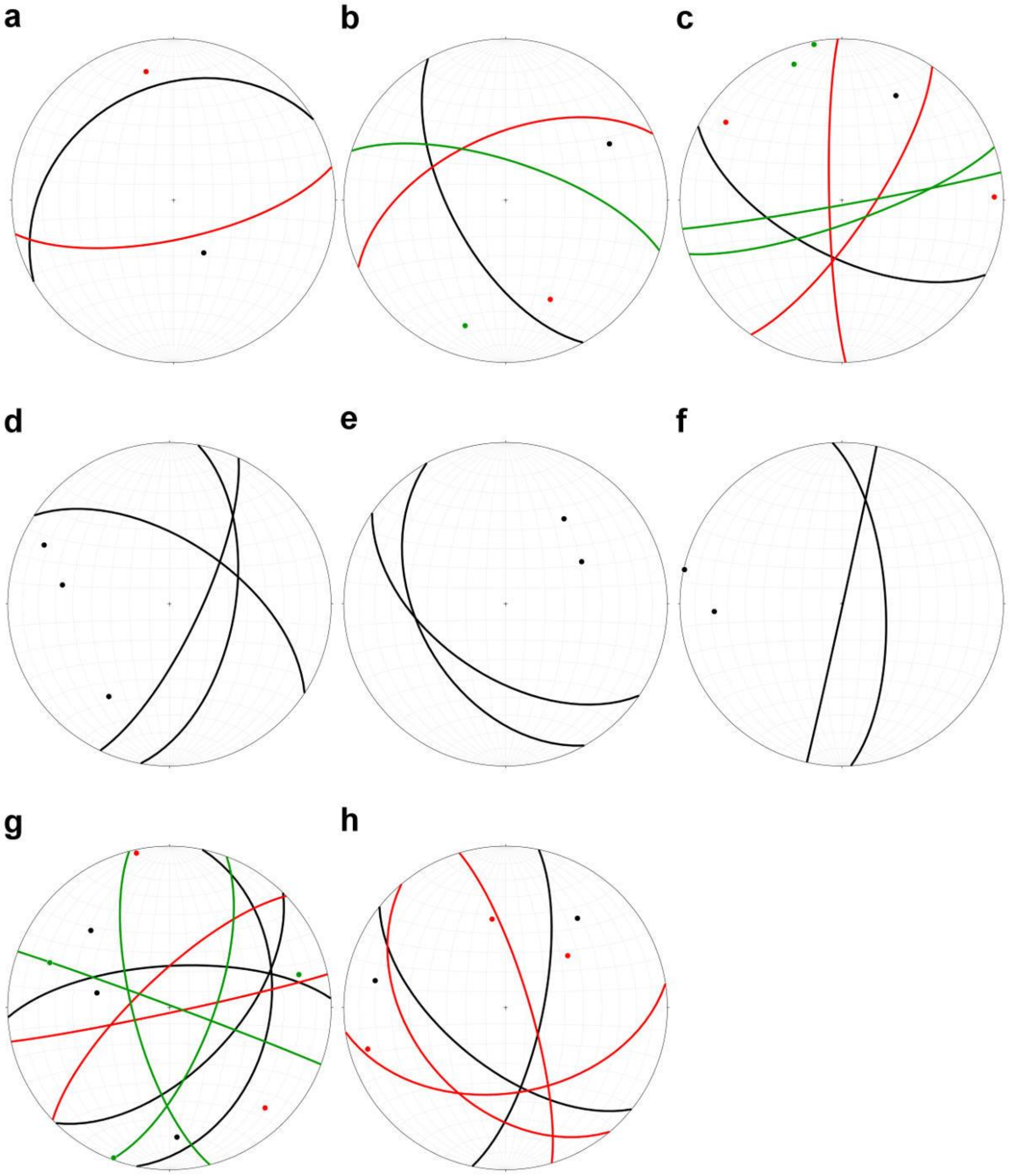

Fig. 4.34 Stereonets presenting the pre-folding vein orientations (planes and poles) in Framura. Each stereonet corresponds to different outcrops in the area. Colors indicate relative ages of the veins: black = oldest, red = intermediate and green = youngest.

Fig. 4.34a: Two veins with observed age relationships after rotation and unfolding obtained new strike directions; the older vein became SW-striking, whereas the younger ENE.

Fig. 4.34b: Orientation of the veins basically remained the same as it was measured on the field, the oldest vein striking SE, the intermediate one SW and the youngest WNW.

Fig. 4.34c: Unfolding these three vein sets preserved the strike directions (oldest SE, intermediate S and NE, and youngest vein ENE) but significantly steepened the dip values.

Fig. 4.34d: Three veins striking NNW, WNW and NNE attained slightly new orientations (NNE, NW and NNE, respectively) with medium and steep dips. Crosscutting relationship could not be established.

Fig. 4.34e: Orientation of a conjugate vein set (striking SE and SSE with medium dips) barely changed after the unfolding.

Fig. 4.34f: Orientation of the only conjugate vein set (striking W and SW) measured in an overturned bed shifted almost 90° due to the unfolding. They obtained new strike directions NNE and N, respectively.

Fig. 4.34g: Strike directions of the three sets of veins with recorded crosscutting relationship remained the same as measured, only the dip magnitudes changed due to unfolding. The oldest veins strike NNE, NE and W; the intermediate veins SW and WSW; whereas the youngest set SSE, NNE and WNW.

Fig. 4.34h: Unfolding also retained the strike directions of these veins, where the youngest set was striking NNE and NW, whereas the older set was striking E, SW and NNW.

Three sets of conjugate veins presented a clear age relationship, where the oldest set was oriented N-S, the intermediate set NW and the youngest set ENE (Fig. 4.35). These orientations were not rotated and unfolded.

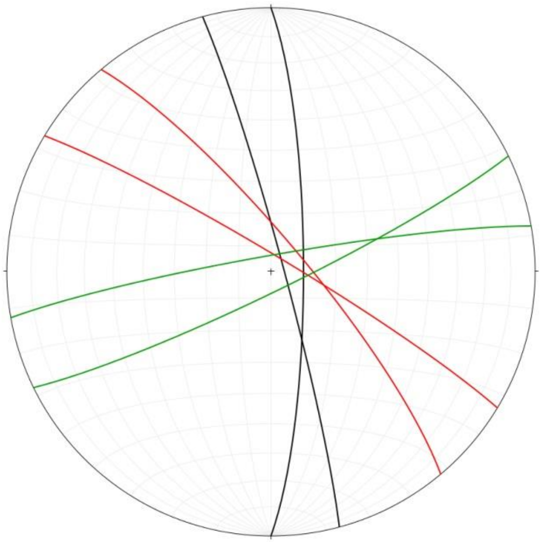

Fig. 4.35 Three sets of conjugate veins plotted on a stereonet illustrate relative age relationships in Framura.
Black = oldest, red = intermediate and green = youngest vein set.

Plotting all the pre-folding vein orientations on one stereonet reveals three major vein directions: NNE-SSW, NW-SE and ENE-WNW (Fig. 4.36).

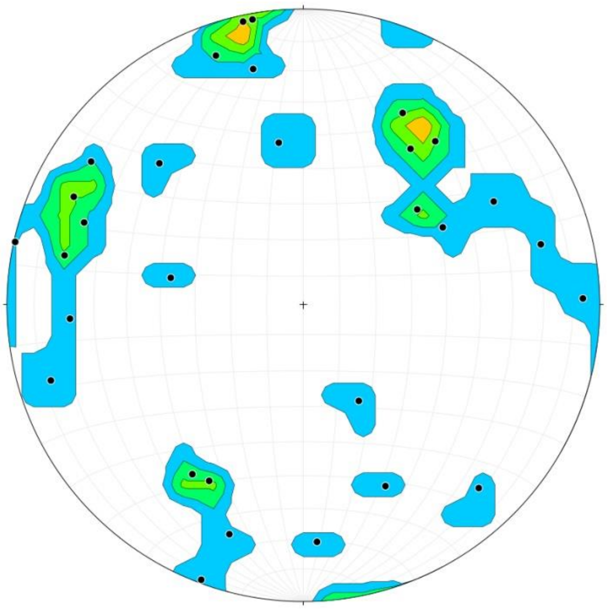

Fig. 4.36 Summary stereonet presenting all the pre-folding vein orientations (poles) in Framura.

4.4 Fluid inclusion microthermometry

As mentioned before (chapter 3.1.3), four different veins in the Val Lavagna Shale were collected for fluid inclusion microthermometry: non-dirty bed-parallel veins (one calcite and one quartz), blobs of mineralization (quartz) and one vein perpendicular to this one. Examination of the wafers showed that (1) quartz crystals hosted significant amount of inclusions, often impeding the view for analysis, (2) occasional calcites were quite deformed and usually not inclusion-rich, (3) both the quartz and calcite crystals were not as clear as expected, so the measurable inclusions were limited, (4) the maximum inclusion size was 4×2 µm, but the average was generally 2×2 µm or less in size and (4) the measured inclusions consisted two phases, liquid and vapor with vapor occupying 10-15% of the inclusions (Fig. 4.37). As the inclusions were extremely small and the crystals not very clear, only two (one from these non-dirty veins, and another from the blobs) ice melting temperatures were obtained, -4°C and -8°C (corresponding to 6.5 wt% and 13.1 wt% NaCl content). This amount of measurement, however, is not representative and therefore should be used with caution. In addition to this, defining the inclusions' origin (primary / secondary / pseudosecondary) was problematic due to the crystals' shape and lack of zoning. No cracks or healed fractures, along which secondary trails would generally occur, were observed within the veins. Neither were transgranular trails (inclusion trails across several grains), which would also indicate secondary origin. The inclusions mainly occurred in random distribution or in groups within single crystals and thus exhibited primary characteristics. However, as uncertainty is quite large, I will refer to them as inclusions with unknown origin. These observations, i.e. crystal and inclusion characteristics, inclusion size and problematic origin, stand for all the wafers.

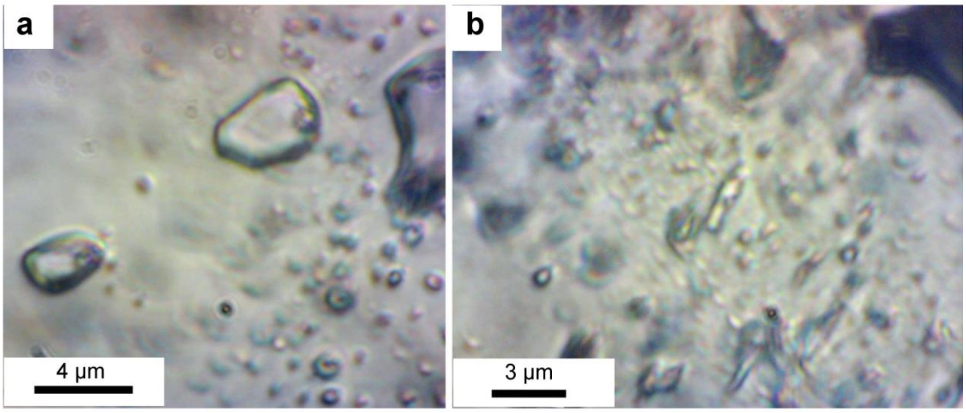

Fig. 4.37 Microscope images of the largest inclusions found in quartz crystals developed in the blob of mineralization (a) and in the non-dirty bed-parallel vein.

The bed-parallel non-dirty veins were the only ones where fluid inclusions in calcite were also measured. The obtained homogenization temperatures (T_H) are illustrated on Fig. 4.38. Inclusions in quartz crystals display relatively constant temperatures: the peak T_H is in the range of 160-170°C, with a smaller but distinct peak between 150°C and 160°C. Only a few measurements show smaller/larger values. The calcite inclusions, on the other hand, homogenized at slightly higher temperatures. Most of them had T_H around 200°C with a few homogenizing at 220°C, 243°C and 273°C. Homogenization temperatures of the fluid inclusions in the blobs and a blob-perpendicular vein revealed two distinct ranges: one centered around 160°C, whereas the other around 220°C (Fig. 4.39).

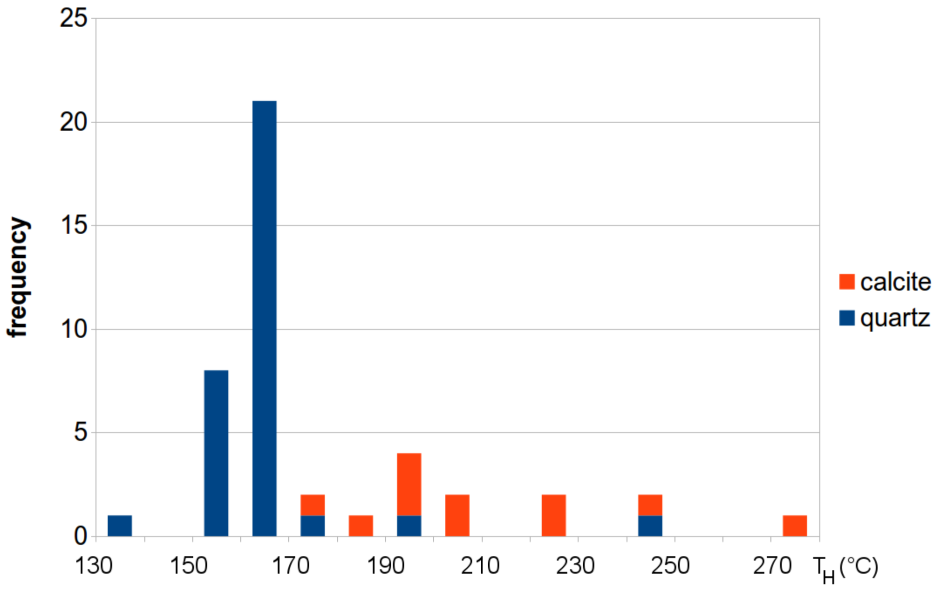

Fig. 4.38 Homogenization temperatures for non-dirty, bed-parallel veins of quartz and calcite.

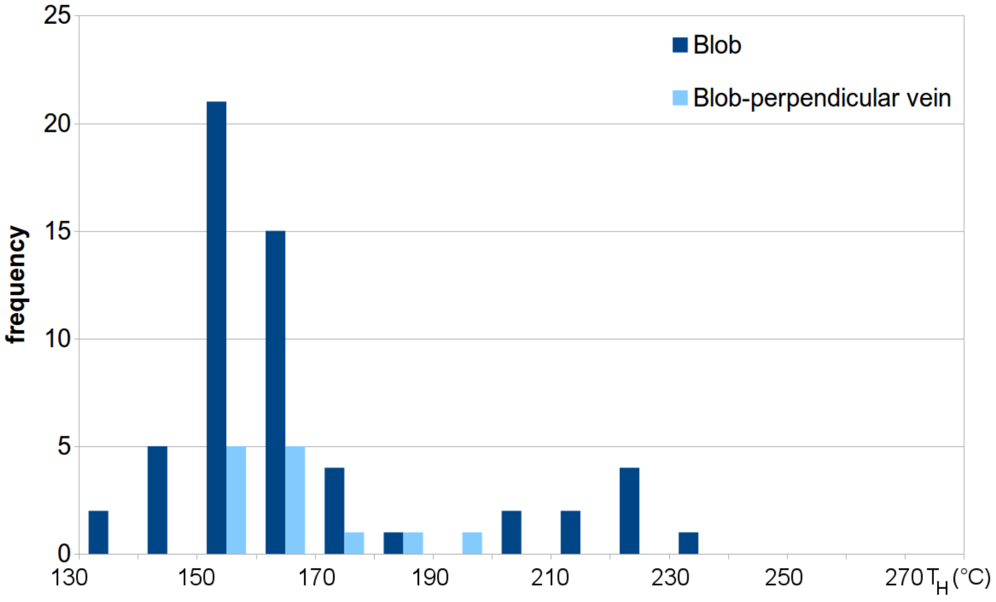

Fig. 4.39 Homogenization temperatures of fluid inclusions within the (quartz) blobs of mineralization and in a blob-perpendicular vein.

Compiling all the data on one chart the dominance of two T_H ranges, 150-160°C and 160-170°C, is apparent (Fig. 4.40). Lower and higher temperatures are subordinate.

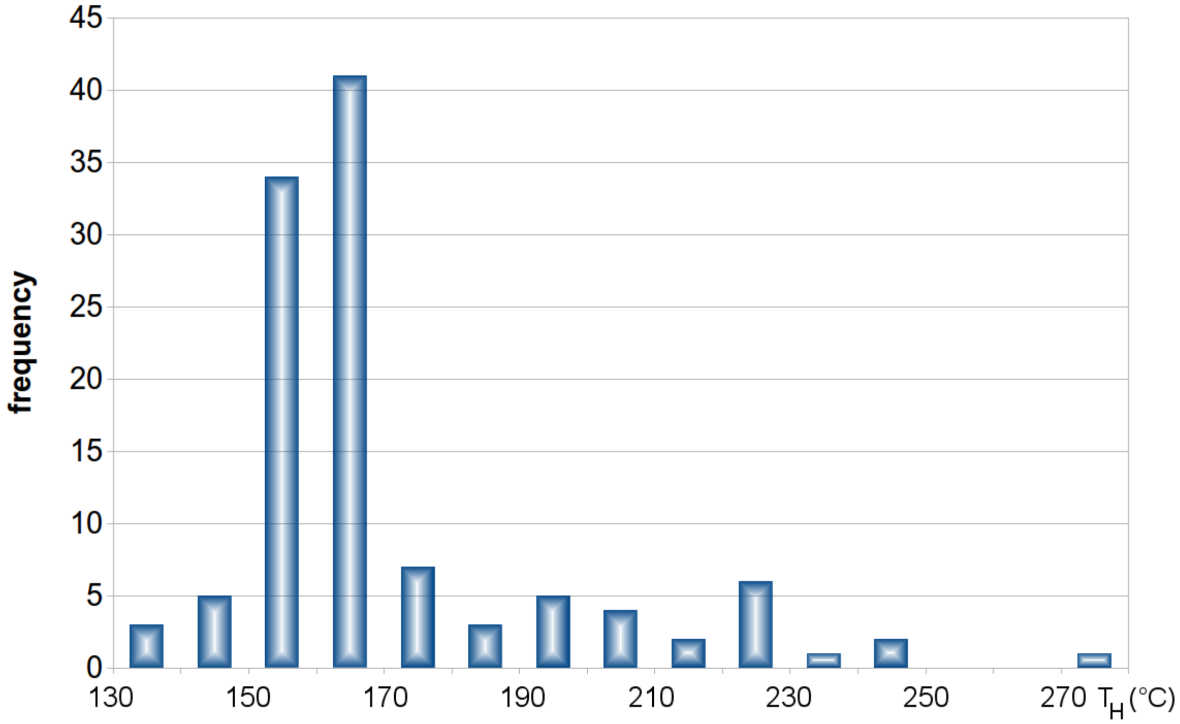

Fig. 4.40 Summary of the homogenization temperatures measured in the different samples.

4.5 Discussion

4.5.1 Deformation

The tectonic regime and the linked deformation history that affected the Northern Apennines and thus the Internal Ligurian Unit are not yet fully understood. It is out of this thesis's scope to propose a new model and provide a detailed/complete description of the evolution of the area. However, the mapping of the structures along with the field observations shed a light on the deformation history, which together with the vein data can further support previous deformation models.

Variations in the bedding orientations outline a roughly stepping (i.e. 90°) strike changes of the main structures, synclines and anticlines (Fig. 4.1). Fold axes also follow this stepping characteristic with local variations that show transitions between the different directions. As mentioned before, a few outcrops displayed a clear relationship between the different folds, where the NE-SW-plunging folds were folded by the NW-plunging ones. This would indicate that a NW-SE compression (forming the NE-SW-plunging folds) pre-dated a NE-SW compression which developed the NW-SE folds. Looking at the crenulation cleavages (Fig. 4.6), most of the first ones (S1) represent compression in the northwesterly directions, whereas the second cleavages (S2) mainly show an E-W to NE-SW compression. Two crenulation axes (S2) measured elsewhere also indicate northeasterly compression (Fig. 4.3b). Tectonic stylolites further revealed an easterly compression (Fig. 4.8). Considering these two compression directions, NW-SE and NE-SW, as well as their presumed relative timing, we can look at the tectonic model again (Fig. 4.41). According to this model these stress orientations can be clearly traced from the Late Mesosoic up to the Neogene period. A NW-SE-directed compression can be attributed to the E-SE-dipping subduction zone between Corsica and Adria during the Late Cretaceous (Fig. 4.41a). This subduction zone, which experienced a polarity flip during the Eocene, migrated anticlockwise towards the NW. This migration caused the rotation of the maximum horizontal stress from E-W to NE-SW, the latter characterizing the main accretion phase (Fig. 4.41b to d). The geodynamic evolution highlights a continuous subduction and accretion, which caused deformation of the Internal Ligurian Unit (among others). This continuity is one of the reasons why identifying and separating the different deformation phases in this area are so difficult, giving rise to a variety of tectonic models and debate between the researchers.

In the current study, however, I am considering two deformation phases: the first (D1) related to a NW-SE, whereas the second related to an E-W to NE-SW compression (D2). I chose to separate the D1 from D2 based on the inferred subduction polarity flip. Deformation occurring after the polarity flip is considered to be D2. For the purpose of this research it is unnecessary to define more deformation phases. Nevertheless, I would like to address that since the deformation was continuous, the rotation of the maximum stress formed structures with a variety of orientations. This means that no clear direction can be assigned to a single deformation phase. Even though I did assign specific orientations, I want to stress the existence of transitional orientations. These transitional orientations, therefore, can be clearly detected in the bedding, fold axes and cleavage variations throughout the area.

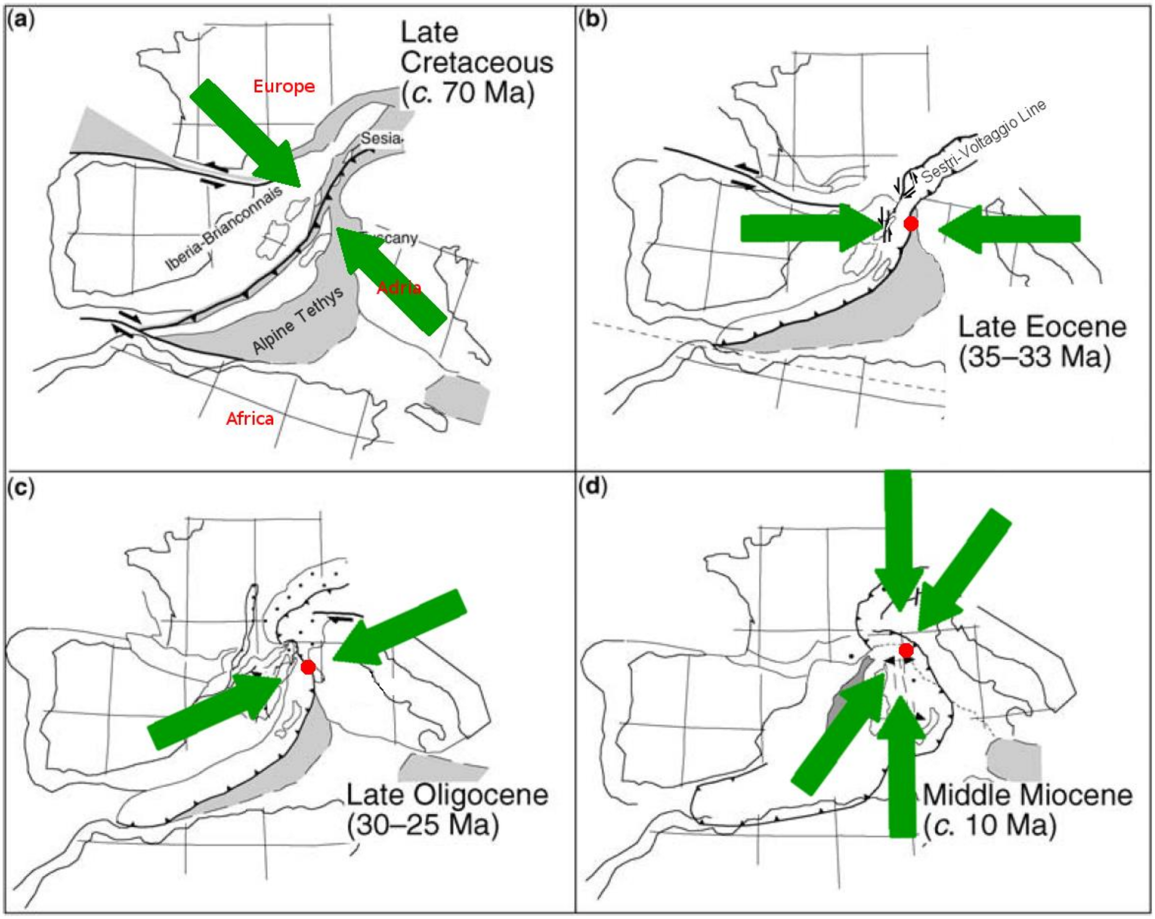

Fig. 4.41 Tectonic map presenting the evolution of the Northern Apennines with the indication of the field area (red dot) and the main stress directions (green arrows).
Figure modified after Molli (2008).

Fig. 4.42 outlines the orientations of different deformation structures that could form as a result of a NW-SE and an E-W to NE-SW compression. As it can be seen there, a N-S compression has been added to the D2. Tectonic stylolites showed evidence for this compression direction (Fig. 4.8). Occurrence of a late (post-orogenic) N-S and orogen-parallel compression has also been reported in the literature (Carosi et al., 2002; Carosi et al., 2004; Molli, 2008). This can certainly represent a different deformation event, but again, considering this orientation as a separate phase would be irrelevant for this study. I therefore recognize the N-S compression as a late D2 event.

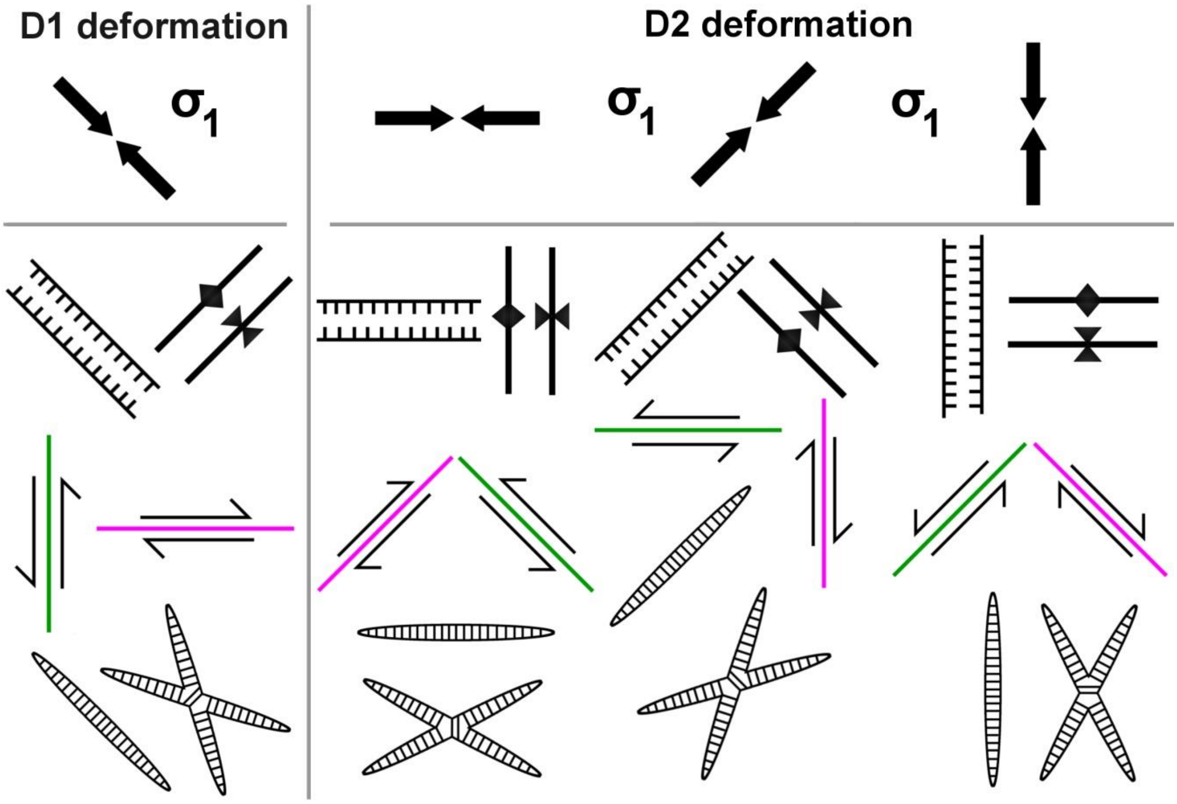

Fig. 4.42 Expected orientations of different structures (folds, normal and strike-slip faults, tensional fractures/veins and conjugate fractures/veins) formed during the defined D1 and D2 phases.

Comparing the fault orientations and movements (Fig. 4.7) with the established main stress directions and triggered deformation shows a nice correlation. Both of the sinistral faults indicate E-W (Fig. 4.7a) and NE-SW (Fig. 4.7b) principal stress directions which correlate to the D2 deformation event. Orientations of the dextral faults (Fig. 4.7d to f) also agree with the expected directions (Fig. 4.42). The fact that two dextral faults first experienced dip-slips indicate that they formed as normal faults (again, their orientations match what is expected), which then accommodated further deformation via strike-slip movements. Orientations of the faults measured in the sandstone and between the sandstone and Val Lavagna (Fig. 4.7f) could also be associated with the D2 deformation phase. Assuming that the medium-dipping faults are normal faults and the E-W-striking steep strike-slip fault is sinistral, the orientations of these are in accordance with a NE-SW compression. Sinistral or dextral, the NE-SW-striking vertical fault in both cases represents D2 formation. The only fault that would potentially match the D1 event is the normal fault on Fig. 4.7c. However, as this fault is clearly a young one, it could not have formed during D1. One explanation could be that it formed during the exhumation and the late orogen-parallel compression, which would explain its age and orientation.

Pre-D2 (conjugate) vein orientations and their age relations are also in accordance with the outlined major horizontal stress directions. Stylolites related to veins indicate NE-SW compression (Fig. 4.29c, Fig. 4.32), which would mark the major accretion phase. Only one conjugate set, seen on Fig. 4.35, contradict the relative timing of stresses, since the oldest conjugates showed N-S compression, whereas I attributed this direction to late-D2. One explanation could be that there was an error of judgment in the field and wrong relative age relations were documented. If this was not the case then the conjugate set marks an old N-S compression direction which could not be explained by paleotectonics. Probably a more likely reason is that these conjugates were not rotated and unfolded due to the lack of bedding and fold axis measurement, so they do not reflect pre-D2 orientations but the current one.

The presented pre-folding conjugate vein orientations nicely demonstrate how small-scale structures can capture kilometer-scale geodynamic history. This has also been reported in the Jabal Akhdar dome in the Oman Mountains (Gomez-Rivas et al., 2014). The area is characterized by a complex geodynamic evolution that includes obduction of the ophiolite sequence followed by uplift and compression due to the convergence of the Arabia and Eurasia plates. The Jabal Akhdar dome consists of crystalline basement rocks and overlying thick carbonate (limestone and dolomite) sequences, which exhibit complex calcite-quartz veining along with both bed-parallel and bed-perpendicular stylolites. These veins and stylolites captured the main, kilometer-scale tectonic events that affected the Oman Mountains. The fact that the small-scale structures correlate well with the major tectonic events is important as it proves that studying sub-seismic structures (i.e. those that cannot be seen on seismic profiles) can and probably should complement seismic surveys, especially if those surveys are carried out in hydrocarbon-bearing basins. Thu current study on the Internal Ligurian Units in Italy also shows how large-scale geodynamic evolution can be unraveled through the study of small-scale structures. The large and small-scale deformation structures are thus in agreement with previously reported compression directions. The accretion phase representing the major deformation has formed tightly folded sequences with rotating (stepping) orientations. The lower part of the Internal Ligurian Unit (ILU), the Palombini Shale, is in fault contact with the underlying ophiolite sequence (see at Framura on Fig. 4.1). This fault contact could represent one of the major thrusts that exist in the area. The orogen-parallel faults (striking NW-SE) on Fig. 4.1 have only been shown on a few previous geological maps (Giancarlo Molli, personal communication). Their orientations, as well as the fault contact between the Palombini Shale and ophiolite, would suggest that these are part of the major thrusts that form the Northern Apennines.

4.5.2 Fractures as mineral-precipitation sites

A variety of vein patterns were documented in the studied area. Field observations and microstructural analysis gave an insight into the vein-forming mechanisms and the deformation characteristics of the ILU.

Veins could generally be grouped into two major categories: those that have clearly tectonic origin and those with uncertain origin. Veins that formed due to tectonic forces are the conjugates, veins related to layer-stretching (boudin-filling veins and outer arc veins), and fault veins. The other veins do not have clear tectonic origin; these are the bed-parallel dirty and non-dirty veins, blobs of mineralization and the bed-perpendicular and parallel set.

In all cases, the veins generally showed elongate blocky textures that correspond to syntaxial vein formation. This indicates that in most cases there was a fluid-filled fracture where mineral-precipitation occurred. As most veins therefore probably formed as fractures, it is worth to discuss what could have triggered and influenced fracturing. Bed-perpendicular fractures likely formed either due to the overburden stress or layer-stretching during folding. The layer-parallel stylolites in the host rock, as well as the vein-parallel dissolution seams within the bed-parallel veins both in the Palombini and Val Lavagna shales suggest that the overburden stress not only contributed to major dissolution within the sequences but probably to bed-perpendicular fracture formation as well.

Conjugates found in the shales nicely reflect the dominance of horizontal stress compression generated by the subduction and accretion. The compression is further supported by the tectonic stylolites within the host rocks, as well as the dissolution seams along bed-perpendicular veins.

Formation of the bed-parallel veins could generally be attributed to three processes: (1) horizontal compression that overcomes the overburden stress (i.e. compressional regimes), (2) elevated fluid pressures that can modify the stress directions and magnitudes causing horizontal failure, and (3) a combination of both. It is a widely accepted view that the ILU sequence was mainly affected and deformed by a compressional regime that would promote horizontal fracturing. The subduction and accretion, however, cause both the increase of overburden by accreting sediments onto the continental crust and decrease of overburden due to the exhumation of sequences by erosion or detachment faults that bring nappes to upper crustal levels. These competing effects influence the relationship between the lithostatic and major horizontal stresses, and would thus also affect horizontal failure. Whether fluid pressures contributed to horizontal failure is difficult to determine. Fluids have been known to lower shear stresses of sequences (interfaces), so they could have promoted horizontal failure. According to Meneghini et al. (2007) the dirty veins are hydrofractures formed in unlithified sediments as pressures built up due to the lithified and low-permeability overlying layers. However, there are no signs of solidification differences in the sequences that would support this view. Regardless of this, dirty veins could still be hydrofractures but there is no clear evidence that would point towards this. In addition to these, the origin of the bed-parallel and perpendicular set of veins is also questionable. First, they seem to mimic fluid flow and in theory the perpendicular set connecting the parallel sets could have formed due to high fluid pressure gradients. As discussed in chapter 1.1.2, fluid pressure gradients can modify the orientation and the magnitude of the principle stresses promoting horizontal failure under lithostatic conditions (Cobbold and Rodrigues, 2007). This means that horizontal fractures/veins could have formed as a result of high fluid pressure gradients, just like in the hydrobreccia experiment shown in chapter 6.2 (Fig. 6.36). In light of this the bed-parallel and perpendicular vein set could have had an evolution, where first either the lithostatic pressure and/or (local?) extension formed bed-perpendicular veins but the fluid-pressure build-up switched the principal stresses and promoted horizontal failure. These horizontal fractures therefore bounded the perpendicular veins. Recent Elle experiments, however, showed that these layer-confined patterns can also be reproduced purely by applying tectonic stresses and thus without any fluid involvement (Daniel Koehn, unpublished data). The regular spacing between the perpendicular sets can also suggests tectonic stress dominance where the fractures probably formed due to infilling. On the other hand, the classical views on the development of fracture spacing in layered sequences cannot explain the observed spacing variations, especially the one seen on the Fig. 4.20b. Contrasting mechanical properties of the layers, such as those discussed in chapter 5.3 could have had influence on the spacing. Previous studies also examined closely spaced microveins that were considered to form as a result of the tensile strength contrast between the veins and the host rock; a process termed as crack-jump mechanism (Caputo and Hancock, 1999; Holland and Urai, 2010; Virgo et al., 2013; Virgo et al., 2014). The regular microvein apertures led researchers to believe that veining took place in a constant remote stress field where the cyclic fluid-pressure variations caused fracturing and veining in the carbonate sequences in Oman (Holland and Urai, 2010). The presented bed-perpendicular veins linking bed-parallel veins also have quite regular apertures and spacing, and they do not show evidence of crack-seal mechanisms. These would relate them to the microveins shown in Oman.

Microstructural analysis of these bed-parallel and perpendicular sets revealed that the veins are in continuum, i.e. crystals grow out from the bed-parallel veins and these seed the parallel sets. Other samples (e.g. dirty and non-dirty veins) showed that perpendicular veins provide bridges between parallel ones and are in continuum with them too. Bed-parallel stylolites have also been found to dissolve some conjugate veins, while leaving others unaffected. All these, in addition to the co-existence of bed-parallel and perpendicular stylolites, indicate that the ILU sequence was subjected to alternating cycles of horizontal and vertical compression. This cyclic behavior could be explained by the alternating cease and onset of deformation (subduction and accretion) or by the rotation and folding of layers. The latter could refer to a scenario where the compression of a horizontal layer causes bed-perpendicular stylolites, but as this sequence rotates new stylolites form perpendicular to the initial ones (and thus parallel to the beds). The overburden sequence can also exert enhanced compression further promoting stylolite formation.

4.5.3 Dominant transport mechanisms

Veins consisted of dominantly calcites and subordinately quartz. As the host rocks (shales) are made up of large amount of silica, quartz veins in shales could directly imply a closed system where the quartz originates from the host rock. However, the calcites in the veins suggest different mechanism as the host rock completely lacks calcium (Fig. 4.24b).

Field observations showed that the intensity of veining is increasing towards the Val Lavagna-Palombini Shale boundary. The boundary itself was a zone, rather than a distinct line, which exhibited complex structures including chaotic, occasionally broken beds, and cleavages. Due to this and the general characteristics of the two shale formation, it was difficult to distinguish between the Palombini and Val Lavagna outcrops close to the boundary. Previous geological maps assigned a fault contact between the two lithologies. A fault between these two formations could also justify the increased veining intensity in these areas. This would therefore suggest that veining occurred due to a localized fluid flow along a fault. Other transport mechanisms, such as diffusion or pervasive flow, would not form increasing vein intensity adjacent to a fault contact. Fluid flow through the fault could also transport calcium from deeper levels that might have provided the source for calcium veining.

While the localized fluid flow seems to correlate well with field observations, this section analysis revealed other transport mechanisms within the ILU that were also prominent. Most of the veins were dissolved by bed-parallel (either in the host rocks or within the veins) and/or bed-perpendicular stylolites. The dissolved vein materials (mostly calcites) could have transported over distances of various scales, and precipitated the dissolved materials in fractures. Calcite veins might have therefore provided materials for the formation of other calcite veins. This could have been especially important in case of the older calcite veins (e.g. bed-parallel ones).

CL-banding observed in the bed-parallel and perpendicular vein set showed Mg, Al and Fe-concentrations along the vein margins and the depletion of these elements in the host rock adjacent to the vein indicating local diffusion from the host rock towards the vein. Considering that these veins have syntaxial textures, the oldest part of the vein lies along the margins, where the CL-banding and quartz crystals have been found. This could suggest that at first cracks with small apertures formed facilitating diffusion (probably pressure gradient-driven) from the host rock towards the cracks, which resulted in element-concentration and quartz precipitation in small amounts. As cracks widened, fluids from the fracture networks (in this case from the bed-parallel fractures) entered the cracks precipitated calcites in a continuous manner. Considering the vein-width and spacing ratio on Fig. 4.20b it is apparent that diffusion alone could not have filled the cracks, and it would not explain the origin of calcite either. Taking all these into account it seems that fluid flow through the fault between Val Lavagna-Palombini formations, in addition to the connected fracture networks, were responsible for the veining in the ILU, with locally-derived fluids (e.g. through diffusion and dissolution) contributing to veining as well.

4.5.4 Vein microstructures

Vein microstructures showed the co-existence of calcites and quartz as vein-filling minerals. Quartz generally occurred in selvages, along the vein-wall rock boundary or as smaller grains within the veins. The relationship between the quartz and calcite along the vein-walls indicate coupling, where the calcites lock onto the quartz at the boundaries. This coupling has been reported before (Hilgers and Urai, 2002b). In the examples seen on Fig. 4.11, Fig. 4.16 and Fig. 4.17, the calcite and quartz coupled appearance is also evident.

Different generations of calcite were only observed (clearly) in the bed-parallel dirty and non-dirty veins. The various degrees of twinning and the microstructural observations suggest that calcite precipitation occurred throughout the structural evolution of the sequence, since some crystals exhibited signs of larger deformation than others. This was not detected in the other veins (e.g. conjugates), where the calcites showed homogeneous deformation and structural features. The only exception is probably the bed-parallel and perpendicular set, where larger, wall-to-wall twinned calcites were juxtaposed to smaller, non-twinned calcites. The perpendicular veins were characterized by local, bed-parallel shearing creating vein offsets and foliation in the matrix. These shearing sites indicate that local twinning of the calcite crystals could have developed, which are bordered by recrystallized calcite grains. The dominant shearing probably rotated the crystals and caused generally homogeneous crystal orientations in a few veins (Fig. 4.22a and d). It is apparent where shearing did not affect the veins, crystal orientations are quite dispersed (Fig. 4.22e). The abundance of host rock intrusions might have arisen due to a 2D problem. In 3D the veins are curving and fill micron-width splays that interact with each other. A 2D thin section thus could incorporate a large amount of host rock. In addition to this, the vein-wall rock boundary is usually not well-defined, not continuous or irregular. Seldom can we observe a sharp, smooth boundary (see Fig. 4.24). This also stands for the other samples, where the vein-wall rock boundaries are typically irregular.

Veins generally lacked of crack-seal textures. Only one set of conjugates were found where several inclusion bands parallel to the vein-wall rock boundary represented crack-sealing of the veins (Fig. 4.43). Otherwise no transgranular inclusions bands were observed, which suggests that refracturing and rehealing of the veins were probably not a dominant process during deformation, only affected veins locally.

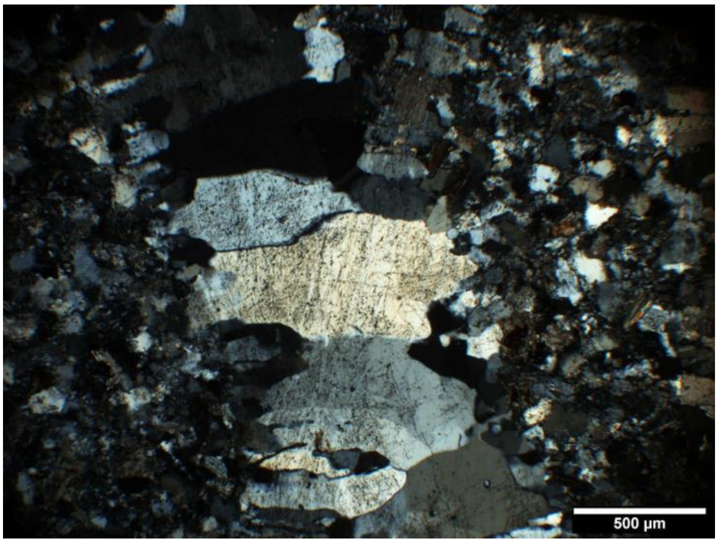

Fig. 4.43 Conjugate vein from the Val Lavagna Shale (Riva Trigoso) showing inclusion bands indicating crack-seal mechanism.

Deformation is not only captured via recrystallized calcite and quartz grains, and calcite twinning, but via bulging as well. Bulging typically indicates low-temperature deformation, which correlates well with the previously reported degree of metamorphism under sub-greenschist facies. This could provide some basis for unraveling the pressure-temperature conditions during veining.

4.5.5 Pressure-temperature conditions during veining

Fluid inclusion analysis was performed to gain an insight into the pressure-temperature conditions during veining. Inclusions from bed-parallel veins and blobs of mineralization were measured, where the homogenization temperatures (T_H) correlated well with each other indicating that the two are hydraulically (and thus structurally) related. The relatively wide distribution of T_H between 150-230°C could either indicate one generation of crystallization from a cooling fluid or could mark two generations of precipitation; one with a T_H around 160°C and a second generation with 200-220°C. Due to the underrepresentation of the high homogenization temperatures (>200°C) more measurements would be required to define whether the inclusions represent one or two generations.

Pressure-temperature conditions of the host rocks are relatively well-documented. As mentioned in the literature review chapter (Chapter 2.1.2) the ILU was subjected to metamorphism under sub-greenschist facies. This already limits pressure-temperature conditions, and is further supported by recent Raman analysis of the Val Lavagna host rock where a maximum temperature of 250°C was found that affected the shale sequence (Giancarlo Molli, unpublished data). Taking this into account the ILU was subjected to a maximum pressure of around 300 MPa (considering the metamorphic facies diagram). Assuming that 300 MPa corresponds to the maximum lithostatic pressure, a maximum of ~11 km depth can be inferred. This depth not only lies within the reported range of 8-12 km (Meneghini et al., 2009), but would also suggest a geothermal gradient of 22°C/km, slightly below the average 30°C/km, which is expected in an accretionary wedge. As the bed-parallel veins represent the earliest vein formations affected by polyphase deformation (folding), it is a reasonable assumption to consider that the host rocks during the veining were close to their maximum P-T conditions. Even though P-T conditions of the host rock seem to be solid, it is important to mention that these conditions can be (and probably were) quite heterogeneous within the ILU sequence (and within each unit). This can be attributed to the temporal and spatial variations in the overburden thickness, as well as the structural levels at which the formations appeared. Especially the existence of a fault between boundaries can create heterogeneous P-T conditions. These are the reasons why it is extremely hard to estimate the P-T environment at the studied area at time of veining.

Prior to making assumptions regarding the microthermometry results, it is apparent that all the T_H (except one) lies below 250°C, which was measured as the maximum temperature of host rock, Val Lavagna Shale, more inland from the studied area (Giancarlo Molli, unpublished data). This, however, does not mean that the trapping temperatures (T_T) were within that range. As there are no (pressure) independent geothermometers available for the sequences in the studied area, it is not possible to obtain trapping conditions (P_T, T_T) without making several assumptions. First of all, assuming a 10 wt% NaCl content, the isochores can be calculated along which the inclusions trapped. Calculations are according to equations 3.1 – 3.4 outlined in Chapter 3.1.3. The slope of the isochore shallows with increasing T_H. For T_H = 150°C the isochore for this two-phase 10 wt% NaCl-H_2O system is 20 bar/°C, whereas for T_H = 220°C it is 15.7 bar/°C. If we assume that the 250°C is the minimum T_T, since the fluid were probably hotter and the temperature-drop could have caused oversaturation of the fluid, then we obtain a P_T range between 48 MPa (for T_H = 220°C) and 201 MPa (for T_H = 150°C), referring to depths of 1.7 and 7.5 km, respectively. It is more likely, however, that the P_T lies closer to 200 MPa as the overburden was minimum 3 km (~80 MPa). The absolute minimum T_T should be 230°C, since in this case the inclusions homogenizing at 220°C would correspond to a P_T of ~16 MPa and thus 600 m depth, which is extremely unlikely. Considering that the sequence was subjected to a maximum of 12 km overburden, the max T_T should be 308°C at which the inclusions with T_H = 150°C would have trapped. Inclusions homogenizing at higher temperatures would have then formed at structural levels up until ~5 km depths.

Inclusions with	Assuming T_T=250°C P_T (MPa)	Assuming T_T=230°C P_T (MPa)	Assuming T_T=308°C P_T (MPa)
T_H = 150°C	201 MPa	161 MPa	317 MPa
T_H = 160°C	175 MPa	136 MPa	288 MPa
T_H = 200°C	85 MPa	51 MPa	183 MPa
T_H = 220°C	48 MPa	16 MPa	139 MPa

Table 5 Trapping pressures of fluid inclusions assuming various trapping temperatures.

The uncertainties regarding (1) the inclusions' origin, whether they are all primary or some trapped as secondary inclusions and (2) the prevailing P-T conditions during veining at the studied area (especially due to the existence of a fault) do not make it possible to determine, but only to estimate the trapping pressures and temperatures. Assuming that the inclusions are of primary origin and that the trapping temperatures lied between 230°C and 308°C, the bed-parallel veins formed between 16 MPa and 318 MPa where trapping was more likely in the 80-318 MPa range.

4.5.6 Limitations and possibilities for further work

Prior to drawing conclusions of the presented field study it is important to discuss the limitations that (could have) affected the results. First of all, the size of the studied area and thus the results might not be representative of the entire Internal Ligurian Unit. Additional structural measurements in a wider area would shed more light on the geodynamic evolution of the unit. Second of all, the fluid inclusion data should be treated cautiously as the samples did not allow proper analysis (i.e. the crystals were cloudy, small, deformed, and the inclusions extremely small) (see Chapter 3.1.3). This resulted in the lack of proper identification of inclusion origin (i.e. primary, secondary or pseudosecondary), lack of ice melting temperatures and in general, the small amount of measurements. The chemistry of the inclusions is also unknown. While I attempted to use Raman analysis on the inclusions to obtain the fluid chemistry, the size of the inclusions (around 1 micron) made it impossible to focus the laser on them. Only the spectrum of the hosting crystal was constantly obtained, not the fluid spectra. The fluid chemistry would help to unravel in more detail the fluid flow within the sequence, in addition to calibrating the homogenization temperatures and thus acquiring more accurate trapping temperature conditions. The fluid inclusion data is also limited by the lack of independent geothermometers that would help unraveling the true pressure conditions during veining. Moreover, attaining the P-T conditions is also limited by the existing fault between the shale sequences as faults and fluid pressures alter local stress directions and magnitudes, which in turn modify local P-T conditions. This makes it especially difficult to estimate pressures-temperatures during veining.

These limitations and the presented results can thus provide a base for further work. More thin sections of the various veins should be analyzed to gain an extensive view on the veining within the ILU. SEM, CL and EBSD for each section, in addition to further fluid inclusion measurements on other veins as well could shed more light on the transport mechanisms, veining processes and the P-T conditions during veining. Carbon and oxygen isotope analysis could also be carried out but sampling might be challenging in the very thin and undulating veins (e.g. bed-parallel and perpendicular set). In order to determine what controls the spacing in the layers, and the development of the bed-parallel veins along certain interfaces but not along other, sampling and analysis of the adjacent layers could be carried out focusing on the mineralogy and the mechanical parameters (e.g. elastic and tensile strength, porosity, interface strength).

Additional data could also be compared to those obtained from outcrops further inland but still within the ILU, or from the juxtaposed nappes (e.g. Tuscan nappe).

4.6 Conclusions

Field work was carried out in the Internal Ligurian Unit (ILU) of the Northern Apennines, Italy. Outcrops in the studied area represented the entire sequence from the ophiolite at the base to the Bocco Shale on top. Structural measurements (bedding, cleavage, fold axes) captured the complex evolution of the area that included polyphase deformation in an accretionary wedge. Two main folding directions, NW-SE and NE-SW, were found that created tight isoclinals folds in a variety of scales and alternating juxtaposition of normal and overturned sequences. Orientations of the large-scale structures, synclines and anticlines, showed rotation and were generally 90° to each other. Field observations, fold axes and crenulation cleavages indicated that the first folding had a direction of NW-SE, whereas the second main folding was in the direction of NE-SW. These orientations are in accordance with previous studies attributing the first folding to a E-SE-dipping, early subduction, and the second (main) folding to the accretion of the sequence towards the NE in a W-SW-dipping subduction zone.

Unfolding of conjugate veins along the second folding axes showed the rotation of the main horizontal stresses. Oldest conjugates formed during the deformation in the SE-dipping subduction zone. As the subduction polarity-flip occurred and the subduction zone migrated towards its current strike direction, NW-SE, the main horizontal stresses also rotated forming conjugates triggered by E-W, NE-SW and N-S compression. Tectonic stylolites found in the Val Lavagna Shale also reflect these compression directions. In addition to conjugates, several other vein types (e.g. bed-parallel and perpendicular, folding-related veins, blobs of mineralization) were observed in the Palombini and Val Lavagna Shale. As the veins intensity was increasing towards the Palombini-Val Lavagna boundary that is considered a fault-contact, I proposed that fluid flow along the fault was responsible for the veining. Microstructural evidence, however, also suggested that diffusion from the host rock and dissolution of the veins could have contributed locally to material transport. Vein patterns and their microstructures did not show signs for high fluid pressure involvement, which means that they are probably not hydrofractures but tectonic-triggered ones. Fluids could have still contributed to fracturing by facilitating bed-parallel failure. In addition to this, crack-seal textures were only found in a few conjugate veins but others generally lacked these textures indicating that existing veins did not refracture but the host rocks failed and new veins formed there.

Fluid inclusion microthermometry was carried out on the bed-parallel veins. Homogenization temperatures of the solid-vapor NaCl-H_20 inclusions peaked at 150-160°C with a few homogenizing at higher temperatures (up to 230°C). Assuming trapping temperatures between 230°C and 308°C, and considering a minimum depth of 3 km, bed-parallel veining took place at pressures between 80-317 MPa, but more likely in the 140-318 MPa range. These data and observations can provide a good basis for further analyses in order to better construct the tectonic and structural evolution, and the deformation history of the Internal Ligurian Unit in relation to the Northern Apennines.

5 Modeling hydrofracture and healing

This chapter aims to demonstrate the complex behavior of deforming, fluid-filled layered sequences. Simulations focus on the healing mechanism (vein formation) to establish the importance of veining on the deformation dynamics. All the simulations represent layered-systems extending in the horizontal direction with a strain rate of 10^{-14} s^{-1}, where the initially hydrostatic gradients are increasing at the base of the model in successive time steps. The model parameters for the first three experiments can be found in Table 6. Parameters for further simulations (veins' elastic and tensile constants, multilayered systems) are shown in the relevant chapters.

		Fig. 5.1	Fig. 5.2	Fig. 5.3	Fig. 5.4	Fig. 5.5
Matrix	E (GPa)	7.5	7.5	7.5	7.5	7.5
	σ_u (MPa)	20	20	20	20	20
	φ (%)	26.9	26.9	26.9	26.9	26.9
Layer	E (GPa)	60	60	2.25; 11.25; 33.75	60	30
	σ_u (MPa)	40	20	20	6; 40	20
	φ (%)	26.9	26.9	26.9	26.9	0.5; 10; 35
Healed bonds	E (GPa)	7.5	15	7.5	7.5	7.5
	σ_u (MPa)	20	20	20	20	20

Table 6 Real scale properties for simulations comparing healing and non-healing system (Fig. 5.1), showing fracture evolution (Fig. 5.2) and the effects of contrasting mechanical properties (Fig. 5.3 to Fig. 5.5).

E = elastic modulus, σ_u = breaking strength, φ = porosity. The default overall breaking strength is 20 MPa representing the central value of threshold.

I first introduce a simulation to compare the dynamics of a non-healing and a healing system. This is followed by an experiment illustrating the fracture evolution in a healing system, as well as the effects of the contrasting mechanical properties of layers. I then investigate how the veins elastic and tensile properties influence the system's behavior. Lastly I examine the fracture patterns in multi-layered systems, where the lowermost layers are seals to illustrate a sealed reservoir.

5.1 Comparison of a healing and a non-healing system

I present two simulations with and without healing, but with identical material properties. In both cases the deformation boxes contain a layer with an elastic modulus that is eight times and a breaking strength that is twice that of the matrix (Table 6). Veins in the healing system have the same tensile and elastic properties than the matrix.

In case healing is not applied (Fig. 5.1a, b, c) a considerable amount of open fractures can be seen that are directly linked to higher porosity values. The unfractured areas keep their background porosity values that are uniformly lower than those observed in the fractured areas. The major fracture that cuts through the entire system shows the highest porosities due to constant refracturing. When healing is not applied, the porosity increases almost linearly with progressive deformation from the initial 26.9% to almost 27.8% (Fig. 5.1c).

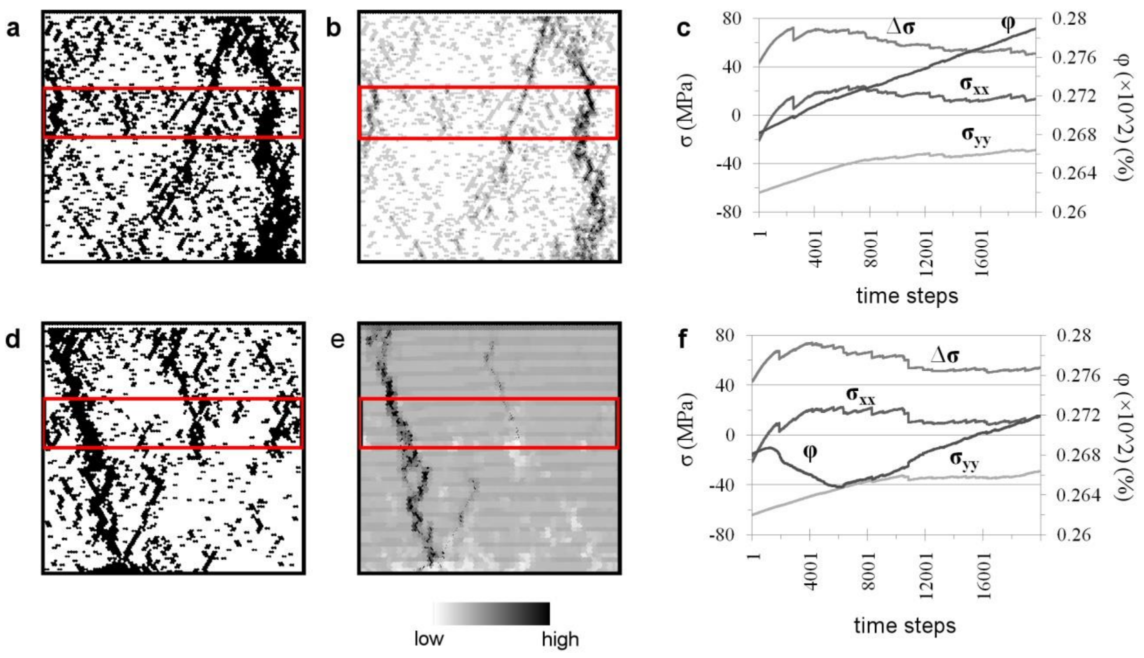

Fig. 5.1 A non-healing (a, b, c) and a healing (d, e, f) system with identical parameters showing open fractures (a, d), porosity (b, e), as well as the bulk stress and porosity evolution (c, f) throughout 20000 time steps.
$\Delta\sigma$ = differential stress, σ_{xx} = horizontal stress, σ_{yy} = vertical stress, φ = porosity. Color of the unfractured areas represents the background porosity (26.9%), whereas the other colors show relative porosities compared to the background. Red rectangle in the middle represents a stiff layer embedded in a soft matrix. Healed bonds have the same breaking strength and stiffness as the matrix. Healing has a major effect on the fracture patterns and lowers the porosity. The stress curves, however, are quite similar, whereas the porosity in the healing case first drops and only rises after 6000 time steps (~16.4 ka). Figure from Vass et al. (2014).

The effect of healing can be seen directly on the number of open fractures (Fig. 5.1d). Compared to the non-healing case less open fractures are present since the cracks are subjected to closure. The most apparent difference is that here the stiff layer and the matrix show fewer fractures away from the larger fracture zones. The overall pattern, however, is similar to that observed on Fig. 5.1a. Similarly to the non-healing case the developed thorough-going fracture is the most porous within the system, whereas the healed fractures (veins) represent areas of lowest porosities (Fig. 5.1e). This means that porosity in the system has both decreased and increased compared to the initial background values. The porosity evolution significantly differs from the non-healing simulation. The porosity first declines and only starts to rise after time step 6000 (~16.4 ka), which in turn results in overall porosity increase of the system (from 26.9% to 27.2%).

Both simulations show identical stress evolution (Fig. 5.1c and f). As deformation is applied stress builds up and reaches a maximum value after which the system relaxes due to major fracturing and only minor fluctuations (slip/fracturing along existing fractures and minor fracturing in matrix) can be observed. The horizontal stress (σ_{xx}) quickly moves from compressional to the tensional regime around time step 1000 (~2.8 ka) and experiences its highest magnitude during time steps 4000 – 6000 (~11 – 16.4 ka). The vertical stress (σ_{yy}) on the other hand stays in the compressional regime during the entire simulation. Both simulations show that after time step 12000 (~32.8 ka) the stresses relax and fluctuate around semi-constant values. In the healing system, however, there is a major drop in the σ_{xx} and in the differential stress ($\Delta\sigma$) around time step 10000 (~27.4 ka), which is not detected in the non-healing system.

5.2 Fracture evolution with healing

Evolution of open fractures in a healing system is shown in Fig. 5.2. In this simulation the layer’s elastic modulus is eight times that of the matrix, whereas its breaking strength is identical to the matrix. The healed bonds’ elastic moduli are twice to those in the matrix, whereas their breaking strengths are identical to them (Table 6).

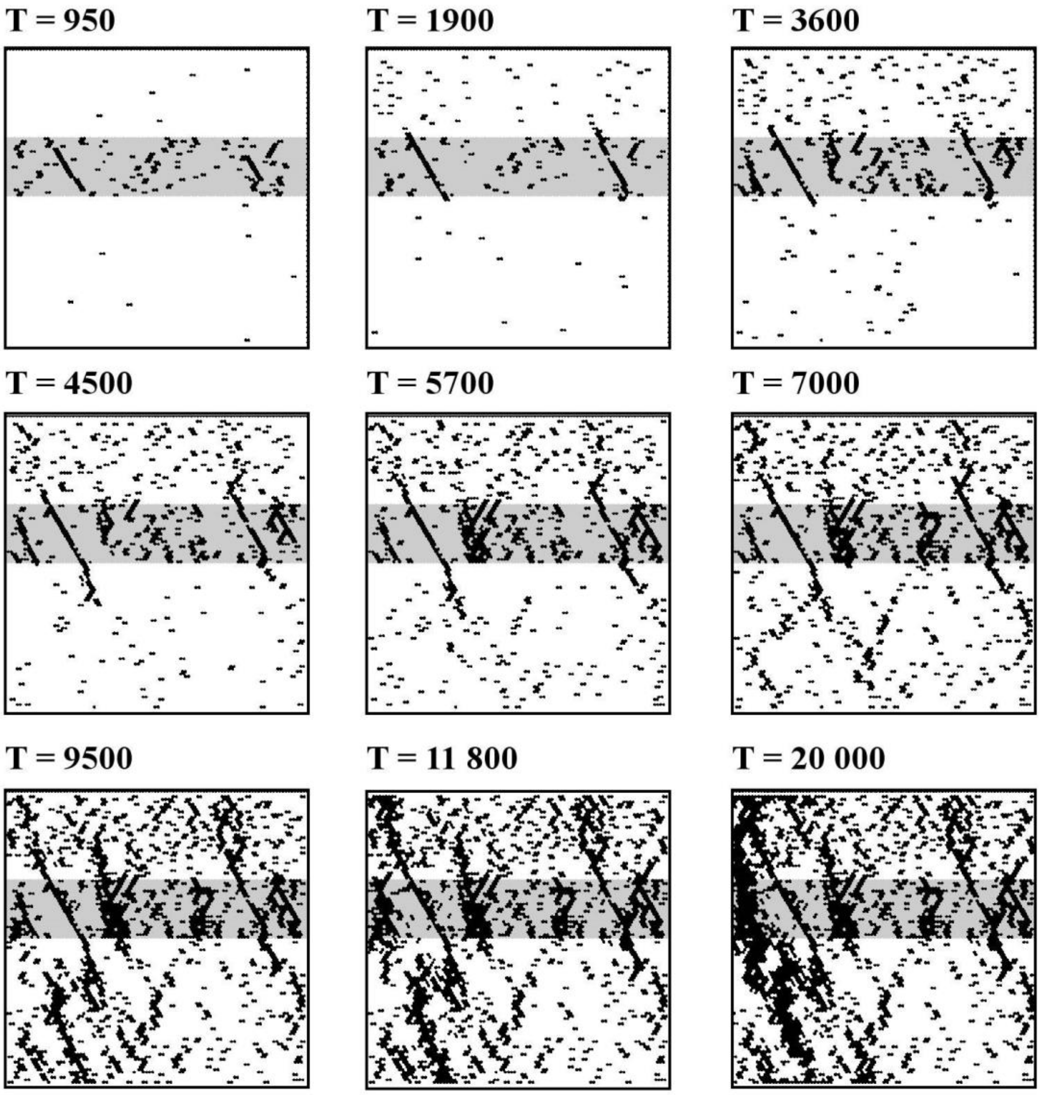

Fig. 5.2 Evolution of fractures (black segments) in a healing system throughout 20000 time steps (~54.8 ka).
T is the model time, whereas the shaded grey rectangle in the middle represents a stiff layer embedded in a softer matrix. Healed bonds have the same breaking strength and stiffness as the matrix. First fractures form in the layer and these propagate into the matrix by linking up smaller cracks. Towards the end of the simulation strain seems to be accommodated by existing fractures and only a limited amount of new fractures form. A through-going fault develops at the end providing connection between the lower and the upper end of the system. Figure from Vass et al. (2014).

Larger tensile stresses develop at lower strain in the layer due to its high stiffness, therefore it fractures first and only small amount of fracturing can be seen in the matrix. Fractures propagate by interconnections of smaller cracks. In the early stages fracturing is limited to the stiff layer, where the first bed-confined fractures propagate into the matrix at time step 1900 (~5.2 ka). Their propagation within the matrix is impeded due to the softness of the matrix until time step 5700 (~15.6ka), when deformation in the matrix becomes more significant. After this stage fracturing in the layer is subordinate, whereas fracture propagation in the matrix is becoming the dominant process. Except for the formation of the large fracture zone along the left boundary, fracturing is limited after time step 9500 (~26 ka) which indicates that the system is approaching a somewhat steady-state. The developing fracture pattern shows that fracture spacing is smaller in the competent layer than it is in the softer matrix.

5.3 Contrasting mechanical properties of a layered system

5.3.1 Effects of contrasting elastic moduli

Three simulations shown on Fig. 5.3 examine the influence of contrasting elastic moduli in layered systems. Horizontal layers with various stiffness are embedded in a matrix, where the Young's modulus of the layers 0.3, 1.5 and 4.5 (model scale). These correspond to layers with scaled elastic moduli of 2.25 GPa, 11.25 GPa and 33.75 GPa embedded in a matrix of 17 GPa stiffness (Table 6).

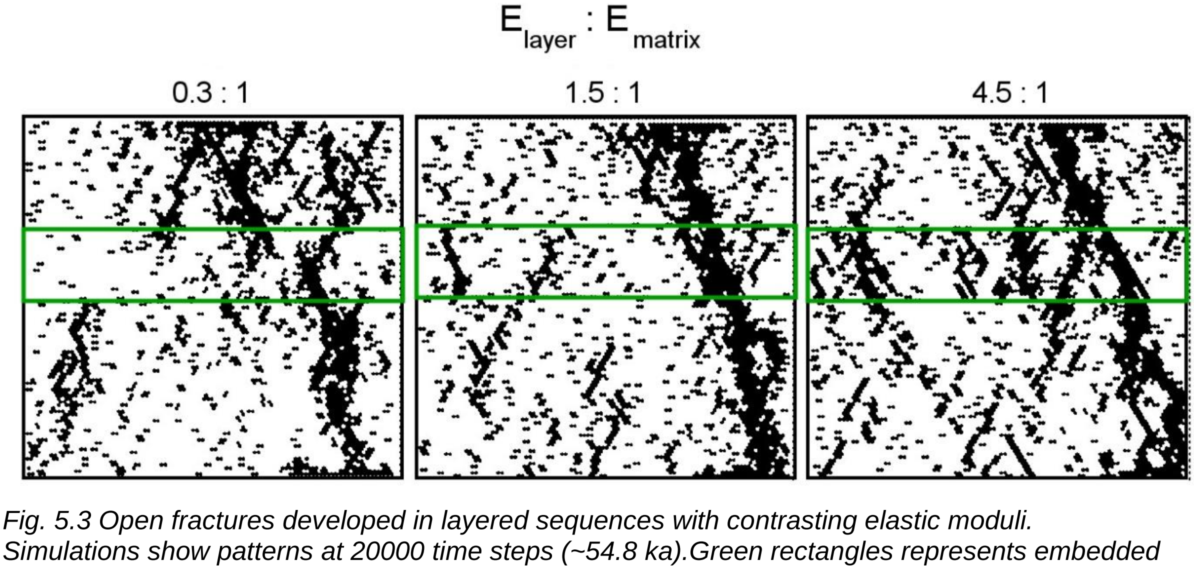

Fig. 5.3 Open fractures developed in layered sequences with contrasting elastic moduli. Simulations show patterns at 20000 time steps (~54.8 ka).Green rectangles represents embedded layers with various stiffnesses compared to the matrix. The ratio of layer's Young's to matrix's Young's range from 0.3 to 4.5, indicating a softer and stiffer layer embedded in the matrix.

The simulation with the soft layer shows that fracturing dominates the upper and lower part of system leaving the layer relatively intact (Fig. 5.3). The matrix adjacent to the layer is generally more fractured than the base of the model where stresses are the highest due to the fluid injection and the overburden. The layer fails as larger fracture zones above and below the layer link up. The final pattern exhibits tighter fracture spacing in the stiffer matrix than in the soft layer.

In case the layer is slightly stiffer than the matrix (layer to marix Young's ratio is 1.5), fracturing becomes more heterogeneous in the system. Fractures are well distributed and there is no clear dominance of preferred failure area. This results in a constant fracture spacing that characterizes the entire system.

As a stiffer layer is embedded, fracture patterns follow the same evolution as described on Fig. 5.2. During the initial stages the stiff layer dominates fracturing. Layer-confined fractures propagate into the softer matrix developing a through-going fracture and heterogeneous fracture spacing within the system, where spacing is larger in the soft matrix than it is in the stiff layer.

5.3.2 Effects of contrasting breaking strengths

Two simulations shown on Fig. 5.4 illustrate the effects of contrasting breaking strengths in layered sequences. They show stiff (60 GPa) layers with breaking strengths lower (6 MPa) and higher (40 MPa) than that of the matrix (Table 6). The stiffness together with the low breaking strength causes extreme fragmentation of the layer (Fig. 5.4a), which is coupled with intense healing within (Fig. 5.4c). On Fig. 5.4b the breaking strength counteracts the stiffness and impedes fracturing within the layer decreasing the spacing both in the layer and matrix. This results in less healing in the layer (Fig. 5.4d) leading to higher overall porosity compared to the simulation on Fig. 5.4a and c.

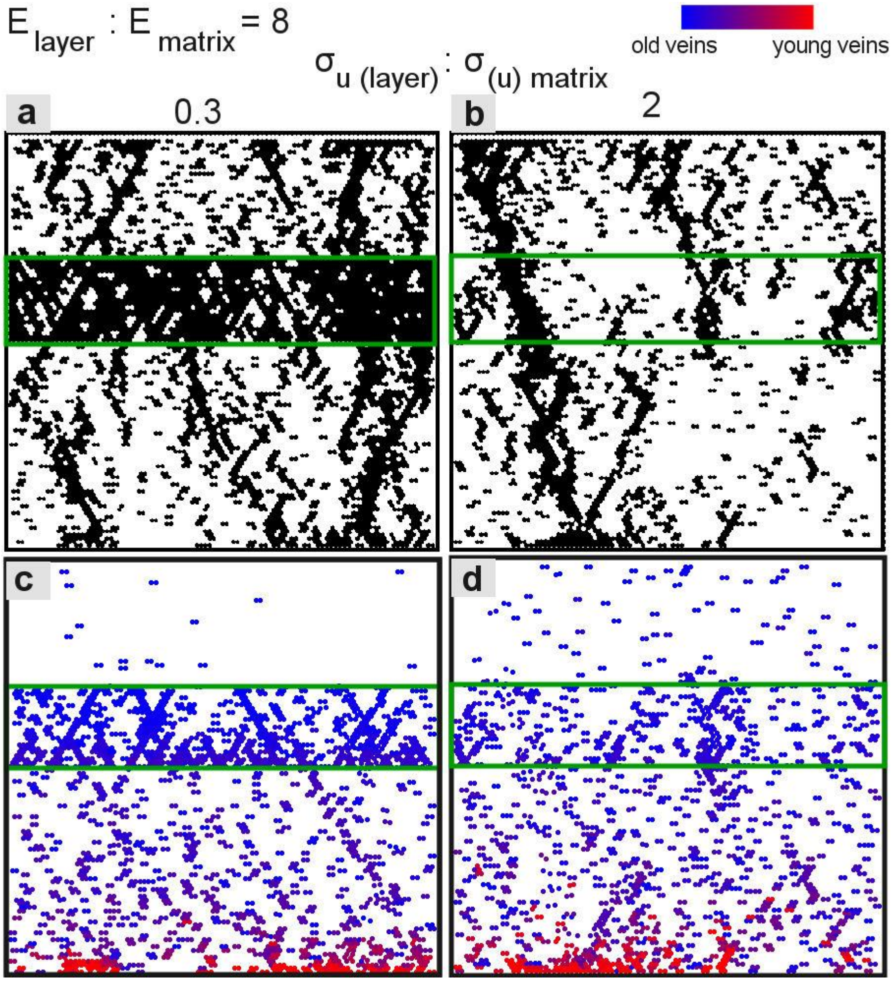

Fig. 5.4 Open fractures (a, b) and veins (c, d) developed in layered sequences with contrasting breaking strengths and elastic moduli.
Simulations show patterns at 20000 time steps (~54.8 ka).Green rectangles represents embedded layers with identical stiffnesses but with various breaking strengths compared to the matrix. The ratio of layer to matrix breaking strength (σ_u) is 0.3 (a, c) and 2 (b, d), indicating a weaker and stronger stiff layer embedded in the matrix. Color code indicates relative age of vein (healed bonds).

5.3.3 Effects of contrasting porosity

Previous simulations included layers with identical background porosity than that of the matrix (i.e. 26.9%). Fig. 5.5 illustrates three simulations where the stiff layer’s porosities are 0.5% (Fig. 5.5a), 10% (Fig. 5.5b) and 35% (Fig. 5.5c), representing lower and higher porosities than the background (and thus matrix). The layer is eight times stiffer than the matrix with identical breaking strength (Table 6). Fracture patterns in the three simulations are quite similar. The host rocks (matrix) show basically identical fragmentation, whereas fracture spacing in the layers demonstrates a minor decrease with increasing layer porosity. In all cases healing is applied but show uniform patterns, therefore cannot be accountable for the observed spacing variations.

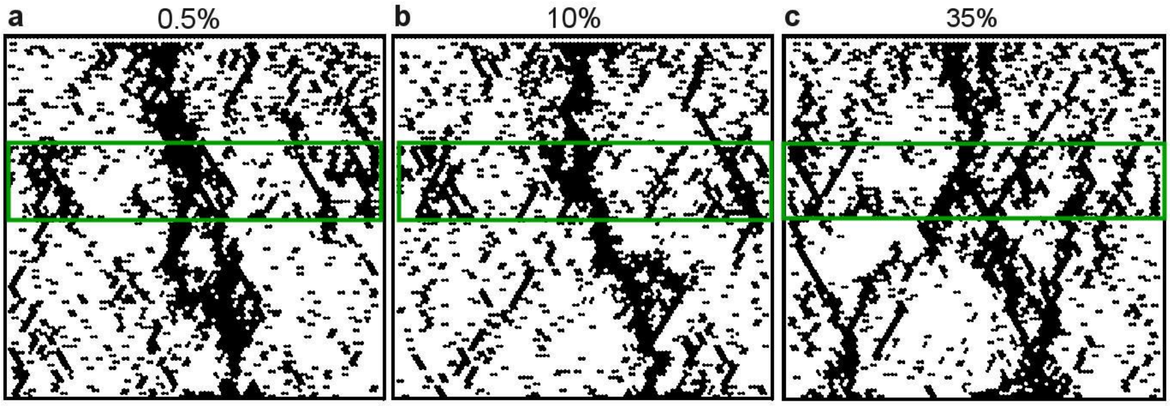

Fig. 5.5 Open fractures developed in layered systems with various porosities.
Simulations show patterns at 20000 time steps (~54.8 ka).Green rectangles represents layers with porosities of 0.5% (a), 10% (b) and 35% (c) embedded in a high-porosity (26.9%) matrix. Layers are eight times stiffer than the matrix.

5.4 Veins' mechanical properties on the system dynamics

Previous simulations represented healing systems where the veins' mechanical properties were identical to those in the matrix. In the followings, however, the systems heal with different tensile and elastic constants than those of the matrix. Table 7 lists the real scale parameters of the presented simulations.

		Fig. 5.6	Fig. 5.8
Matrix	E (GPa)	7.5	7.5
	σ_u (MPa)	20	20
	φ (%)	26.9	26.9
Layer	E (GPa)	60	60
	σ_u (MPa)	20	20
	φ (%)	26.9	26.9
Healed bonds	E (GPa)	7.5	2.25; 5.63; 17; 37.5; 75
	σ_u (MPa)	8; 20; 60; 200	20

Table 7 Real scale properties for simulation shown on Fig. 5.6 and Fig. 5.8.
E = elastic modulus, σ_u = breaking strength, φ = porosity. Default overall breaking strength is 20 MPa, which represents the central value of the threshold.

5.4.1 The effect of the veins' breaking strengths

The influence of breaking strength of the healed bonds was investigated by varying only this parameter in the same simulation setup (Table 7). Four cases are presented on Fig. 5.6; one where the breaking strength of the veins is two fifths of the matrix, one where it is the same, one where it is three and ten times the matrix. Fig. 5.6 shows the age of the open fractures (Fig. 5.6a) and the healed bonds (i.e. veins) (Fig. 5.6b), fractures that healed and refractured several times (i.e. crack-seal veins) (Fig. 5.6c) and the relative porosity within the solid matrix (Fig. 5.6d).

Breaking strengths of the healed bonds (veins) greatly influence the developing patterns and behavior of the system. The number of open fractures decreases with increasing vein strength (Fig. 5.6a). When the veins are three times stronger than the matrix there is a significant decrease in the number of open fractures compared to the default case (i.e. vein strength identical to that of the matrix). The lower part of the model shows intense healing which decreases the number open fractures. This effect is the most pronounced when the veins are ten times stronger than the matrix. Only one large fracture remains that cuts through the system, whereas other parts are basically unfragmented. Fractures that are open also differ with regard to their formation age. When the healed bonds are the weakest many older fractures (i.e. those that formed at earlier timesteps) are still open, whereas most of these are closed when the veins are strong. In all four cases the formation of new fractures is localized along the through-going fractures (faults) that develop at the end of the simulations.

The healing patterns reflect a dramatic change from a moderately healed system with weak veins to a system which is basically clogged up due to the strong veins (Fig. 5.6b). When the new bonds are weaker, the oldest veins appear mainly above and in the layer and subordinately in the matrix. Veins are progressively getting younger towards the bottom. When the new bonds are the strongest (ten times the matrix) the older veins still appear mainly in the layer but as the entire system is constantly healing it is difficult to observe any preferred locations of the younger veins. The youngest veins, however, seem to be associated with the fault.

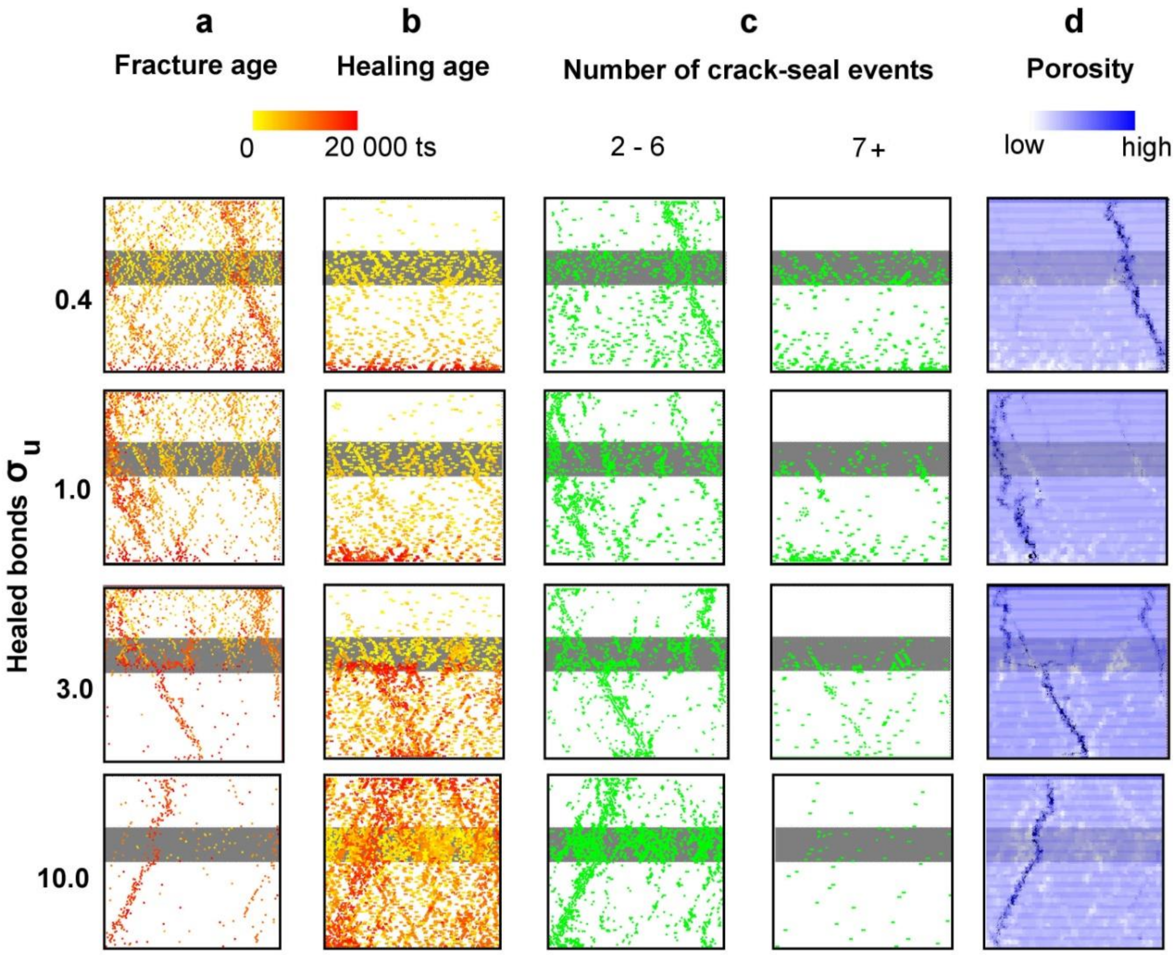

Fig. 5.6 Four simulations with varying vein strengths showing open (a) and healed (b) fractures, number of crack seal events (c) and relative porosities within the systems (d).
Breaking strengths (σ_u) of the healed bonds are two fifths of the matrix (0.4), identical to the matrix (1.0), three times (3.0) or ten times (10.0) the matrix. Shaded grey rectangle represents a stiff layer embedded in a softer matrix. Age of the fracturing and healing is also shown. Simulations show patterns after 20000 time steps (~54.8 ka).

Vein strength also influences the number of crack-seal cycles by determining the refracturing and healing localization (Fig. 5.6c). When the veins are weaker than the matrix, they tend to fracture easily. This is reflected in the similarity of the healing and the crack-seal (7<) pattern, which implies that after the bonds heal they will constantly fail and heal again. Localities that experienced less crack-seal events (2-6) coincide mainly with the younger open fractures. Slightly different behavior can be seen when the veins have the same strength as the matrix. Fewer veins undergo more than seven crack-seal events, whereas most of the veins and fractures only experiences limited crack-sealing (2-6 events). The number of crack-seal cycles decreases further when the veins are three times stronger than the matrix. Fewer veins fracture and close, i.e. the frequency of crack-seal events is decreasing compared to the previous simulations. The majority of the veins only fracture and heal a few times. This behavior is further enhanced in the strongest case. When the breaking strength of the veins is ten times that of the matrix, most of the box only fractures and heals once (see the older veins in the background in Fig. 5.6b). As healing now makes the entire system progressively stronger initiation of new fractures is impeded. Even if veins refracture, the refracturing itself seems to be restricted to the layer and to a few bigger fracture zones. Only a limited amount of locations experience more than seven crack-seal events. Increasing vein strengths therefore make the veins and the entire systems less prone to refracturing.

Relative porosities in all four cases seem to have the same characteristics (Fig. 5.6d). Large through-going faults are associated with the highest porosities, whereas healed fractures decrease the local porosities.

Fig. 5.7 shows stress and porosity curves related to the presented four simulations. They clearly illustrate how the behavior of the systems changes with increasing vein hardness. In the first case when the veins are weaker than the matrix's strength the vertical stress component (σ_{yy}) linearly increases until time step 9000 (~24.6 ka) after which the increase is less intense and the σ_{yy} fluctuates around a mean value. In the early stages of deformation the slope of the horizontal stress component (σ_{xx}) is steeper than that of σ_{yy} but it progressively flattens out as smaller shear fractures form. A major stress drop at time step 9000 (~24.6 ka) marks a sudden failure of the system which relaxes stresses afterwards. The porosity (φ) shows a sudden drop to the value of 26.45% at the beginning of the simulation which is then followed by a porosity-increase towards the end of the simulation reaching a value of 27.2%. The point where the porosity begins to rise coincides with the maximum differential stress ($\Delta\sigma$). Stress and porosity evolution is quite similar when the veins are the same strength as the matrix. The only difference is that the porosity reaches its minimum at 26.6% and its maximum at 27.4%. However, when the veins are three times stronger than the matrix stress and porosity curves reveal a change in behavior. The horizontal stress component reaches slightly higher values than previously, so does the vertical stress component (σ_{yy}) that increases until time step 16000 (~43.7 ka) after which it fluctuates around a semi-constant value. The σ_{yy} therefore shows an increase until a later stage than previously observed.

The porosity reaches its minimum 26.2% at time step 12000 (~32.8 ka), which marks a major stress drop after which the porosity increases to its final value of 26.5%. This shows that while porosity increase characterized the second half of the simulation, the overall porosity at the end was still lower than the initial porosity, i.e. the system became less porous.

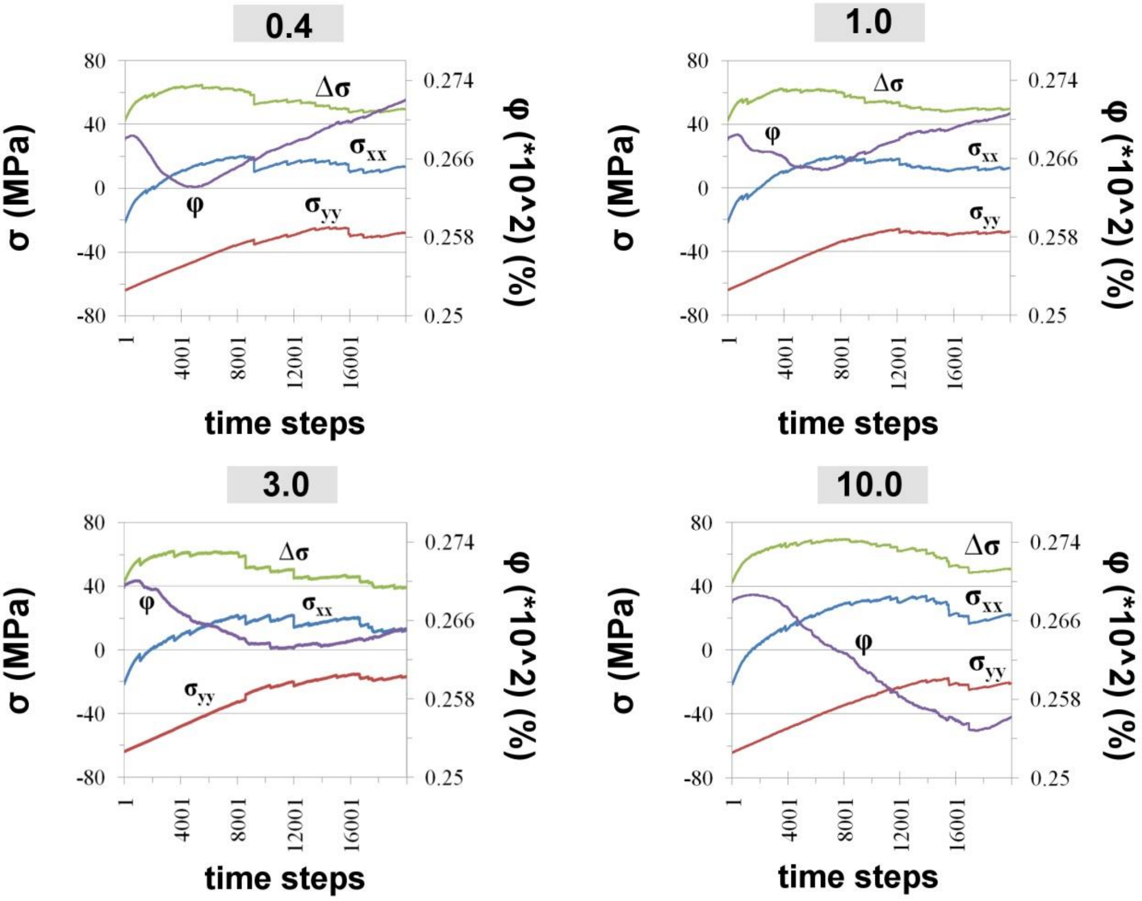

Fig. 5.7 Stress and porosity evolutions during simulations with increasing vein strengths.
The four simulations represent the ones on Fig. 5.6, where the vein strengths are two fifths of the matrix (0.4), identical to the matrix (1.0), three (3.0) or ten times (10.0) the matrix. $\Delta\sigma$ = differential stress, σ_{xx} = horizontal stress, σ_{yy} = vertical stress, φ = porosity.

When the veins are the strongest the horizontal (σ_{xx}) and vertical stress (σ_{yy}) are much higher than they were in the weaker cases. As the system is becoming successively stronger during healing, elevated stresses are expected. Stress curves suggest that the stress build-up is prolonged and the quasi steady-state, when the stresses show only minor fluctuations, is reached at a later stage of the deformation. Similarly to the weaker cases the system experiences its maximum Δσ at earlier stages (around time step 7000(~19.1 ka)) but the porosity continuously decreases until time step 17000 (~46.5 ka) reaching its minimum at 25.5%, after which a small increase results in a porosity of 25.6% at the end of the simulation. A system with strong veins can therefore be characterized with delayed behavior, higher stresses and major porosity decrease.

5.4.2 The effect of the veins’ elastic moduli

After investigating how the vein strength influences the deformation of a system, I focus on the effects of the varying elastic moduli on the system behavior. Five simulations were performed where the breaking strength of the veins were identical to the matrix, whereas their Young’s modulus varied between a third to ten times that of the matrix (Table 7). Fig. 5.8 shows the influence of the stiffening veins on the fracture and healing patterns of the systems. The stiffer the veins the more open fractures are present. These fracture patterns are coupled with healing patterns as the increasing number of open fractures reflects a decrease in healing in the system. Intense healing can be observed in the lower part of the model when the veins are the softest resulting in a more intact matrix (Fig. 5.8a). In addition to the matrix, the stiff layer that develops the first fractures heals with soft veins. These veins do not refracture due to their low stiffness, which directly influences fracture spacing within the layer. The layer exhibits the largest fracture spacing in this simulation. When the model heals with stiffer veins (Fig. 5.8d and e) healing is impeded resulting in a fractured system with tight fracture spacing.

Fig. 5.9 illustrates the stress and porosity evolutions for the two end-member cases corresponding to the patterns on Fig. 5.8a and Fig. 5.8e. Stress magnitudes and evolutions are identical in spite of the pattern differences. Porosities, on the other hand, show that the values start to increase much earlier (around 5000 time steps (~13.6 ka)) in the stiff case than in the soft one, and surpass the initial porosity reaching an overall higher value of 27.3%. The overall porosity of the system decreases to 26.8% in the soft case.

The elastic moduli of the veins thus do not seem to have as great an affect as the breaking strengths on the deformation of the system.

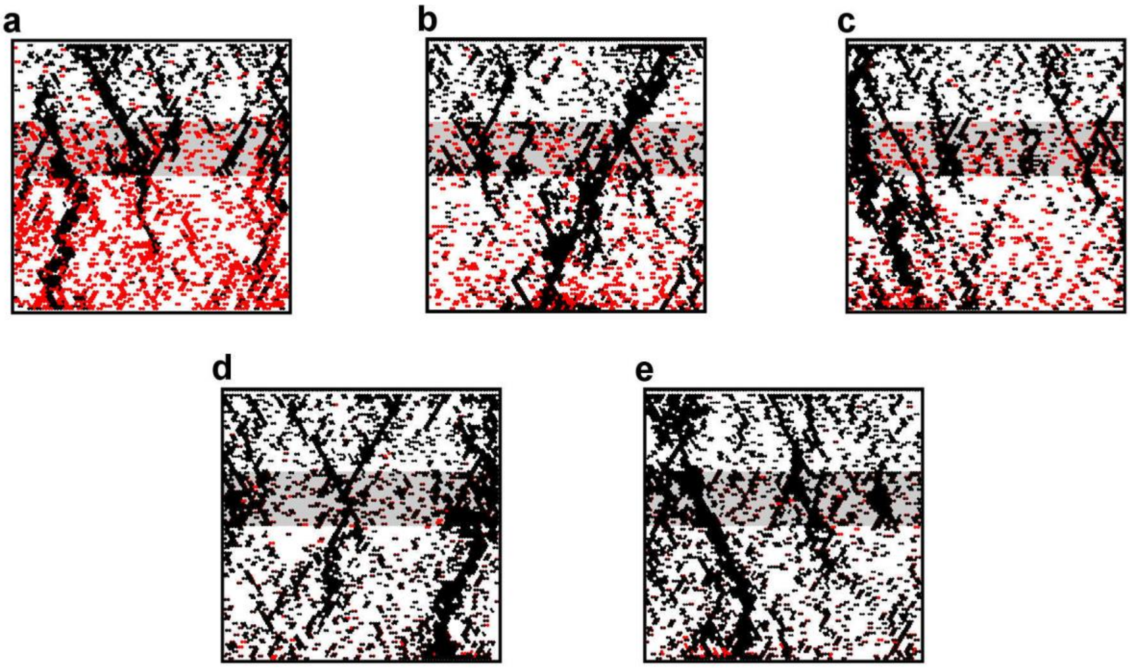

Fig. 5.8 Open fractures (black) and healed bonds (red) in healing systems with various vein stiffnesses.
Ratio of veins' elastic moduli over the matrix one is 1/3 (a), 3/4 (b), 1 (same as the matrix) (c), 5 (d) and 10 (e). Shaded grey rectangle represents a stiff layer embedded in a softer matrix. All simulations show patterns after 20000 time steps (~54.8 ka).

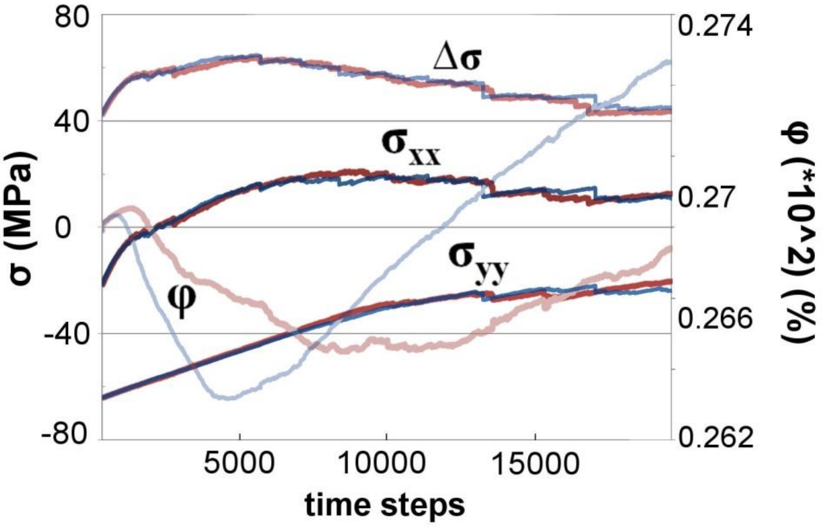

Fig. 5.9 Stress and porosity evolutions of healing systems with soft and stiff veins.
Red shades represent the simulation where the ratio of veins' elastic moduli over the matrix one is 1/3 (see Fig. 5.8a), whereas the blue shades represent the simulation where the ratio is 10 (see Fig. 5.8e). $\Delta\sigma$ = differential stress, σ_{xx} = horizontal stress, σ_{yy} = vertical stress, φ = porosity.

5.5 Multilayered system with a seal

Multilayered seal reservoirs are quite common in nature. High-porosity sequences can be compartmentalized (sealed off) due to embedded low-permeability layers (Jolley et al., 2010). In the following simulations seals are added in order to mimic sealed multilayer systems and to study the interplay between fluid pressures and deformation. Fluid, just like in the previous simulations, is injected along the lower boundary but this time the lowermost seal restricts upward fluid flow, which builds up fluid pressure gradients at the bottom of the model. Four layers are introduced at regular intervals in the following simulations out of which the lowermost is a seal with 0.51% porosity (Table 8). Other layers have a background porosity of 26.9%, representing sequences of high-permeabilities.

		Fig. 5.10a	Fig. 5.10b
Matrix	E (GPa)	7.5	7.5
	σ_u (MPa)	20	20
	φ (%)	26.9	26.9
Bottom layer	E (GPa)	60	2.25
	σ_u (MPa)	20	20
	φ (%)	0.51	0.51
Other layers	E (GPa)	60	60
	σ_u (MPa)	20	20
	φ (%)	26.9	26.9
Healed bonds	E (GPa)	7.5	7.5
	σ_u (MPa)	20	20

Table 8 Real scale properties for simulations on multilayered systems with seals.
E = elastic modulus, σ_u = breaking strength, φ = porosity. Default overall breaking strength is 20 MPa, which represents the central value of the threshold.

Fig. 5.10a illustrates a simulation where all the layers (gray rectangles) are eight times stiffer than the matrix (white rectangles). The competent seal at the bottom of the model does not seem to have a great affect on the fracture patterns. Fracturing appears to be quite uniform in the system where the stiff layers break first and develop closely-spaced fractures. The beds interact with each other by connecting these closely-spaced layer-confined fractures. These then evolve to large through-going faults that not only localize crack-sealing, but also provide direct communication between the lower and upper part of the system.

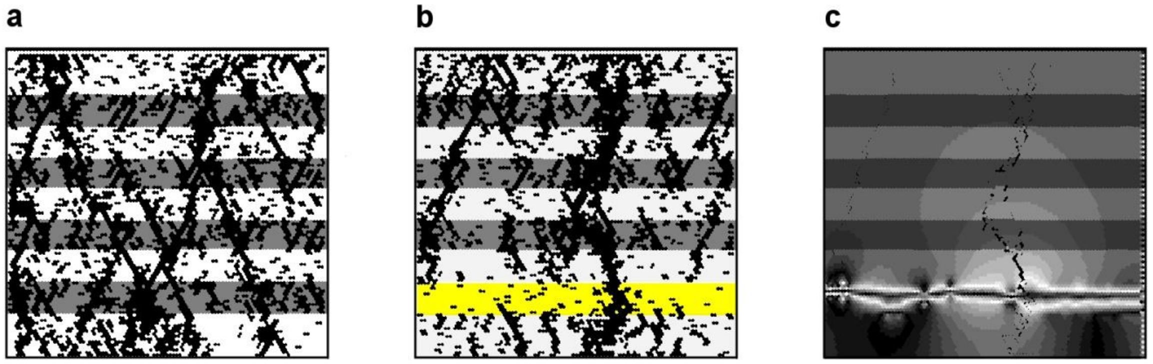

Fig. 5.10 Multilayered systems with seals showing fracture patterns (a, b) and fluid pressures (c). Patterns represent 20000 time steps (~54.6 ka), whereas the dark grey shaded rectangles are stiff layers and the yellow one is a soft layer. The lowermost layers (just above the bottom one) are seals with porosities of 0.51%. Other layers have a background porosity of 26.9%. Fluid pressures in the simulation (b) are illustrated as fringes on (c). Figure modified after Vass et al. (2014).

The same simulation was performed with a soft seal in order to inhibit seal failure and thus stimulate fluid pressure build-up below the seal. This scenario does seem to have a greater effect on the developing patterns (Fig. 5.10b). The seal in this case acts like a stress barrier that hampers fluid pressure gradients to transfer through the seal, thus inhibiting fracture initiation. As a result the soft seal remains more intact. This stress barrier directly affects the soft matrix and the competent layer above which develop less fractures compared to the previous scenario shown on Fig. 5.10a. Fracture patterns and spacing in the upper part of the model is similar to those on Fig. 5.10a. Failure below the seal is also similar. At the end of the simulation a large, through-going fracture (or fault) develops that links the upper layers with the bottom of the model allowing fluid pressures to decrease. This results in seal-failure and drainage of the system. This is shown on Fig. 5.10c, where fluid pressures are displayed as a grey-scale map. Closely-spaced isobars creating apparent fringes correspond to areas with high fluid pressure gradients. The seal experiences the largest fluid pressure gradients. Fringes along the through-going fault indicate drainage due to the upward flow of fluids.

5.6 Discussion

The presented simulations have shown that regardless of the vein properties healing decreases the local porosity and mainly affects the small scattered fractures. This is a result of the implemented healing as currently the healing probability is a function of the distance between particles, which causes smaller cracks to heal faster. As a result smaller fractures tend close, whereas larger fracture zones reopen as the deformation progresses and localizes along these larger structures. This explains the fewer fractures in the layer and in the matrix when healing is applied compared to the non-healing system (Fig. 5.1a and d).

The porosity evolutions in all simulations with healing exhibit an initial decrease followed by an increase towards the end of the simulations. The porosity drop at onset of deformation can be explained by the fast healing of smaller cracks that are more dominant than the extension in the system. Healing therefore works against the extension in the horizontal direction. This is why the non-healing system has an approximate linear porosity increase (Fig. 5.1c). Once deformation localizes along larger fractures it opposes the fracture closure in a healing system, elevating the overall porosity linearly as the function of the extension.

The fracture patterns are also strongly influenced by the heterogeneous stress field created by the gravity, the tectonic stretching and the fluid pressure gradients. This is consistent with the findings of Ghani et al. (2013), who also pointed out that unless the fractures are formed exclusively by fluid pressure gradients, they will not look fundamentally different to the tectonic ones. Consequently a range of different fracture sets can develop due to the interplay between the applied driving forces. The results show that the developing fractures are a combination of mode I and mode II shear fractures, which were also observed by Ghani et al. (2013). The triangular lattice that represents the solid framework also influence (and to some extent limit) fracture orientations but as the simulations mimic extension with overburden stress, mode I and mode II fractures would be expected in such setting any way.

The deformation is strongly controlled by the layer as its fragmentation defines propagation and localization of faults. Fractures in the model saturate in accordance with the fracture saturation mechanism described in previous studies (Bai et al., 2000; Bai and Pollard, 2000a; Becker and Gross, 1996; Gross and Eyal, 2007). According to Tang et al. (2008), saturation is reached either by fracture formation, strain accommodation or stress shadows. Saturation in the model can be examined throughout the stress evolution. As seen on Fig. 5.1c and f the differential stresses that are responsible for failure are decreasing in the early stages of simulations due to fracturing within the systems. Fractures saturate via strain localization along developing larger fractures that open, whereas other parts of the models do not develop fractures any more. This process is accompanied by quasi steady-state stresses where stresses remain constant with only minor fluctuations.

Fracture saturation within the model takes place in two stages corresponding to saturation on different scales. Fig. 5.2 shows how the layer-confined fractures start to propagate into the matrix only after fracture initiation in the bed becomes subordinate or even ceases. This first stage could correspond to the described saturation of the layer on a local scale. With progressive deformation the entire system also reaches saturation (second stage of saturation on a larger scale), which is characterized by steady-state stresses with additional strain being accommodated by the opening or slip along pre-existing fractures (Koehn et al., 2005). This saturation is also reached, only at later stages, when the system heals. It has been previously argued that if the cataclasite in a fault heals and gains certain strength, it might fail catastrophically at high stresses (Koehn et al., 2005; Scholz, 2002). The presented simulations, however, do not support this concept. This can be either due to the fact that in the model high fluid pressures gradients are constantly applied and are keeping the evolving faults open through which draining of the system is possible. As opposed to this, in nature a possible scenario could be that after the fault heals the fluid source that produced the high pressure gradients exhausts and stresses relax so that there is no major deformation. However, if there is a sudden increase in stresses for instance either due to an earthquake or high-pressure fluid (e.g. seismic pumping), the healed fault could indeed fail catastrophically (Hacker, 1997; Sibson et al., 1975). In addition to this, pace of the healing also affects the stress build-up and failure. In a system where healing is slow stresses can dissipate over a long spatial and time-scales leaving the fault relaxed. If, however, the system heals very fast sealing the fault instantly, large stresses can build up failing the fault. This effect can be more profound when the veins are extremely strong, as was illustrated on Fig. 5.6b, since larger stresses are needed to reactivate the fault which can lead to catastrophic failure.

Elastic modulus has long been considered as an important factor in fracture evolution (Simonson et al., 1978), whereas others argue that its importance in strata-bound systems is overrated (McDermott et al., 2013; Smith et al., 2001). The simulations show that the elastic modulus of the veins does influence the fracture patterns, fracture spacing, as well as the porosities of the systems. The stiffer the veins, the more fractures are open (Fig. 5.8). This is expected as stiff veins develop higher stresses and thus fracture more easily, whereas the soft veins need larger strains to refracture. This ultimately means that the stiffer veins undergo more crack-seal events than the soft ones, and therefore might provide more efficient paths for fluid flow. Layers with increasing elastic modulus, just like with decreasing breaking strength, decrease fracture spacing and thus influence fragmentation of the system (Fig. 5.2, Fig. 5.3, Fig. 5.4). The elastic constant, however, seems to play a more important role in combination with other mechanical properties. Together with the veins' strength it produces strong localization of crack-seal events in the layer when the veins are ten times stronger than the matrix. In the multilayered system, on the other hand, the seal's effectiveness is influenced by the elastic modulus. The stiff seal fails during deformation decreasing pressure gradients and contributing to flow channelization across the seal (Fig. 5.10a). The soft seal, on the other hand, suppresses fracturing within and thus behaves as a stress barrier that controls the fracture evolution and the fluid flow (Fig. 5.10b). Fig. 5.5 and Fig. 5.11 also illustrates that a stiff seal embedded in a soft matrix does not affect fracture patterns, only spacing. These combined effects of different mechanical parameters in fact demonstrate how one cannot single out properties or at least how one should be cautious when it comes to understanding the behavior of a system.

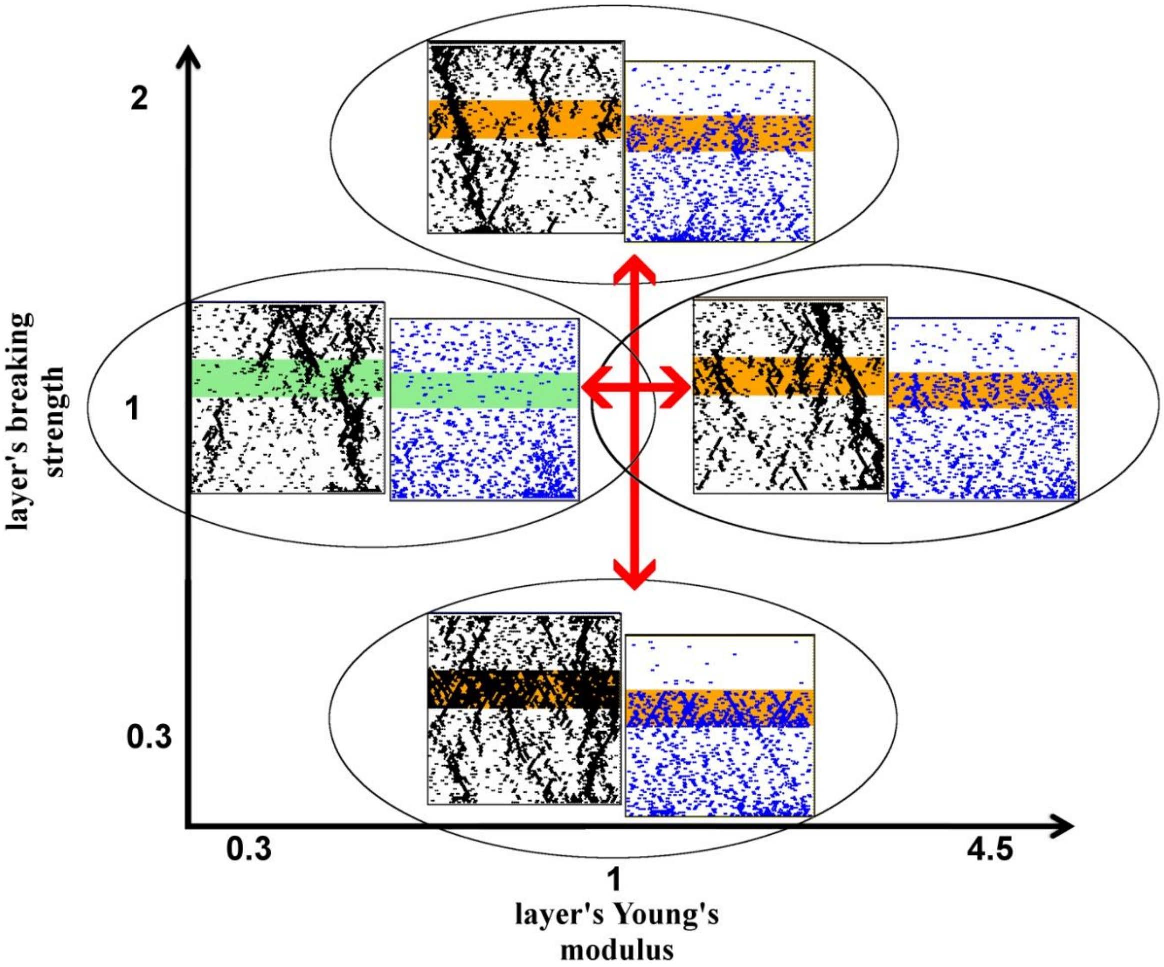

Fig. 5.11 Summary picture showing how the fracture (black) and vein (blue) patterns change with variable contrasting mechanical properties of the embedded layer.
Shaded orange rectangle is a stiff layer, whereas the green rectangle is a softer layer compared to the matrix.

The breaking strength of the veins has a greater influence on the evolving patterns and stresses than the elastic modulus does (Fig. 5.6, Fig. 5.7, Fig. 5.12). The veins breaking strength depends on the different mineral assemblages within. Calcite, especially combined with other soft minerals such as gypsum, makes the veins weak in a strong host rock (e.g. sandstone). Quartz or ore minerals could particularly strengthen the veins in a mudstone host rock, whereas very high breaking strengths could correspond to ore bodies. The simulations have shown that systems hosting stronger veins than their matrix undergo less crack-seal cycles since progressive deformation makes the system stronger. Since higher stresses are required to break strong veins, fractures form and propagate in the unfractured domains. The system eventually becomes too strong to refracture resulting in a significant porosity decrease, which would limit fluid flow. However, as strains localize opening larger fracture zones the porosity starts to increase, promoting fluid flow through the system. Strong veins elevate stresses that are sustained for longer periods causing a delay in model saturation compared to the weaker scenarios. Healing with various mechanical properties and deformation thus have a competing effect on the system dynamics, and determines the temporal and spatial permeability as well.

The shown simulations correspond to approximately 54.8 ka meaning that the results assume a constant deformation path throughout this period, which might not be the case. It is therefore worth to note that an interruption in the deformation and re-application of previously occurred stresses might produce different geometries (Mahrer, 1999).

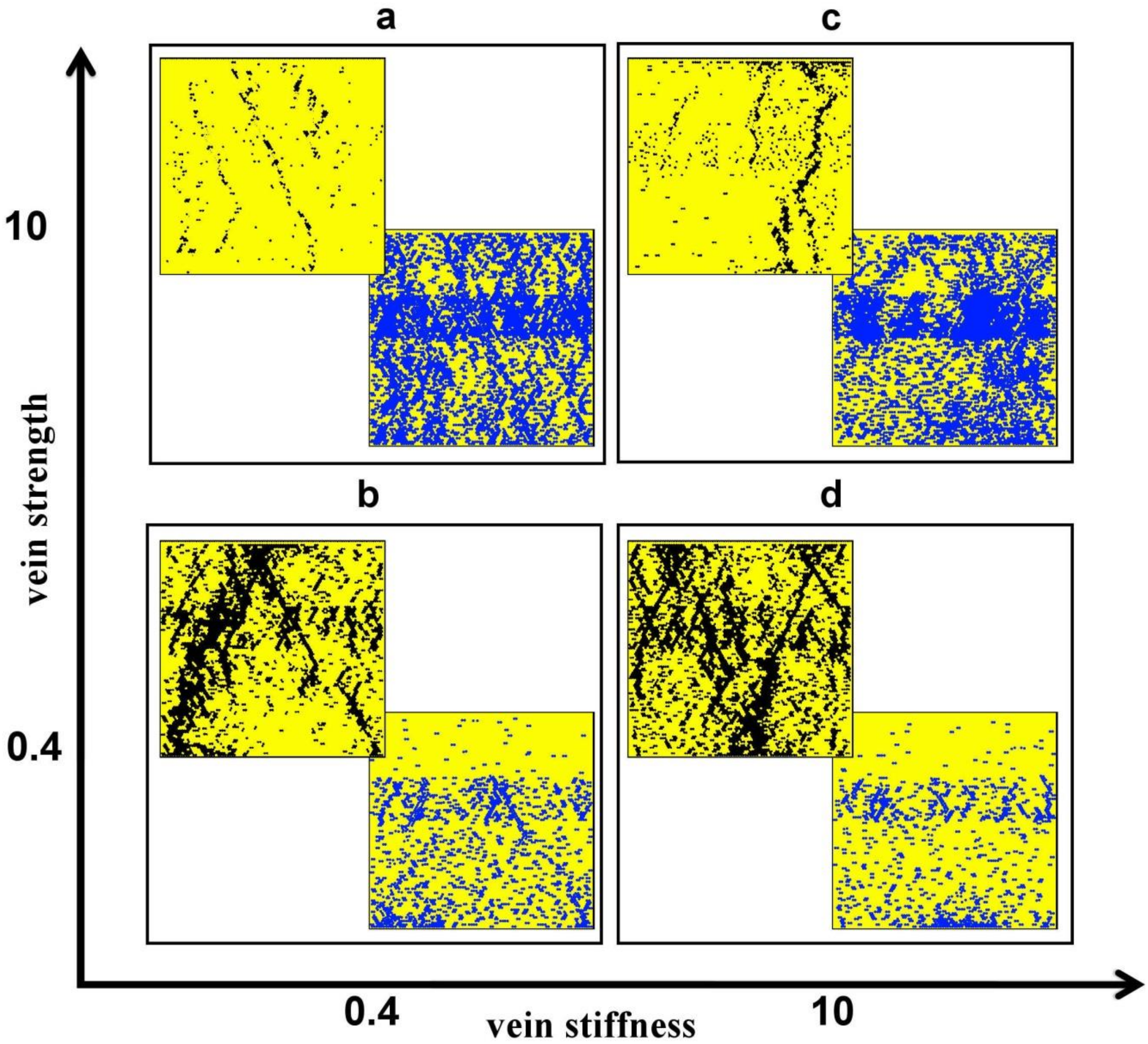

Fig. 5.12 Summary figure comparing the effects of variable elastic and tensile constants on the fracture (black) and vein patterns (blue).
0.4 and 10 represent the vein to layer constant ratio. Simulations show systems with relative (a) strong and soft, (b) weak and soft, (c) stiff and strong and (d) stiff and weak veins. Figure modified after Vass et al. (2014).

The presented model has a few limitations that might alter the outcomes of the study. First of all, there are a few issues with the porosity that must be mentioned. First of all, on all porosity figures a background artifact layering can be seen. This layering is produced by the triangular lattice, does not affect the porosity values in the system and is a plotting problem that needs to be addressed in our further work. Second of all, on numerous occasions one can observe that the open fractures do not necessarily correspond to higher porosities which they should (Fig. 5.1 or Fig. 5.6). The reason for this is that the background porosity is currently too high (26.9%) and basically the relative (the very surrounding) porosity is plotted. Places that experience intense healing thus might indicate lower porosities even if there is a fracture going through it. Although the accuracy of the porosity plot could be somewhat questioned because of this artifact, it still reflects the true porosity differences within the system and thus should not be neglected.

There is much room for improvement regarding the mass balance of the model. While there is some mass added during healing the model does not include transport mechanisms (e.g. fluid flow, diffusion) and dissolution processes which play crucial part in the mass balance of the system. This means that while these processes actually remove and redistribute masses within the rock systems, currently the Elle model does not incorporate these. The results therefore do not represent accurately natural systems but still give valuable information on the pure dynamics.

Another limitation of the presented model is that during these simulations only normal forces were considered, which means that the system can only fail via mode I, tensional fracturing. Recent changes to the model now make it possible to fail via shearing but the simulations within this thesis do no present these results. With the additional shearing, however, the fracture patterns seem much more realistic.

Anisotropy is not modeled specifically either. Heterogeneity is produced by the normal distribution of model parameters, but anisotropy is only achieved when healing is applied. As discussed in chapter 3.2 the healing cycle introduces new bonds that are generally longer. These longer bonds essentially create anisotropy. This also means that the more the system heals, the more anisotropic it is. Experiments with different healing extent (e.g. the weak and strong vein simulations in chapter 5.4.1) therefore exhibit anisotropy differences as well, which could contribute to the various fracture and vein patterns. Anisotropy does play a major role in the developing patterns as it can modify the effective stress direction and magnitude (Chen and Nur, 1992; Healy, 2009; Olson et al., 2009).

All these limitations therefore show that there is room for improvement. Introducing transport and dissolution mechanisms for a correct mass balance, anisotropy, along with shear failure would greatly enhance the model. At that point re-running the presented simulations would be necessary to see how those processes influence the system dynamics and the developing fracture and vein patterns.

5.7 Conclusions

The presented numerical model incorporated the intimate coupling of the elastic framework (solid) with the pore-pressure evolution. This setup allows a dynamic, porosity-controlled deformation. Deformation is applied by introducing gravity, tectonic stretching and high fluid pressure gradients in the system. The model fractures and heals with mechanical parameters that can be different to those of the unbroken bonds. The model was tested through several simulation where varying the mechanical properties of the system allowed to investigate the evolving patterns as well as the stress and porosity evolution. The results showed that at the early stages of deformation the porosity falls and it only increases after the maximum differential stress is obtained. Examining the influence of the healing properties revealed that the breaking strength of the healed bonds (veins) has a major influence on the behavior of the system. The stronger the vein, the (1) less it fractures (i.e. fewer crack-seal cycles and open fractures), (2) the greater the stresses and (3) the more limited the possible fluid flow. Strong veins can correspond to ore or even quartz-filled veins in a weak host rock, such as mudstone. A calcite vein would represent a typically weak vein in a strong host (e.g. sandstone). The veins elastic modulus, on the other hand, only plays a minor role in fracture patterns, does not affect the stress states significantly and is only important in combination with other mechanical parameters. In spite of the healing, the system in all cases reaches a somewhat steady state (saturation) by accommodating additional strain along pre-existing fractures. Small-scale fractures link up to form larger fractures which eventually evolve to through-going faults that drain the system. Moreover, it has been shown that in a multilayered structure seals only act as stress barriers if they are soft (low elastic modulus) and lie close to the fluid source that provides the high pressure gradients. The results provide a good basis for understanding large spatial and temporal scale fracturing and healing of a system characterized by the interplay between tectonic stresses and pressure gradients.

6 Characterizing fracture networks using graph theory

This chapter aims to demonstrate that graph theory can be successfully applied to characterize geological fracture network evolution. First I will analyze mudcracks, then I will move onto the flour experiments. Lastly, one hydrobreccia fracture network will be presented.

The following measures will be analyzed on each graph: probability density function of vertex degree distribution, entropy of vertex degree distribution, number of vertices and edges, graph density, global efficiency, mean and global clustering coefficients and graph assortativity. As explained in Chapter 2.3, vertices are junctions and dead ends that are joined by edges in a graph. The degree of a vertex (*k*) equals the number of edges that emerge from the vertex. The probability density function of **vertex degree distribution** shows the probability that a randomly chosen vertex in the graph has a degree of *k*.

The **entropy of vertex degree distribution** is directly related to this measure as it shows the disorder in the graph. If the entropy is low then there is a dominating vertex degree characterizing the graph, i.e. the probability for a certain degree is higher than 50%. High entropy, on the other hand, represents disorder in the system since the probabilities for various vertex degrees are close to equal.

The number of vertices and edges will also be presented, along with the **graph density** that corresponds to the graph completeness. The higher the density, the closer is the graph of being complete (that is all pairs of vertices are connected).

The **global efficiency** represents the inverse of the average shortest path length and thus indicates how efficient the network is in transferring information. Decreasing efficiency indicates that the average shortest path length between any pairs of vertices is increasing, whereas high efficiency shows that path length decreases and thus the network becomes more efficient in transferring information.

The **mean** and **global clustering coefficient**s measure the amount of clustering in the system, that is how tightly connected are the vertices within the graph.

Assortativity then shows the tendency of vertices with similar degrees to connect to each other. A graph is assortative when the value is positive and indicates that vertices with similar degrees tend to cluster together. Disassortative graphs have negative values, which indicate that high-degree vertices tend to be linked to low-degree vertices.

6.1 Mudcracks

6.1.1 Elle simulations

Six mudcrack experiments with different mechanical parameters (Young’s modulus and breaking strength) are analyzed. Changing these parameters result in different style of fracture nucleation and propagation. In light of this, it is especially interesting to see whether the evolved fracture networks differ in a quantitative manner as well.

While I carried out the experiments from A to E, experiment F is a published experiment found in the book of Bons et al. (2008) using the same model. The mechanical parameters (Young’s modulus and breaking strength) in the model and their scaled values are listed in Table 9.

	Model scale		Real scale (mean values of the normal distribution)		Particle area change per time step (value × particle area)
	Young’s modulus	Breaking strength	Young’s modulus (GPa)	Breaking strength (MPa)	
Experiment A	0.6	1	6	17	0.0005
Experiment B	1	1	10	17	0.0005
Experiment C	5	1	50	17	0.0005
Experiment D	10	1	100	17	0.0005
Experiment E	10	5	100	85	0.0005

Table 9 Model and real scale properties of the mudcrack experiments.

6.1.1.1 Experiment A

Experiment A represents shrinkage of a soft layer with a mean Young’s modulus of 6 GPa, whereas the breaking strength of the material is kept at default (i.e. 17 MPa - mean). Even though the layer is softer than those in the other experiments, fracturing still takes place early on. Fracturing initiates at one part of the simulation box (Fig. 6.1). This fracture propagates in all directions, and eventually reaches the box boundaries. At this point the fracture propagation shifts focus onto non-fractured areas. By time step 4000 the entire box is fractured. The second half of the simulation is characterized by bridging. Bridging refers to a process where new fractures form between existing ones. This causes the areas between the fractures (polygons) to decrease in size as the new fractures cut through the unfractured areas (i.e. polygons) (see polygon sizes in time steps 4500 and 7580 on Fig. 6.1).

Converting the simulation results to graph, we can look at the fracture evolution in a quantitative manner. Only during the earliest stages of simulation (see Fig. 6.2, 100 time steps) is the probability for a vertex degree 1 higher than a vertex degree 3. After this stage, the probability for a degree of 1 is successively decreasing, and simultaneously the probability that a vertex has a degree of 3 is increasing. From time step 1000 it is always more likely that a vertex has three connected neighbors. Degree of 2 is subordinate throughout the experiment, whereas at time step 7000 a degree of 4 is appearing. At the very last stage around 80% of the vertices reach a degree of 3 (Fig. 6.2). All these trends are mirrored in the entropy values (Fig. 6.3). The more dominant a vertex degree is, the lower is the entropy. As the probability of degree 3 overcomes and then dominates the system over degree 1, the entropy lowers. This can be observed from time step 1000.

During the early stages of the simulation the number of vertices and edges are increasing with approximately the same amount (Fig. 6.4a). As soon as we see that the fracturing affects the non-fractured areas and bridging starts to take place, the edge number increases more steeply than the vertex number. At the end of the simulation the vertex number seems to stagnate, whereas the edge number continues to rise.

The graph density indicating graph completeness resembles an exponential decay during the simulation (Fig. 6.4b). As the simulation starts and only a few vertices and edges exist, the graph density is relatively high. The increasing graph size (i.e. vertex number) results in an exponential decrease in graph density. Towards the end, however, the graph density slope flattens out.

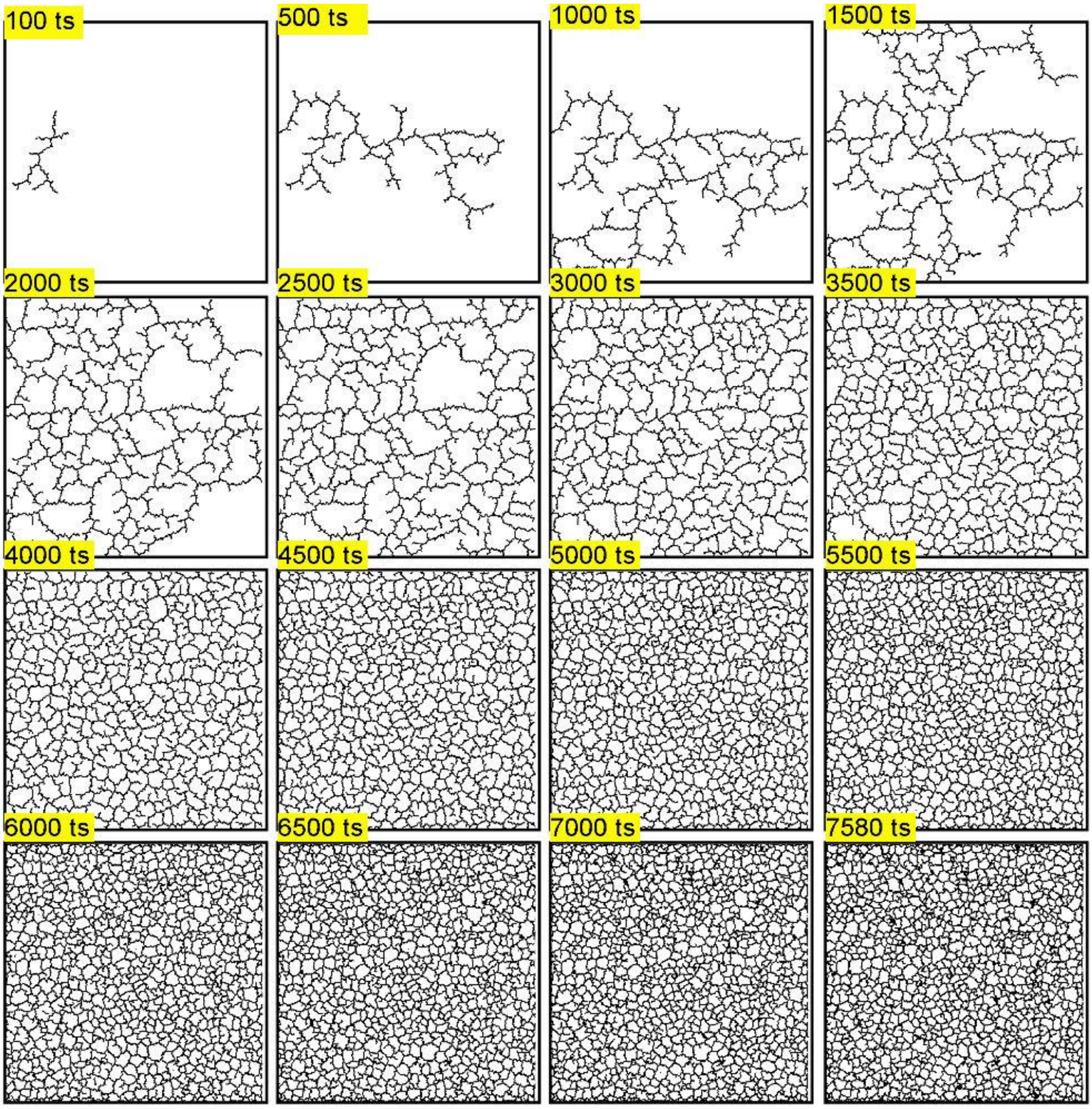

Fig. 6.1 Progressive fracture development at different time steps during the mudcrack experiment A.
The layer is soft (mean Young's modulus is 6 GPa) and has the default breaking strength (17 MPa – mean value). Images capture the top surface of the shrinking layer.

The global efficiency, similarly to the graph density, shows a major drop during the onset of the experiment (Fig. 6.4c). Its slope resembles an exponential decay until time step 3000. After this stage a slight increase in the global efficiency values can be observed, which continues until the end of the simulation.

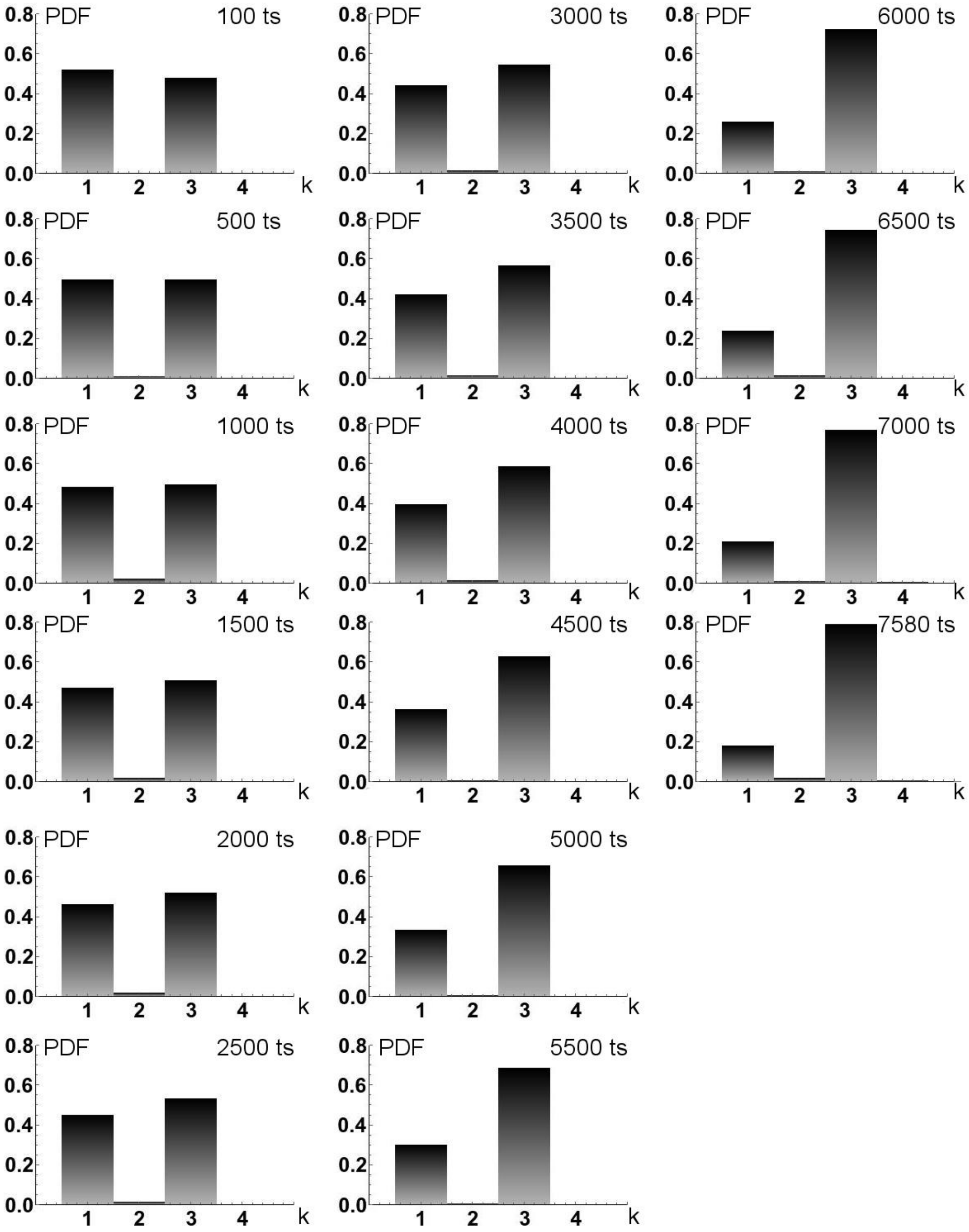

Fig. 6.2 Probability density function (PDF) of vertex degree (k) distribution at different time steps during experiment A.
The dominant vertex degree shifts from 1 to 3 as the network becomes more interconnected.

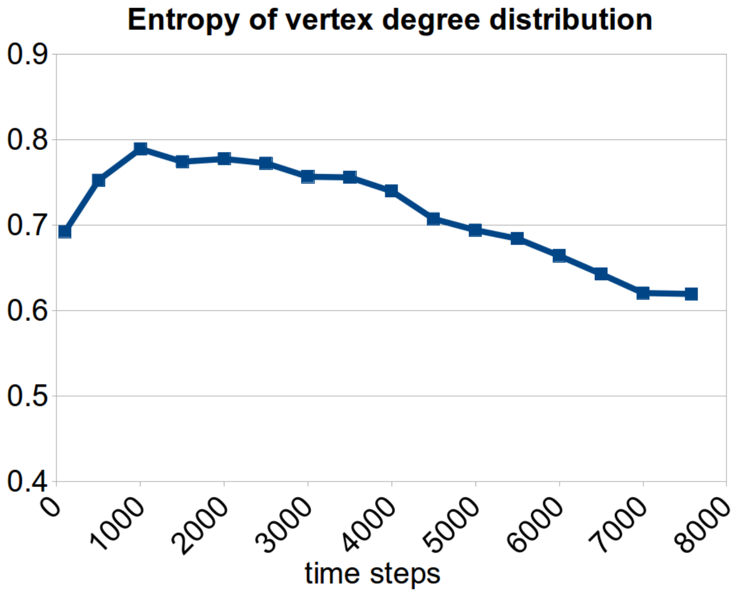

Fig. 6.3 Entropy of vertex degree distribution for experiment A.

Looking at the mean and global clustering coefficients we see that they follow the same trend, therefore it is more convenient to describe them together (Fig. 6.4d). As opposed to the previous measures the clustering coefficients do not show a clearly defined trend. During the first 1000 time steps the clustering coefficients are zero. Approximately around the time when the number of edges overcomes the vertices, the coefficients start to increase. Except for time steps 3000 and 7000, the clustering coefficients show a dynamic increase. The drop at 3000 time steps can be simultaneously detected in the global efficiency values. As opposed to this, the drop at 7000 time steps is not reflected in a decrease but a slight increase in the global efficiency.

The assortativity values are all positive indicating assortative mixing and show a general increase throughout the simulation with only minor fluctuations (Fig. 6.5). Its maximum is around 0.55, which is reached at the end of the simulation.

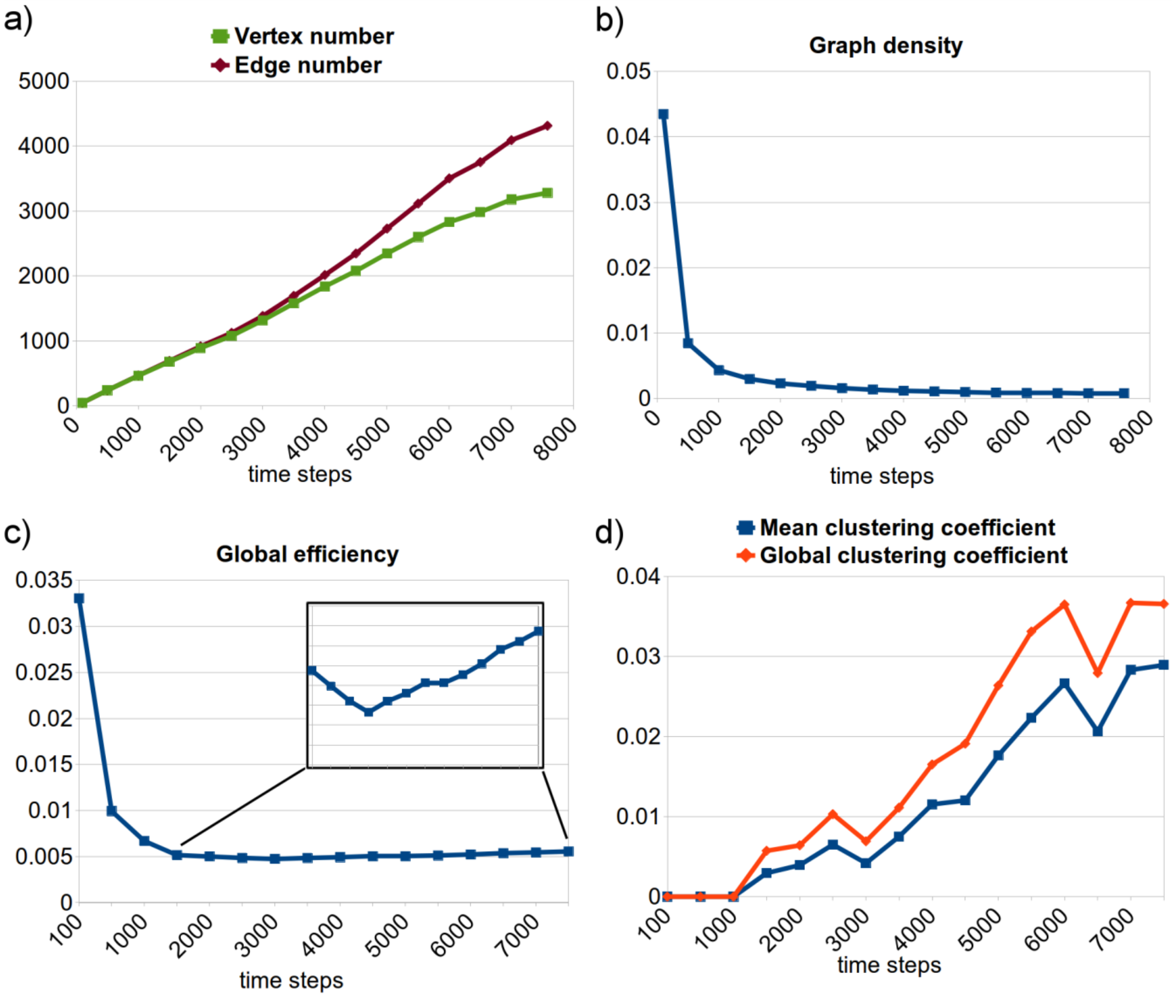

Fig. 6.4 Charts showing the vertex and edge number (a), the graph density (b), global efficiency (c) and clustering coefficients (d) of the fracture network in experiment A.

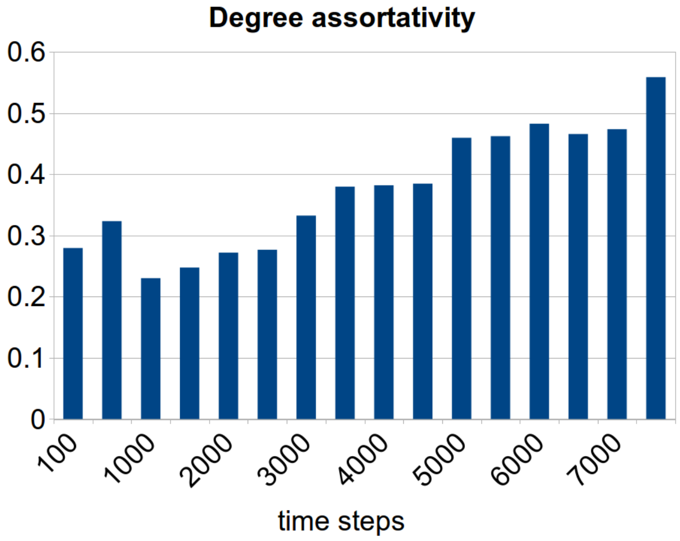

Fig. 6.5 Vertex degree assortativity indicating the network evolution during experiment A.

6.1.1.2 Experiment B

Experiment B represents the default case when the mean Young's modulus and breaking strength are set to 10 GPa and 17 MPa, respectively. The fracture evolution show similar characteristics compared to experiment A (Fig. 6.6).

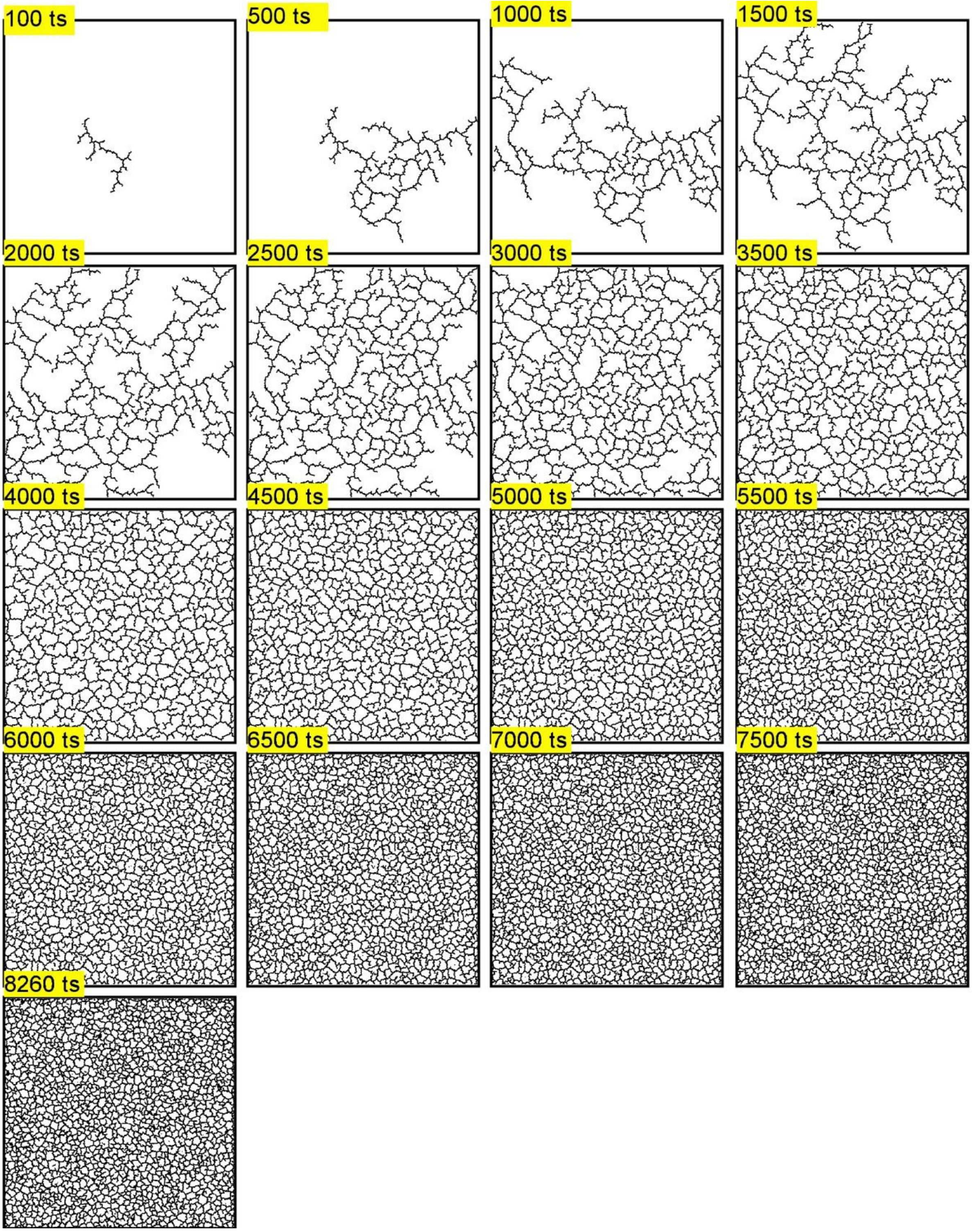

Fig. 6.6 Progressive fracture development at different time steps during the mudcrack experiments B.
The layer's mechanical properties are set to default, i.e. mean Young's modulus is 10 GPa and the mean breaking strength is 17 MPa. Images capture top surface of the shrinking layer.

A fracture nucleates at one part of the simulation box and propagates in all directions towards the box boundaries. Once the boundaries are reached and the non-fractured areas also break, bridging dominates the second half of the simulation (from 4000 time steps).

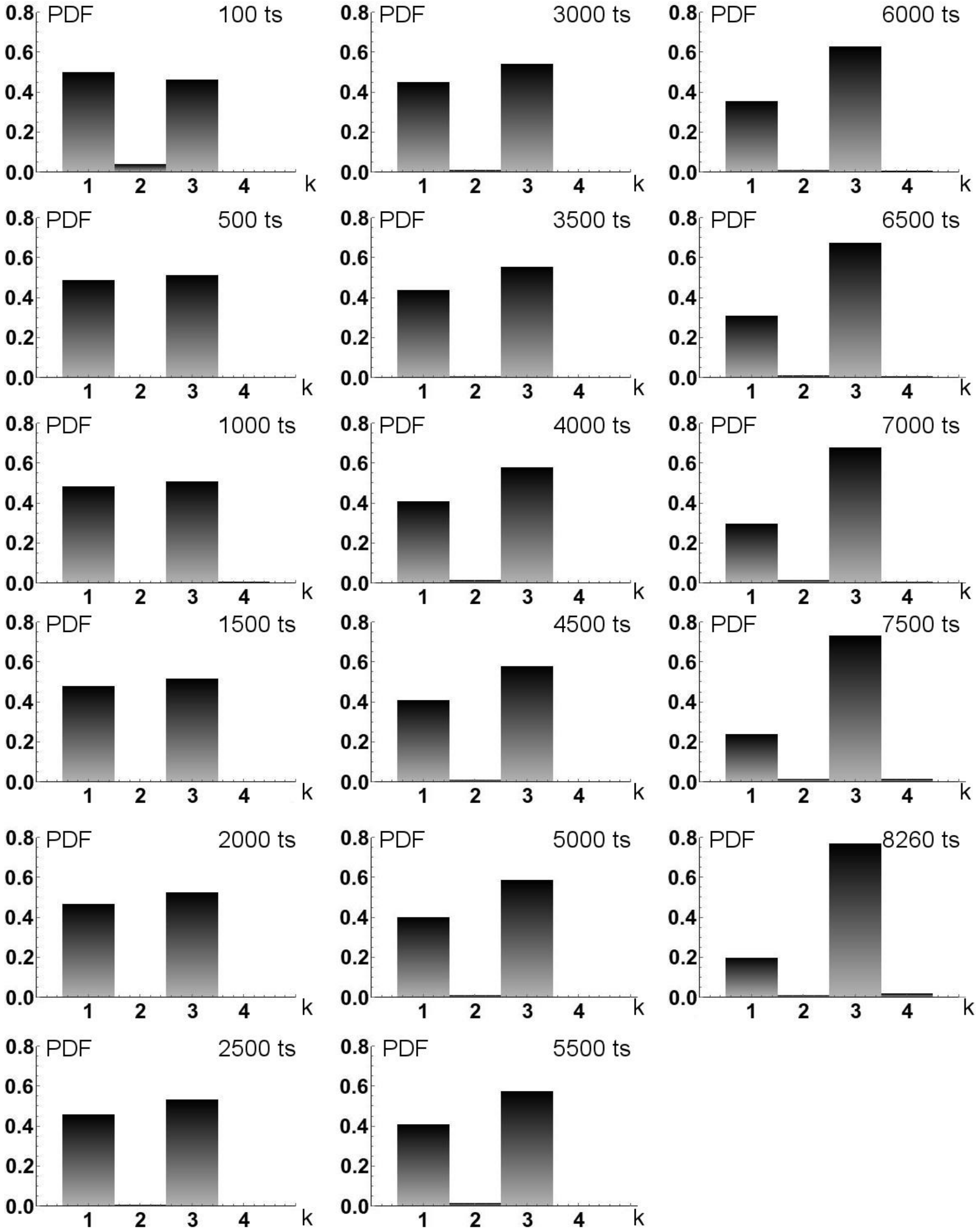

Fig. 6.7 Probability density function (PDF) of vertex degree (k) distribution at different time steps during experiment B.
The dominant vertex degree shifts from 1 (time step 100) to 3 after time step 500 due to fracture interconnections.

Converting the network to graph shows that vertices are initially slightly dominated by degrees of 1 (Fig. 6.7, 100 time steps). However, after time steps 500 the probability that a vertex has a degree of 3 is always higher. The decrease in probability of degree 1 simultaneously increases the degree of 3. This shift can be nicely observed on Fig. 6.7. Similarly to experiment A, the degree 2 is subordinate, whereas the degree of 4 appears towards the end of the simulation. The experiment ends with 80% of the vertices having three connected neighbors. Entropy of the system follows the change in the degree probabilities (Fig. 6.8). When approximately an equal amount of vertices have 1 and 3 connected neighbors, the entropy is high. However, as soon as bridging takes place and vertices become triple junctions the entropy declines.

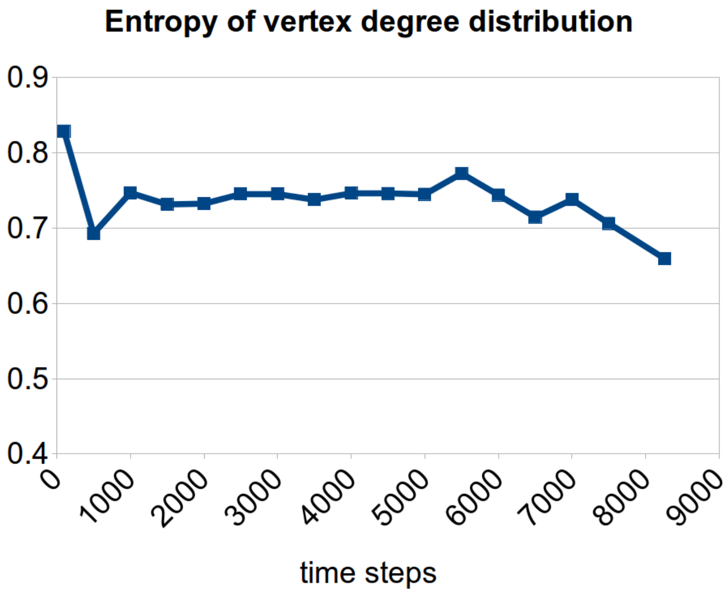

Fig. 6.8 Entropy of vertex degree distribution for experiment B.

The vertex and edge numbers initially increase (approximately linearly) with the same amount in the early stages of the experiment (Fig. 6.9a). From time step 1500, however, the edge number rises more steeply than the vertices. This effect is reflected in the graph density values, which show that the simulation starts with high graph densities and resembles an exponential decrease afterwards (Fig. 6.9b).

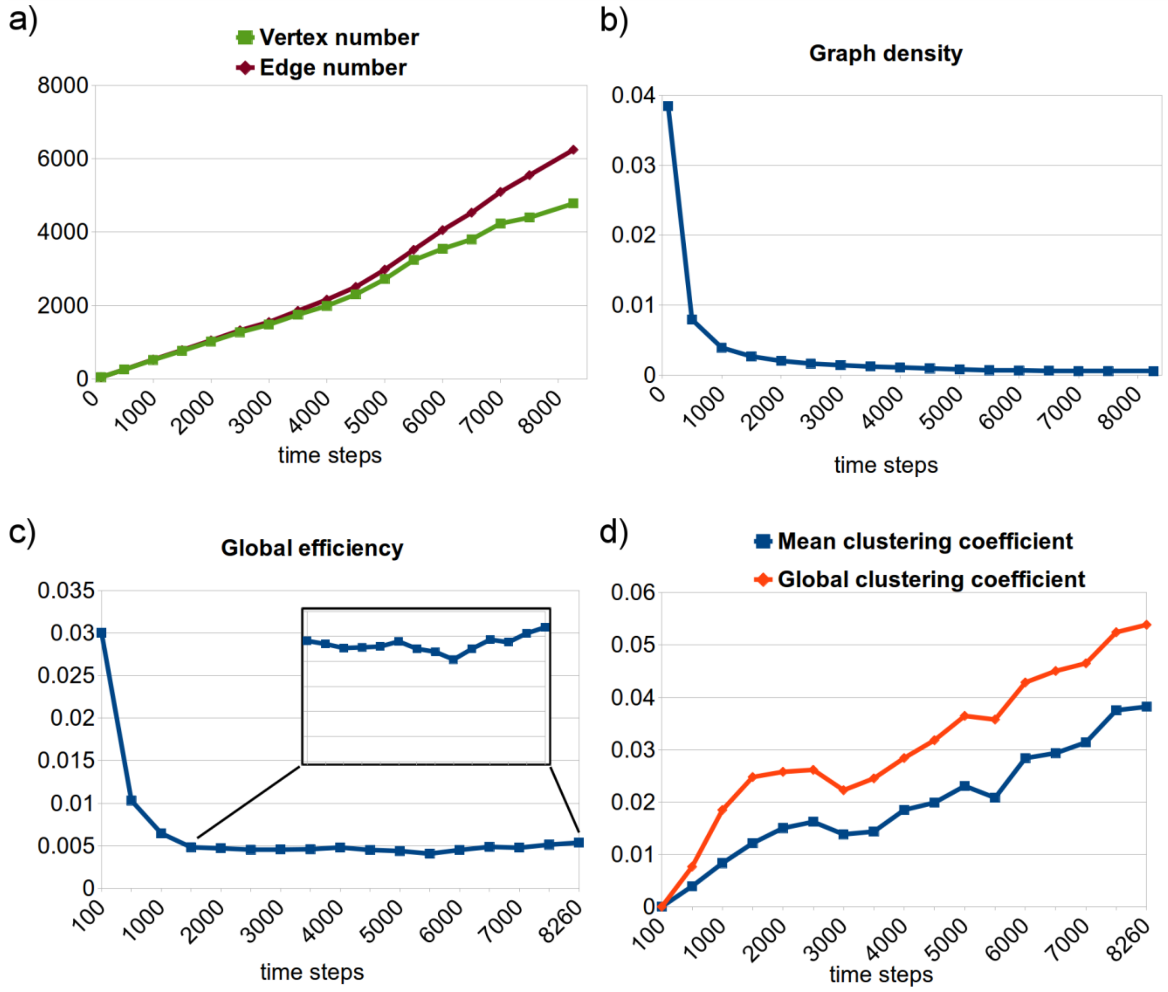

Fig. 6.9 Charts showing the vertex and edge number (a), graph density (b), global efficiency (c) and clustering coefficients (d) for experiment B.

The global efficiency values exhibit a steep decrease between the onset of the simulation and time step 1500 (Fig. 6.9c). After this stage, the values fluctuate around 0.005, and finally (between time steps 7000 and 8260) show a slight increase.

Similarly to the previous case (experiment A) the clustering coefficients do not show a consistent, well-defined trend (Fig. 6.9d). However, there is a general increase in the coefficient values with a few smaller drops occurring at time steps 3000 and 5500. While the former does not seem to be reflected in any other change in measurements, the latter coincides with a decrease in the global efficiency.

The degree assortativity of the network also shows assortative mixing as its values are all positive, and generally increase throughout the simulation reaching 0.5 (Fig. 6.10).

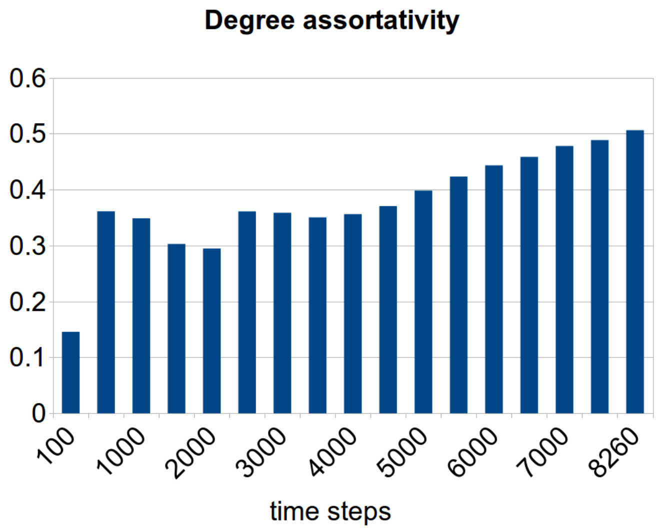

Fig. 6.10 Vertex degree assortativity for experiment B.

6.1.1.3 Experiment C

Experiment C represents layer shrinkage of a stiffer (50 GPa mean) layer, whereas the breaking strength of the bonds is kept at the default value (17 MPa mean). Compared to the previous cases (experiments A and B) the fracturing here shows a different characteristic. The most apparent difference is that the fractures nucleate at random locations within the deformation box (see time step 100 and 500, Fig. 6.11). This simultaneous fracturing results in many smaller clusters all over the box, rather than one major propagating fracture as in experiments A and B. The deformation thus is clearly driven by fractures forming further away from the initial ones. When most of the layer is fractured and the clusters lie close to each other, the fractures/clusters join together. The end result will be a completely fractured deformation box, which looks similar to the experiments A and B, but the non-fractured domains appear to be smaller.

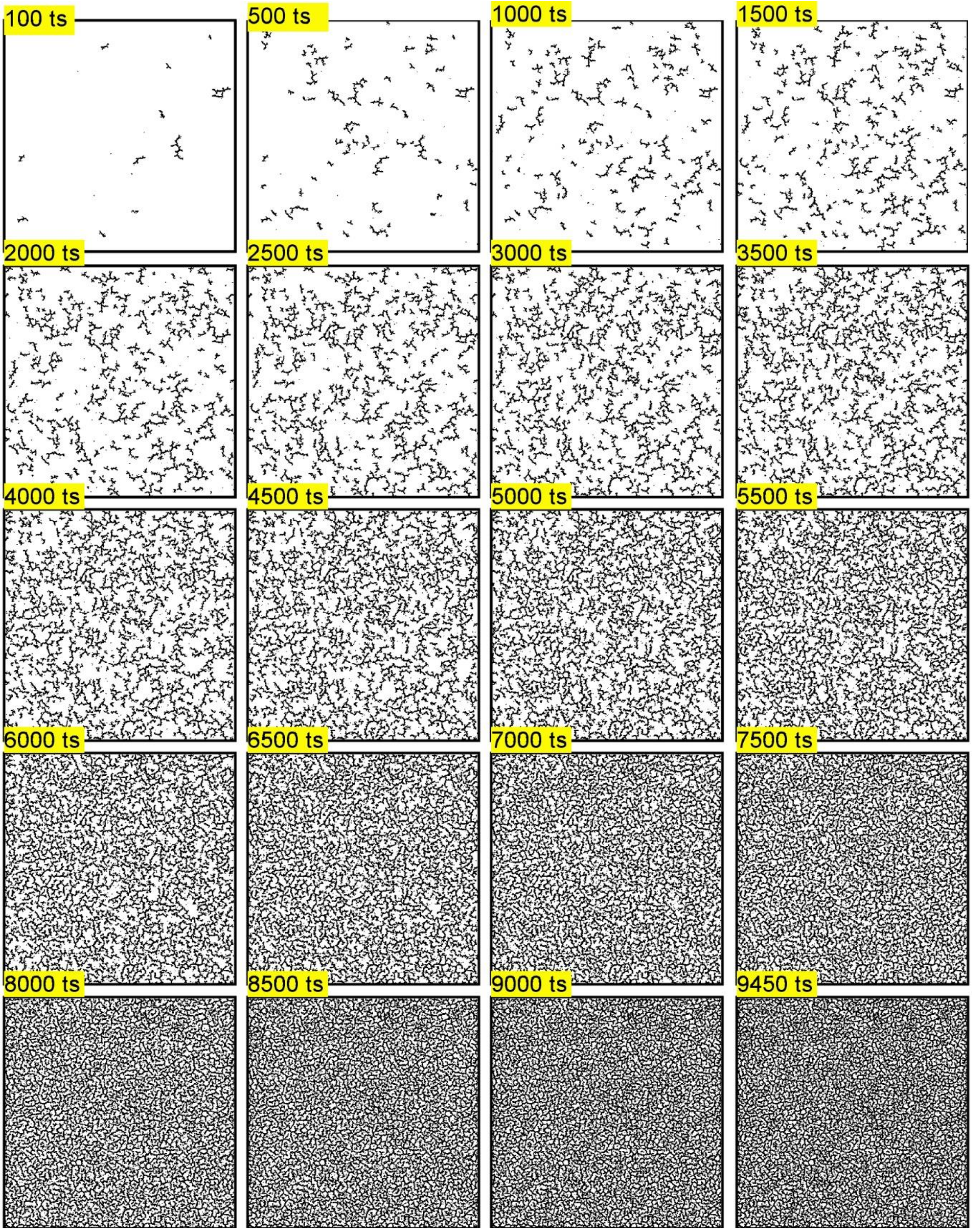

Fig. 6.11 Progressive fracture development at different time steps during the mudcrack experiment C.
The layer has a mean stiffness of 50 GPa, whereas the breaking strength is kept at 17 MPa (mean). Images capture the top surface of the shrinking layer.

This different fracturing characteristic is also reflected in the graph measures. The network is much longer (until time step 8000) dominated by vertices with a degree of 1 (Fig. 6.12). This dominance gradually decreases as more and more vertices have three neighbors. At time step 8500, the vertex degree 3 overcomes the degree of 1 and from then on it increases up to 0.6, meaning that 60% of the vertices have three connected neighbors. In addition to this, the probability for two or four connected neighbors is higher than in previous cases. This increases the entropy as well (Fig. 6.13). The entropy otherwise is rising throughout the simulation as the probabilities for degree 1 and 3 are equalizing. Its lowest value is at time step 100 because only three different degrees are present (1, 2 and 3) and the probability difference between degree 1 and 3 is the largest here.

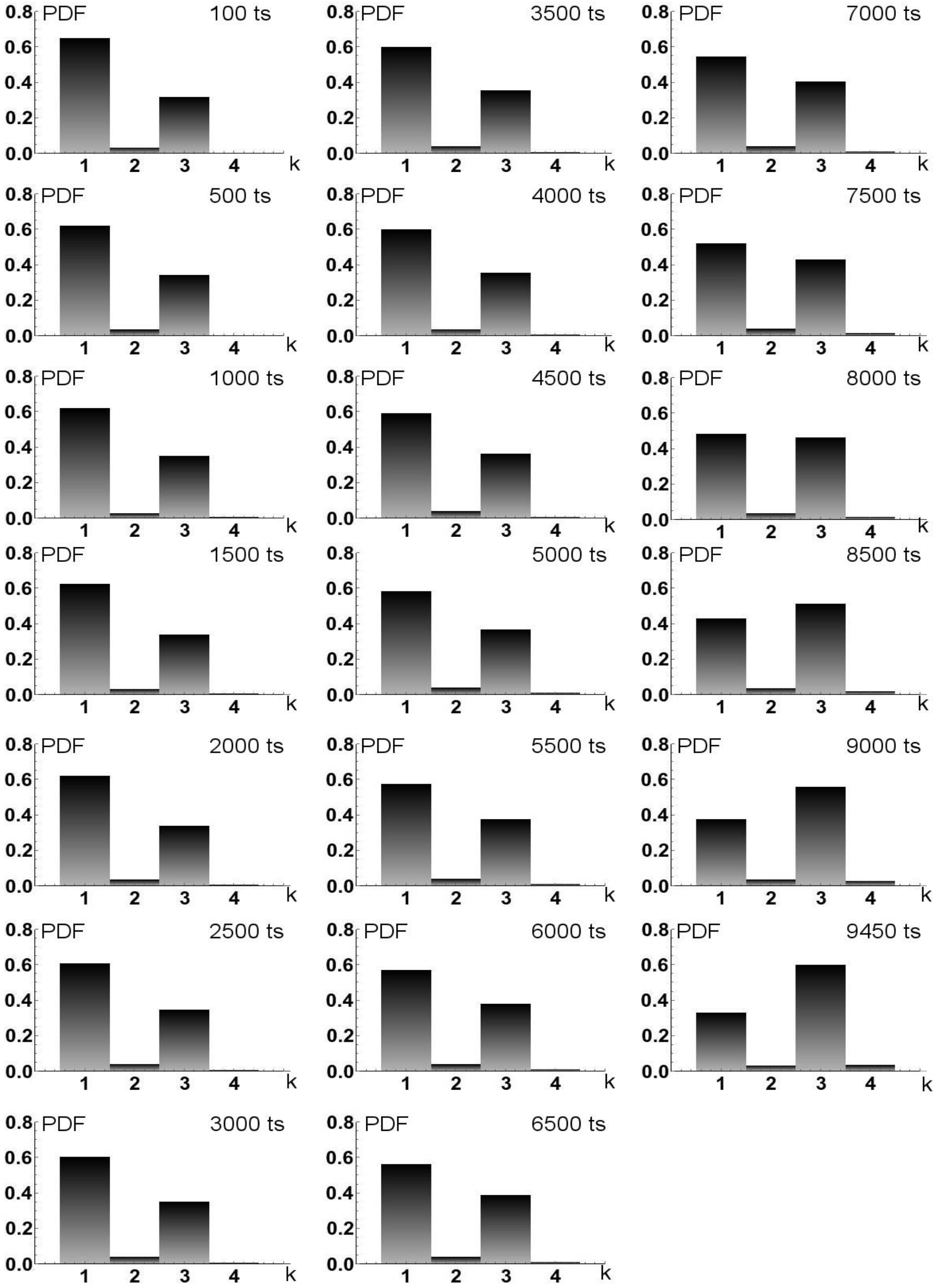

Fig. 6.12 Probability density function (PDF) of the vertex degree (k) distribution at different time steps during experiment C.
Most of the vertices have only one connected neighbor until time step 8000. However, from time step 8500 there are more triple junctions due to interconnections within the network.

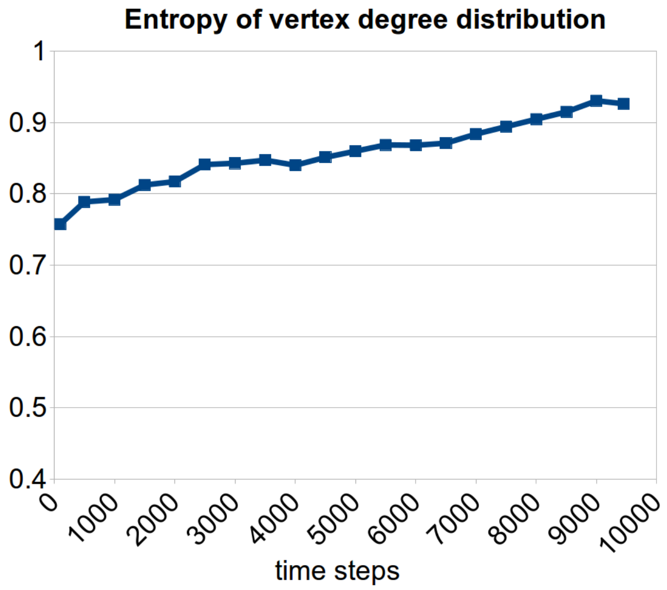

Fig. 6.13 Entropy of vertex degree distribution for experiment C.

The network is characterized by more vertices than edges until time step 7500 (Fig. 6.14). From time step 8000 the edge number overcomes the vertex number and rises more steeply. This coincides with the switch that was observed in the vertex degree distribution. In addition to this, both the number of vertices and edges are significantly larger (reaching 12000) than in the previous experiments (maximum between 3000 and 6000).

The graph density here also reveals an exponential decline throughout the simulation (Fig. 6.14b). However, in contrast to the earlier cases the density values are approximately a magnitude lower.

The same, i.e. significantly lower values, applies to the global efficiency of the network. The evolution of the efficiency resembles a similar, earlier observed, decreasing trend until time step 7000. After this stage the global efficiency rises steeply, reaching a final value of 0.0045, which is almost identical to the efficiency values at the end of experiments A and B.

The clustering coefficients on the other hand are also greater than during the previous cases; the global reaches 0.1, whereas the mean clustering coefficient has a maximum value of 0.06 (Fig. 6.14d). They both display a dynamic increase with only minor fluctuations during the simulation.

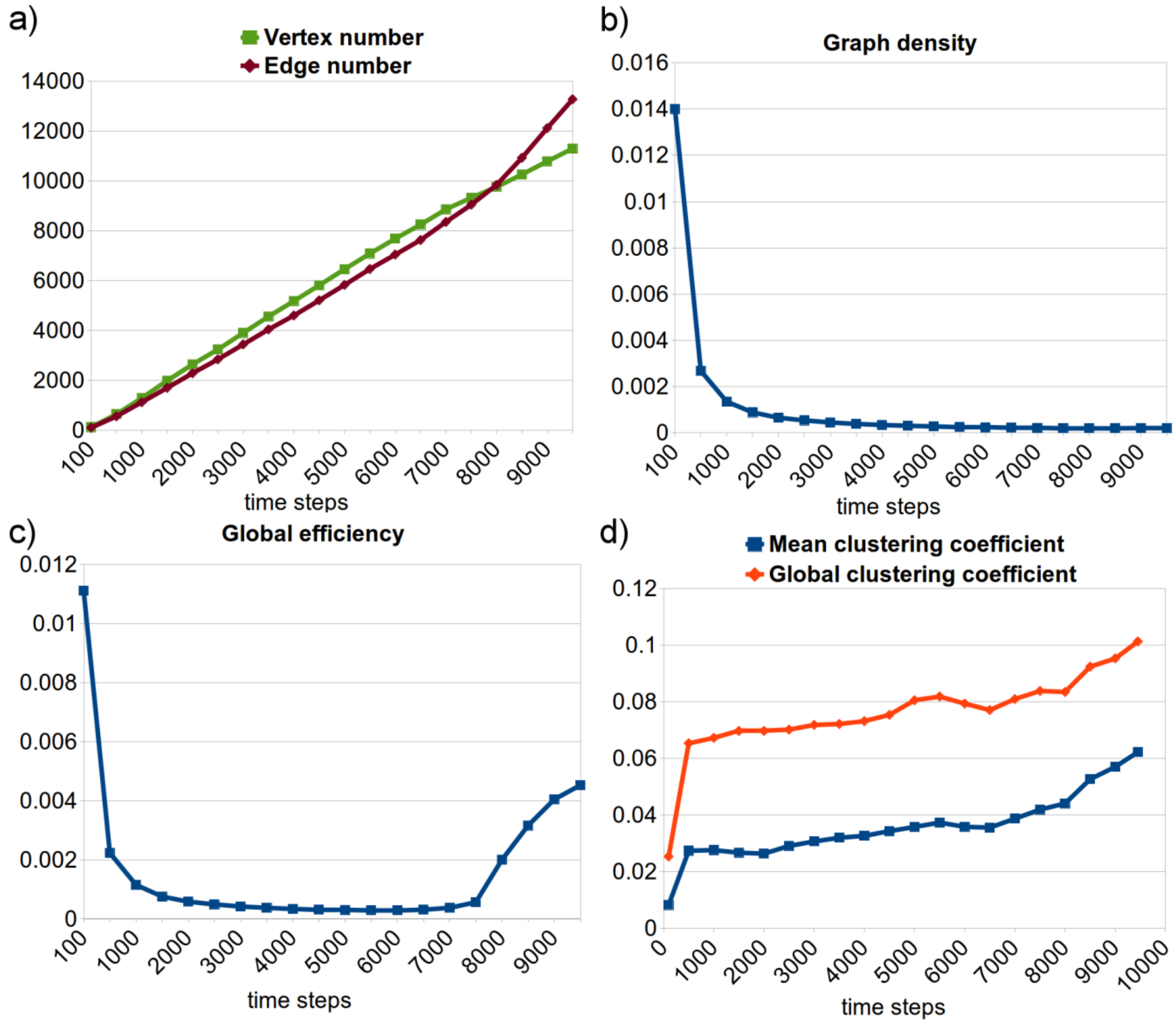

Fig. 6.14 Charts showing the vertex and edge numbers (a), graph density (b), global efficiency (c) and clustering coefficients (d) for experiment C.

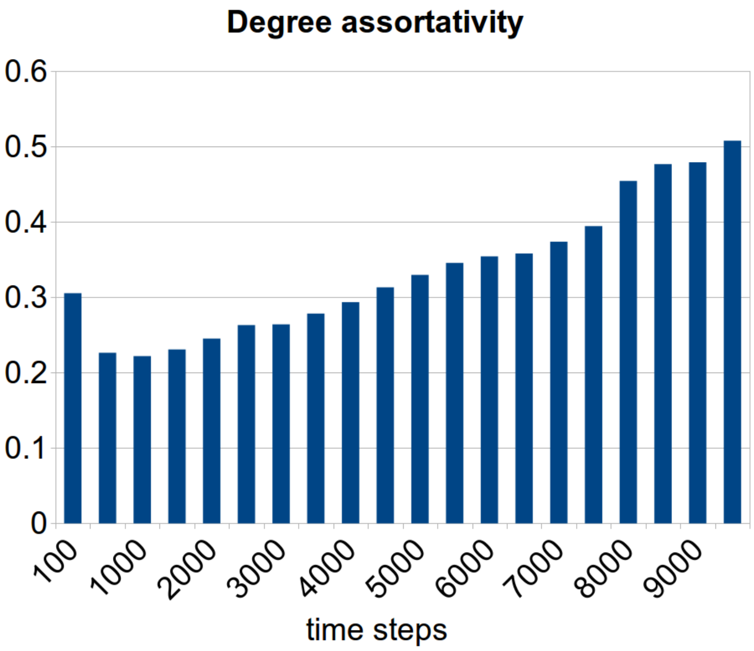

Fig. 6.15 Vertex degree assortativity for experiment C.

The network again displays assortative mixing, which generally increases during the simulation. At the final stage the network is the most assortative with a value of around 0.5. This is equivalent to the final value observed in experiments A and B.

6.1.1.4 Experiment D

Experiment D represents the stiffest case where the layer's mean Young's modulus is 100 GPa and its breaking strength is kept at the default value (17 MPa - mean). Due to the extreme stiffness the fracture evolution displays the same characteristics as in experiment C. Fractures nucleate at random locations in the deformation box (Fig. 6.16). As these fractures do not seem to propagate, the deformation is dominated by fracturing of areas further away from the initial fractures (see time steps 500 to 2000, Fig. 6.16). This process creates fracture clusters that appear all over the deformation box. As the clusters become close to each other and most of the layer is deformed, the clusters interconnect (from time step 4000). This creates a network which will further evolve due to bridging. The non-fractured domains (polygons) become smaller as fracture bridges cut through them (from time step 7500). The end result will be a completely fractured deformation box which looks similar to the one at the end of experiment C.

The graph measures overall are similar to those calculated in experiment C. Looking at the probabilities of vertex degree distribution it is apparent that a degree 1 dominates the network until time step 7500 (Fig. 6.17). This dominance is slowly decreasing during the simulation as the degree 3 is rising. At time step 8000 the degree 1 and 3 equalizes, after which most of the vertices have three connected neighbors. The probability for a vertex to have two or four connected neighbors is also higher during the entire simulation than it was during experiments A or B. These characteristics are reflected in the entropy values, which show an increasing trend due to the relative vertex degree probabilities (Fig. 6.18).

The vertex and edge numbers exhibit a dynamic increase similar to experiment C. Until time step 7500 the network consists of more vertices than edges (Fig. 6.19a). However, from time step 8000 the number of edges rises more steeply than the vertices. This results in a large network (vertices around 10000) with even more edges.

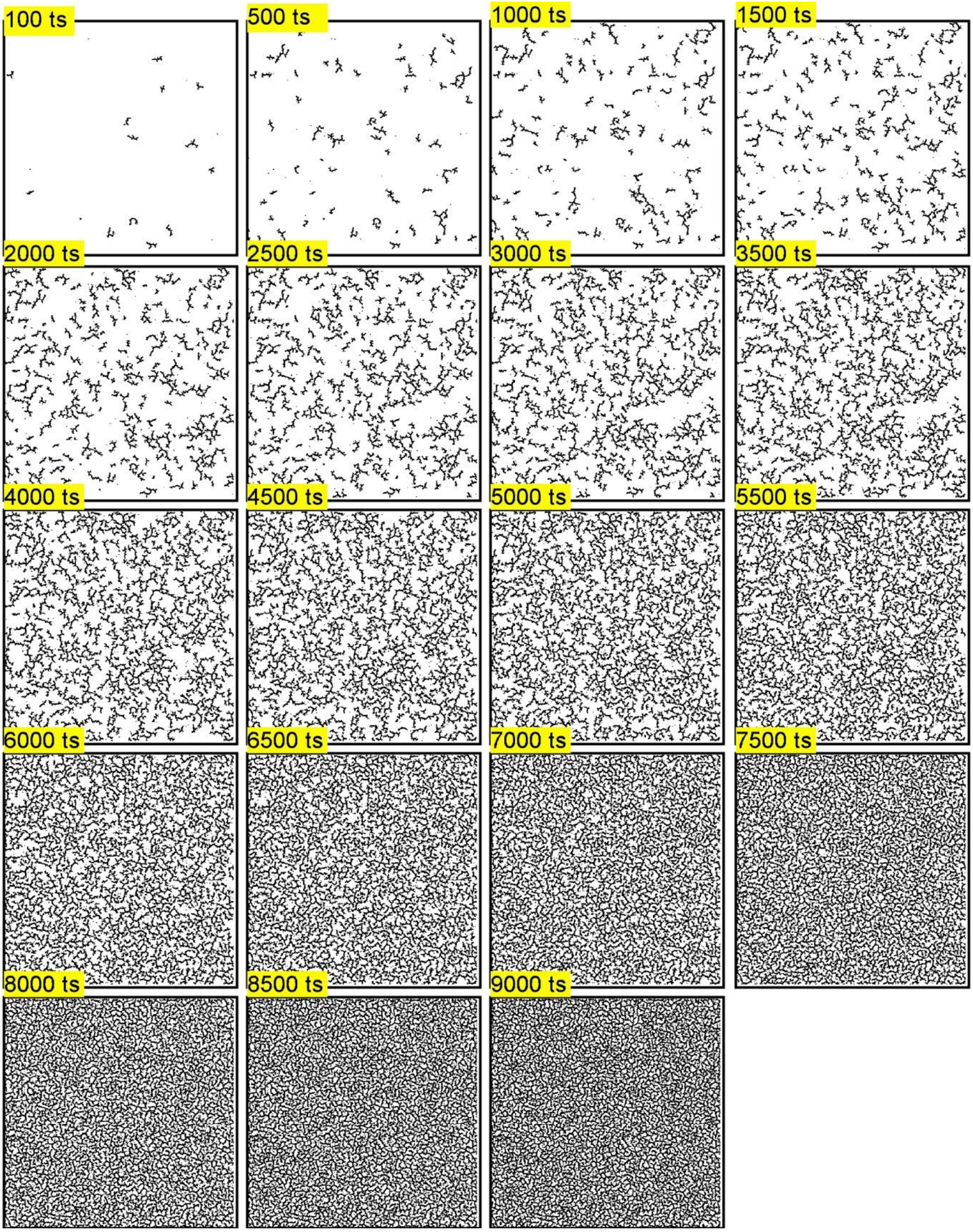

Fig. 6.16 Progressive fracture development at different time steps during the mudcrack experiment D.
The layer has a mean stiffness of 100 GPa representing an extreme case, and a mean breaking strength of 17 MPa. Images capture the top surface of the shrinking layer.

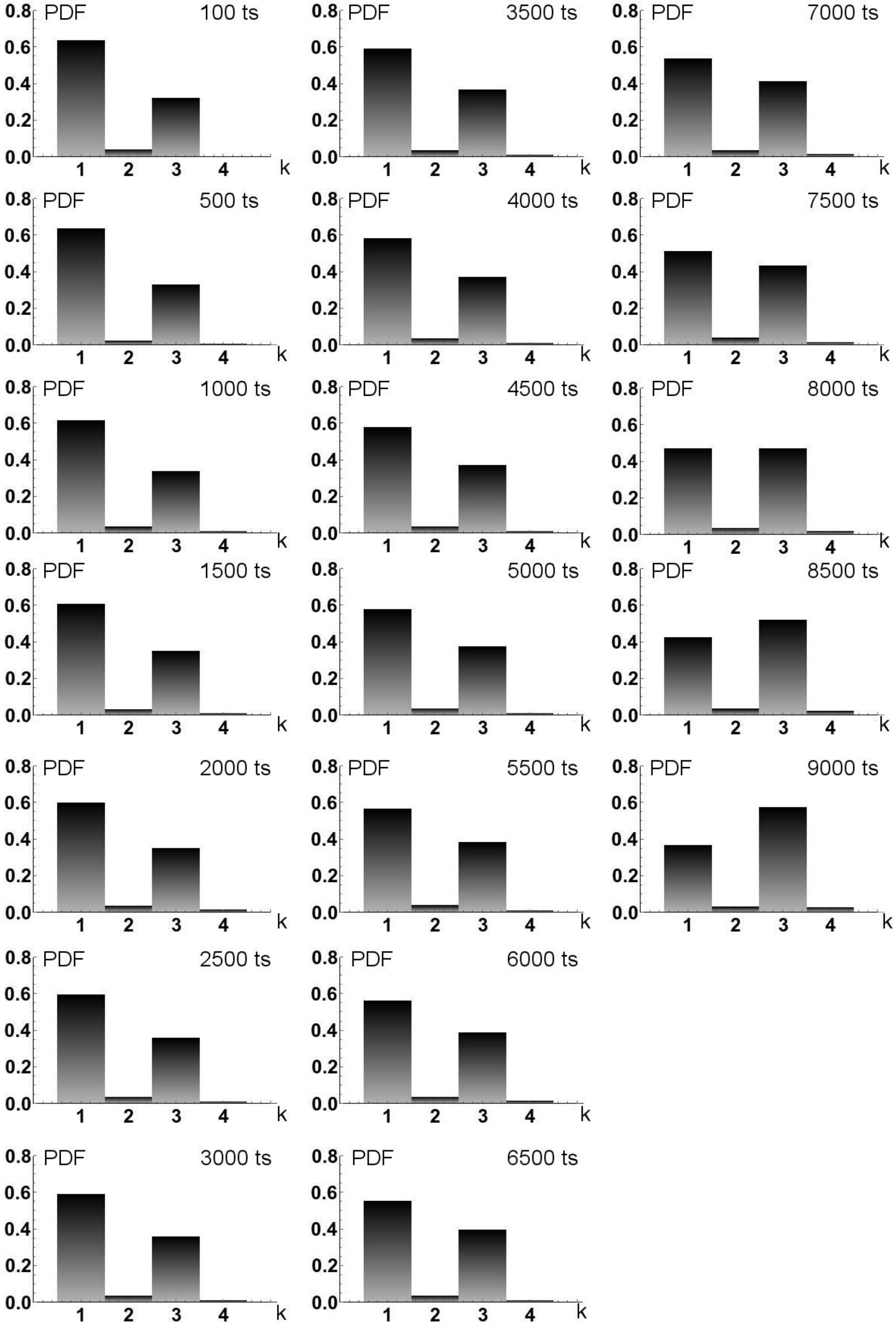

Fig. 6.17 Probability density function (PDF) of vertex degree (k) distribution at different time steps during experiment D.
The network is dominated by vertices with one connected neighbor until time step 8000. At the last two stages, however, triple junctions are more abundant than vertices with one neighbor.

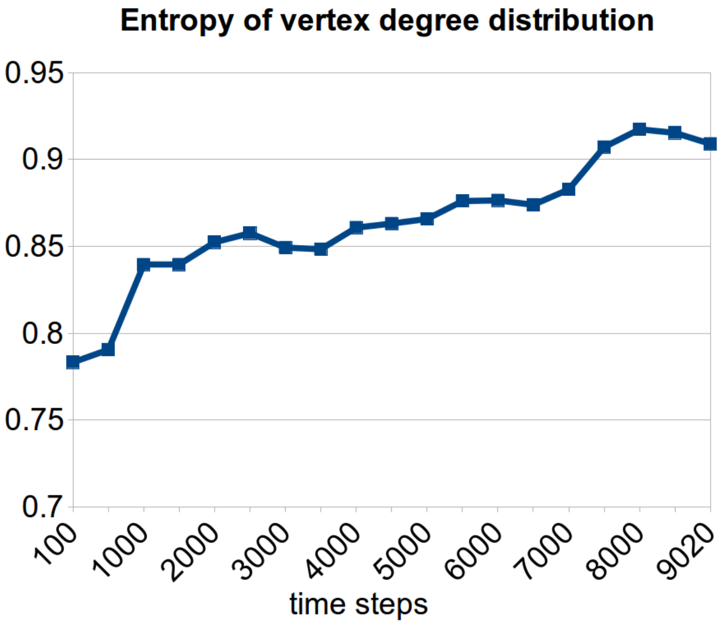

Fig. 6.18 Entropy of vertex degree distribution for experiment D.

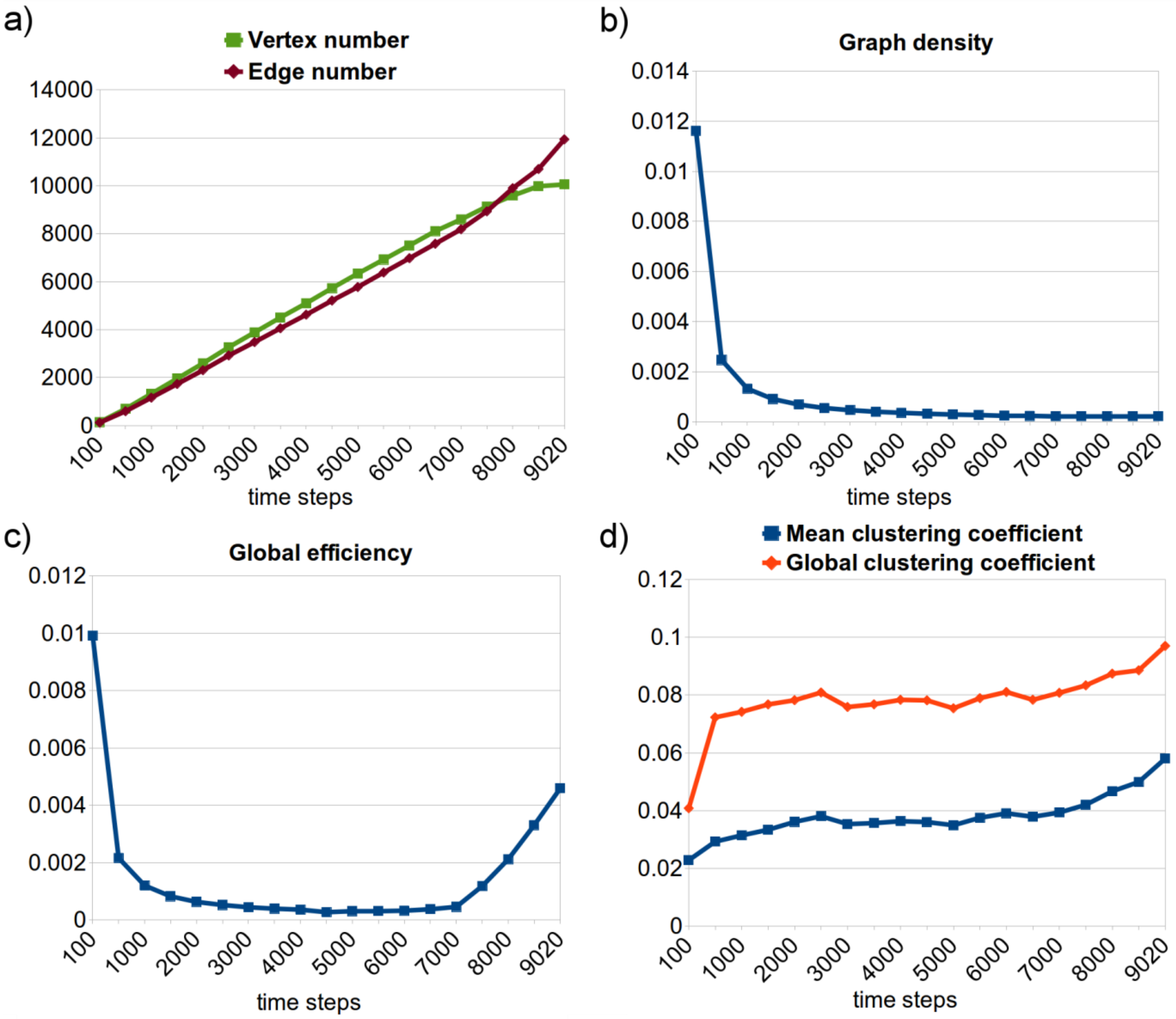

Fig. 6.19 Charts illustrating the vertex and edge numbers (a), graph density (b), global efficiency (c) and clustering coefficients (d) for experiment D.

The graph density values are in the same orders as in experiment C (Fig. 6.19b). As the network evolves the graph density exponentially decreases.

The initial (until time step 1000) steep decrease of the global efficiency slows down until time step 7000 (Fig. 6.19c). After this stage, however, a significant increase can be observed reaching a final value of 0.0045. This value is close to the efficiency values of the previous experiments. The rising efficiency correlates well with the increase in edges relative to the vertices, as well as with the switch in vertex degree dominance.

The clustering coefficients are in the same order than the ones in experiment C. There is a continuous, relatively slow rise throughout the simulation (Fig. 6.19d). However, the slopes of the coefficients are steeping from time step 7500, which coincides with the efficiency value rise at the end of the experiment.

The network shows assortative mixing from the start of the simulation, which increases towards the end (Fig. 6.20). The last two stages especially show preferential attachments of similar degree vertices to each other. The assortativity reaches a maximum value of 0.55 at the end of the simulation.

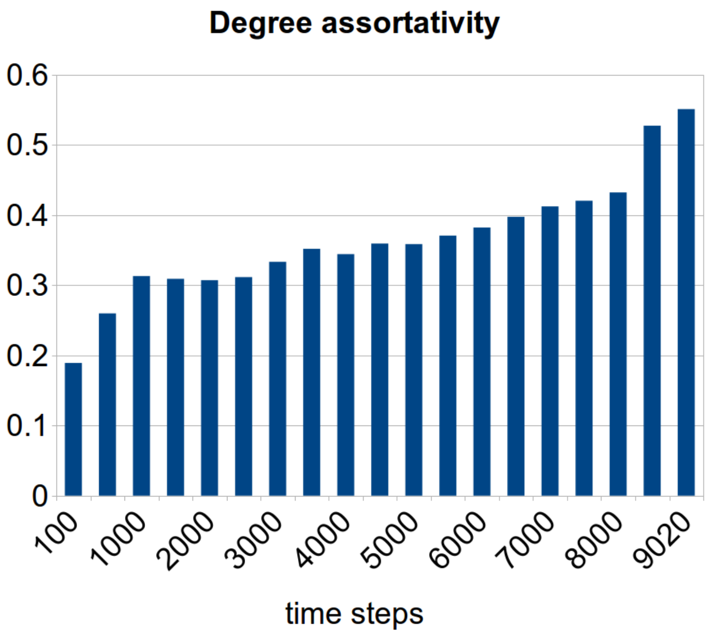

Fig. 6.20 Vertex degree assortativity for experiment D.

6.1.1.5 Experiment E

Experiment E represents the mudcrack formation and evolution in a stiff (mean Young's modulus 100 GPa) and a strong (mean breaking strength 85 MPa) layer (Fig. 6.21). These values are extreme but the aim was to observe the deformation of a stiff and strong layer.

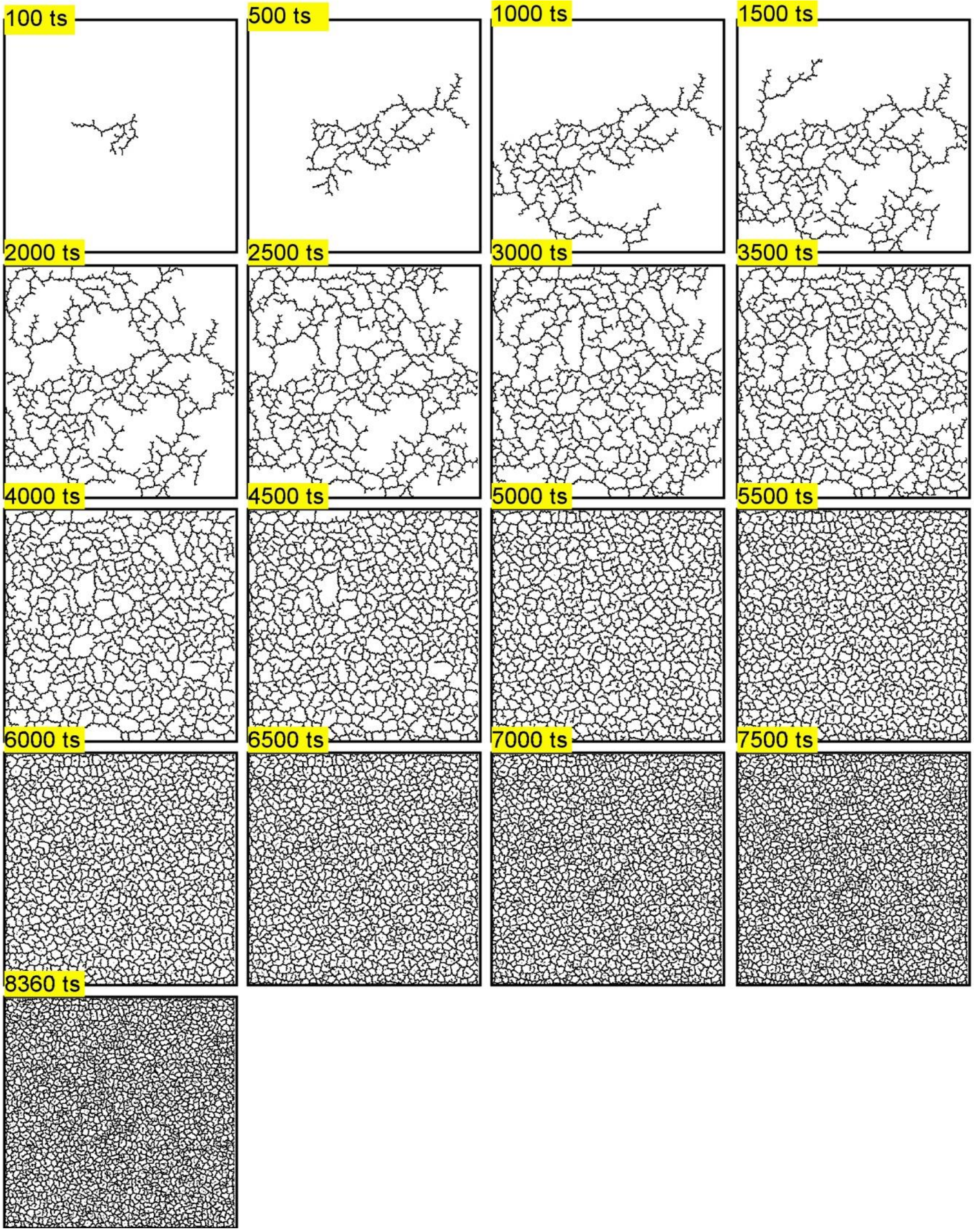

Fig. 6.21 Progressive fracture development at different time steps during mudcrack experiment E. The layer's mean Young's modulus is 100 GPa and its mean breaking strength is 85 MPa. Images capture the top surface of the shrinking layer.

A fracture nucleates at one location within the box and propagates towards the boundaries. When most of the layer is broken (time step 500, Fig. 6.21) the deformation will be characterized by the bridging process where new fractures cut through unbroken areas (polygons) joining fracture segments together. This type of fracture evolution was observed in experiments A and B. The final network, however, seems to be a transition between experiments A-B and C-D, as the unfractured domains look smaller here than in A-B but larger than in C-D.

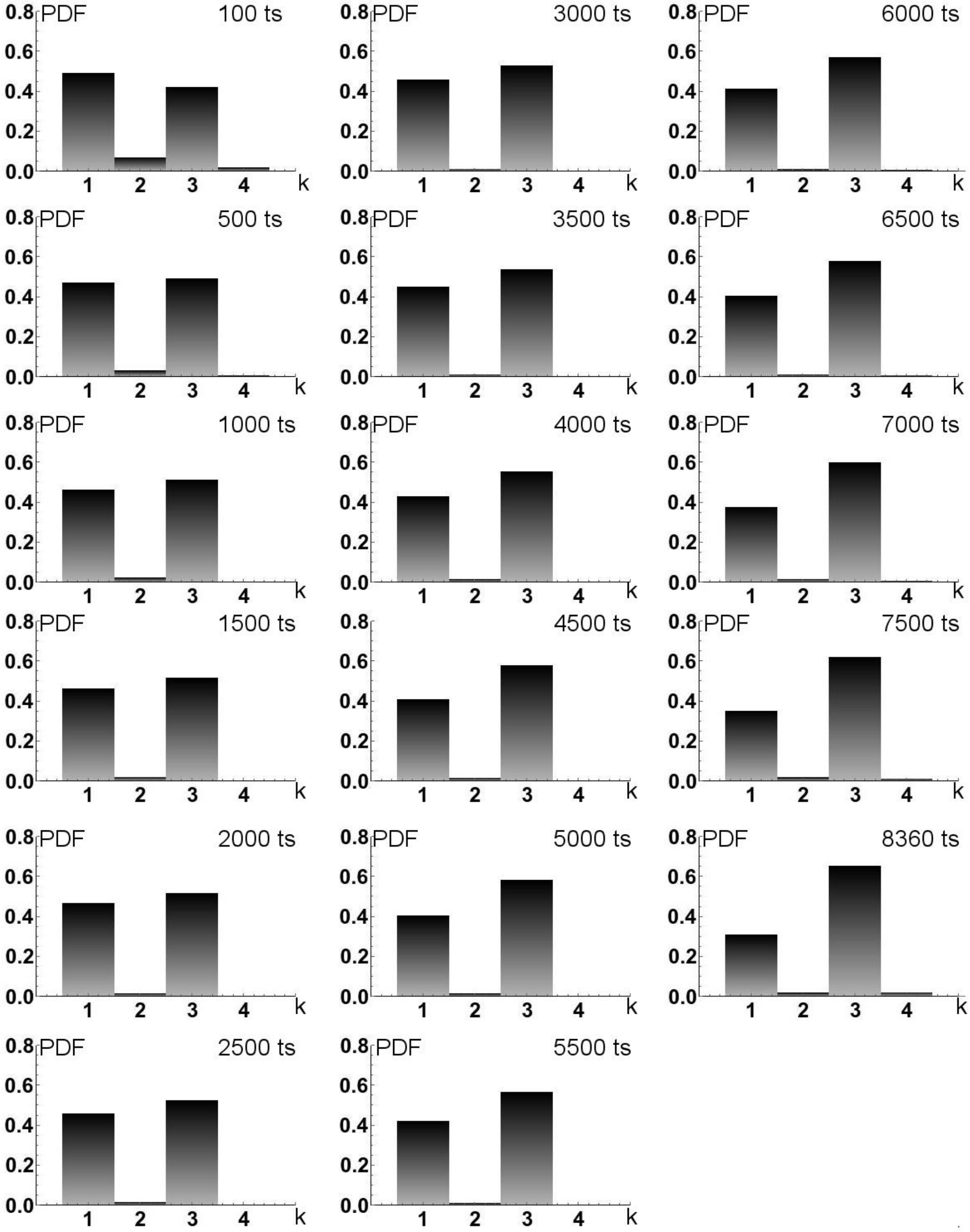

Fig. 6.22 Probability density function (PDF) of vertex degree (k) distribution at different time steps during experiment E.
While at time step 100 the degree 1 slightly dominates the network, the rest of the simulation shows that more and more vertices have a degree of 3.

Looking at the vertex degree distribution we see that at time step 100 around 50% of the vertices have one neighbor, whereas the rest mainly have three, subordinately two and four (Fig. 6.22). This is the only time when 1 is the ruling degree in the network. After this stage the dominance of degree 1 is progressively decreasing with degree 3 simultaneously increasing. At the end of the simulation more than 60% of the vertices have three neighbors indicating that the network mainly consists of triple junctions. The evolution (timing and characteristics) of the vertex degree distribution is similar to that observed in experiments A and B.

The entropy values fluctuate around 0.75 throughout the simulation (Fig. 6.23). This is due to the fact that probabilities for degree 1 and 3 are very close to each other and the degree 2 and 4 are also present, which makes the entropy relatively high.

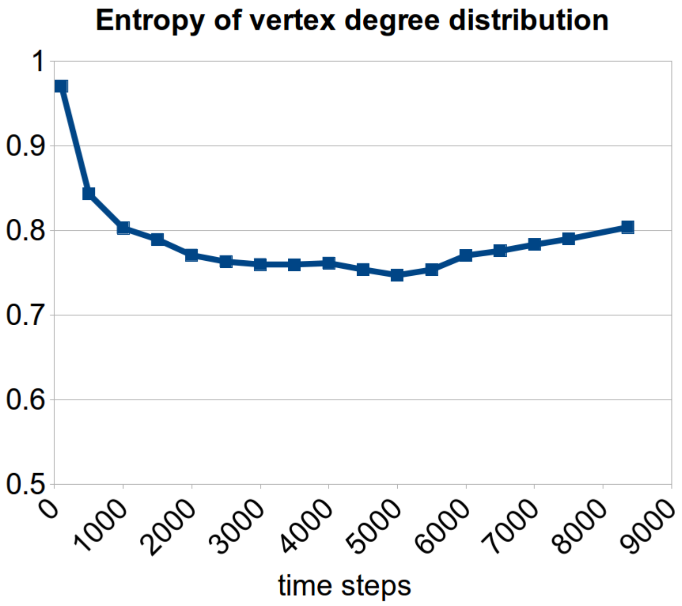

Fig. 6.23 Entropy of vertex degree distribution for experiment E.

The fracture evolution results in a continuous rise in both the vertices and edges (Fig. 6.24a). Although the number of edges is higher than the vertex number from time step 500, the values stay quite close to each other. Their slopes only diverge after time step 4000 and the difference becomes larger as the network develops. These characteristics coincide with the vertex degree probabilities seen on Fig. 6.22.

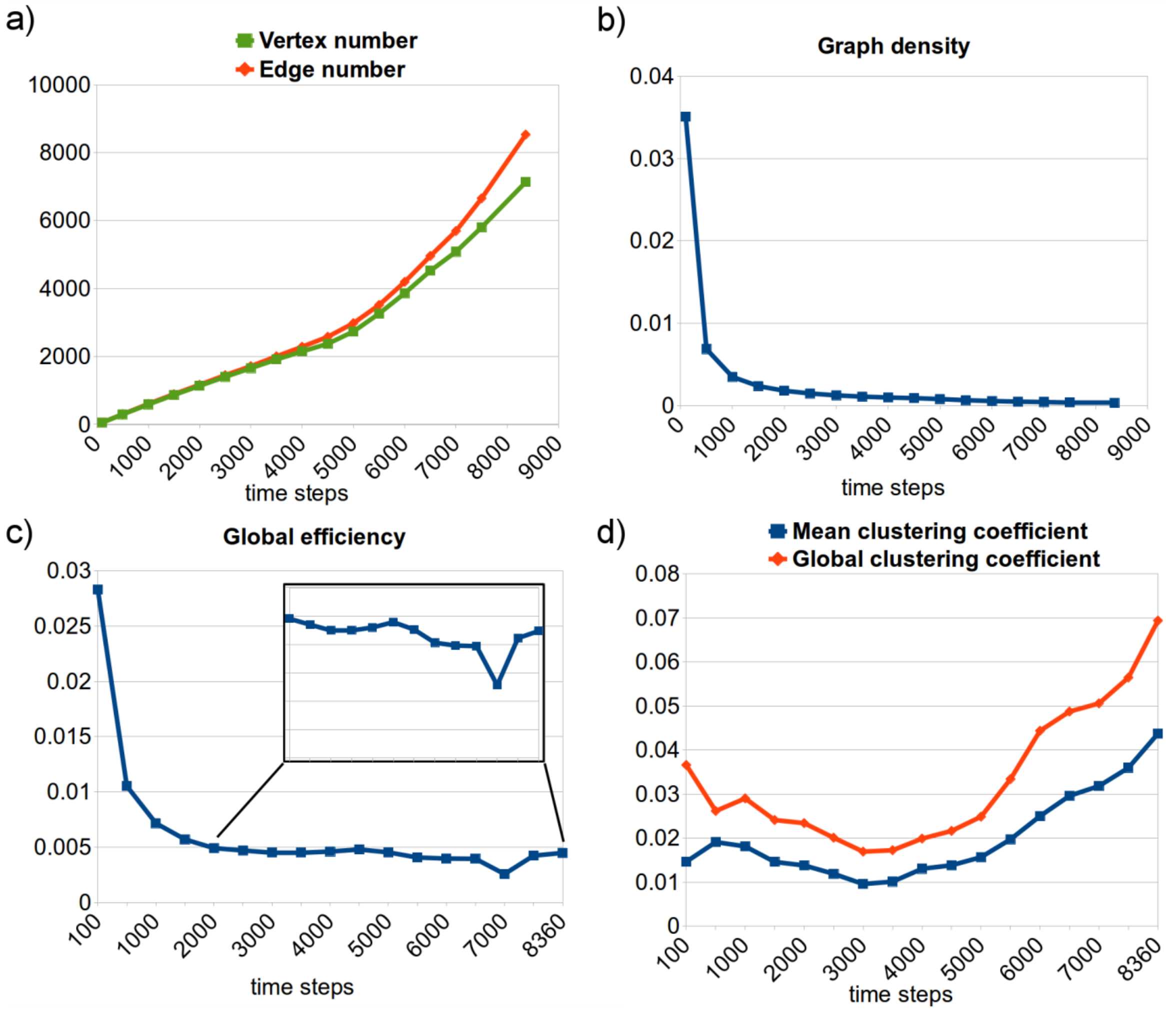

Fig. 6.24 Charts showing the vertex and edge numbers (a), graph density (b), global efficiency (c) and clustering coefficients (d) for experiment E.

The graph density, like in the previous experiments, shows an exponential decrease (Fig. 6.24b). The values are in the same order as observed during experiments A and B, confirming the similarity between the systems.

A decline of the global efficiency with minor increase between time steps 3500 and 4500 can be seen on Fig. 6.24c. There is a relatively large drop at time step 7000 but the efficiency quickly restores and rises up to 0.005 at the end of the simulation.

The clustering coefficients decrease until time step 3000 (Fig. 6.24d). This is followed by first a slow (until time step 5000), then a faster (between time steps 5500 and 8360) increase in the values. Both the global and mean clustering coefficients are greater than those in the experiments A-B, but lower than in experiments C-D.

As seen in the experiments A to D, assortative mixing characterizes the network again throughout the entire simulation. Between time steps 500 and 3500 the assortativity declines, which correlates with the decreasing clustering coefficients. The assortativity rises afterwards, so do the clustering coefficients. The network is the most assortative at the end of the simulation with an approximate value of 0.5.

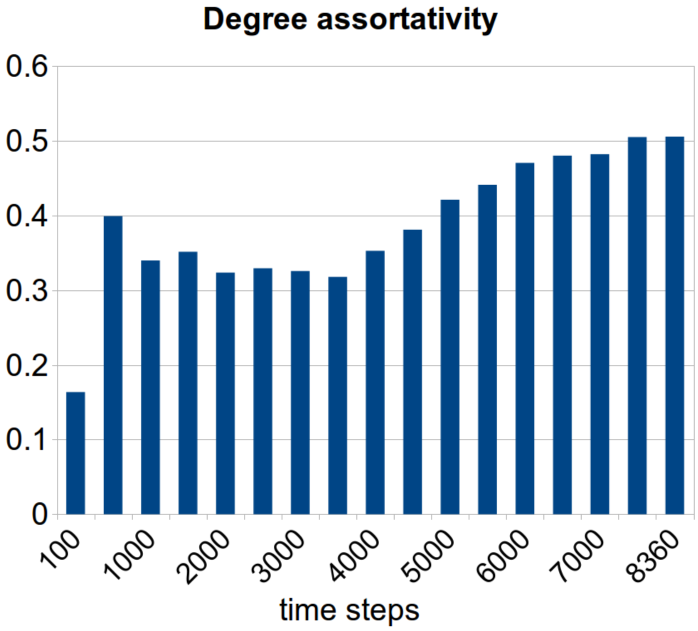

Fig. 6.25 Vertex degree assortativity during experiment E.

6.1.1.6 Experiment F

Experiment F represents the published mudcrack simulation (Bons et al., 2008). The layer's Young's modulus is twice the default (corresponding to a mean of 20 GPa), whereas the breaking strength is kept at default (that is 17 MPa - mean). The experiment was carried out in lower resolution (box width 200 particles instead of 400 used in experiments A to E), whereas the particle area change per time step was twice that of the previous experiments (0.001 instead of 0.0005). In addition to this, it only ran for 240 time steps. This essentially means that experiment F can correspond to the very start of experiment B.

Fracture nucleation is shown on Fig. 6.26 at time step 10. This fracture propagates through the layer in all directions. By time step 200 the entire box is fractured, whereas time step 240 already indicates evolving interconnections.

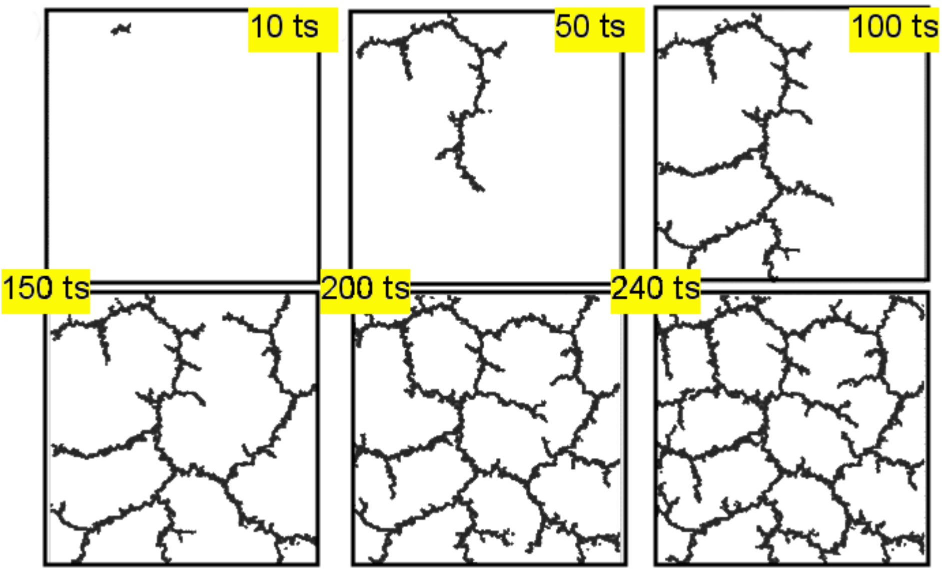

Fig. 6.26 Progressive fracture development at different time steps for experiment F. Images capture the top surface of the shrinking layer. Modified after Bons et al. (2008).

Converting the images to graphs show that there are slightly more vertices that have one neighbor than vertices that have three (Fig. 6.27). As degree 1 decreases, the degree 3 simultaneously increases, which results in the slight dominance of the latter (see time step 240 on Fig. 6.27). Entropy also rises as degree 1 and 3 are equalizing (Fig. 6.28).

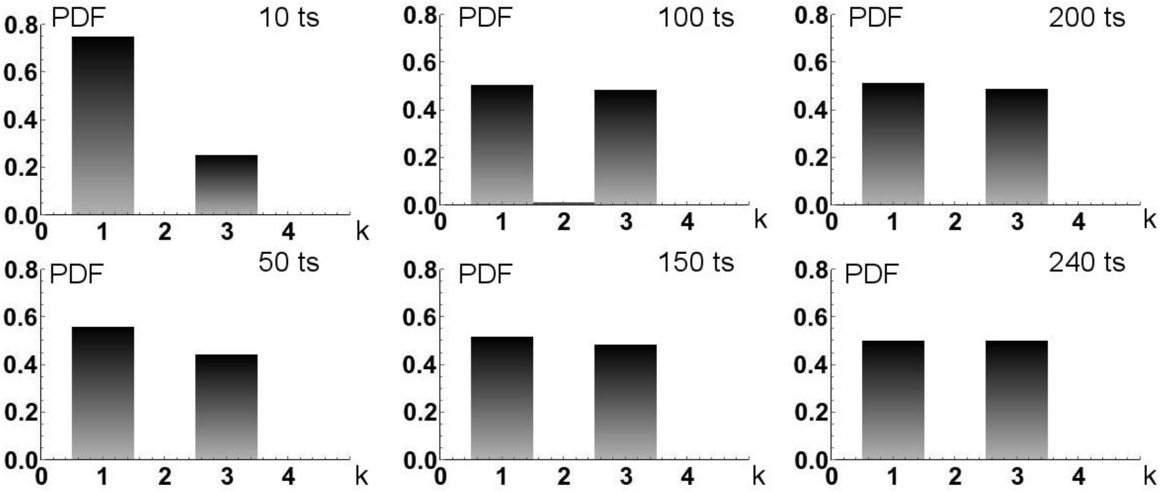

Fig. 6.27 Probability density function (PDF) of vertex degree (k) distribution at different time steps during experiment F.

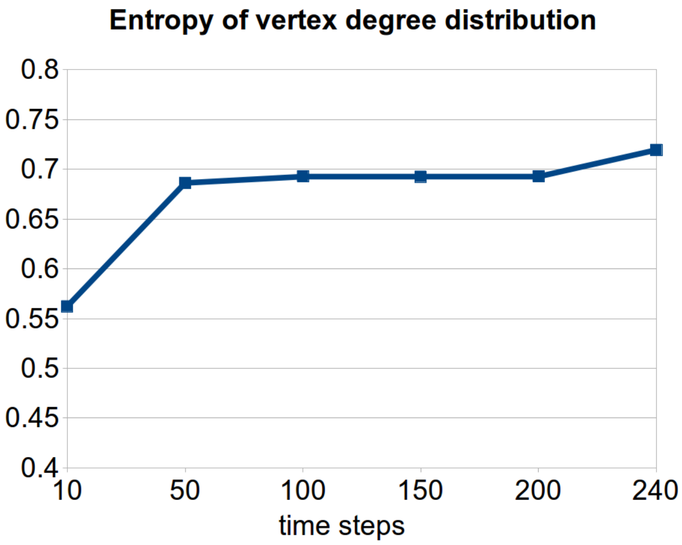

Fig. 6.28 Entropy of vertex degree distribution during experiment F.

The number of vertices and edges rises with the latter overcoming the former at time step 240 (Fig. 6.29a).

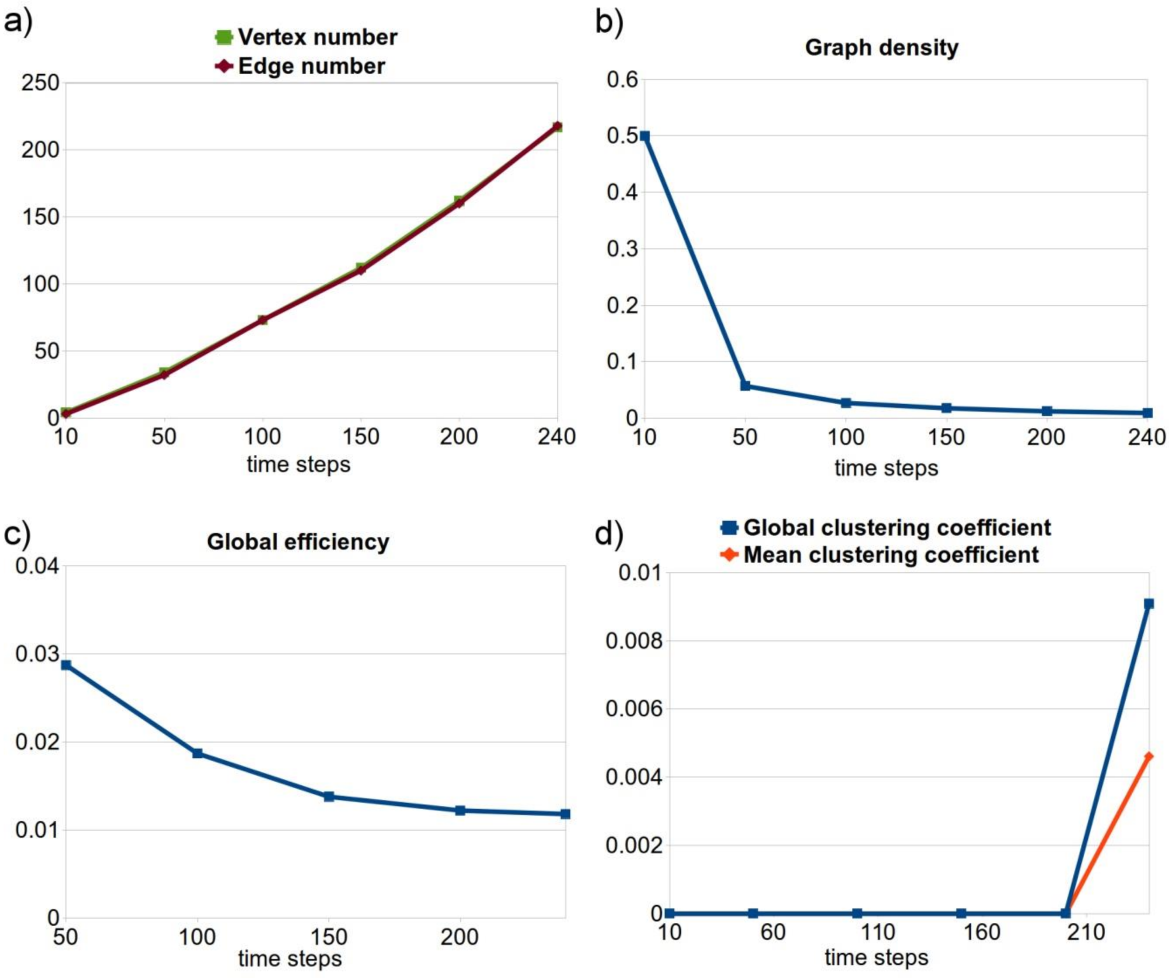

Fig. 6.29 Charts illustrating the vertex and edge number (a), graph density (b), global efficiency (c) and clustering coefficients (d) for experiment F.

Both the graph density (Fig. 6.29b) and the global efficiency (Fig. 6.29c) fall during the simulation. The trend of the reduction resembles similarities to the previous experiments.

The clustering coefficients are zero until the very last stage. At 240 time step they both increase, which correlates well with the existence of more edges than vertices (Fig. 6.29d).

The assortativity coefficients indicate that at time step 10, the system is disassortative, indicating high degree vertices connecting to low degree ones and vice versa. The fracture at this point (see Fig. 6.26) essentially consists of four vertices out of which three connect to a main vertex (i.e. triple junction). This main vertex has a degree of 3, whereas the others have a degree of 1. The graph at this point is certainly disassortative, which is reflected in the coefficient value as well. The network afterwards is characterized by assortative mixing.

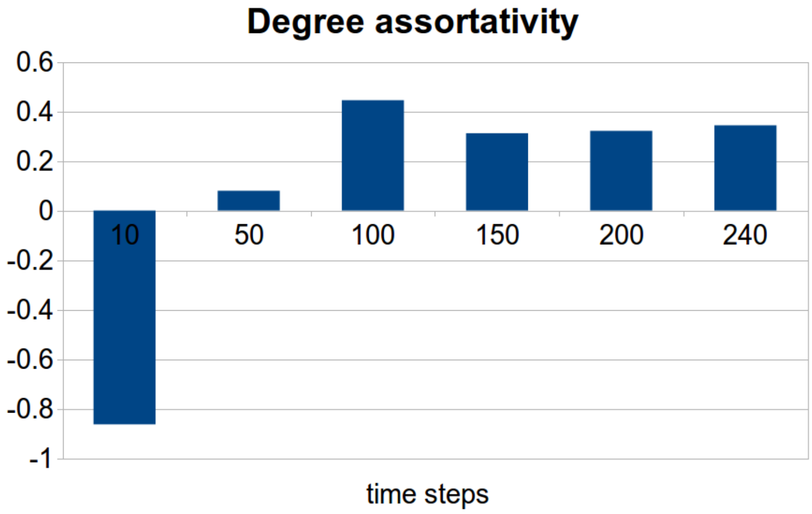

Fig. 6.30 Degree assortativity at different time steps for experiment F.

6.1.2 Flour experiments

The final networks of four flour experiments are analyzed. The experiments differ in flour thickness (5-10-24 mm), in addition to one where the flour was not compressed by a rolling pin (indicated with *, like 10 mm*).

Fracture networks of the different experiments are shown on Fig. 6.31. As the flour thickness is increased, the network becomes less tight, which means that fracture spacing increases creating larger polygons. Compressing the flour does not seem to affect the appearance of the final network as seen at 10 mm and 10 mm* (Fig. 6.31).

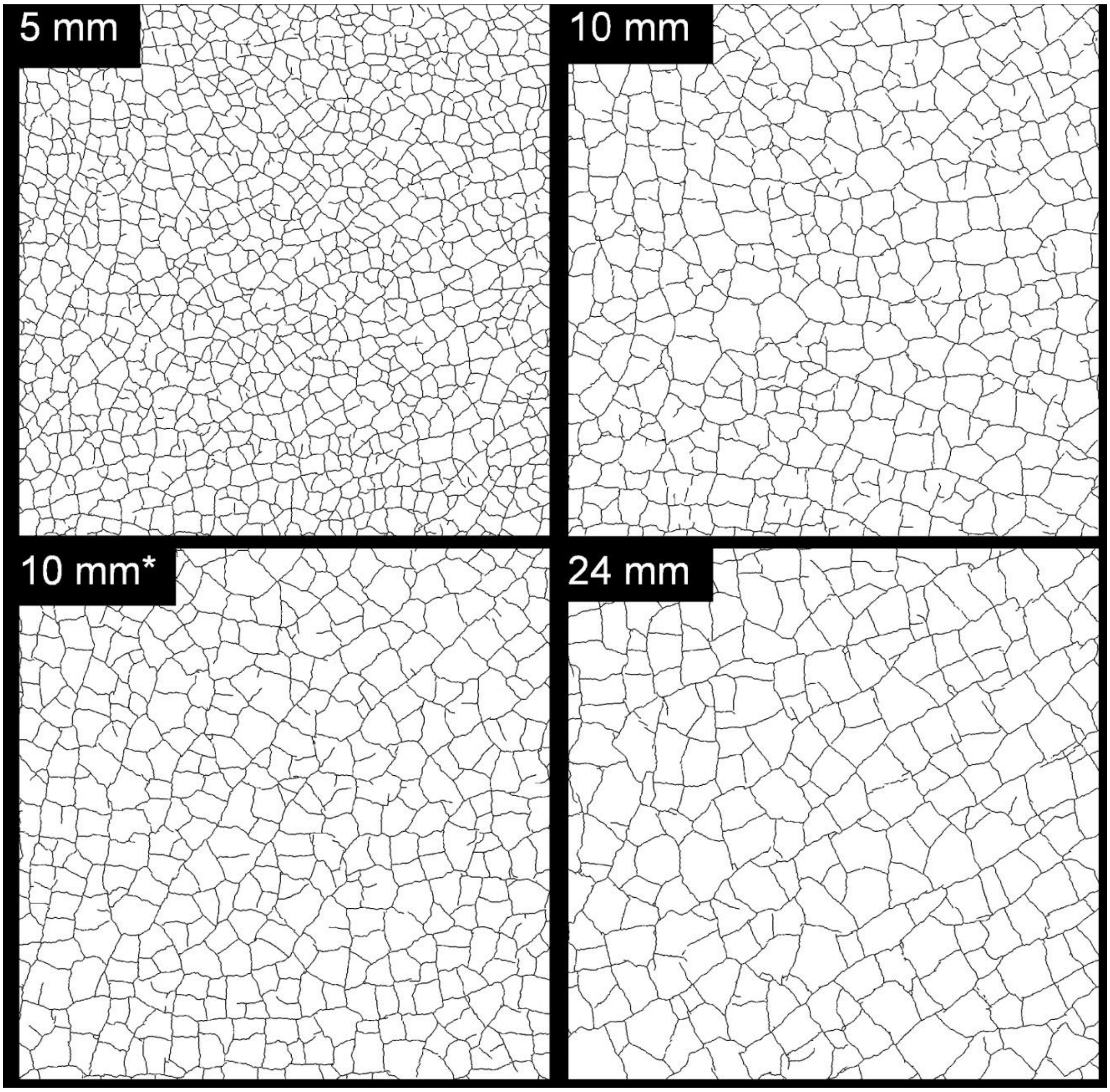

*Fig. 6.31 Results of the flour experiments showing developed fracture networks. Images are binarized and thinned. Numbers represent the thickness of the flour. * indicate that the flour was not compressed by a rolling pin. Images capture the top surface of the stretching layer.*

The different network appearances are reflected in the graph measures. Looking at the vertex degree distributions we see that in all cases the degree 3 dominates the network over degree 1 and 2. This dominance, however, varies throughout the experiments. The 5 mm case shows the largest, whereas the 24 mm case has the smallest difference between the probabilities for degree 1 and 3. Degree 2 and 4 subordinately (below probability 0.01) appears in all the compressed cases.

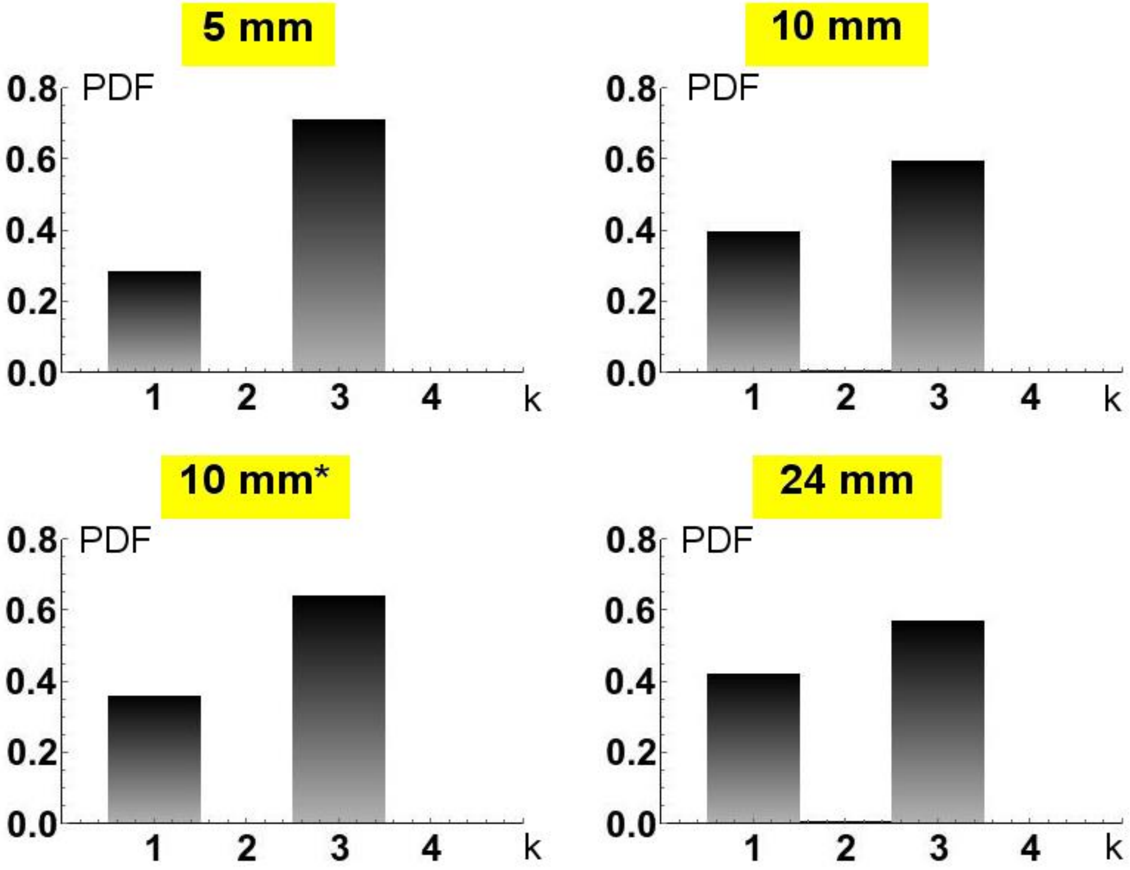

Fig. 6.32 Probability density function (PDF) of the vertex degree (k) distribution for the networks developed during the flour experiments.
Flour thicknesses are 5-10-24 mm, whereas 10 mm indicates the experiment where the flour was not compressed by a rolling pin.*

The entropy of the vertex degree distributions follows the characteristics observed on Fig. 6.32. The 5 mm case has the lowest, whereas the 24 mm the highest entropy (Fig. 6.33). Since the probability difference between degree 1 and 3 is the second largest and only these two degrees appear in the 10 mm*'s network, it has a lower entropy than its compressed equivalent (10 mm).

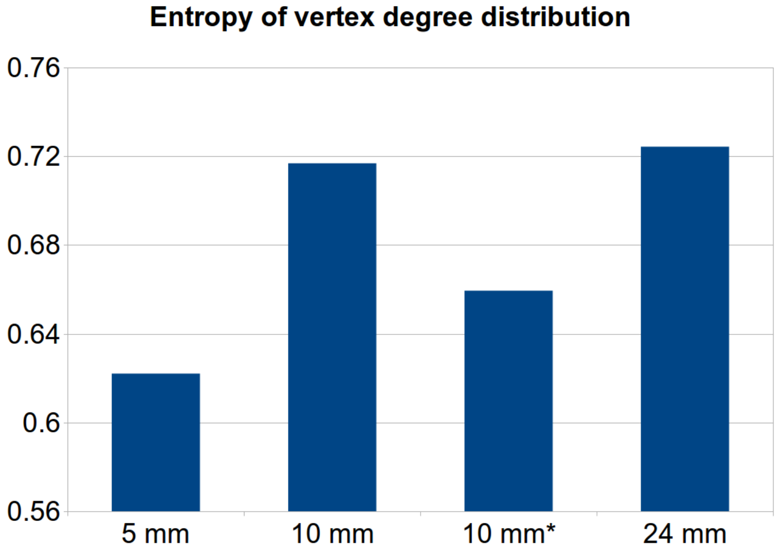

Fig. 6.33 Entropy of vertex degree distribution for the networks developed during the flour experiments.
*X axis shows the flour thicknesses with * indicating the non-compressed case.*

Based on the vertex and edges numbers, the 5 mm case represents the largest and the 24 mm the smallest network (Fig. 6.34a). In all four experiments the edge numbers overcome the vertex numbers but with different magnitudes. The largest difference appears at the 5 mm experiment, whereas the smallest at the 24 mm. The second largest difference can be observed at 10 mm*, which can be explained by the lower number of vertices relative to the 10 mm case.

While the graph density increases with decreasing vertex number (Fig. 6.34b), the global efficiency shows a different pattern (Fig. 6.34c). The highest efficiency is found at the 5 mm experiment, whereas the next most efficient network is the one developed during the 10 mm* experiment. Its compressed equivalent, the 10 mm case, obtains the lowest efficiency. As the efficiency is image size dependent, size-normalized values are also shown on Fig. 6.34c so that these networks could be compared to the Elle ones. Efficiencies in this case are higher, but are still a magnitude lower than previously measured.

The 10 mm experiment, however, has the highest clustering coefficients, whereas the most efficient network, the 5 mm, shows the lowest clustering in the experiments (Fig. 6.34d). The coefficients are quite similar in the 10 mm* and 24 mm cases (with the former being slightly higher).

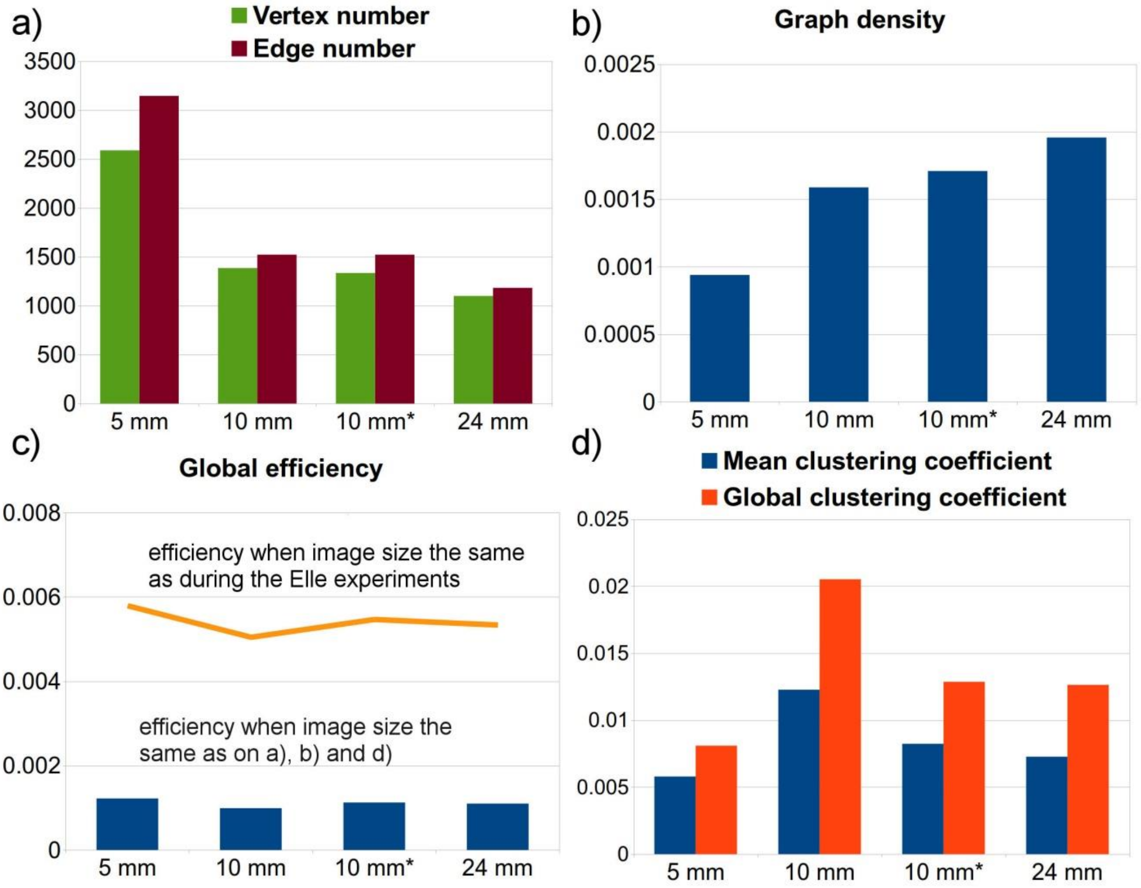

Fig. 6.34 Charts showing the vertex and edge numbers (a), the graph density (b), global efficiency (c) and clustering coefficients (d) for the networks developed in different flour thicknesses.
** indicates the non-compressed case. Global efficiencies in case the image sizes are the same as during the Elle experiments are also shown.*

All four networks display assortative mixing (Fig. 6.35). The least assortative is the 10 mm*, whereas the most assortative network is the one developed at the 24 mm experiment.

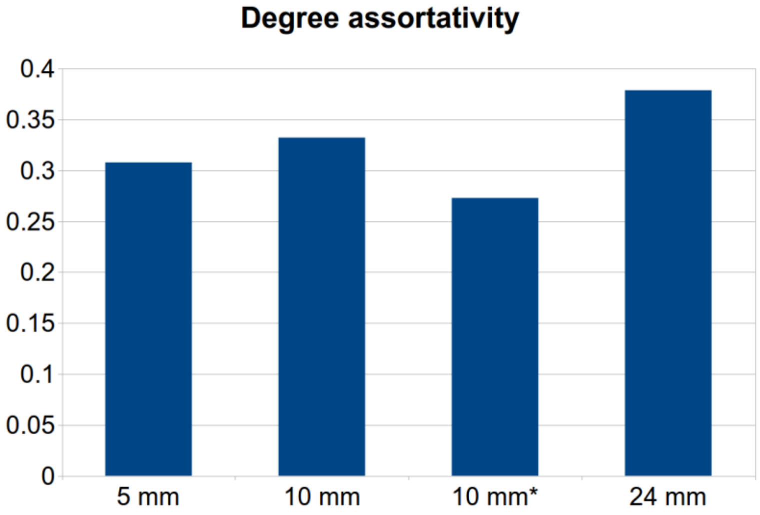

Fig. 6.35 Degree assortativity in the flour experiments.
*Numbers indicate flour thicknesses with * being the only non-compressed case.*

6.2 Hydrobreccia

The hydrobreccia simulation differs in two ways from the previous mudcrack and flour experiments. First of all, the orientation of the simulation box relative to the stresses is different. All the previous simulation networks (i.e. images) developed due to homogeneous stress fields because of the shrinking. The hydrobreccia experiment, however, represents a cross section of the crust where gravity is applied on top. This means that the stress acts perpendicular to the developing network (analyzed images) and stress field responsible for the deformation is heterogeneous. Second of all, during this simulation fluid pressures also contribute to the deformation and thus to the network development. These differences make it especially interesting to compare the evolution of the hydrobreccia with the earlier networks in a quantitative and qualitative manner.

Deformation is initially characterized by vertical fracture formation (Fig. 6.36). These fractures appear in clusters and until time step 4000, propagate mainly in the vertical direction, i.e. in the direction of the gravity. Images from the successive time steps show that fracture propagation shifts in the horizontal direction. This is due to the fluid pressure build-up below the seal, which causes the main stress direction to switch from vertical to horizontal. The horizontal fractures make it possible for the clusters to interconnect. As a result, a well-connected fracture network is developed by the end of the simulation.

Graph equivalents show that at time steps 3000 and 4000 the network is dominated by vertices with one connected neighbor and only a small amount of vertices have three connected ones (Fig. 6.37). At time step 5000, however, the degree 3 starts to rise, which coincides with the formation of the horizontal fractures. Time step 6000 still shows that slightly more vertices have one connected neighbor rather than three. The successive time steps, however, exhibit the increasing dominance of degree 3 over 1 as the network becomes more connected.

The entropy is initially small as the network is mainly made up of vertices with degree 1 (Fig. 6.38). As the degree 1 and 3 probabilities are equalizing, the entropy increases. When the degree 3 becomes increasingly dominant, the entropy starts to fall, which points to a more heterogeneous system.

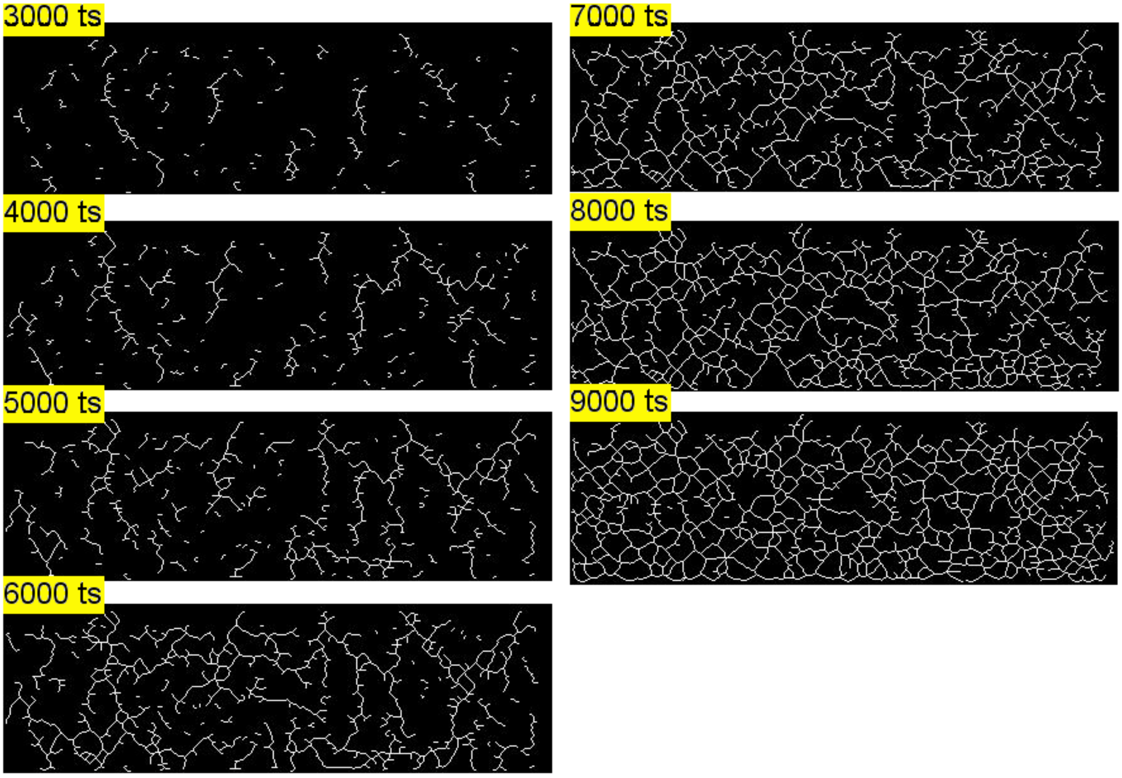

Fig. 6.36 Progressive development of the hydrobreccia network.
Images are binarized and thinned. They represent a cross section through the crust, and the area between the seal (on top) and the bottom of the deformation box.

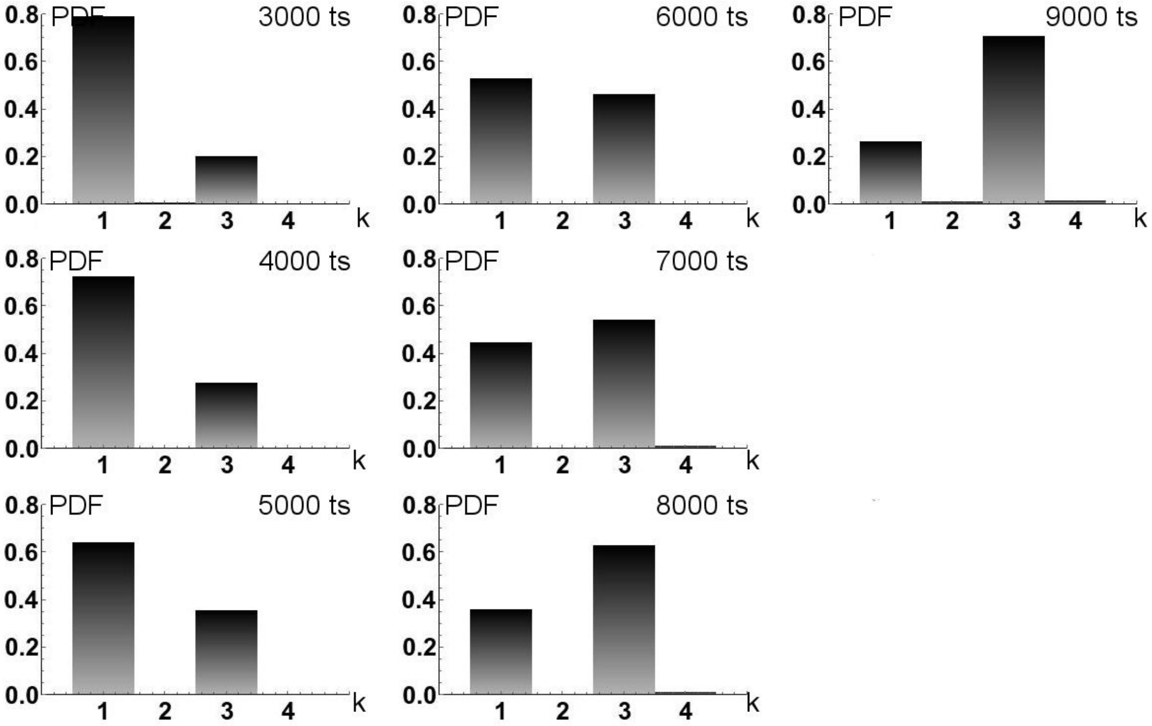

Fig. 6.37 Probability density function (PDF) of the vertex degree (k) distribution during the hydrobreccia experiment.

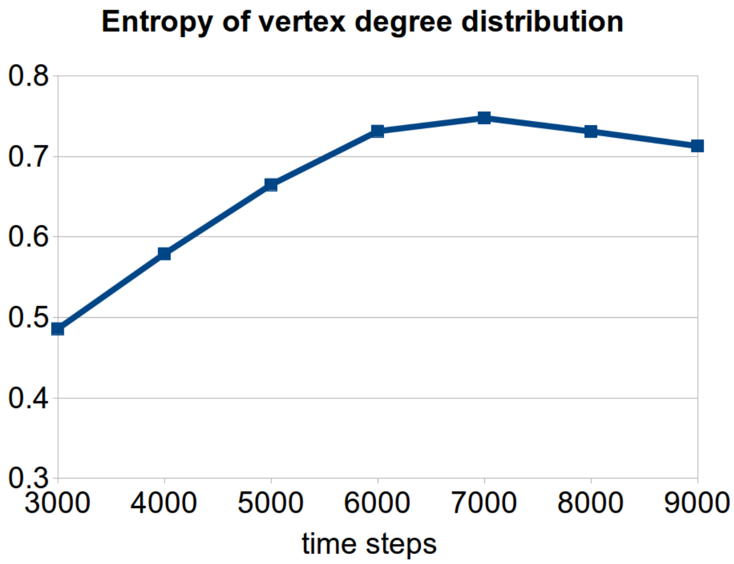

Fig. 6.38 Entropy of vertex degree distribution during the hydrobreccia experiment.

The slope for the vertex and edge number is converging until time step 6000, after which they diverge (Fig. 6.39a). While new vertices barely form at the end of the simulation (the slope flattens out), new edges still develop between existing ones. The numbers clearly reflect the vertex degree shift seen on Fig. 6.37.

The graph density values fall until time step 7000 (Fig. 6.39b). There is a slight increase in the graph density at time steps 8000 and 9000, which coincides with the entropy decrease described before.

The global efficiency stays relatively constant until time step 5000, and steeply increases throughout the simulation (Fig. 6.39c). The maximum value of 0.01 is reached at the end of the simulation, which is larger than in any of the previous cases.

The clustering coefficients during time steps 3000 and 4000 are zero. They show a general rise afterwards with a minor drop at time step 7000 (Fig. 6.39d).

The network, similarly to the previous cases, exhibits increasing assortative mixing reaching a maximum value of 0.047 (Fig. 6.40). This is close to what was found in the other experiments.

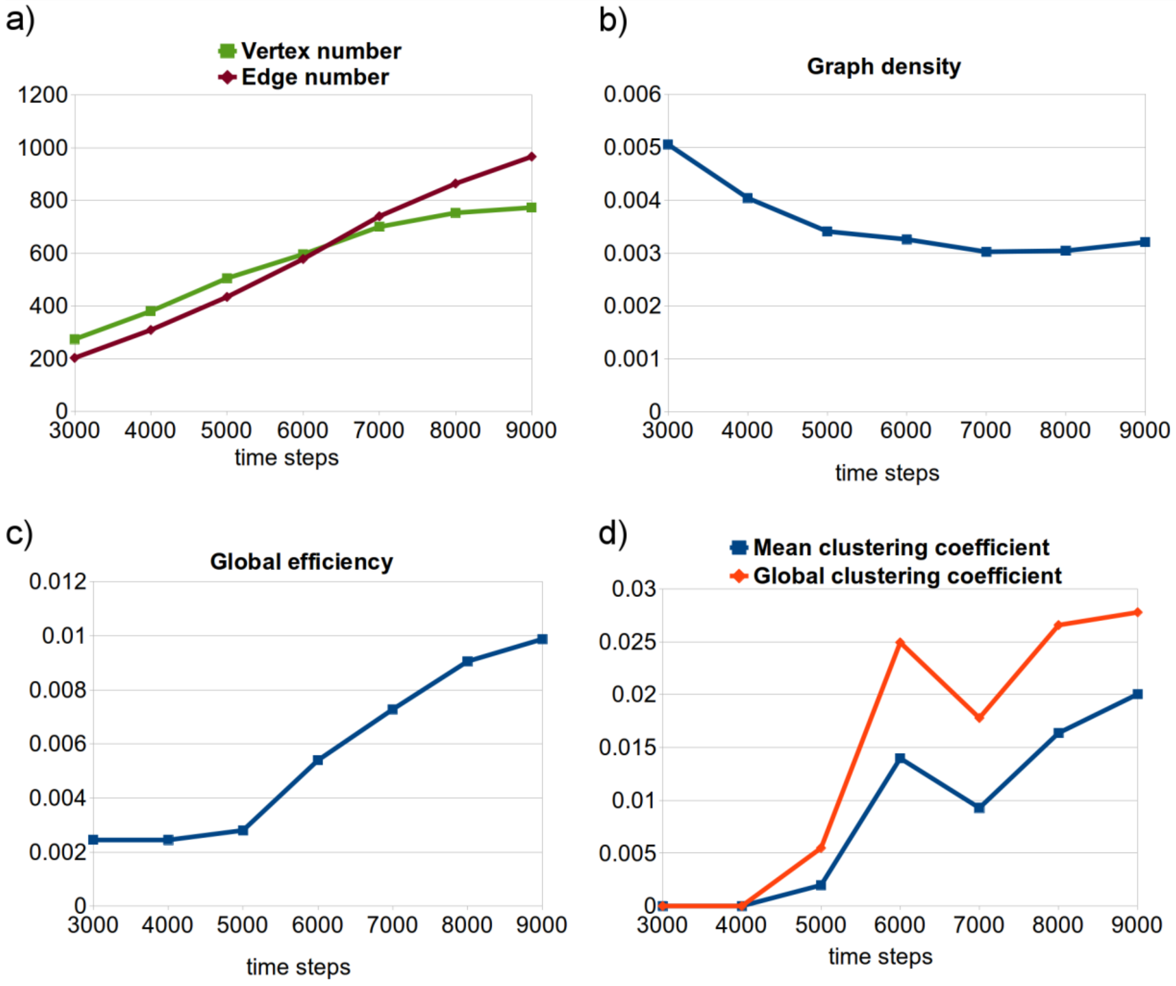

Fig. 6.39 Charts showing the vertex and edge numbers (a), graph density (b), global efficiency (c) and clustering coefficients (d) for the hydrobreccia experiment.

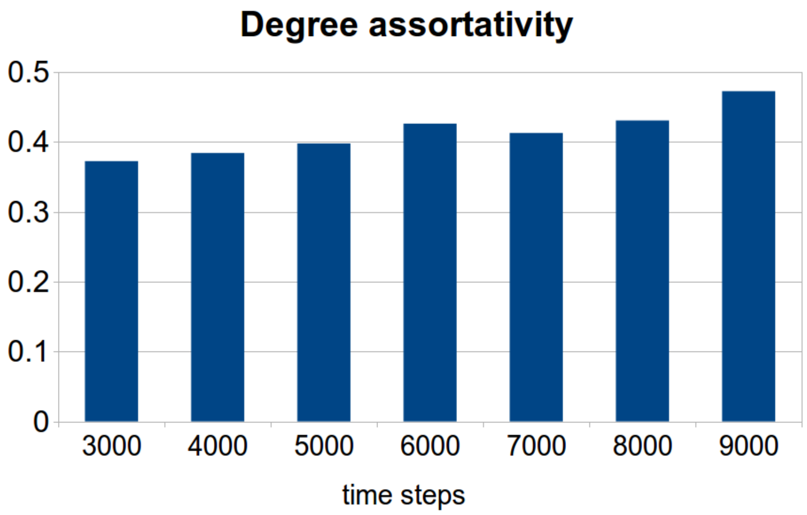

Fig. 6.40 Vertex degree assortativity during hydrobreccia experiment.

6.3 Discussion

This chapter presented graph theory as a possible tool to analyze dynamic fracture network evolution in a quantitative and qualitative manner. Prior to any calculations, one has to decide what kind of networks are they dealing with, what their scopes are and what limitations (/simplifications) are they willing to take. The image processing, graph representation of the fracture network and calculations on the graphs can vary depending on their choices.

I chose to treat fractures as segments connecting vertices that represent either end-points or junctions. This means that if two fractures cross each other at one point, they will be segmented into four fractures (lines) joined by one vertex (Fig. 6.41b). However, one can choose to treat fractures as a whole and not segmenting them (Andresen et al., 2013). The graph in this case will show the crosscutting relationship between the fractures. An example of this is illustrated on Fig. 6.41c. A vertex is placed on the middle of the fracture. When two fractures cross each other, the relevant vertices will be joined contributing to the graph. The end-result will be a smaller graph with fewer edges. This representation might be better if one is dealing with several generations of fractures and/or veins with different orientations. According the Andresen et al. (2013) segmentation of the fractures (i.e. like on Fig. 6.41b) narrows the vertex degree distribution with an upper limit of 4. Their representation (like on Fig. 6.41c), however, allows a much wider degree distribution, since a long fracture that crosscuts several others will have a degree equal to the number of fractures it crosses. It is therefore self-evident that the graph measures in the two graph representations will be completely different. In addition to this, the graph on the Fig. 6.41c is much closer to being complete (that is having higher graph density) than in the other case (Fig. 6.41b). The graph of the latter will never reach completeness since in order to do so fractures need to join all the pairs of vertices without cutting any existing fractures and creating new vertices. This would not be a real geological fracture pattern. The networks I have presented are mainly characterized by interconnections rather than crosscuttings, and the propagating new fractures halt at existing ones. Due to these, segmenting the fractures is probably more suitable.

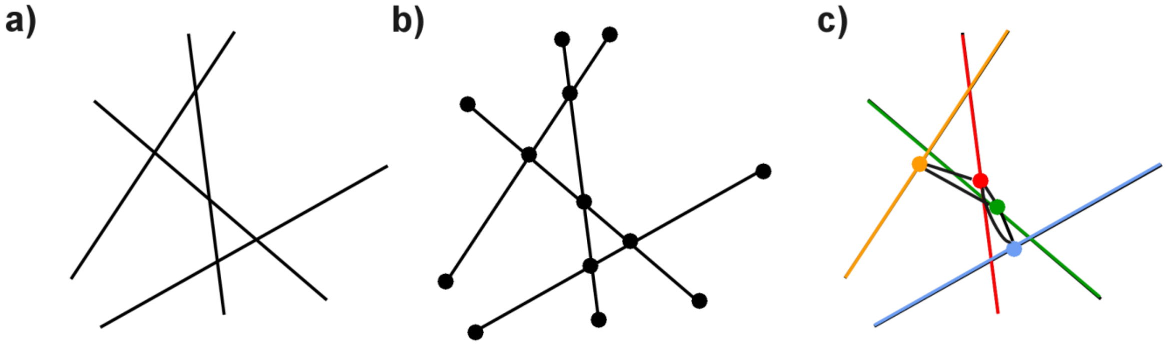

Fig. 6.41 Different ways of representing a fracture network as a graph.
(a) Initial fracture pattern. (b) Segmenting fractures so that they connect end-points and junctions.
(c) Treating fractures as a whole, and creating graph based on the crosscutting relationship between the fractures.

Prior to discussing the dynamic network topology, I will first briefly comment on the fracture patterns.

6.3.1 Observed fracture patterns

Fracture initiation and the developed patterns during experiments A to E showed fundamental differences. These differences can be attributed to the mechanical properties of the layer. Experiments A and B represented layers with low stiffness. Under the same strain, a material which has low stiffness breaks harder than the one which has a higher stiffness. The driving stress for fracturing is the tensile stress, and if this overcomes the strength of the material, fracturing will take place. In the case of experiments A and B the soft layer develops low stresses in response to deformation, and thus fracturing is impeded. When a fracture finally initiates, the driving stress around the fracture is larger than the stress developed elsewhere, which means that it takes less stress to propagate an existing fracture than to initiate another one at a different location in the deformation box. This allows fracture propagation, which explains why the entire fracture network is developed from one fracture that initiated at the start of the simulation (Fig. 6.42). In contrast to this, the network develops by joining separate clusters during experiments C and D (Fig. 6.42). This is due to the existence of a high stiffness layer, which develops higher stresses and therefore can fracture more easily than the softer ones. A fracture in this case affects a much narrower area of the simulation box than in the soft case and thus a single fracture cannot relax the whole box. This will impede the propagation and favor the formation of new fractures elsewhere in the deformation box. The result is the development of fracture clusters all over the box, which will eventually interconnect. In experiment E the stiffness of the layer is compensated with high breaking strength, which counteracts the stiffness and allows fracture propagation. As seen in experiment F, the scaled mean of 20 GPa still favors the propagation, therefore the switch between the two types of fracturing should be somewhere between 20 and 50 GPa in the model.

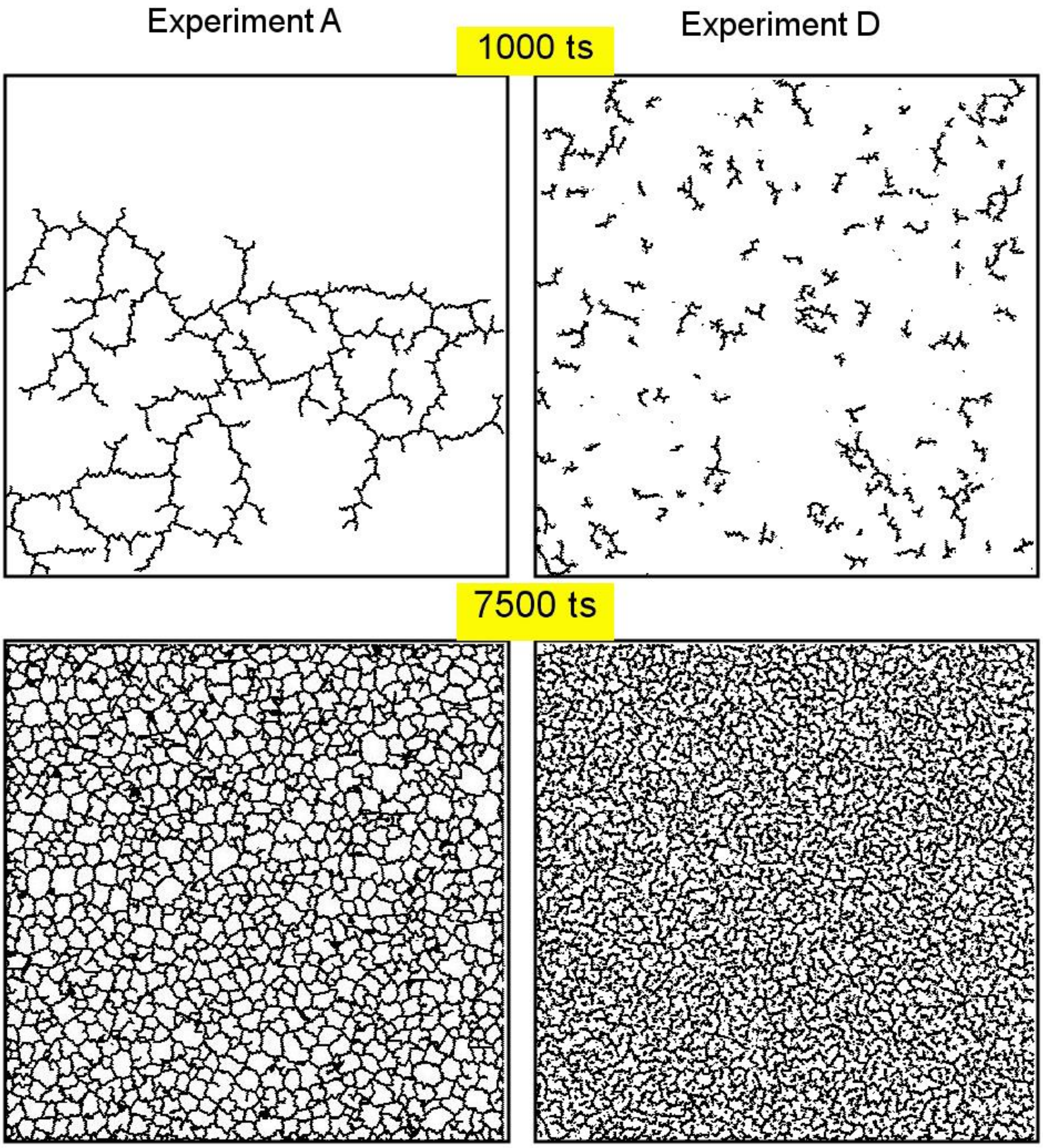

Fig. 6.42 Comparing the fracture network evolution of Experiments A and D at time steps 1000 and 7500.

The hydrobreccia experiment illustrates the importance of fluid pressures. As the seal's stiffness impedes fracturing, the fluid pressure can build up below it leading to a switch in the main stress direction. This is clearly responsible for the formation of the horizontal fractures which allows the development of a connected network.

Fracture patterns evolved during the flour experiments clearly indicate that the increasing flour thickness increases the fracture spacing. This has also been reported for mudcracks (Goehring et al., 2010). Flattening the flour with a rolling pin, however, did not affect the patterns.

The differences in network appearances were clearly reflected in the topology measures.

6.3.2 Dynamic fracture topology

Characterizing topology of the fracture network can be approached from many directions. In this chapter I presented the following dynamic measures: probability density function of vertex degree distribution (PDF), entropy of vertex degree distribution, number of vertices and edges, graph density, global efficiency, mean and global clustering coefficients, and graph assortativity. Table 10 lists these variables and show how they change throughout the experiments at different stages of the fracture network evolution.

	Stage 1 Fracture initiation	Stage 2 Fracture propagation	Stage 3 Fracture interconnection
Vertex vs. Edge number	Vertex > Edge	Vertex ≥ Edge	Vertex < Edge
PDF: $P(k_1)$ vs. $P(k_3)$	$P(k_1) >> P(k_3)$	$P(k_1) \geq P(k_3)$	$P(k_1) < P(k_3)$
Global efficiency	High	Decreasing	Increasing
Graph density	High	Decreasing	Decreasing
Clustering coefficients	0	Increasing	Increasing
Assortativity	Low	Increasing	Increasing

Table 10 Summary table showing how the variables change as the fracture network develops. PDF corresponds to probability density function that a vertex has a certain degree: $P(k_1)$ is the probability that the vertices have one connected neighbor, whereas $P(k_3)$ is the probability that the vertices have three connected neighbors. Entropy is not listed as it is related to the PDF.

Looking at the probability that a randomly chosen vertex has a certain degree can shed some light on the network connectivity. Vertices in the networks shown here have degrees between 1 and 4. If the probability for a degree 1 is higher than any other, then most of the vertices have only one connected neighbor. These can correspond to dead ends in a larger fracture or in smaller disconnected segments (e.g. two vertices linked to each other but not to the main fracture). During the initial stages, all the experiments showed higher probabilities for degree 1. This was due to either the dominance of fracture propagation over interconnections (experiments A, B, E, F) or dominance of disconnected fracture clusters (experiments C, D). The fact that most of the vertices have a degree of 1 therefore does not mean that the network is not well connected. It can be fully connected and have lots of dead ends, and fractures could act as local percolation sites. The small amount of links, however, indicates that the network is not very robust against edge-removal, which -in geological terms- means that if one fracture heals, the system can become fully disconnected. The probability for degree 1 is decreasing in all cases, whereas the probability for a degree of 3 simultaneously increases. The timing for the switch in dominance depends on the mechanical properties. During experiments A, B, E and F, the switch takes place by time step 500 (or in the latter case by time step 240). This early timing can be explained by the fracturing characteristics. The network is much tighter (small spacing), which means that the cracks are much closer to each other. The high differential stresses surround their tips as shadows, which, due to the small spacing, can easily overlap each other. Fractures will propagate into these areas causing the dead end segments to join together and the vertices with a degree 1 to disappear. This is the main process that decreases the degree 1 and ultimately increases the probability for degree 3. During experiment C and D the switch between these two major probabilities occurs much later, by time steps 8500. This can be due to the formation of fracture clusters all over the deformation box as explained before. Since fracture spacing in the beginning is quite large, fractures do not interact, which result in many dead ends (i.e. vertices with only one connected neighbor). Clusters only interconnect at the end of the simulations resulting in the probability switch. In general we can say that the higher the probability is for a vertex degree 3, the more interconnected the network. The degree 2 is relatively subordinate during all the experiments, which can be explained by the fact that these vertices tend to become triple junctions quite quickly. A vertex having four connected neighbors is also rare due to the nature of the networks (fractures rather halt at existing ones than to crosscut them).

The entropy of the vertex degree distribution is often considered as a tool to characterize disorder in the system. A high disorder, that is a heterogeneous network, features high entropy values, whereas a homogeneous one would have low entropy. It is apparent from the entropy definition that its values are completely unrelated to any connectivity measures. A network with low entropy can represent a system with all its vertices having one connected neighbor, as well as a system with all its vertices being triple junctions. In both cases, the networks are considered homogenous but the connectivity and other measures can be (and are) fundamentally different. Yet, the evolution of the entropy in the experiments nicely shows that the networks are in the process of becoming more homogenous by increasing the dominance of triple junctions.

The relative quantity of edges to vertices is indicative of the connection in the system. A nucleating fracture has two vertices and one edge. If this fracture propagates, the edge becomes longer but the vertex number remains the same. When a junction forms both the edges and vertices increase but the vertices still overcome the edges in number. In case an edge forms between two existing vertices, the number of edges starts to rise faster than the vertices. These interconnections lead to a higher amount of edges relative to vertices. During the early stages of experiments more vertices exist than edges. As the latter overcomes the former (and this coincides with the probability degree 1 and 3 switch), their slopes diverge which shows the increasing interconnections in the system. The timing of this depends on the mechanical properties – similarly to what has already been described earlier. In general the larger the difference between the vertex and edge numbers, the larger is the difference between the probability for a degree 1 and 3 as well.

The graph density in all cases decreases with increasing graph size. This indicates that the networks are getting further away from being complete graphs in spite of the interconnections. This is an artifact emerging from segmenting the fractures (as seen on Fig. 6.41b). Fig. 6.43c illustrates why the graphs in this chapter cannot reach completeness. A graph is complete (reach a density of 1) if all the pairs of vertices are joined together. While some can be linked without crossing any existing edges, others do need to cut through them. As in our definition when two edges cross each other, a vertex is placed at the junction. This process therefore creates more vertices, which ultimately makes the network further away from completeness since even more edges needed to connect all the vertices. As discussed before, by defining networks in a different way like Andersen et al. (2013) did, the graph equivalents would have much higher densities.

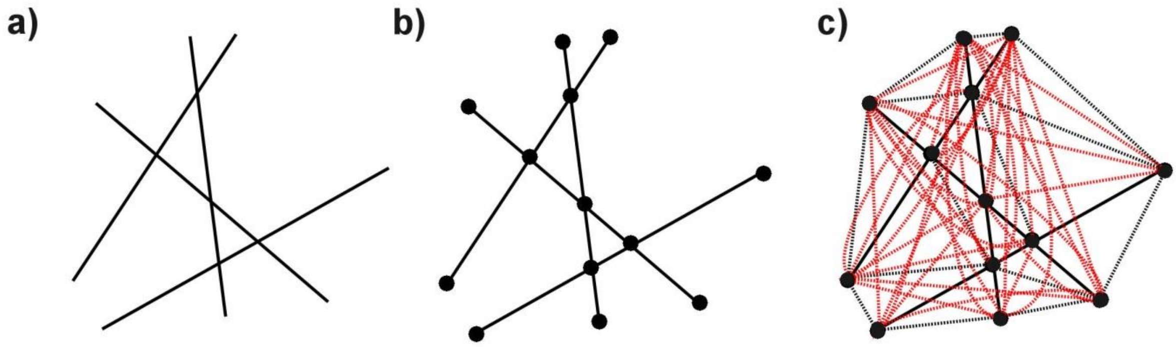

Fig. 6.43 Example illustrating why the graphs cannot reach completeness, i.e. high density. (a) A simple fracture pattern and its graph equivalent (b). (c) Same graph with more connections but not complete. By linking the vertices, a few edges do not cross other edges (black dashed lines). Red dashed lines are the links that connect even more vertices but by doing so they cut through existing edges and - in our definition - create even more vertices.

Global efficiency shows how efficient the network is in transferring information. It is defined as the inverse average shortest path distance between all the pairs of vertices. The efficiency evolution of the mudcrack experiments reveals that in all cases there is a decrease in efficiency during the early stages of deformation. This can be explained by two processes. (1) Fracture propagation elongate the edges, creating a longer path through which information also travels longer, making the network less efficient. In addition to this, (2) as the network is becoming larger the vertices are getting further away from each other, which also decreases the efficiency. As the experiments proceed and more interconnections form linking vertices far away from each other, the efficiency values start to increase. This indicates that the shortest path between vertices decrease due the newly formed edges. In geological terms this suggests that fluids could flow through the fracture network much more efficiently (and faster) than earlier. The timing of this permeability increase – again – is highly dependent on the mechanical properties of the matrix. A stiff rock could easily fracture but would (could) delay the development of a network. On the other hand, it would take more stress to fracture a softer rock but a network might develop earlier.

When comparing the efficiencies of the mudcrack and hydrobreccia experiments, evidently not only do the values differ but the slope characteristics too (Fig. 6.44). The efficiency slopes clearly diverge, which can be explained by network orientation relative to the main stress directions. Mudcracks were oriented parallel, whereas the hydrobreccia perpendicular to the main stress direction. This could imply that the mudcracks in cross-sections are much more efficient networks than parallel to the layers. Conversely, the hydrobreccia could be more efficient (has higher permeability) in the presented orientation than layer-parallel.

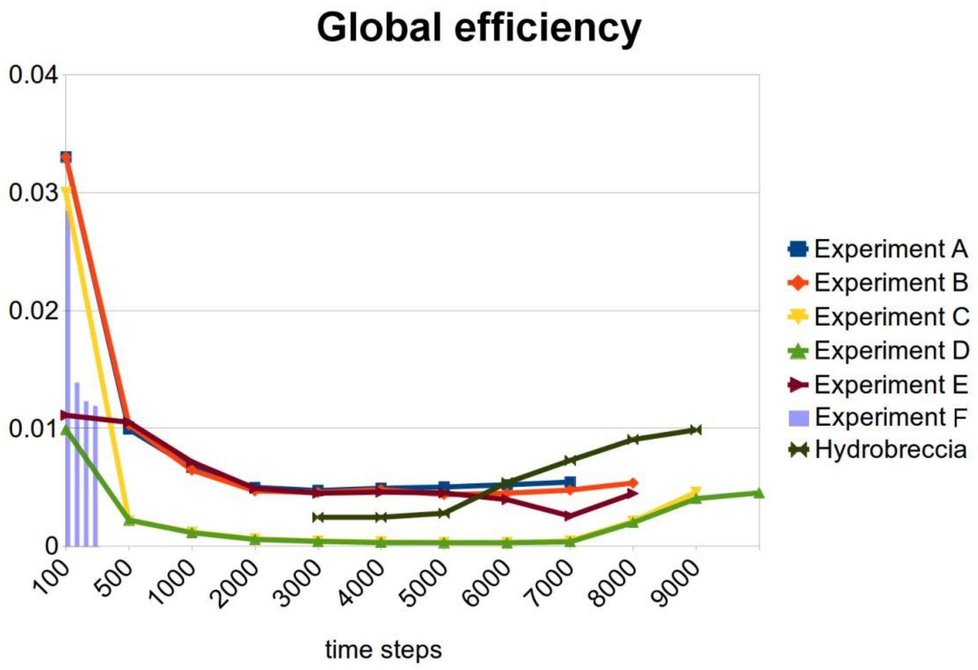

Fig. 6.44 Composite global efficiency chart including all the mudcrack and the hydrobreccia experiments.

The efficiency measure can be of much importance in a geological framework. It can be applied to networks with different nature and appearance to compare their relative efficiency in transferring fluids. Prior to comparison, however, one needs to be aware (1) whether their networks are edge-weighted and (2) if so what do the weights correspond to. In addition, (3) in case the weights are automatically assigned based on the lengths, only networks represented on same-sized images (same pixel width and heights) can be compared. Certainly, if one is dealing with a network and an image where scale is indicated (e.g. outcrop picture showing a scale), it is better to weight the edges based on the true scale, which would get rid of the image-size dependence. Similarly, image size becomes irrelevant when one is carrying out calculations on images that are produced by the same model. This can correspond to the mudcrack and hydrobreccia networks in this chapter. As both types of networks were produced in a default size simulation box by Elle, the captured images have the same (pixel) size, which makes it possible to compare the different values. However, the flour experiments had larger image sizes, so by re-sizing them onto the same pixel width and height as the Elle images, one can calculate and then compare the efficiency values to the Elle networks (as seen on Fig. 6.34c).

Moving onto the clustering coefficients that represent the amount of clustering (tight connections) in the system, we have seen that they do not show a continuous trend, but rather a general one with fluctuations. This can be explained by the fact that both the coefficients calculated in the classical way are very sensitive to where new edges form. The measurements only take the first neighbors into account, which means that in a simple triangle (having a maximum coefficient) if a new edge initiates from the middle of an existing one, the clustering coefficients drop down to zero since the direct connection between the first neighbors is interrupted. The network is still tightly connected but this is no longer reflected in the clustering coefficients. To eliminate this one could calculate the clustering by considering the second, third and so forth order neighbors. This is what Andresen et al. (2013) also suggested. While their measure gets rid of the described issue, the classical clustering formulas also give relevant (and reasonable) results of the presented networks. Most of the analyzed networks in this chapter were targets for dynamic measures to quantify the evolution. Provided that during one stage the clustering issue affected the coefficient values, they quickly got restored due to the fracture propagation and interaction. This is confirmed by all the experiments; if the coefficient decreases at one stage, it does not keep falling but restores and even increases (Fig. 6.45). In addition to this, the general trends clearly indicate increasing connections between the vertices, and thus increasing connectivity of the network overall. However, analysis of a single network (i.e. without any evolution data) would probably require a more precise formula for the clustering, such as the one presented by Andersen et al. (2013).

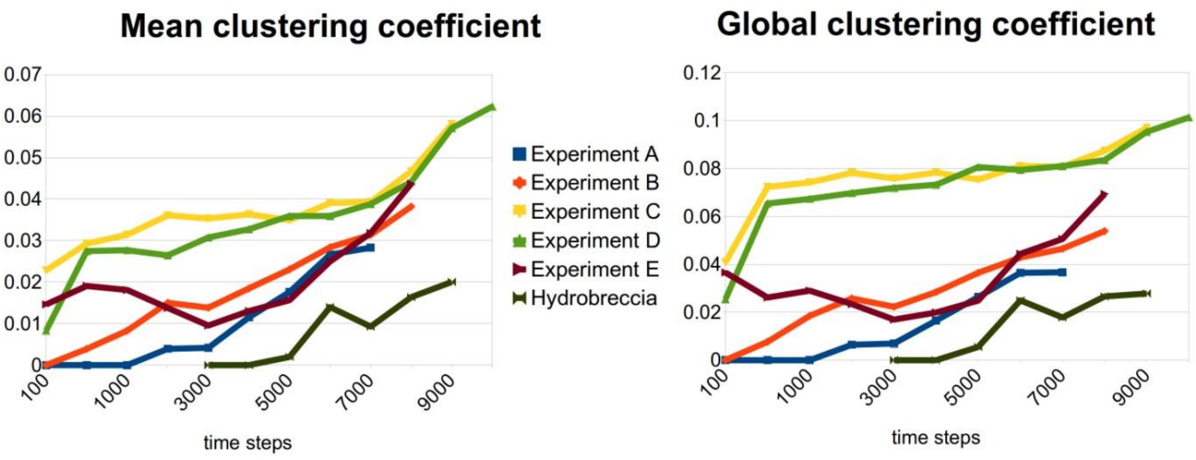

Fig. 6.45 Mean and global clustering coefficients for the mudcrack and hydrobreccia experiments.

The classical clustering formulas can also produce higher values for a disconnected network. This can be seen at experiments C and D, where the disconnected systems show much higher clustering than the other, connected ones. Around time step 9000, however, most of the experiments reach (or are about to reach) the high coefficient values produced by experiments C and D. In general, large clustering indicates tightly connected areas in the network where intense percolation could occur.

All the presented networks exhibit assortative mixing, which means there is a tendency for similar-degree vertices to join together. This finding could be a result of (1) the way the network is defined as a graph (i.e. segmentation) and/or (2) the nature of these networks. I believe the latter is more important in this case. Mudcracks generally represent hexagonal networks, which ultimately are assortative. A tightly fractured rock (breccia) would also certainly have assortative mixing. Andersen et al. (2013) showed that an artificial and a natural network of the same type have assortative and disassortative mixing, respectively. They therefore argue that characterizing networks produced by various models are not –at least statistically- representative of real networks. In order to validate this argument much more artificial and real geological networks need to be tested. I believe that the way of representing networks as graphs and the types of networks have important influences on all the values, including assortativity.

Based on the findings, the perfect geological fracture network would have (1) high global efficiency, (2) high clustering and (3) assortative mixing. High global efficiency is necessary for the fluids to move through the rock faster and more efficiently, which corresponds to well-interconnected fractures raising the potential permeability of the rock suite. High clustering is needed indicating a tightly connected network, which can provide percolation sites. The assortative nature generates a robust network against healing. The same applies to the high efficiency and clustering. In case the fluid that is flowing through the fractures is saturated, mineral precipitation can fully block (heal) open fractures decreasing the permeability. In the graphs this would be represented by removing edges. Provided that the network has those attributes mentioned above, there are more pathways (i.e. fractures) for the fluids to flow into. This means that while the permeability might decrease as a result of healing, it can still remain due to the well-connected network.

6.3.3 Limitations and possibilities for further work

Applying graph theory to geological fracture networks entails some limitations. First of all, graph theory in the presented way is not suitable for determining threshold values that could be related to fracture/vein patterns and/or mechanical parameters. Networks therefore cannot be categorized based on the values that are produced during analysis.

Second of all, it is a two-dimensional characterization method, whereas fracture networks should be analyzed in three-dimensions to obtain true topological and connectivity information. In order to convert these 2D measurements into a 3D network is problematic because even 2D upscaling is problematic due to several reasons. 1) Fracture distribution can be quite heterogeneous even within small (meter-scale) distances. This means that even if one has more than one section (e.g. seismic sections) crossing each other but they happen to be taken from areas with high fracture density, then one might overestimate the connectivity of the network. Conversely, sections through low fracture density might result in underestimation of the network connectivity. This heterogeneity of fracture distribution therefore makes it extremely difficult to upscale properties. 2) Each sampling method (through which image data can be obtained) includes difficulties and bias. Detection and characterization of fractures found within well cores or image logs from boreholes is affected by the borehole inclination with regard to the fracture orientations. Indirect techniques, such as seismic or ground penetration radar, are limited by resolution and penetration depths. During network characterization, therefore, one needs to be aware that the image they are working with are very likely not truly representative of the real network. 3) Scaling issues. Fractures range from microns to kilometers in length. Dealing with e.g. trace-line maps on a kilometer-scale eliminates smaller, centimeter-length fractures that might as well play crucial part in connecting larger fracture (/fault) segments. This means that on a larger scale the network might not be as well connected as in smaller scale.

In spite of these limitations, the presented results provide a good base for further work. Networks of different nature and origin could be analyzed the same way. Further work could therefore focus on networks including outcrop patterns of different orientations relative to the main stresses, trace-line maps, networks produced by computer models or laboratory experiments. After the necessary image processing, graphs need to be generated. One could create graphs by linking fractures based on crosscutting relationships. It would be worth to examine to what extent does the network exhibit a statistically different nature with different graph-generation methods.

As the graph is produced, one could apply weights on the edges. In a geological framework this could correspond to the fracture aperture. A fracture with low aperture would have low weight, and thus would contribute less to the measures. As fluid flow can be constrained by less open fractures (or completely healed ones), weighting the edges based on the fracture aperture would be a valid approach.

Measurements on the network could further include different clustering formulas, or if the network is not tree-like, then analyzing how many edges need to be removed to disconnect the system. This would be also applicable to the healing process. Distribution of angles between fracture segments is a classical method for characterization. So is analyzing the polygon areas (or areas straddled by a continuous, circle fracture). However, not all the presented mudcrack experiments would be suitable for such analysis. As seen on Fig. 6.46, the soft cases (experiments A and B) do present well-defined polygon areas. The straddled areas in the stiffer cases, however, are highly irregular, much larger and contain smaller fracture segments. Comparing the sizes of these areas to the polygons would not give reasonable or valuable results. When polygons are clearly defined, measuring the areas, their distributions, and the tendency of similar-sized areas to group together would provide additional topology information.

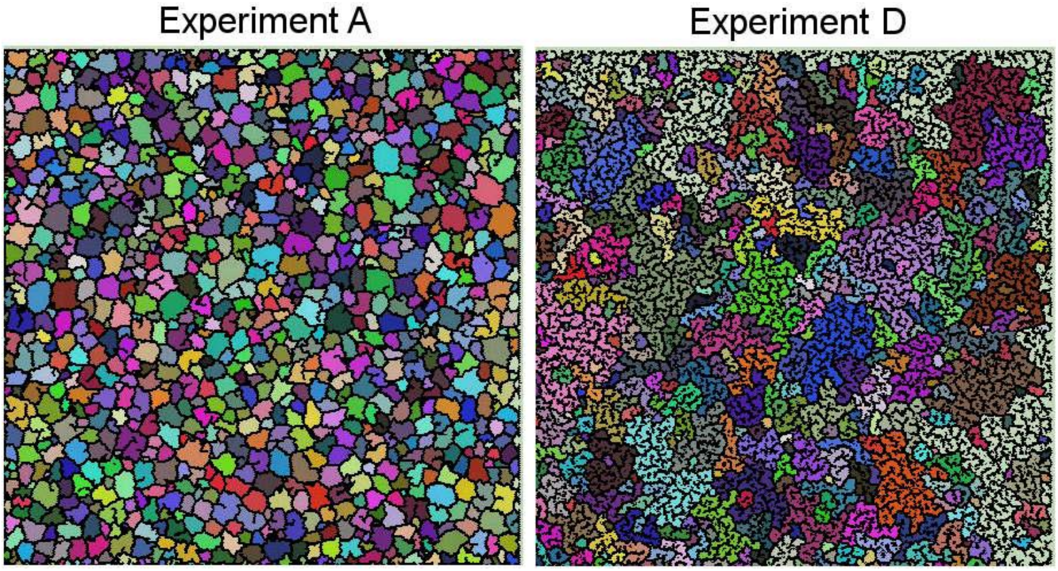

Fig. 6.46 Comparing the shapes of areas straddled by continuous (circles) of fractures.

6.4 Conclusions

Characterizing fracture networks is of crucial importance in many areas, such as oil or geothermal reservoir modeling. The main interests focus on network topology, connectivity and the evolution of these features. The purpose of this chapter was to present the graph theory as a possible tool to extract this information. The study was based on a collection of patterns (mudcracks and hydrobreccia) produced by the Elle numerical model or by analogue experiments. The former supplied dynamic measures, whereas the latter were available to compare the networks relative to each other.

Images from the experiments were imported into Mathematica, where after binarization and skeletonization the patterns were converted into graphs made up of vertices and edges. Vertices represented fracture junctions or dead ends, whereas the edges were the fracture segments linking the vertices. Calculations on the graphs included vertex degree distribution and its entropy, vertex and edge numbers, global efficiency, clustering coefficients and assortativity. The defined measures indicated increasing connectivity with network growth. The dominance of triple junctions over dead end fractures, the increasing edge number over vertices and the clustering showed more links in the system, which could potentially provide more pathways for the fluid to flow through. This was also reflected in the global efficiency values that started to rise due to the fracture interconnections. High global efficiency has shown to be more important than high clustering, since calculating the clustering in the classical way can correspond to a disconnected network with high coefficients. I conclude that a rock in which the fracture network has (1) more edges than vertices, (2) high global efficiency, (3) high clustering and (4) high assortativity would represent a very robust reservoir. The fracture connectivity contributes to high permeability, whereas the topology can potentially make the system robust against healing.

Graph theory opens possibilities to characterize networks in a quantitative and qualitative manner. It can be applied to networks of different nature and size. Using the presented method and measures it is possible to examine grain microfractures in a thin section, fracture and vein patterns in a hand sample or on an outcrop, fracture traces obtained by scan-line mapping or appearing on other geological maps, and any linear patterns generated by computer models or laboratory experiments. Combined with other methods, graph theory can be a powerful tool to characterize fracture networks and their dynamic evolution.

7 Conclusions

This thesis includes studies of large-scale dynamic hydrofracturing, healing and fracture network characterization. Field work, numerical modeling, image analysis and graph theory attempted to give answers to the research questions presented in chapter 1.3. In this chapter I will first outline answers to these questions, and I will then summarize the general conclusions that can be drawn from the thesis.

What are the dynamics of fracturing in a multilayered reservoir rock over time?

Fracturing is a highly, temporally and spatially, dynamic process that depends on the (contrasting) mechanical properties of the system. Regardless of these properties, the systems reach saturation both on layer and reservoir-scale. Saturation is identified by strain localization along pre-existing fractures and stress relaxation.

How does the healing affect the rock behavior?

Healing decreases local porosity, influences failure, fracture localization and stress magnitudes, which directly affect the saturation of the system.

How do the different healing properties affect the healing and the refracturing process?

Tensile properties of the veins have found to be more important with regard to system dynamics than the elastic properties of the veins. Veins stronger than their matrix make the system less fractured (i.e. fewer crack-seal cycles and open fractures), elevate stresses and limit possible fluid flow. Results show that intense veining does not necessarily correspond to high paleopermeability.

What is the stress evolution during fracturing, healing and refracturing?

Strain increases stresses that are released, i.e. drop, upon fracturing. Healing can either increase stresses when veins are stronger than the matrix, or do not affect stresses when they are weaker or have similar properties than their host rocks. Refracturing generally corresponds to strain localization and thus stress relaxation.

Can we assign characteristic fracture patterns to certain conditions?

Fracture spacing, the amount of open fractures relative to the vein intensity, facture/vein orientations relative to the main tectonic stresses do give indications for the mechanical properties of the host and veins, and their formation origin. Field observations and extensive microstructural analysis, however, are necessary to explain fracture patterns.

What influences fracture/vein spacing in the rock?

Spacing in the rock is found to be dependent on the mechanical properties of the host. Increasing elastic modulus decreases fracture spacing. This effect is especially pronounced with increasing breaking strength.

How does the permeability evolve over time?

Permeability is an extremely, temporally and spatially, dynamic property that depends on several factors such as (contrasting) mechanical properties of the host and veins, structural anisotropies within the host (e.g. existing faults), magnitude and direction of applied stresses, velocity of healing and strain rate.

What does the model tell about natural systems?

The model highlighted the importance of (contrasting) mechanical properties, anisotropies, healing, soft seals and fluid pressures. It also showed the deformation complexity due to the direct feedbacks between deformation processes.

Can we reproduce fracture/veining patterns found in nature using numerical modeling?

Yes, we can. Although boundary conditions and lattice geometry can impede the formation of natural patterns.

What are the fluid flow characteristics in natural hydrofractures within the Internal Ligurian Unit, Italy?

Field evidence did not confirm veins to be of hydrofracture origin. However, it has been found that fluid flow, in conjunction with local diffusion was responsible for veining in the studied area.

Can graph theory be applied to geological networks?

Yes, graph theory can be successfully applied to geological fracture networks.

Can we quantify and compare the connectivity of different networks?

Connectivity of networks can be quantified based on the relative amount of vertices (junctions and dead ends) and edges (links), amount of clustering, the average shortest path lengths in the system (inverse of global efficiency) and the tendency of hubs linking together (assortativity).

How can we quantify a good reservoir?

A good reservoir would have (1) more edges than vertices, (2) high global efficiency, (3) high clustering coefficient and (4) high assortativity. These properties together would create high permeabilities and would make the reservoir robust against healing.

Do the connectivity and other topological information relate to mechanical properties of the rocks?

Mechanical properties (e.g. Young's modulus) are reflected in the topological measures. Patterns and mechanical properties cannot be related to exact values.

This thesis presented a hybrid numerical model (Elle) which included the coupling between the fluid and the solid framework, i.e. the poroelasticity. Many earlier numerical models lack this coupling even though it has proven to be crucial in fracture formation (chapter 1.1.2 and chapter 2.2.2). In contrast to earlier models, the presented Elle model deals with porous media, calculates real-scale parameters and the simulations are not limited spatially and temporally (chapter 3.2). On top of these, healing has been introduced in to model to simulate how healing affects the deformation dynamics of layered, fluid-filled rock systems. The simulations show that since healing has a major influence on the deformation (see chapter 5) a healed system (veined rocks) should not be treated as a fractured system (rocks without veins). This is due to the fact that the veins create heterogeneity and the veins mechanical properties create anisotropy within the rock systems. These give rise to spatial-temporal variations in open fractures, which directly affects the permeability of the rock suite (chapter 1.2.3). The contrasting mechanical properties thus create various fracture and vein patterns, which nicely correlates with earlier studies (chapters 1.1.1 and 1.2.3).

Field observations from the Internal Ligurian Unit, Italy, also support the modeling results. Veins found within thick shale sequences exhibit various patterns, some of which have been attributed to the contrasting mechanical properties between the vein material and host rock (see chapter 4.5.2). These closely-spaced, bed-perpendicular calcite veins, which do not show signs of crack-sealing, can also be related to veins found in the Oman Mountains. Unfolding conjugate vein sets revealed successive major compression directions that showed rotation of the subduction-accretionary zone between Corsica and the Adriatic plate. The revealed stress directions nicely fit previous geodynamic models (see chapter 4.5.1), which proves that even small-scale (centimeter-scale) structures can capture large, kilometer-scale geodynamic evolution. This has also been reported from the Oman Mountains (chapter 4.5.1).

Fracture/vein networks are usually characterized based on their current state, i.e. no previous work has attempted to statistically capture how the network evolves. In addition to this, topological measures have not been related to mechanical properties of the fractured system, and graph theory in the presented way has not yet been applied to geological fracture networks either. This thesis therefore aimed to fill this gap. It succeeded in the sense that it showed graph theory can successfully be applied to geological networks even though it has some limitations (chapter 6.3.3). The dynamic network evolution has also been captured and summarized in Table 10. The thesis, however, failed to relate topological measures to mechanical properties. In spite of this, it showed that topology can make the network robust against healing. One example can be seen on Fig. 7.1. Many fracture networks are tree-like, i.e. vertices (junctions/dead ends) have only one parent vertex. This means that if healing takes place and one edge is removed, the network disconnects. Non-tree networks that have loops within are much more robust against healing as edge removal does not result in network disconnection. The examples on Fig. 7.1 also indicate that fracturing in Italy show signs of both types of networks. However, tree-like veins are much more common, which means that the fracture network in the studied area was probably not very well connected. This is supported by the vein intensities and the veins spatial distribution (chapter 4.5.3).

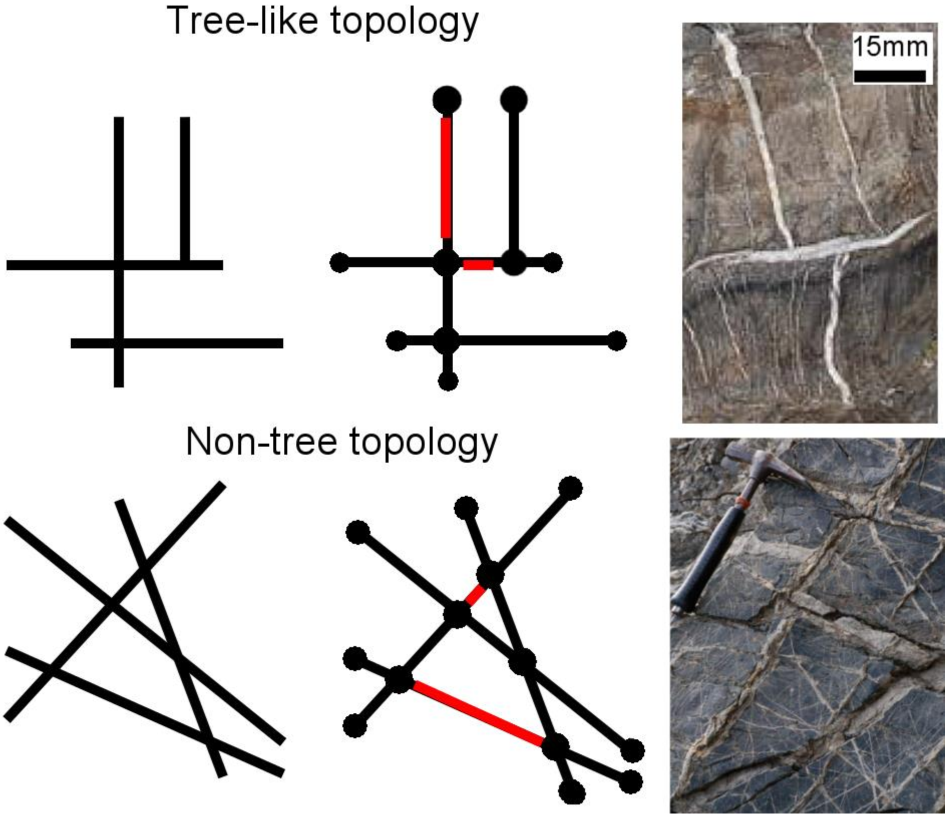

Fig. 7.1 A tree-like and a non-tree fracture network topology and their field equivalents. Removing either or both of the indicated red fracture segments disconnects the network in the tree-like topology, but does not disconnect the non-tree network.

The results of the thesis therefore generally support earlier studies and also managed to answer the research questions. Fig. 7.2 shows the most important outcomes of each research method and how they link together.

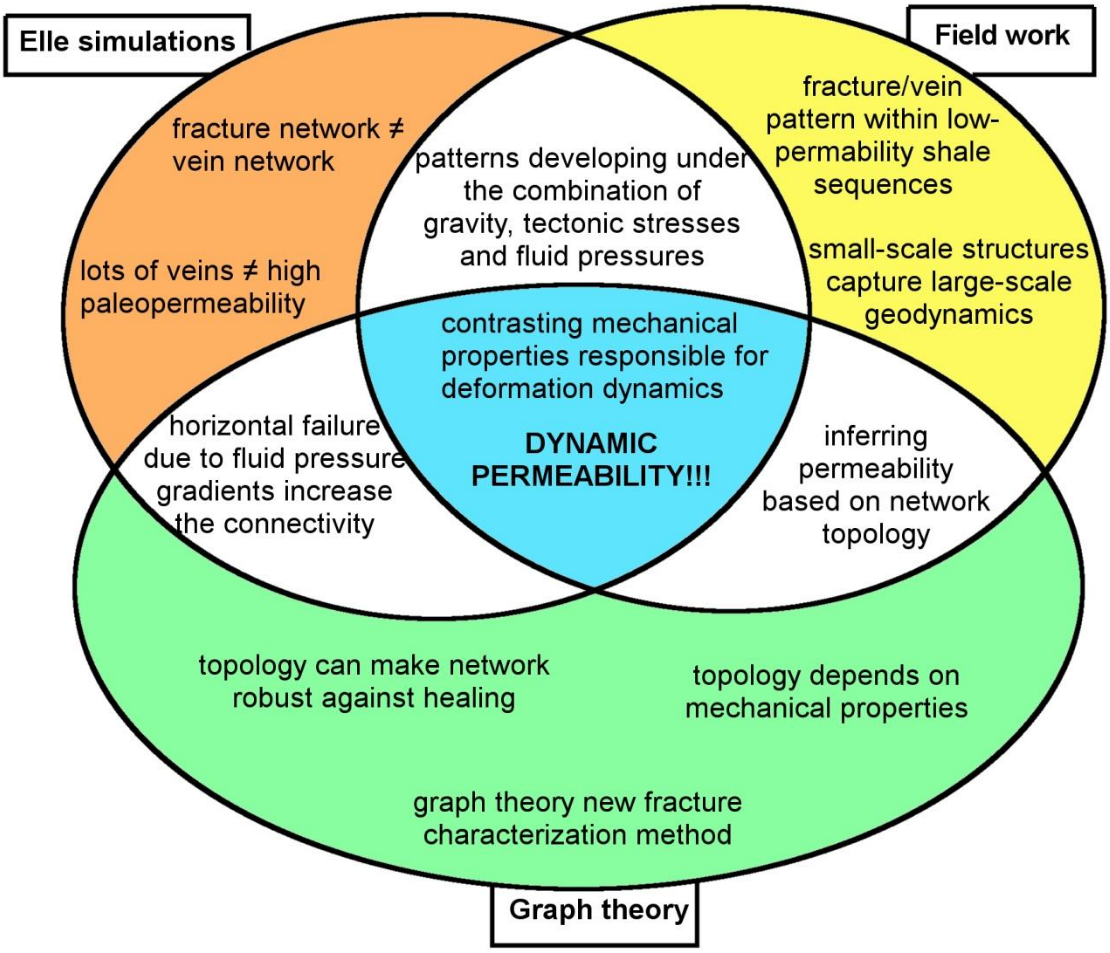

Fig. 7.2 Figure listing the most important results of each method and showing how they link together.

The outcomes of the research can be applicable to several projects, such as reservoir modeling (hydrocarbon/geothermal), ore exploration or underground waste management. In the oil and gas industry reservoirs are hoped to exhibit connected fracture network so that they could potentially contain large amounts of hydrocarbons. These reservoirs, however, need to be confined by non-permeable boundaries, such as healed, non-active faults or a low-permeability caprock. The thesis showed that 1) healed faults could also fail under certain conditions, 2) how important are the poroelastic effects that the fluids (e.g. hydrocarbons or the fluids pumped in during fracking) exert on the solid framework and 3) the contrasting mechanical properties influence the deformation. These results can be incorporated in the current reservoir models and would give more realistic prediction on hydrocarbon production and seal failure. The same applies to underground waste disposal as a non-permeable system is required in order to avoid leakage that would pollute the underground and/or groundwater system.

The thesis also shows how small-scale structures can capture kilometer-scale tectonic evolution, therefore proves how important it is to carry out field work to accompany seismic surveys that do not detect these small-scale structures.

Ore exploration needs to understand the fracture network evolution as mineralizing fluid use these channels to precipitate valuable ore minerals within veins or larger bodies. The thesis outcomes deals with the network evolution and the controlling factors which could therefore be incorporated in the exploration models.

Including graph theory as a complimentary fracture characterization method within the current fracture models would also provide more details on the network and thus could improve production predictions.

Appendices

A. Fracture network evolutions for Elle experiments

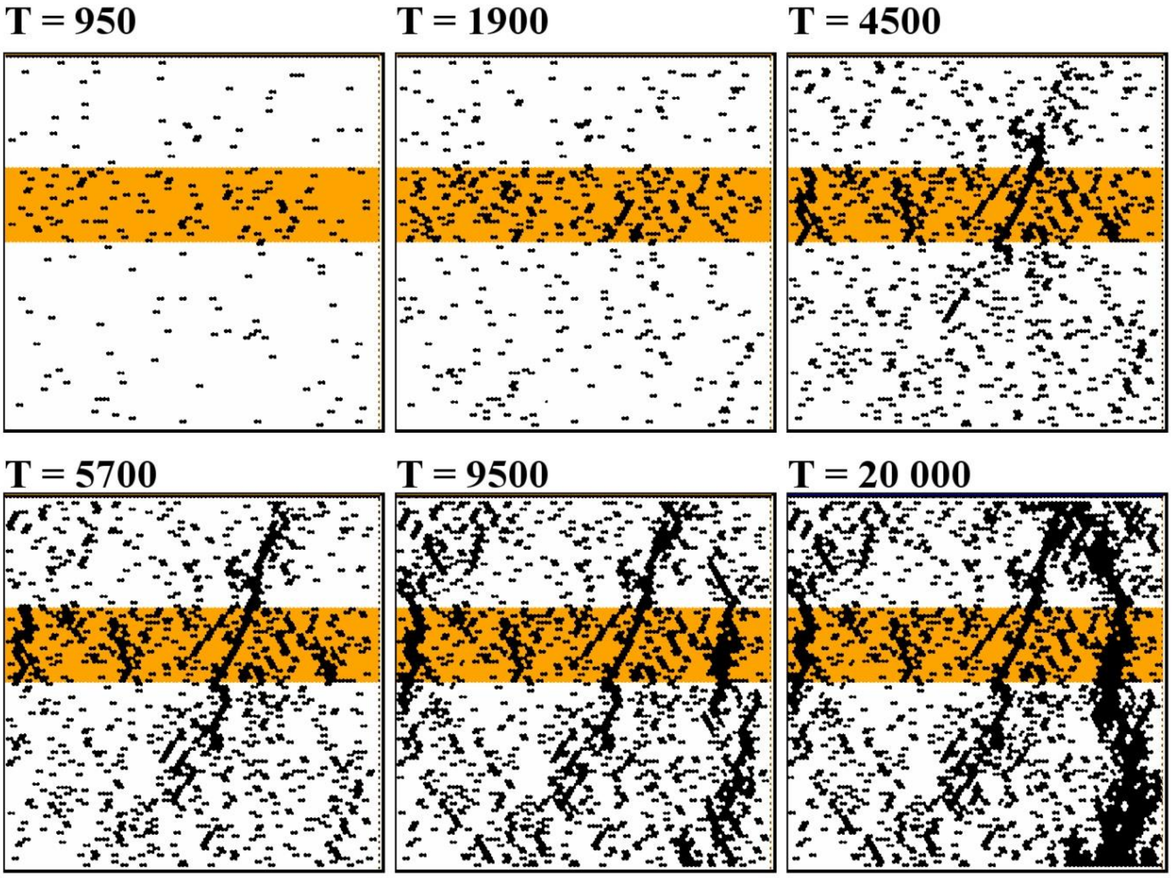

Fig. A 1 Fracture evolution of Elle experiment shown on Fig. 5.1a,b,c.
T corresponds to time steps (1 time step = 1000 days), whereas the shaded orange rectangle represents a stiff layer embedded in a softer matrix.

Fracture evolution of experiment shown on Fig. 5.1d,e,f is presented on Fig. 5.2.

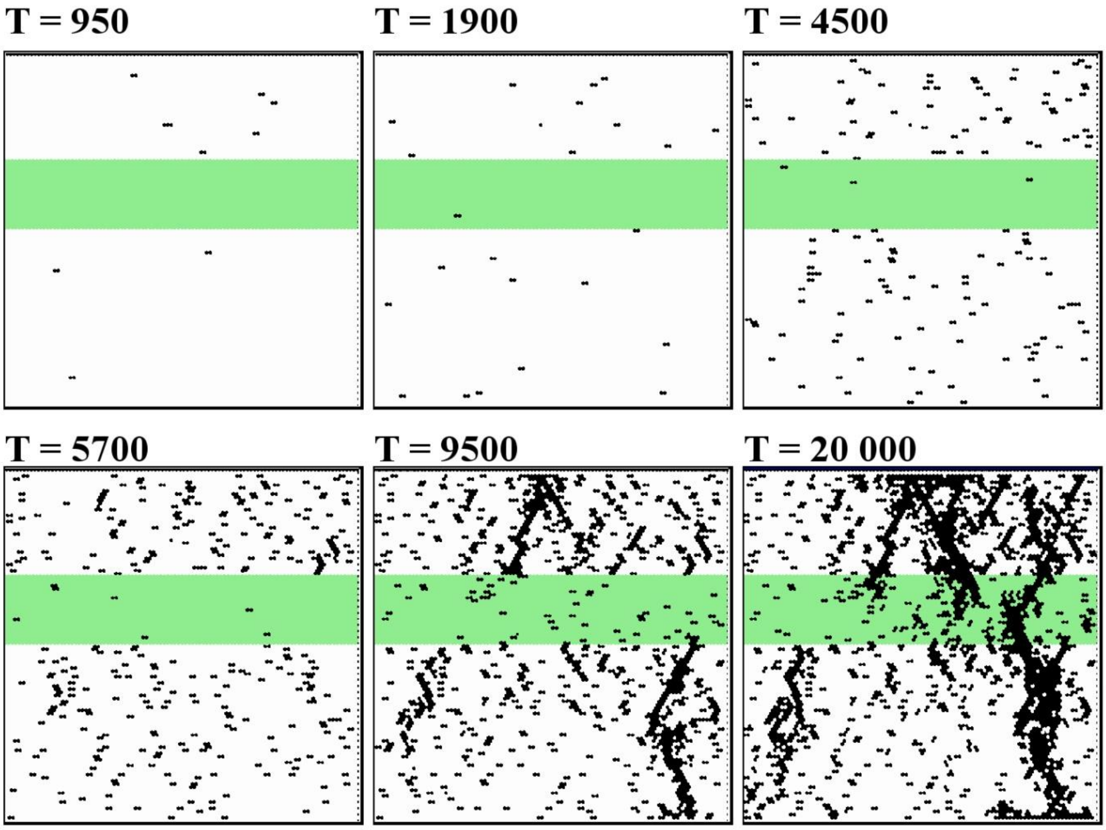

Fig. A 2 Fracture evolution of Elle experiment shown on Fig. 5.3, when the Young's modulus ratio of the embedded layer (green rectangle) to the matrix is 0.3, i.e. the layer is softer than the matrix. T corresponds to model time steps, where 1 time step = 1000 days.

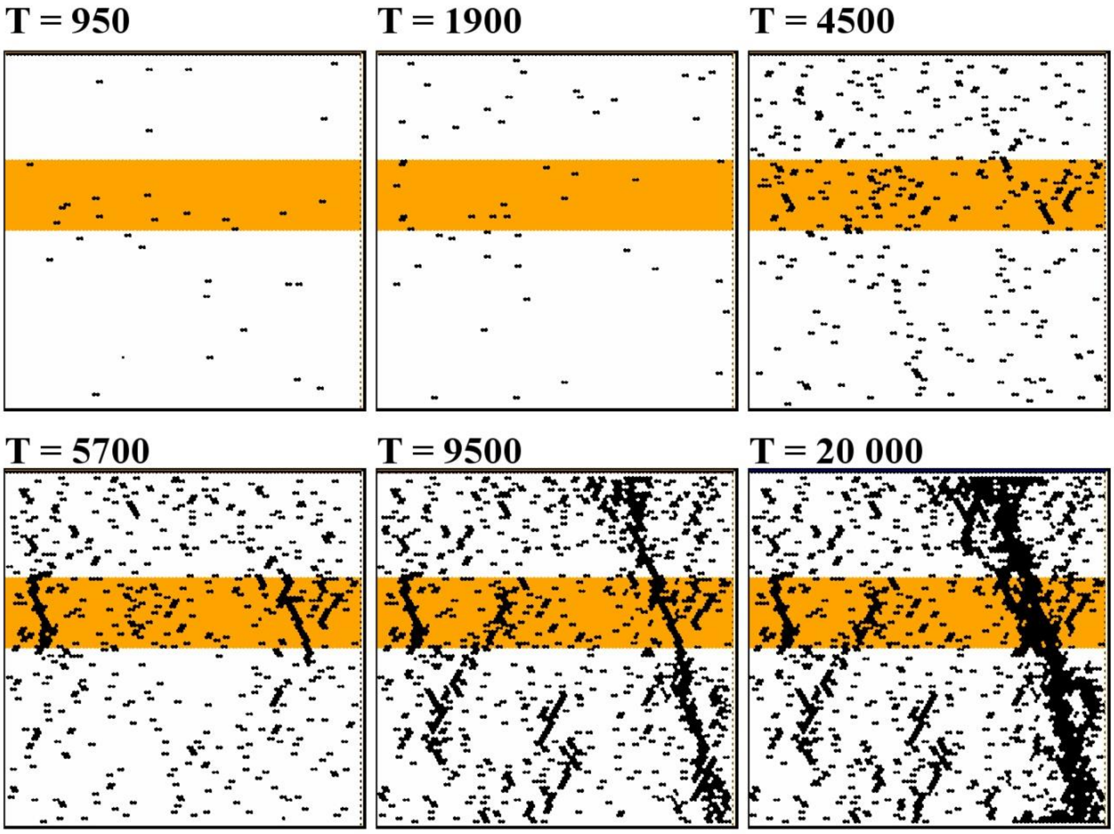

Fig. A 3 Fracture evolution of Elle experiment shown on Fig. 5.3, when the Young's modulus ratio of the embedded layer (orange) to the matrix is 1.5, i.e. the layer is slightly stiffer than the matrix. T corresponds to the model time steps, where 1 time step = 1000 days.

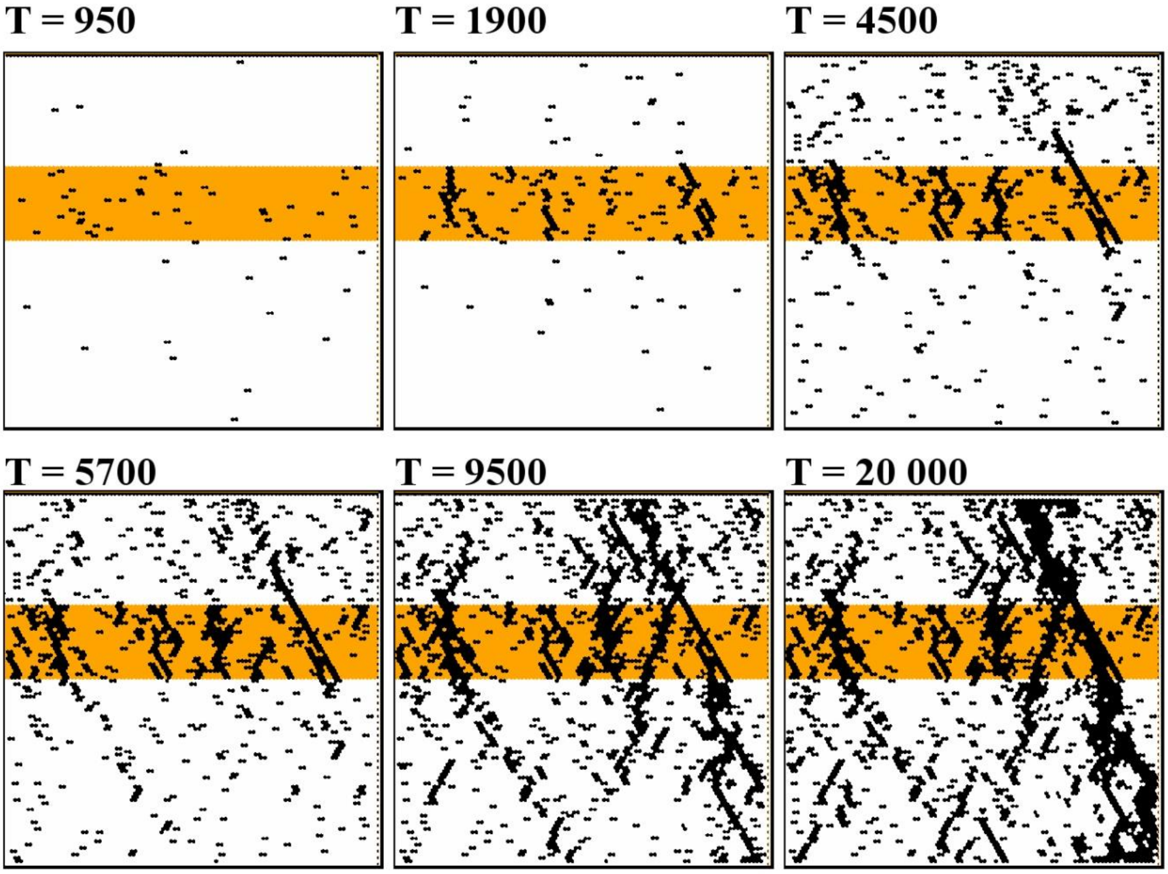

Fig. A 4 Fracture evolution of Elle experiment shown on Fig. 5.3, where the Young's modulus ratio of the embedded layer (orange rectangle) to the matrix is 4.5, i.e. the layer is more than four times stiffer than the matrix.
T corresponds to model time steps, where 1 time step = 1000 days.

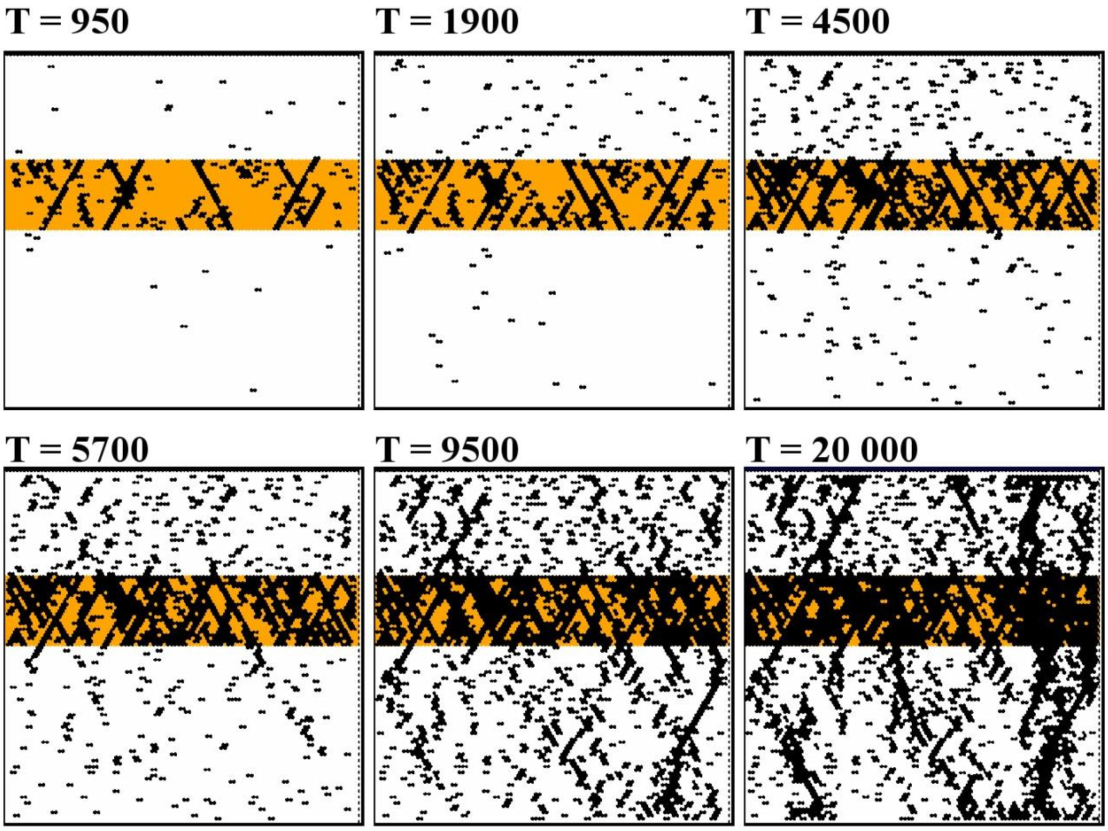

Fig. A 5 Fracture evolution of the Elle experiment shown on Fig. 5.4a,c, where the breaking strength ratio of the layer (orange) to the matrix is 0.3, i.e. the layer is much weaker than the matrix.
T corresponds to model time steps, where 1 time step = 1000 days.

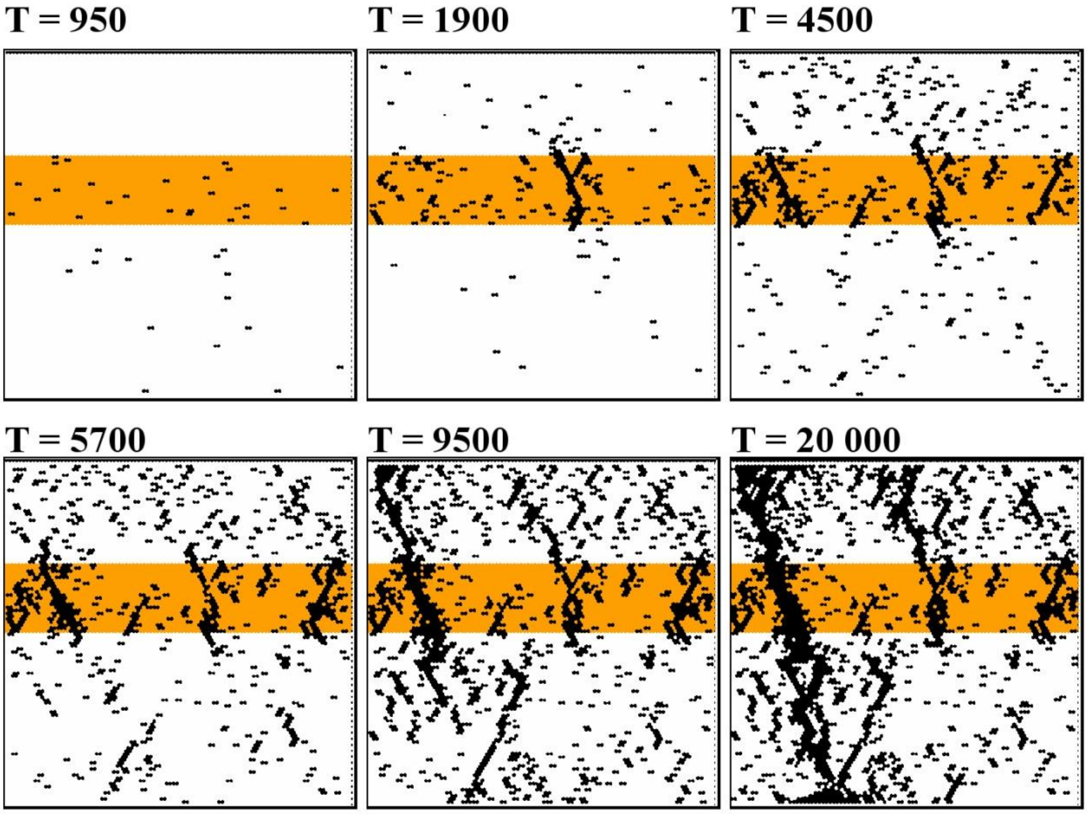

Fig. A 6 Fracture evolution of Elle experiment shown on Fig. 5.4b,d, where the breaking strength ratio of the layer (orange) to the matrix is 2, i.e. the layer is twice as strong as the matrix.
T corresponds to model time steps, where 1 time step = 1000 days.

B. Locations of measurements and field images presented in Chapter 4

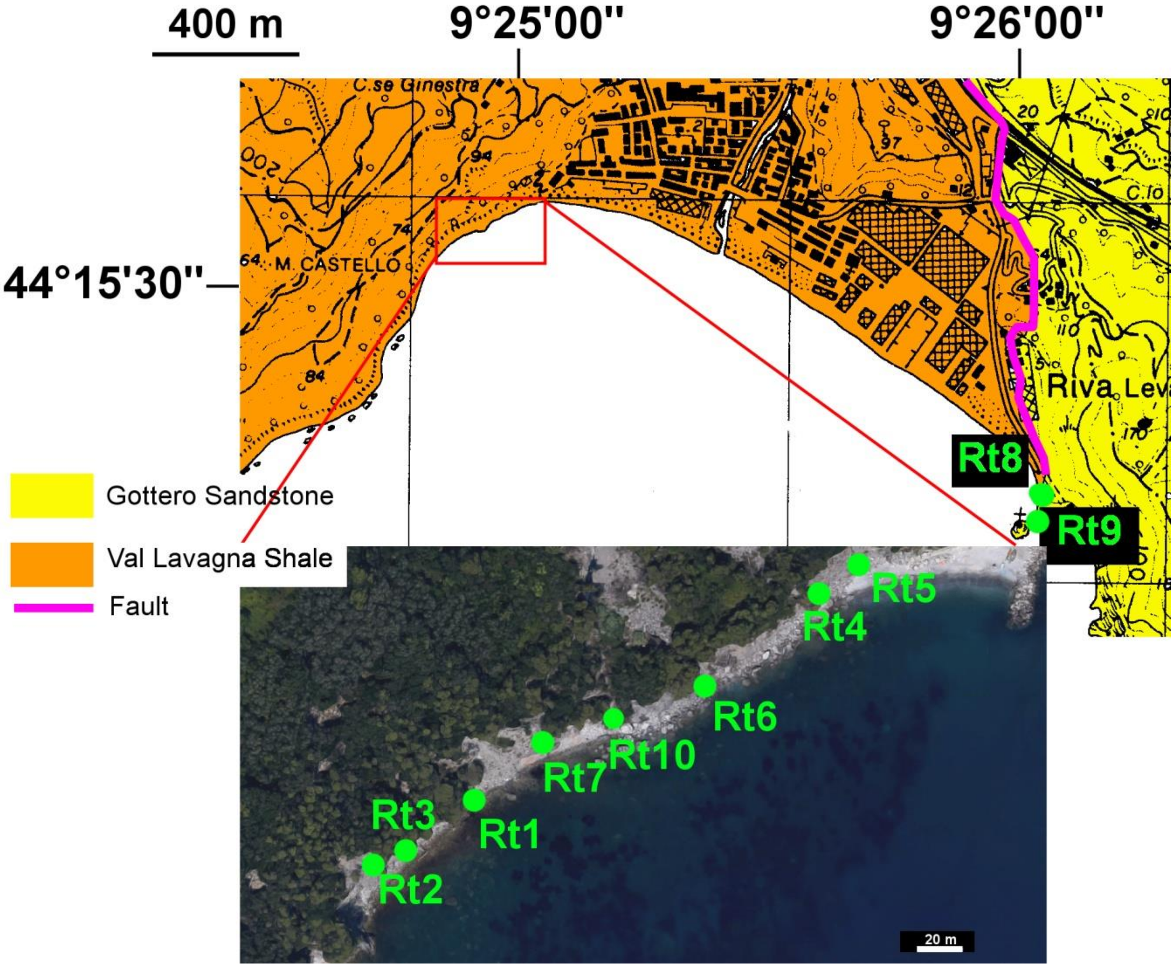

Fig. B 1 Small scale (geological) maps showing measurement and image locations around Riva Trigoso.

Locations shown on Fig. B 1.	Images, measurements
Rt1	Fig. 4.29a
Rt2	Fig. 4.7a, Fig. 4.28b, Fig. 4.29f
Rt3	Fig. 4.7b, Fig. 4.29g, Fig. 4.29h
Rt4	Fig. 4.26a
Rt5	Fig. 4.9a, Fig. 4.9c, Fig. 4.18
Rt6	Fig. 4.29e
Rt7	Fig. 4.7c, Fig. 4.29d
Rt8	Fig. 4.7d, Fig. 4.7e
Rt9	Fig. 4.7f
Rt10	Fig. 4.29b, Fig. 4.29c

Table B 1 Listed locations presented on Fig. B 1 and their corresponding measurements and images in the thesis.

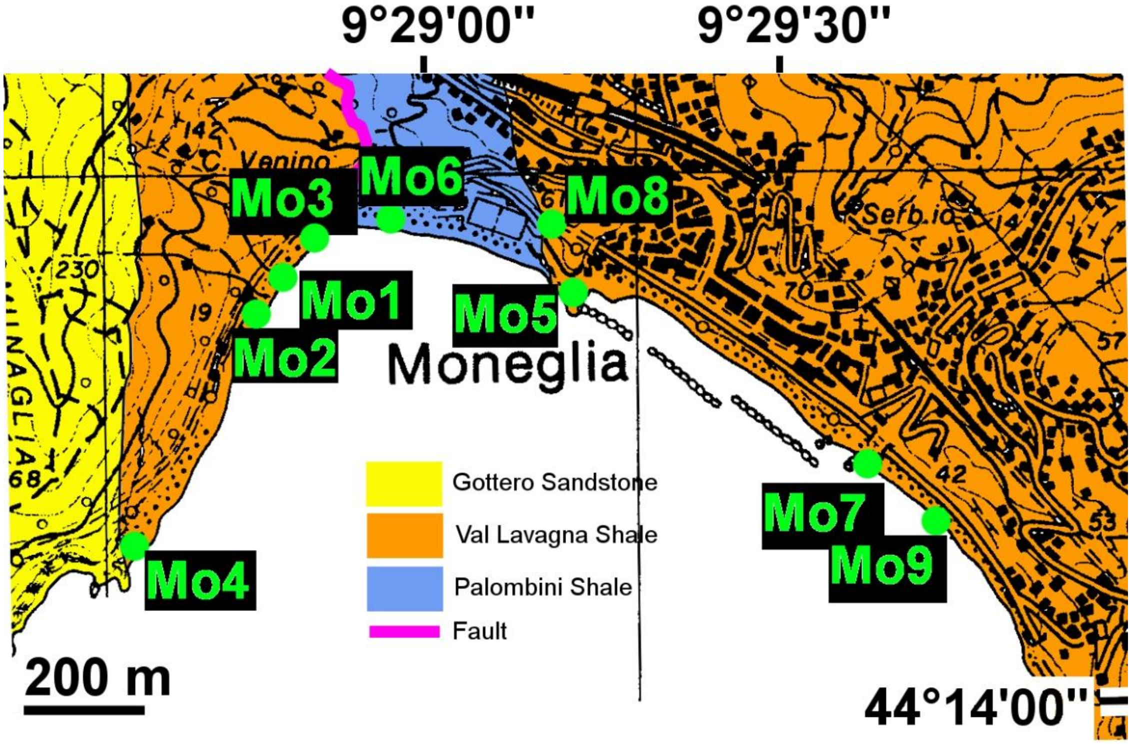

Fig. B 2 Small scale geological map of Moneglia showing the measurement and image locations presented in the thesis.

Locations shown on Fig. B 2.	Images, measurements
Mo1	Fig. 4.9b, Fig. 4.31h
Mo2	Fig. 4.6 (black set), Fig. 4.7d, Fig. 4.15, Fig. 4.31c, Fig. 4.31i
Mo3	Fig. 4.6 (purple set), Fig. 4.20, Fig. 4.25, Fig. 4.27b, Fig. 4.31a, Fig. 4.31b, Fig. 4.31f, Fig. 4.31g, Fig. 4.32
Mo4	Fig. 4.28a
Mo5	Fig. 4.6 (gray set)
Mo6	Fig. 4.6 (pink set)
Mo7	Fig. 4.6 (yellow set)
Mo8	Fig. 4.31e
Mo9	Fig. 4.31d

Table B 2 Listed locations on Fig. B 2 with the corresponding measurements and images and throughout the thesis.

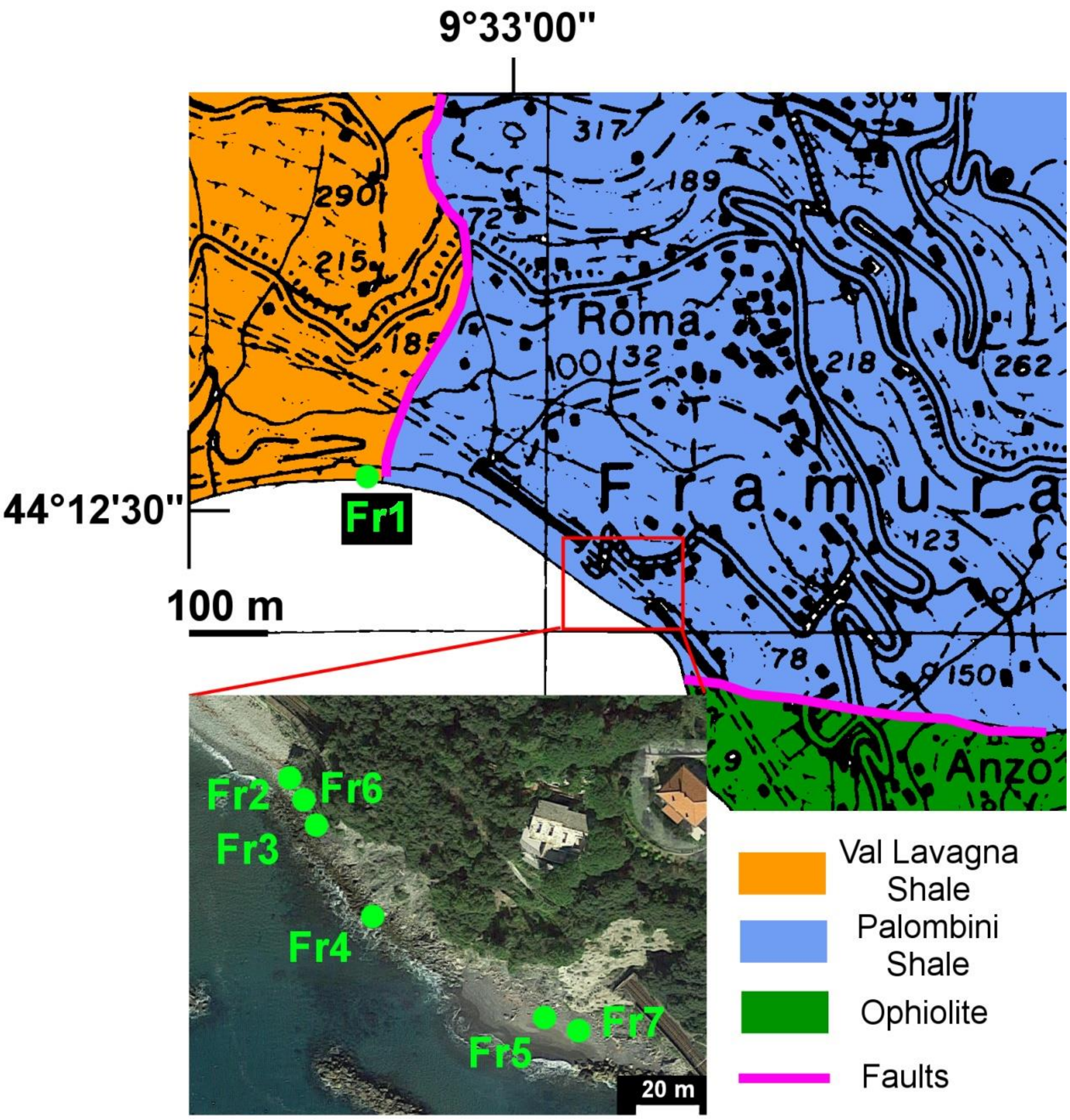

Fig. B 3 Small scale map of Framure indicating the locations for measurements and images presented in the thesis.

Locations shown on Fig. B 3.	Images, measurements
Fr1	Fig. 4.8, Fig. 4.34d
Fr2	Fig. 4.4a, Fig. 4.34e
Fr3	Fig. 4.4b
Fr4	Fig. 4.34a, Fig. 4.34b
Fr5	Fig. 4.34c, Fig. 4.34g
Fr6	Fig. 4.34f
Fr7	Fig. 4.34h

Table B 3 Listed locations on Fig. B 3 with the corresponding measurements and images and throughout the thesis.

List of references

Adachi, J., Siebrits, E., Peirce, A., Desroches, J., 2007. Computer simulation of hydraulic fractures. International Journal of Rock Mechanics and Mining Sciences, 44(5): 739-757. DOI:http://dx.doi.org/10.1016/j.ijrmms.2006.11.006

Adler, P.M., Thovert, J.-F., 1999. Fractures and fracture networks. Springer Netherlands, Dodrecht, 452 pp.

Advokaat, E.L. et al., 2014. Eocene rotation of Sardinia, and the paleogeography of the western Mediterranean region. Earth and Planetary Science Letters, 401: 183-195. DOI:10.1016/j.epsl.2014.06.012

Albert, R., Barabási, A.L., 2002. Statistical mechanics of complex networks. Reviews of Modern Physics, 74(1): 47-97. DOI:10.1103/RevModPhys.74.47

Albert, R., Jeong, H., Barabási, A.L., 2000. Error and attack tolerance of complex networks. Nature, 406(6794): 378-382. DOI:10.1038/35019019

Allmendinger, R.W., Cardozo, N.C., Fisher, D.M., 2013. Structural Geology Algorithms: Vectors and Tensors. Cambridge University Press, Cambridge, England.

Altmann, J.B. et al., 2014. Pore pressure stress coupling in 3D and consequences for reservoir stress states and fault reactivation. Geothermics, 52: 195-205. DOI:10.1016/j.geothermics.2014.01.004

Andresen, C.A., Hansen, A., Le Goc, R., Davy, P., Hope, S.M., 2013. Topology of Fracture Networks. Frontiers in Physics, 1(7). DOI:10.3389/fphy.2013.00007

Argnani, A., 2009. Plate tectonics and the boundary between Alps and Apennines. Italian Journal of Geosciences, 128(2): 317-330.

Argnani, A., 2012. Plate motion and the evolution of Alpine Corsica and Northern Apennines. Tectonophysics, 579: 207-219. DOI:10.1016/j.tecto.2012.06.010

Arslan, A., Koehn, D., Passchier, C.W., Sachau, T., 2012. The transition from single layer to foliation boudinage: A dynamic modelling approach. Journal of Structural Geology, 42: 118-126. DOI:10.1016/j.jsg.2012.06.005

Atkinson, A.B., 2002. A model for the PTX properties of H_20-NaCl, Virginia Polytechnic Institute and State University, Blacksburg, Virgina, USA, 133 pp.

Bai, T., Pollard, D.D., Gao, H., 2000. Explanation for fracture spacing in layered materials. Nature, 403(6771): 753-756.

Bai, T.X., Pollard, D.D., 2000a. Closely spaced fractures in layered rocks: initiation mechanism and propagation kinematics. Journal of Structural Geology, 22(10): 1409-1425. DOI:10.1016/s0191-8141(00)00062-6

Bai, T.X., Pollard, D.D., 2000b. Fracture spacing in layered rocks: a new explanation based on the stress transition. Journal of Structural Geology, 22(1): 43-57. DOI:10.1016/s0191-8141(99)00137-6

Barabási, A.L., 2009. Scale-free networks: A decade and beyond. Science, 325(5939): 412-413. DOI:10.1126/science.1173299

Barabási, A.L., Albert, R., 1999. Emergence of scaling in random networks. Science, 286(5439): 509-512. DOI:10.1126/science.286.5439.509

Barabási, A.L., Bonabeau, E., 2003. Scale-free networks. Scientific American, 288(5): 60-69.

Barrat, A., Barthélemy, M., Vespignani, A., 2008. Dynamical Processes on Complex Networks. Cambridge University Press, New York, NY, USA.

Bea, F., Arzamastsev, A., Montero, P., Arzamastseva, L., 2001. Anomalous alkaline rocks of Soustov, Kola: evidence of mantle-derived metasomatic fluids affecting crustal materials. Contributions to Mineralogy and Petrology, 140(5): 554-566.

Becker, A., Gross, M.R., 1996. Mechanism for joint saturation in mechanically layered rocks: An example from southern Israel. Tectonophysics, 257(2-4): 223-237. DOI:10.1016/0040-1951(95)00142-5

Bethke, C.M., 1985. A numerical model of compaction-driven groundwater flow and heat transfer and its application to the paleohydrology of intracratonic sedimentary basins. Journal of Geophysical Research-Solid Earth and Planets, 90(NB8): 6817-6828. DOI:10.1029/JB090iB08p06817

Biot, M.A., 1941. General theory of three-dimensional consolidation. Journal of Applied Physics, 12(2): 155-164. DOI:10.1063/1.1712886

Blanpied, M.L., Marone, C.J., Lockner, D.A., Byerlee, J.D., King, D.P., 1998. Quantitative measure of the variation in fault rheology due to fluid-rock interactions. Journal of Geophysical Research-Solid Earth, 103(B5): 9691-9712. DOI:10.1029/98jb00162

Boccaletti, S., Latora, V., Moreno, Y., Chavez, M., Hwang, D.U., 2006. Complex networks: Structure and dynamics. Physics Reports, 424(4–5): 175-308.

Bodnar, R.J., Vityk, M.O., 1994. Interpretation of microthermometric data for H_2O-NaCl fluid inclusions. In: De Vivo, B., Freccotti, M.L. (Eds.), Fluid Inclusions in Minerals, Methods and Applications. Virgina Polytechnic Institute and State University, Blacksburg, Virgina, USA, pp. 117-130.

Bollobás, B., 1998. Random Graphs, Modern Graph Theory. Graduate Texts in Mathematics. Springer New York, pp. 215-252. DOI:10.1007/978-1-4612-0619-4_7

Bons, P., Koehn, D., Jessel, M.W., 2008. Microdynamics Simulation. Springer.

Bons, P.D., 2001a. Development of crystal morphology during unitaxial growth in a progressively widening vein: I. The numerical model. Journal of Structural Geology, 23(6-7): 865-872. DOI:10.1016/s0191-8141(00)00159-0

Bons, P.D., 2001b. The formation of large quartz veins by rapid ascent of fluids in mobile hydrofractures. Tectonophysics, 336(1–4): 1-17. DOI:http://dx.doi.org/10.1016/S0040-1951(01)00090-7

Bons, P.D., Elburg, M.A., Gomez-Rivas, E., 2012. A review of the formation of tectonic veins and their microstructures. Journal of Structural Geology, 43(0): 33-62. DOI:http://dx.doi.org/10.1016/j.jsg.2012.07.005

Bons, P.D., Jessell, M.W., 1997. Experimental simulation of the formation of fibrous veins by localised dissolution-precipitation creep. Mineralogical Magazine, 61(1): 53-63. DOI:10.1180/minmag.1997.061.404.06

Bons, P.D., Montenari, M., 2005. The formation of antitaxial calcite veins with well-developed fibres, Oppaminda Creek, South Australia. Journal of Structural Geology, 27(2): 231-248. DOI:10.1016/j.jsg.2004.08.009

Bracciali, L., Marroni, M., Pandolfi, L., Rocchi, S., 2007. Geochemistry and petrography of Western Tethys Cretaceous sedimentary covers (Corsica and Northern Apennines): From source areas to configuration of margins. Sedimentary Provenance and Petrogenesis: Perspectives from Petrography and Geochemistry(420): 73-93. DOI:10.1130/2006.2420(06)

Bradshaw, J.Y., 1989. Early Cretaceous vein-related garnet granulite in Fiordland, Southwest New-Zealand - A case for infiltration of mantle-derived CO2-rich fluids. Journal of Geology, 97(6): 697-717.

Bredehoeft, J.D., Hanshaw, B.B., 1968. On the Maintenance of Anomalous Fluid Pressures: I. Thick Sedimentary Sequences. Geological Society of America Bulletin, 79(9): 1097-1106.

Bredehoeft, J.D., Wolff, R.G., Keys, W.S., Shuter, E., 1976. Hydraulic fracturing to determine the regional in situ stress field, Piceance Basin, Colorado. Geological Society of America Bulletin, 82(2): 250-258.

Burnard, P.G., Polya, D.A., 2004. Importance of mantle derived fluids during granite associated hydrothermal circulation: He and Ar isotopes of ore minerals from Panasqueira. Geochimica Et Cosmochimica Acta, 68(7): 1607-1615. DOI:10.1016/j.gca.2003.10.008

Callaway, D.S., Newman, M.E.J., Strogatz, S.H., Watts, D.J., 2000. Network robustness and fragility: Percolation on random graphs. Physical Review Letters, 85(25): 5468-5471. DOI:10.1103/PhysRevLett.85.5468

Calò, M., Dorbath, C., Frogneux, M., 2014. Injection tests at the EGS reservoir of Soultz-sous-Forêts. Seismic response of the GPK4 stimulations. Geothermics, 52(0): 50-58. DOI:http://dx.doi.org/10.1016/j.geothermics.2013.10.007

Caputo, R., Hancock, P.L., 1999. Crack-jump mechanism and its implications for stress cyclicity during extension fracturing. Journal of Geodynamics, 27(1): 45-60.

Cardozo, N., Allmendinger, R.W., 2013. Spherical projections with OSXStereonet. Computers and Geosciences, 51: 193-205. DOI:10.1016/j.cageo.2012.07.021

Carminati, E., Lustrino, M., Doglioni, C., 2012. Geodynamic evolution of the central and western Mediterranean: Tectonics vs. igneous petrology constraints. Tectonophysics, 579(0): 173-192.

Carosi, R., Montomoli, C., Pertusati, P.C., 2002. Late orogenic structures and orogen-parallel compression in the Northern Apennines. Bollettino della Societá Geologica Italiana, 1: 167-180.

Carosi, R., Montomoli, C., Pertusati, P.C., 2004. Late tectonic evolution of the Northern Apennines: the role of contractional tectonics in the exhumation of the tuscan units. Geodinamica Acta, 17: 253-273.

Catalano, E., 2012. A pore-scale coupled hydromechanical model for biphasic granular media (PhD thesis), Université de Grenoble, Grenoble, France.

Catalano, E., Chareyre, B., Barthelemy, E., 2014. Pore-scale modeling of fluid-particles interaction and emerging poromechanical effects. International Journal for Numerical and Analytical Methods in Geomechanics, 38(1): 51-71. DOI:10.1002/nag.2198

Chen, Q., Nur, A., 1992. Pore fluid pressure effects in anisotropic rocks: Mechanisms of induced seismicity and weak faults. Pure and Applied Geophysics, 139(3-4): 463-479. DOI:10.1007/BF00879947

Chi, G., Xue, C., 2011. An overview of hydrodynamic studies of mineralization. Geoscience Frontiers, 2(3): 423-438. DOI:http://dx.doi.org/10.1016/j.gsf.2011.05.001

Cobbold, P.R., Durand, S., Mourgues, R., 2001. Sandbox modelling of thrust wedges with fluid-assisted detachments. Tectonophysics, 334(3-4): 245-258. DOI:10.1016/s0040-1951(01)00070-1

Cobbold, P.R., Rodrigues, N., 2007. Seepage forces, important factors in the formation of horizontal hydraulic fractures and bedding-parallel fibrous veins ('beef' and icone-in-cone). Geofluids, 7(3): 313-322. DOI:10.1111/j.1468-8123.2007.00183.x

Codegone, G., Festa, A., Dilek, Y., Pini, G.A., 2012. Small-scale polygenetic melanges in the Ligurian accretionary complex, Northern Apennines, Italy, and the role of shale diapirism in superposed melange evolution in orogenic belts. Tectonophysics, 568: 170-184. DOI:10.1016/j.tecto.2012.02.003

Cook, B.K., Jensen, R.P., 2002. Discrete element methods: numerical modeling of discontinua. Third International Conference on Discrete Element Methods; September 23-25, 2002, Santa Fe, New Mexico, United States. American Society of Civil Engineers, Geo Institute, Reston, Va.

Cornet, F.H., Valette, B., 1984. In situ stress determination from hydraulic injection test data. Journal of Geophysical Research: Solid Earth, 89(B13): 11527-11537. DOI:10.1029/JB089iB13p11527

Costa, L.D.F., Rodrigues, F.A., Travieso, G., Boas, P.R.V., 2007. Characterization of complex networks: A survey of measurements. Advances in Physics, 56(1): 167-242. DOI:10.1080/00018730601170527

Cox, S.F., 2005. Coupling between deformation, fluid pressures, and fluid flow in ore-producing hydrothermal systems at depth in the crust. In: Hedenquist, J.W., Thompson, J.F.H., Goldfarb, R.J., Richards, J.P. (Eds.), Economic Geology One Hundredth Anniversary Volume. Society of Economy Geologists, Littleton, Colorado, pp. 39-76.

Cundall, P.A., Strack, O.D.L., 1979. A discrete numerical method for granular assemblies. Géotechnique, 29(1): 47-65.

Dahm, T., 2000. Numerical simulations of the propagation path and the arrest of fluid-filled fractures in the Earth. Geophysical Journal International, 141(3): 623-638. DOI:10.1046/j.1365-246x.2000.00102.x

Dorogovtsev, S.N., Mendes, J.F.F., 2002. Evolution of networks. Advances in Physics, 51(4): 1079-1187. DOI:10.1080/00018730110112519

Durney, D.W., Ramsay, J.G., 1973. Incremental strains measured by syntectonic crystal growth. In: De Jong, K.A., Scholten, K. (Eds.), Gravity and Tectonics. Wiley, New York, pp. 67-96.

Eberhardt, E., Stead, D., Coggan, J.S., 2004. Numerical analysis of initiation and progressive failure in natural rock slopes - the 1991 Randa rockslide. International Journal of Rock Mechanics and Mining Sciences, 41(1): 69-87. DOI:10.1016/s1365-1609(03)00076-5

Eberhardt, E., Stimpson, B., Stead, D., 1999. Effects of grain size on the initiation and propagation thresholds of stress-induced brittle fractures. Rock Mechanics and Rock Engineering, 32(2): 81-99. DOI:10.1007/s006030050026

Engelder, T., 1999. Transitional-tensile fracture propagation: a status report. Journal of Structural Geology, 21(8-9): 1049-1055. DOI:10.1016/s0191-8141(99)00023-1

Engelder, T., Lacazette, A., 1990. Natural hydraulic fracturing. In: Barton, N., Stephansson, O. (Eds.), Rock joints. A. A. Balkema, Rotterdam, pp. 35-44.

Erdős, P., Rényi, A., 1959. On random graphs I. Publicationes Mathematicae, 6: 290-297.

Erdős, P., Rényi, A., 1960. On the evolution of random graphs. Bulletin of the International Statistical Institute, 38(4): 343-347.

Evans, J.P., Chester, F.M., 1995. Fluid-rock interaction in faults of the San Andreas system: Inferences from San Gabriel fault rock geochemistry and microstructures. Journal of Geophysical Research-Solid Earth, 100(B7): 13007-13020. DOI:10.1029/94jb02625

Faulkner, D.R., Armitage, P.J., 2013. The effect of tectonic environment on permeability development around faults and in the brittle crust. Earth and Planetary Science Letters, 375: 71-77. DOI:http://dx.doi.org/10.1016/j.epsl.2013.05.006

Faulkner, D.R. et al., 2010. A review of recent developments concerning the structure, mechanics and fluid flow properties of fault zones. Journal of

Structural Geology, 32(11): 1557-1575. DOI:http://dx.doi.org/10.1016/j.jsg.2010.06.009

Fisher, D.M., Brantley, S.L., 1992. Models of quartz overgrowth and vein formation - Deformation and episodic fluid-flow in an ancient subduction zone. Journal of Geophysical Research-Solid Earth, 97(B13): 20043-20061. DOI:10.1029/92jb01582

Fisher, D.M., Brantley, S.L., Everett, M., Dzvonik, J., 1995. Cyclic fluid flow through a regionally extensive fracture network within the Kodiak accretionary prism. Journal of Geophysical Research-Solid Earth, 100(B7): 12881-12894. DOI:10.1029/94jb02816

Flekkøy, E.G., Malthe-Sørenssen, A., Jamtveit, B., 2002. Modeling hydrofracture. Journal of Geophysical Research-Solid Earth, 107(B8). DOI:10.1029/2000jb000132

Fossen, H., 2010. Structural Geology. Cambridge University Press, New York, USA.

Fyfe, W.S., Price, N.J., Thompson, A.B., 1978. Fluids in the Earth's crust. Elsevier, Amsterdam.

Ghani, I., Koehn, D., Toussaint, R., Passchier, C.W., 2013. Dynamic development of hydrofracture. Pure and Applied Geophysics, 170(11): 1685-1703. DOI:10.1007/s00024-012-0637-7

Goehring, L., Conroy, R., Akhter, A., Clegg, W.J., Routh, A.F., 2010. Evolution of mud-crack patterns during repeated drying cycles. Soft Matter, 6(15): 3562-3567. DOI:10.1039/B922206E

Gomez-Rivas, E. et al., 2014. The Jabal Akhdar dome in the Oman Mountains: evolution of a dynamic fracture system. American Journal of Science, 314(7): 1104-1139. DOI:10.2475/07.2014.02

Goren, L., Aharonov, E., Sparks, D., Toussaint, R., 2010. Pore pressure evolution in deforming granular material: A general formulation and the infinitely stiff approximation. Journal of Geophysical Research, 115(B9). DOI:10.1029/2009jb007191

Goren, L., Aharonov, E., Sparks, D., Toussaint, R., 2011. The Mechanical Coupling of Fluid-Filled Granular Material Under Shear. Pure and Applied Geophysics, 168(12): 2289-2323. DOI:10.1007/s00024-011-0320-4

Gross, M.R., Eyal, Y., 2007. Throughgoing fractures in layered carbonate rocks. Geological Society of America Bulletin, 119(11-12): 1387-1404. DOI:10.1130/0016-7606(2007)119[1387:tfilcr]2.0.co;2

Gu, H., Siebrits, E., 2008. Effect of formation modulus contrast on hydraulic fracture height containment. SPE Production & Operations, 23(2): 170-176.

Hacker, B.R., 1997. Diagenesis and fault valve seismicity of crustal faults. Journal of Geophysical Research: Solid Earth, 102(B11): 24459-24467. DOI:10.1029/97JB02025

Hafver, A. et al., 2014. Classification of fracture patterns by heterogeneity and topology. EPL (Europhysics Letters), 105(5): 56004.

Haimson, B.C., 1978. The hydrofracturing stress measuring method and recent field results. International Journal of Rock Mechanics and Mining Sciences & Geomechanics Abstracts, 15(4): 167-178. DOI:http://dx.doi.org/10.1016/0148-9062(78)91223-8

Hancock, P.L., 1985. Brittle microtectonics - Principles and practice. Journal of Structural Geology, 7(3-4): 437-457. DOI:10.1016/0191-8141(85)90048-3

Healy, D., 2008. Damage patterns, stress rotations and pore fluid pressures in strike-slip fault zones. Journal of Geophysical Research: Solid Earth, 113(B12): B12407. DOI:10.1029/2008JB005655

Healy, D., 2009. Anisotropy, pore fluid pressure and low angle normal faults. Journal of Structural Geology, 31(6): 561-574. DOI:http://dx.doi.org/10.1016/j.jsg.2009.03.001

Hickman, S., Sibson, R., Bruhn, R., 1995. Introduction to special section - Mechanical involvement of fluids in faulting. Journal of Geophysical Research-Solid Earth, 100(B7): 12831-12840. DOI:10.1029/95jb01121

Hickman, S.H., Zoback, M.D., 1983. The interpretation of hydraulic fracturing pressure-time data for in-situ stress determination. In: Zoback, M.D., Haimson, B.C. (Eds.), Hydraulic Fracturing Stress Measurements. National Academy Press, Washington, pp. 44-54.

Hilgers, C., Koehn, D., Bons, P.D., Urai, J.L., 2001. Development of crystal morphology during unitaxial growth in a progressively widening vein: II. Numerical simulations of the evolution of antitaxial fibrous veins. Journal of Structural Geology, 23(6-7): 873-885. DOI:10.1016/s0191-8141(00)00160-7

Hilgers, C., Urai, J.L., 2002a. Experimental study of syntaxial vein growth during lateral fluid flow in transmitted light: first results. Journal of Structural Geology, 24(6-7): 1029-1043. DOI:10.1016/s0191-8141(01)00089-x

Hilgers, C., Urai, J.L., 2002b. Microstructural observations on natural syntectonic fibrous veins: implications for the growth process. Tectonophysics, 352(3-4): 257-274. DOI:10.1016/s0040-1951(02)00185-3

Hillis, R.R., 2003. Pore pressure/stress coupling and its implications for rock failure. Subsurface Sediment Mobilization, 216: 359-368. DOI:10.1144/gsl.sp.2003.216.01.23

Holland, M., Urai, J.L., 2010. Evolution of anastomosing crack-seal vein networks in limestones Insight from an exhumed high-pressure cell, Jabal Shams, Oman Mountains. Journal of Structural Geology, 32(9): 1279-1290. DOI:10.1016/j.jsg.2009.04.011

Hoogerduijn Strating, E.H., 1994. Extensional faulting in an intraoceanic subduction complex—working hypothesis for the Palaeogene of the Alps-Apennine system. Tectonophysics, 238(1–4): 255-273. DOI:http://dx.doi.org/10.1016/0040-1951(94)90059-0

Hu, J.C., Angelier, J., 2004. Stress permutations: Three-dimensional distinct element analysis accounts for a common phenomenon in brittle tectonics. Journal of Geophysical Research-Solid Earth, 109(B9). DOI:10.1029/2003jb002616

Hubbert, M.K., Rubey, W.W., 1959. Role of fluid pressure in mechanics of overthrust faulting: I. Mechanics of fluid-filled porous solids and its applications to overthrust faulting. Geological Society of America Bulletin, 70(2): 115-166.

Hubbert, M.K., Willis, D.G., 1957. Mechanics of hydraulic fracturing. Petroleum Transactions, AIME, 210: 153-168.

Hunt, J.M., 1990. Generation and migration of petroleum from abnormally pressured fluid compartments. AAPG Bulleting, 74: 1-12.

Jamtveit, B., Yardley, B.W.D., 1997. Fluid flow and transport in rocks: an overview. In: Jamtveit, B., Yardley, B.W.D. (Eds.), Fluid Flow and Transport in Rocks. Springer, Netherlands, pp. 320.

Johnsen, Ø., Toussaint, R., Måløy, K.J., Flekkøy, E.G., 2006. Pattern formation during air injection into granular materials confined in a circular Hele-Shaw cell. Physical Review E, 74(1). DOI:10.1103/PhysRevE.74.011301

Johnsen, Ø., Toussaint, R., Måløy, K.J., Flekkøy, E.G., Schmittbuhl, J., 2008. Coupled air/granular flow in a linear Hele-Shaw cell. Physical Review E, 77(1). DOI:10.1103/PhysRevE.77.011301

Jolley, S.J., Fisher, Q.J., Ainsworth, R.B., 2010. Reservoir Compartmentalization: an introduction. In: Jolley, S.J., Fisher, Q.J., Ainsworth, R.B., Vrolijk, P.J., Delisle, S. (Eds.), Reservoir Compartmentalization, Special Publications. Geological Society of London, pp. 362. DOI:10.1144/sp347

Kobchenko, N. et al., 2013. Drainage fracture networks in elastic solids with internal fluid generation. EPL (Europhysics Letters), 102(6): 66002.

Koehn, D., Arnold, J., Passchier, C.W., 2005. Fracture and vein patterns as indicators of deformation history: a numerical study. Deformation Mechanisms, Rheology and Tectonics: from Minerals to the Lithosphere, 243: 11-24. DOI:10.1144/gsl.sp.2005.243.01.03

Koehn, D., Hilgers, C., Bons, P.D., Passchier, C.W., 2000. Numerical simulation of fibre growth in antitaxial strain fringes. Journal of Structural Geology, 22(9): 1311-1324. DOI:http://dx.doi.org/10.1016/S0191-8141(00)00039-0

Latora, V., Marchiori, M., 2001. Efficient behavior of small-world networks. Physics Review Letters, 87(198701).

Leoni, L., Marroni, M., Sartori, F., Tamponi, M., 1996. Metamorphic grade in metapelites of the internal liguride units (Northern Apennines, Italy). European Journal of Mineralogy, 8(1): 35-50.

Mahrer, K.D., 1999. A review and perspective on far-field hydraulic fracture geometry studies. Journal of Petroleum Science and Engineering, 24(1): 13-28. DOI:10.1016/s0920-4105(99)00020-0

Mao, J. et al., 2008. The relationship of mantle-derived fluids to gold metallogenesis in the Jiaodong Peninsula: Evidence from D-O-C-S isotope systematics. Ore Geology Reviews, 33(3-4): 361-381. DOI:10.1016/j.oregeorev.2007.01.003

Marchiori, M., Latora, V., 2000. Harmony in the small-world. Physica A, 285(3-4): 539-546. DOI:10.1016/s0378-4371(00)00311-3

Marroni, M., 1991. Deformation history of the Mt. Gottero Unit (Integral Ligurid units, Northern Apennines). Bollettino della Societá Geologica Italiana, 110: 727-736.

Marroni, M., 1994. Deformation path of the Internal Liguride Units (Northern Apennine, Italy): record of shallow level underplating in the Alpine accretionary wedge. Memoire della Societá Geologica Italiana, 47: 179-194.

Marroni, M., Pandolfi, L., 1996. The deformation history of an accreted ophiolite sequence: The Internal Liguride units (northern Apennines, Italy). Geodinamica Acta, 9(1): 13-29.

Marroni, M., Pandolfi, L., 2007. The architecture of an incipient oceanic basin: a tentative reconstruction of the Jurassic Liguria-Piemonte basin along the Northern Apennines-Alpine Corsica transect. International Journal of Earth Sciences, 96(6): 1059-1078. DOI:10.1007/s00531-006-0163-x

Mauldon, M., Dunne, W.M., Rohrbaugh, M.B., 2001. Circular scanlines and circular windows: new tools for characterizing the geometry of fracture traces. Journal of Structural Geology, 23(2-3): 247-258. DOI:10.1016/s0191-8141(00)00094-8

Mazzarini, F., Isola, I., Ruggieri, G., Boschi, C., 2010. Fluid circulation in the upper brittle crust: Thickness distribution, hydraulic transmissivity fluid inclusion and isotopic data of veins hosted in the Oligocene sandstones of the Macigno Formation in southern Tuscany, Italy. Tectonophysics, 493(1-2): 118-138. DOI:10.1016/j.tecto.2010.07.012

McCulloch, M.T., Gamble, J.A., 1991. Geochemical and geodynamical constraints on subduction zone magmatism. Earth and Planetary Science Letters, 102(3-4): 358-374. DOI:10.1016/0012-821x(91)90029-h

McDermott, C.I., Edlmann, K., Haszeldine, R.S., 2013. Predicting hydraulic tensile fracture spacing in strata-bound systems. International Journal of Rock Mechanics and Mining Sciences, 63: 39-49. DOI:10.1016/j.ijrmms.2013.06.004

McNamara, S., Flekkøy, E.G., Måløy, K.J., 2000. Grains and gas flow: Molecular dynamics with hydrodynamic interactions. Physical Review E, 61(4): 4054-4059. DOI:10.1103/PhysRevE.61.4054

Meneghini, F., Marroni, M., Moore, J.C., Pandolfi, L., Rowe, C.D., 2009. The processes of underthrusting and underplating in the geologic record: structural diversity between the Franciscan Complex (California), the Kodiak Complex (Alaska) and the Internal Ligurian Units (Italy). Geological Journal, 44(2): 126-152. DOI:10.1002/gj.1144

Meneghini, F., Marroni, M., Pandolfi, L., 2007. Fluid flow during accretion in sediment-dominated margins: Evidence of a high-permeability fossil fault zone from the Internal Ligurian accretionary units of the Northern Apennines, Italy. Journal of Structural Geology, 29(3): 515-529. DOI:10.1016/j.jsg.2006.10.003

Milgram, S., 1967. The small-world problem. Psychology Today, 1(1): 61-67.

Molli, G., 2008. Northern Apennine-Corsica orogenic system: an updated overview. Tectonic Aspects of the Alpine-Dinaride-Carpathian System, 298: 413-442. DOI:10.1144/sp298.19

Molli, G., Malavieille, J., 2011. Orogenic processes and the Corsica/Apennines geodynamic evolution: insights from Taiwan. International Journal of Earth Sciences, 100(5): 1207-1224. DOI:10.1007/s00531-010-0598-y

Montomoli, C., 2002. Vein development and fluid inclusion data: insight on the evolution of the Tuscan Nappe in the Northern Apennines. Bollettino della Societá Geologica Italiana, 1: 801-817.

Mourgues, R., Cobbold, P.R., 2003. Some tectonic consequences of fluid overpressures and seepage forces as demonstrated by sandbox modelling. Tectonophysics, 376(1-2): 75-97. DOI:10.1016/s0040-1951(03)00348-2

Mourgues, R., Gressier, J.B., Bodet, L., Bureau, D., Gay, A., 2011. "Basin scale" versus "localized" pore pressure/stress coupling - Implications for trap integrity evaluation. Marine and Petroleum Geology, 28(5): 1111-1121. DOI:10.1016/j.marpetgeo.2010.08.007

Munjiza, A., Owen, D.R.J., Bicanic, N., 1995. A combined finite-discrete element method in transient dynamics of fracturing solids. Engineering Computations, 12(2): 145-174. DOI:10.1108/02644409510799532

Narr, W., Suppe, J., 1991. Joint spacing in sedimentary rocks. Journal of Structural Geology, 13(9): 1037-1048. DOI:10.1016/0191-8141(91)90055-n

Navon, O., Hutcheon, I.D., Rossman, G.R., Wasserburg, G.J., 1988. Mantle-derived fluids in diamond micro-inclusions. Nature, 335(6193): 784-789. DOI:10.1038/335784a0

Nermoen, A. et al., 2010. Experimental and analytic modeling of piercement structures. Journal of Geophysical Research-Solid Earth, 115. DOI:10.1029/2010jb007583

Newman, M.E.J., 2002. Assortative mixing in networks. Physical Review Letters, 89(20). DOI:10.1103/PhysRevLett.89.208701

Newman, M.E.J., 2003. The structure and function of complex networks. SIAM Review, 45(2): 167-25.

Newman, M.E.J., Strogatz, S.H., Watts, D.J., 2001. Random graphs with arbitrary degree distributions and their applications. Physical Review E, 64(2): 026118.

Niebling, M.J., Flekkøy, E.G., Måløy, K.J., Toussaint, R., 2010. Sedimentation instabilities: Impact of the fluid compressibility and viscosity. Physical Review E, 82(5). DOI:10.1103/PhysRevE.82.051302

Niebling, M.J., Toussaint, R., Flekkøy, E.G., Måløy, K.J., 2012. Dynamic aerofracture of dense granular packings. Physical Review E, 86(6).

Nilsen, T.H., Abbate, E., 1984. Submarine-fan facies associations of the Upper Cretaceous and Paleocene Gottero Sandstone, Ligurian Apennines, Italy. Geo-Marine Letters, 3: 193-197. DOI:10.1007/BF02462465

Norman, L.B., Lloyd, E.K., Wilson, R.J., 1986. Graph theory 1736-1936. Clarendon Press, 252 pp.

Oliver, J., 1986. Fluids expelled tectonically from orogenic belts - Their role in hydrocarbon migration and other geologic phenomena. Geology, 14(2): 99-102. DOI:10.1130/0091-7613(1986)14<99:fetfob>2.0.co;2

Oliver, N.H.S., 1996. Review and classification of structural controls on fluid flow during regional metamorphism. Journal of Metamorphic Geology, 14(4): 477-492. DOI:10.1046/j.1525-1314.1996.00347.x

Oliver, N.H.S., Bons, P.D., 2001. Mechanisms of fluid flow and fluid-rock interaction in fossil metamorphic hydrothermal systems inferred from vein-wallrock patterns, geometry and microstructure. Geofluids, 1(2): 137-162. DOI:10.1046/j.1468-8123.2001.00013.x

Olson, J.E., Laubach, S.E., Lander, R.H., 2009. Natural fracture characterization in tight gas sandstones: Integrating mechanics and diagenesis. AAPG Bulletin, 93(11): 1535-1549. DOI:10.1306/08110909100

Osborne, M.J., Swarbrick, R.E., 1997. Mechanisms for generating overpressure in sedimentary basins: A reevaluation. AAPG Bulletin, 81(6): 1023-1041.

Pahl, P.J., 1981. Estimating the mean length of discontinuity traces. International Journal of Rock Mechanics and Mining Sciences & Geomechanics Abstracts, 18(3): 221-228. DOI:http://dx.doi.org/10.1016/0148-9062(81)90976-1

Park, W.C., Schot, E.H., 1968. Stylolites - Their nature and origin. Journal of Sedimentary Petrology, 38(1): 175-&.

Passchier, C.W., Trouw, R.A.J., 2005. Microtectonics. Springer-Verlag Berlin Heidelberg.

Patacca, E., Scandone, P., 1989. Post-Tortonian mountain buildingin the Apennines. The role of passive sinking of a relict lithospheric slab. In: Boriani, A., Bonafede, M., Piccardo, G.B., Vai, G.B. (Eds.), The Lithosphere in Italy: Advances in Earth Science Research. Accademia Nazionale Lincei, Rome, pp. 157-176.

Peiró, J., Sherwin, S., 2005. Finite Difference, Finite Element and Finite Volume Methods for Partial Differential Equations. In: Sidney, Y. (Ed.), Handbook of Materials Modeling. Springer Netherlands, pp. 2415-2446. DOI:10.1007/978-1-4020-3286-8_127

Perrone, V., Perrotta, S., Marsaglia, K., Di Staso, A., Tiberi, V., 2014. The Oligocene ophiolite-derived breccias and sandstones of the Val Marecchia Nappe: Insights for paleogeography and evolution of Northern Apennines (Italy). Palaeogeography Palaeoclimatology Palaeoecology, 394: 128-143. DOI:10.1016/j.palaeo.2013.11.024

Pollard, D.D., Segall, P., 1987. Theoretical displacements and stresses near fractures in rocks: with application to faults, joints, veins, dikes, and solution surfaces. In: Atkinson, B.K. (Ed.), Fracture Mechanics of Rock. Academic Press, London, pp. 277-350.

Press, W.H., Teukolsky, S.A., Vetterling, W.T., Flannery, B.P., 1992. Numerical recipes in C (2nd ed.): the art of scientific computing. Cambridge University Press, 994 pp.

Priest, S.D., Hudson, J.A., 1981. Estimation of discontinuity spacing and trace length using scanline surveys. International Journal of Rock Mechanics and Mining Sciences, 18(3): 183-197. DOI:10.1016/0148-9062(81)90973-6

Ramsay, J.G., 1980. The crack-seal mechanism of rock deformation. Nature, 284(5752): 135-139.

Ramsay, J.G., Huber, M.I., 1983. The Techniques of Modern Structural Geology, volume I. Academic Press, London.

Ramsey, J.M., Chester, F.M., 2004. Hybrid fracture and the transition from extension fracture to shear fracture. Nature, 428(6978): 63-66. DOI:10.1038/nature02333

Renard, F., Gratier, J.-P., Jamtveit, B., 2000. Kinetics of crack-sealing, intergranular pressure solution, and compaction around active faults. Journal of Structural Geology, 22(10): 1395-1407. DOI:http://dx.doi.org/10.1016/S0191-8141(00)00064-X

Rice, J.R., Cleary, M.P., 1976. Some basic stress diffusion solutions for fluid-saturated elastic porous media with compressible constituents. Reviews of Geophysics and Space Physics, 14: 227-241.

Rijken, P., Cooke, M.L., 2001. Role of shale thickness on vertical connectivity of fractures: application of crack-bridging theory to the Austin Chalk, Texas. Tectonophysics, 337(1-2): 117-133. DOI:10.1016/s0040-1951(01)00107-x

Rodrigues, N., Cobbold, P.R., Loseth, H., 2009. Physical modelling of sand injectites. Tectonophysics, 474(3-4): 610-632. DOI:10.1016/j.tecto.2009.04.032

Rohrbaugh, M.B., Dunne, W.M., Mauldon, M., 2002. Estimating fracture trace intensity, density, and mean length using circular scan lines and windows. AAPG Bulletin, 86(12): 2089-2104.

Rosenbaum, G., Lister, G.S., Duboz, C., 2002. Reconstruction of the tectonic evolution of the western Mediterranean since the Oligocene. Journal of the Virtual Explorer, 8: 107-130.

Rozhko, A.Y., 2010. Role of seepage forces on seismicity triggering. Journal of Geophysical Research-Solid Earth, 115. DOI:10.1029/2009jb007182

Rozhko, A.Y., Podladchikov, Y.Y., Renard, F., 2007. Failure patterns caused by localized rise in pore-fluid overpressure and effective strength of rocks. Geophysical Research Letters, 34(22). DOI:10.1029/2007gl031696

Sanderson, D.J., Nixon, C.W., 2015. The use of topology in fracture network characterization. Journal of Structural Geology, 72(0): 55-66. DOI:http://dx.doi.org/10.1016/j.jsg.2015.01.005

Santiago, E., Velasco-Hernandez, J.X., Romero-Salcedo, M., 2014. A methodology for the characterization of flow conductivity through the identification of communities in samples of fractured rocks. Expert Systems with Applications, 41(3): 811-820. DOI:10.1016/j.eswa.2013.08.011

Schmidt, M.W., Poli, S., 1998. Experimentally based water budgets for dehydrating slabs and consequences for arc magma generation. Earth and Planetary Science Letters, 163(1-4): 361-379. DOI:10.1016/s0012-821x(98)00142-3

Scholtés, L., Donzé, F.V., 2013. A DEM model for soft and hard rocks: Role of grain interlocking on strength. Journal of the Mechanics and Physics of Solids, 61(2): 352-369. DOI:10.1016/j.jmps.2012.10.005

Scholz, C.H., 2002. The mechanics of earthquakes and faulting. Cambridge University Press, Camridge, United Kingdom.

Schöpfer, M.P.J., Arslan, A., Walsh, J.J., Childs, C., 2011. Reconciliation of contrasting theories for fracture spacing in layered rocks. Journal of Structural Geology, 33(4): 551-565. DOI:10.1016/j.jsg.2011.01.008

Shalev, E., Caló, M., Lyakhovsky, V., 2013. Formation of damage zone and seismic velocity variations during hydraulic simulation: numerical modelling and field observations. Geophysical Journal International, 195: 1023-1033.

Shapiro, S.A., Dinske, C., 2009. Fluid-induced seismicity: Pressure diffusion and hydraulic fracturing. Geophysical Prospecting, 57(2): 301-310. DOI:10.1111/j.1365-2478.2008.00770.x

Shepherd, T.J., Rankin, A.H., Alderton, D.H.M., 1985. A Practical Guide to Fluid Inclusion Studies. Blackie, Glasgow and London, 239 pp.

Sibson, R.H., 1996. Structural permeability of fluid-driven fault-fracture meshes. Journal of Structural Geology, 18(8): 1031-1042. DOI:10.1016/0191-8141(96)00032-6

Sibson, R.H., Moore, J.M.M., Rankin, A.H., 1975. Seismic pumping—a hydrothermal fluid transport mechanism. Journal of the Geological Society: 653-659.

Simonson, E.R., Abousayed, A.S., Clifton, R.J., 1978. Containment of massive hydraulic fractures. Society of Petroleum Engineers Journal, 18(1): 27-32.

Smith, M.B. et al., 2001. Layered Modulus Effects on Fracture Propagation, Proppant Placement, and Fracture Modeling, SPE Annual Technical Conference and Exhibition, 30 September - 3 October. Society of Petroleum Engineers, New Orleans, Louisiana. DOI:10.2118/71654-MS

Snijders, T.A.B., 1981. The degree variance: An index of graph heterogeneity. Social Networks, 3(3): 163-174.

Stampfli, G.M., 2000. Tethyan oceans. In: Bozkurt, E., Winchester, J.A., Piper, J.D.A. (Eds.), Tectonics and Magmatism in Turkey and the Surrounding Area. Geological Society, London, Special Publications, pp. 1-23.

Stampfli, G.M., 2005. Plate tectonics of the Apulia-Adria cicrocontinents. In: Finetti, I.R. (Ed.), CROP PROJECT: Deep Seismic Exploration of the Central Mediterranean and Italy, Atlases in Geoscience. Elsevier B. V., pp. 747-766.

Stampfli, G.M., Hochard, C., 2009. Plate tectonics of the Alpine realm. Ancient Orogens and Modern Analogues, 327: 89-111.

Swarbrick, R.E., Osborne, M.J., Yardley, G.S., 2002. Comparison of overpressure magnitude resulting from the main generating mechanisms. In: Huffman, A.R., Bowers, G.L. (Eds.), Pressure Regimes in Sedimentary Basins and Their Prediction, AAPG Memoir, 76: 1-12.

Tang, C.A. et al., 2008. Fracture spacing in layered materials: A new explanation based on two-dimensional failure process modeling. American Journal of Science, 308(1): 49-72. DOI:10.2475/01.2008.02

Tenthorey, E., Cox, S.F., Todd, H.F., 2003. Evolution of strength recovery and permeability during fluid-rock reaction in experimental fault zones. Earth and Planetary Science Letters, 206(1-2): 161-172. DOI:10.1016/s0012-821x(02)01082-8

Terzaghi, K., 1923. Die Berechnung der Durchlässingkeitsziffer des Tones aus dem Verlauf der hydrodynamischen Spannungserscheinungen.

Sitzungsberichte der Akademie der Wissenschaften in Wien, mathematisch-naturwissenschaftliche Klasse, 132: 125-138.

Tzschichholz, F., Herrmann, H.J., Roman, H.E., Pfuff, M., 1994. Beam model for hydraulic fracturing. Physical Review B, 49(10): 7056-7059. DOI:10.1103/PhysRevB.49.7056

Urai, J.L., Williams, P.F., Vanroermund, H.L.M., 1991. Kinematics of crystal-growth in syntectonic fibrous veins. Journal of Structural Geology, 13(7): 823-836. DOI:10.1016/0191-8141(91)90007-6

Valkó, P., Economides, M.J., 1995. Hydraulic fracture mechanics. Wiley, Chichester, 318 pp.

van der Pluijm, B., Marshak, S., 2004. Earth Structure: An Introduction to Structural Geology and Tectonics. WW Norton, New York, USA.

van Wamel, W.A., 1987. On the tectonics of the Ligurian Apennines (northern Italy). Tectonophysics, 142(1): 87-98. DOI:10.1016/0040-1951(87)90296-4

van Wamel, W.A. et al., 1985. A structural geologic traverse through the Northern Apennines from Rapallo to Bettola (N. Italy). Geologie En Mijnbouw, 64(2): 181-197.

van Zutphen, A.C.A., van Wamel, W.A., Bons, A.J., 1985. The structure of the Lavagna Nappe in the region of Monte Ramaceto and Val Graveglia (Ligurian Apennines, Italy). Geologie En Mijnbouw, 64(4): 373-384.

Vass, A., Koehn, D., Toussaint, R., Ghani, I., Piazolo, S., 2014. The importance of fracture-healing on the deformation of fluid-filled layered systems. Journal of Structural Geology, 67: 94-106.

Vinningland, J.L., Johnsen, Ø., Flekkoy, E.G., Toussaint, R., Måløy, K.J., 2007a. Experiments and simulations of a gravitational granular flow instability. Physical Review E, 76(5). DOI:10.1103/PhysRevE.76.051306

Vinningland, J.L., Johnsen, Ø., Flekkøy, E.G., Toussaint, R., Måløy, K.J., 2007b. Experiments and simulations of a gravitational granular flow instability. Physical Review E, 76(5). DOI:10.1103/PhysRevE.76.051306

Vinningland, J.L., Johnsen, Ø., Flekkøy, E.G., Toussaint, R., Måløy, K.J., 2007c. Granular Rayleigh-Taylor instability: Experiments and simulations. Physical Review Letters, 99(4). DOI:10.1103/PhysRevLett.99.048001

Vinningland, J.L., Johnsen, Ø., Flekkøy, E.G., Toussaint, R., Måløy, K.J., 2010. Size invariance of the granular Rayleigh-Taylor instability. Physical Review E, 81(4). DOI:10.1103/PhysRevE.81.041308

Virgo, S., Abe, S., Urai, J.L., 2013. Extension fracture propagation in rocks with veins: Insight into the crack-seal process using Discrete Element Method modeling. Journal of Geophysical Research-Solid Earth, 118(10): 5236-5251. DOI:10.1002/2013jb010540

Virgo, S., Abe, S., Urai, J.L., 2014. The evolution of crack seal vein and fracture networks in an evolving stress field: Insights from Discrete Element Models of fracture sealing. Journal of Geophysical Research-Solid Earth, 119(12): 8708-8727. DOI:10.1002/2014jb011520

Wang, B., Tang, H., Guo, C., Xiu, Z., 2006. Entropy optimization of scale-free networks' robustness to random failures. Physica A: Statistical Mechanics and its Applications, 363(2): 591-596. DOI:http://dx.doi.org/10.1016/j.physa.2005.08.025

Wang, Y., Mora, P., 2008. Modeling wing crack extension: Implications for the ingredients of discrete element model. Pure and Applied Geophysics, 165(3-4): 609-620. DOI:10.1007/s00024-008-0315-y

Wangen, M., 1992. Pressure and temperature evolution in sedimentary basins. Geophysical Journal International, 110(3): 601-613. DOI:10.1111/j.1365-246X.1992.tb02095.x

Wangen, M., 2002. Effective permeability of hydrofractured sedimentary rocks, Norwegian Petroleum Society Special Publications. Elsevier, pp. 61-74. DOI:http://dx.doi.org/10.1016/S0928-8937(02)80007-8

Wangen, M., 2011. Finite element modeling of hydraulic fracturing on a reservoir scale in 2D. Journal of Petroleum Science and Engineering, 77(3–4): 274-285. DOI:http://dx.doi.org/10.1016/j.petrol.2011.04.001

Watkins, H., Bond, C.E., Healy, D., Butler, R.W.H., 2015. Appraisal of fracture sampling methods and a new workflow to characterise heterogeneous fracture networks at outcrop. Journal of Structural Geology, 72: 67-82. DOI:http://dx.doi.org/10.1016/j.jsg.2015.02.001

Watts, D.J., 1999. Small Worlds: The Dynamics of Networks between Order and Randomness. Princeton University Press, Princeton, NJ.

Watts, D.J., Strogatz, S.H., 1998. Collective dynamics of 'small-world' networks. Nature, 393(6684): 440-442.

Wu, H.Q., Pollard, D.D., 1995. An experimental study of the relationship between joint spacing and layer thickness. Journal of Structural Geology, 17(6): 887-905. DOI:10.1016/0191-8141(94)00099-l

Zeeb, C., Gomez-Rivas, E., Bons, P.D., Blum, P., 2013. Evaluation of sampling methods for fracture network characterization using outcrops. AAPG Bulletin, 97(9): 1545-1566. DOI:10.1306/02131312042